Simulation of Transient Effects in High-Temperature Superconducting Magnets

Simulation von transienten Effekten in supraleitenden Hochtemperatur-Magneten
Zur Erlangung des akademischen Grades Doktor-Ingenieur (Dr.-Ing.)
genehmigte Dissertation von Lorenzo Bortot aus Belluno, Italien
Fachbereich Elektrotechnik und Informationstechnik
Tag der Einreichung: 14.09.2021, Tag der Prüfung: 26.11.2021
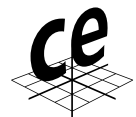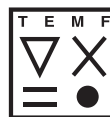
1. Gutachten: Prof. Dr. Sebastian Schöps
2. Gutachten: Prof. Dr. Benoît Vanderheyden
Darmstadt – D 17

CERN Supervisor: Dr. Ir. Matthias Mentink

TECHNISCHE
UNIVERSITÄT
DARMSTADT

T E M F

ce

Fachbereich Elektrotechnik
und Informationstechnik
Computational
Electromagnetics Group

Simulation of Transient Effects in High-Temperature Superconducting Magnets
Simulation von transienten Effekten in supraleitenden Hochtemperatur-Magneten

genehmigte Dissertation von Lorenzo Bortot aus Belluno, Italien
Fachbereich Elektrotechnik und Informationstechnik

1. Gutachten: Prof. Dr. Sebastian Schöps
2. Gutachten: Prof. Dr. Benoît Vanderheyden

Tag der Einreichung: 14.09.2021
Tag der Prüfung: 26.11.2021

Darmstadt – D 17

Erklärungen laut Promotionsordnung

§8 Abs. 1 lit. c PromO

Ich versichere hiermit, dass die elektronische Version meiner Dissertation mit der schriftlichen Version übereinstimmt.

§8 Abs. 1 lit. d PromO

Ich versichere hiermit, dass zu einem vorherigen Zeitpunkt noch keine Promotion versucht wurde. In diesem Fall sind nähere Angaben über Zeitpunkt, Hochschule, Dissertationsthema und Ergebnis dieses Versuchs mitzuteilen.

§9 Abs. 1 PromO

Ich versichere hiermit, dass die vorliegende Dissertation selbstständig und nur unter Verwendung der angegebenen Quellen verfasst wurde.

§9 Abs. 2 PromO

Die Arbeit hat bisher noch nicht zu Prüfungszwecken gedient.

Darmstadt, 14.09.2021

_____

Lorenzo Bortot

Philosophers are people who know less and less about more and more, until they know nothing about everything. Scientists are people who know more and more about less and less, until they know everything about nothing.

KONRAD LORENTZ

Zusammenfassung

Teilchenbeschleuniger sind wichtige Werkzeuge in der Hochenergiephysik, um die fundamentale Struktur von Materie zu untersuchen. In Ringbeschleunigern ist die Kollisionsenergie proportional zum ablenkenden magnetischen Feld und dem Radius des Rings. Als Folge verwenden Ringbeschleuniger wie der Large Hadron Collider am CERN traditionellerweise Magnete aus Niedrigtemperatur-Supraleitern, die starke Magnetfelder erzeugen, um die Ausmaße der Teilchenstrahlen auf akzeptable Dimensionen zu beschränken. Diese Klasse von Supraleitern weist ein praktisches Limit für die erreichbaren Magnetfelder innerhalb der Magnetöffnung von ungefähr $8\,\mathrm{T}$ für eine $\mathrm{Nb-Ti}$ Legierung und $16\,\mathrm{T}$ für eine $\mathrm{Nb_3Sn}$ Verbindung. Um diese Limitierungen in Beschleunigermagneten zu überwinden, müssen Hochtemperatur-Supraleiter (HTS) verwendet werden, insbesondere „rare-earth barium copper oxide" (ReBCO) Bänder.

Im Vergleich zu ihrem niedrigtemperatur-supraleitenden Gegenstück verhalten sich Beschleunigermagnete auf Basis von ReBCO Bändern unterschiedlich im Bezug auf die magnetische Feldqualität sowie die Absicherung gegen Quenches. Die Bänder sind äquivalent zu breiten und anisotropischen Mono-Filamenten, was zu Abschirmströmen führt, welche die Feldqualität insbesondere bei niedrigen Strömen negativ beeinflussen. Gleichzeitig ist das Auftreten von Quenches weniger wahrscheinlich aufgrund der größeren thermischen Stabilität der Bänder, die Detektion derselben und die anschließende Absicherung gegen deren Folgen gestaltet sich jedoch als schwieriger. Zudem wird das dynamische Verhalten von Beschleunigermagneten auch vom umliegenden elektrischen Schaltkreis beeinflusst, weswegen dieser berücksichtigt werden muss. Dies führt zu multiphysikalischen Multiskalen- und Multiratenproblemen. Numerische Methoden spielen eine zentrale Rolle, um die Herausforderungen im Bezug auf magnetische Feldqualität und Absicherung gegen Quenches zu überwinden.

In dieser Arbeit wird die magnetothermische Dynamik von hochtemperatur-supraleitenden Magneten mittels eines Wirbelstromproblems im Zeitbereich modelliert. Eine gemischte Feldformulierung wird entwickelt, um dem nichtlinearen spezifischen Widerstand der supraleitenden Materialien gerecht zu werden. Die Formulierung wird um Distributionsfunktionen erweitert, um externe Quellspannungen und/oder Quellströme ans Feldproblem zu koppeln. Weitere Vereinfachungen werden für den Fall von Bändern mit großen Aspektverhältnissen und multi-filamenten Leitern diskutiert. Weiterhin wird eine Kopplung von Feldproblem und Schaltkreis als optimierte Schwarz-Transmissionsbedingung hergeleitet, sodass die Formulierung zur Lösung solcher gekoppelten Probleme mittels Methoden der Co-Simulation eingesetzt werden kann. Die Implementierung der Formulierung in der Finite-Elemente-Methode wird mittels analytischer und Referenzlösungen aus der Literatur verifiziert und mittels Messungen des auf HTS basierenden Dipolmagnet Feather-M2 validiert.

Als Fallstudie wird die Formulierung auf „proof-of-concept" ReBCO Abschirmungen für passive Feldfehlerreduzierung in Beschleunigermagneten angewandt. Das vorgeschlagene Design heißt HALO („harmonics-absorbing layered object"), da es aus geschichteten Bändern besteht, welche voll skalier- und erweiterbar sind. Die Abschirmungen werden so positioniert, dass ihre persistente Magnetisierung das Magnetfeld im Inneren der Magnetöffnung formt und dabei ungewünschte Feldfehler ausgleicht. Experimentelle Messungen bei $77\,\mathrm{K}$ in flüssigem Stickstoff zeigen eine signifikante Reduktion des Feldfehlers, bis zu einem Faktor von vier. Außerdem verdeutlicht numerische Extrapolation für beschleunigerähnliche Bedingungen, dass ein sorgfältiges Design der supraleitenden Abschirmungen die typischen Anforderungen an die Feldqualität in Beschleunigermagneten erfüllt.

Abstract

Particle colliders for high-energy physics are important tools for investigating the fundamental structure of matter. In circular accelerators, the collision energy of particles is proportional to the bending magnetic field and the radius of the machine. As a consequence, circular accelerators such as the Large Hadron Collider at CERN have traditionally relied on high-field magnets made of low-temperature superconductors, confining the particle beams within a complex of acceptable dimensions. This class of superconductors shows a practical limit in the achievable magnetic field in the magnet aperture of about $8\,\mathrm{T}$ for a $\mathrm{Nb-Ti}$ alloy, and $16\,\mathrm{T}$ for a $\mathrm{Nb_3Sn}$ compound. Overcoming these limits requires the use of high-temperature superconductors (HTS) in accelerator magnets, in particular rare-earth barium copper oxide (ReBCO) tapes.

With respect to the low-temperature counterpart, accelerator magnets based on ReBCO tapes are known to behave differently in terms of magnetic field quality and protection from quench events. The tapes are equivalent to wide and anisotropic mono-filaments, resulting in screening currents detrimentally affecting the magnetic field quality, in particular at low currents. At the same time, quenches are less likely to occur due to the enhanced thermal stability of the tapes, but are more difficult to detect and mitigate. Moreover, the dynamic behavior of accelerator magnets is also affected by the surrounding circuitry which must be taken into account, leading to multiphysics, multirate and multiscale problems. Numerical methods play a crucial role for overcoming the challenges related to magnetic field quality and quench protection.

In this work, the magnetothermal dynamics in high-temperature superconducting magnets is modeled by means of an eddy-current problem in the time domain. A mixed field formulation is developed to cope with the nonlinear resistivity law of superconducting materials. The formulation is complemented with distribution functions for the coupling of external voltage and/or current source quantities. Further simplifications are discussed in case of tapes with high aspect ratio, and multifilamentary conductors. Moreover, a field-circuit coupling interface is derived as an optimized Schwarz transmission condition, such that the formulation can be used in field-circuit coupled problems by means of co-simulation methods. The implementation of the formulation in the finite element method is verified against analytical and reference solutions available in literature, and validated against measurements on the HTS-based dipole magnet Feather-M2.

As a case-study, the formulation is applied to proof-of-concept ReBCO screens for the passive field-error cancellation in accelerator magnets. The proposed design is called HALO (harmonics-absorbing layered object) as it is made of stacks of tapes arranged in layers which are fully scalable and expandable. The screens are positioned such that their persistent magnetization shapes the magnetic field in the magnet aperture, canceling the undesired field imperfections. Experimental measurements at $77\,\mathrm{K}$ in liquid nitrogen show a significant reduction of the field error, up to a factor of four. Moreover, numerical extrapolation for accelerator-like conditions shows that a careful design of the superconducting screens allows matching the typical field quality requirements for accelerator magnets.

Contents

List of figures

List of tables

1 Introduction

Particle colliders for high-energy physics are powerful tools for investigating the fundamental structure as well as the governing forces of matter. In circular accelerators, beams of charged particles traveling in opposite directions are accelerated by means of alternating electric fields generated within radio-frequency cavities. Lorentz forces act on the particles such that the beams are kept on a circular trajectory. Dipole and quadrupole magnets located all around the ring provide the steering force and the focusing effect, keeping the particles on the intended trajectory and preventing the beams from diverging. Once the particles reach the desired energy, they are made to collide at designated interaction points, where collisions are transformed into showers of particles which are subsequently studied in particle detectors. The energy of particles W_p and the consequent collision energy scales directly with the radius of the accelerator ring r_r and the bending dipole magnetic field B, that is, $W_p \propto r_r B$. Although a higher energy can be reached by increasing the radius of particle colliders, this may lead to unpractical dimensions. Therefore, it is necessary to use magnetic fields as high as possible, for which superconductivity is needed [1].

To date, the European Organization for Nuclear Research (CERN) operates near Geneva, Switzerland, the largest and most powerful circular accelerator in the world, the Large Hadron Collider (LHC) [3] which is shown in Figure 1.1. The LHC is located in a complex of tunnels about 100 m underground, featuring a ring of 27 km which is composed of eight arcs linked by straight sections, and organized in octants. Four interaction points host the main detectors ALICE [4], ATLAS [5], CMS [6] and LHCb [7], optimized for tracking the particle showers from collisions. The LHC consists of over 1500 main dipole and quadrupole superconducting
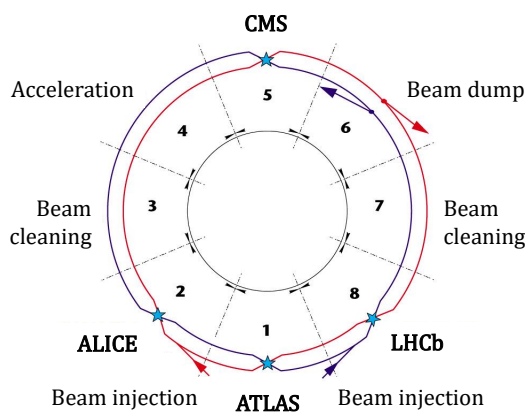
(a) LHC schematic representation.
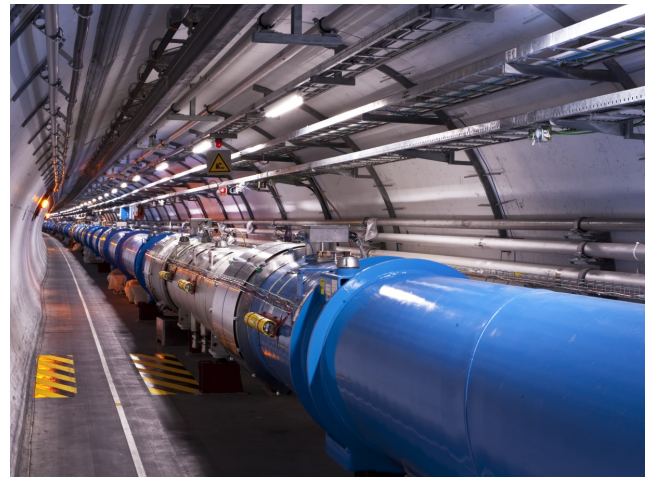
(b) LHC tunnel.

Figure 1.1. The Large Hadron Collider. (a) Schematic representation highlighting the octants and the interaction points. (b) Photograph taken in the tunnel of the LHC. Figures taken from [2], © CERN.

(a) Cross section of the magnet.
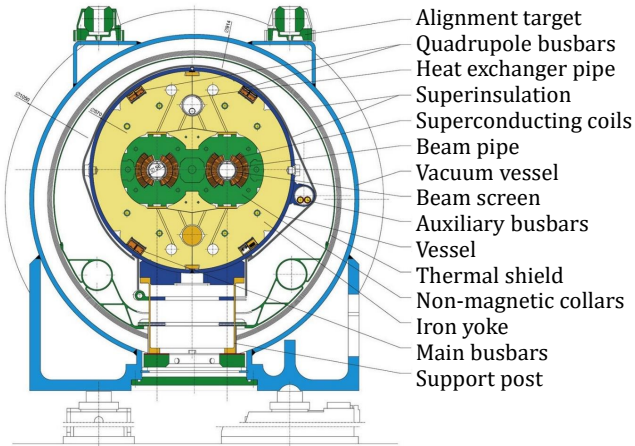
| Alignment target |
| Quadrupole busbars |
| Heat exchanger pipe |
| Superinsulation |
| Superconducting coils |
| Beam pipe |
| Vacuum vessel |
| Beam screen |
| Auxiliary busbars |
| Vessel |
| Thermal shield |
| Non-magnetic collars |
| Iron yoke |
| Main busbars |
| Support post |
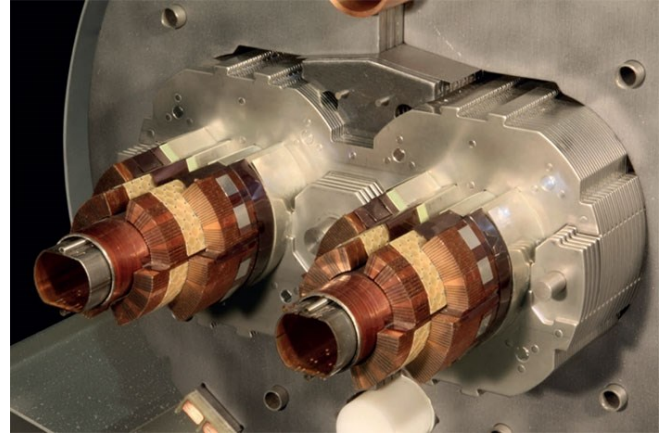
(b) Cut-away demonstration model.

Figure 1.2. LHC main bending dipole magnet. (a) Cross section of the magnet, highlighting the main components. (b) Photograph of a cut-away demonstration model. Figures taken from [2], © CERN.

magnets, operated at the cryogenic temperature of $1.9\,$K. Liquid helium in superfluid state [8] is used as a coolant, since it is a very effective thermal stabilizer. Thanks to the lack of electrical resistance, superconducting coils can withstand high densities of current, making it possible to implement compact designs reaching much higher magnetic fields than the typical $1.5\,$T in traditional iron-cored, copper-coil magnets. The 15-m-long dipole magnets used for bending the particle beams produce a nominal magnetic field of $8.33\,$T when operated at a current corresponding to the intended maximum collision energy of $14\,$TeV. Figure 1.2 shows the cross section of an LHC main bending dipole magnet and the surrounding structure with the principal components. The twin-aperture design comprises two ultra-high vacuum beam pipes and dipole coils embedded in the same iron yoke, mechanical structure, and cryostat. Within each LHC octant, the magnets are electrically connected in series, composing a circuit which spans over $7\,$km length within $3.5\,$km of tunnel and includes for example power converters and energy-extraction resistors, warm and cold busbars, current leads, bypass diodes, and diagnostic systems. The total energy stored in a superconducting circuit is equal to the sum of energies stored in the magnetic field of each magnet, and can exceed $1\,$GJ. If released in an uncontrolled way, this stored energy can lead to irreversible damage. Therefore, dedicated circuit and magnet protection systems must be put in place. The analysis of circuits containing superconducting magnets and their protection systems is crucial to ensure smooth operations in particle accelerators.

The energy of particles W_{p} is of paramount importance because it determines which particles are created during collisions, and may be consequently discovered. The successor of the LHC, named the Future Circular Collider (FCC) [9] is already under study, a $80\,$km long accelerator using $16\,$T dipole magnets, aiming in the next decades at proton-proton collision energies of $100\,$TeV.

1.1 Superconductivity for Magnets

This section introduces basic concepts of superconductivity which are relevant for applications; for an in-depth discussion see for example [10]. The phenomenon of superconductivity was firstly observed in 1911 [11] as the complete vanishing of the electrical resistance in certain materials, occurring below a certain critical

temperature T_c. Superconducting materials are classified into the type-I and type-II superconductors, depending on their behavior with respect to an externally applied magnetic field. Type-I superconductors are typically chemical elements such as mercury, lead, and aluminum, and while entering the superconducting state, they generate electric currents which expel the magnetic field. This phenomenon is known as the Meissner-Ochsenfeld effect [12], and it can occur only for magnetic fields below a critical field B_c, above which the superconductivity is lost.

Type-II superconductors include alloys and compounds such as niobium titanium (Nb-Ti), niobium tin (Nb$_3$Sn) and rare-earth barium copper oxides (ReBCO). These materials feature both a first critical field B_{c1}, and an upper critical field B_{c2}. As B_{c2} is typically orders of magnitude higher than B_{c1}, type-II superconductors are suitable for practical applications. Below B_{c1}, the behavior of type-I and type-II superconductors is identical. Once B_{c1} is exceeded, the magnetic field penetrates in the material through Abrikosov vortices [13], each carrying a flux quantum which is surrounded by screening currents. The result is a mixed state where the normal conducting center of the vortices is surrounded by material in superconducting state. Depending on the material and its micro-structure, some or all of the vortices are located on micro-structural defects in the material, resulting in a behavior known as flux pinning [1]. When a current is applied to the material, and a magnetic field transverse to the direction of the current is present, then the vortices are exposed to Lorentz forces. However, it is energetically favorable for the vortices located on micro-structural defects to remain there, and the equivalent force holding the vortices in place (either directly for vortices located on pinning sites or indirectly through mutual repulsion for unpinned vortices) is known as the pinning force. If the Lorentz force exceeds the pinning force, the vortices start to move and dissipate energy, and the property of zero resistance is lost. The critical current density J_c is the current density at which the pinning force and Lorentz force are equal in magnitude and opposite in direction. A superconducting material may conveniently be described with the parameters T_c, B_{c2}, and J_c. These three parameters span a critical surface $f(T_c, B_{c2}, J_c) = 0$ which defines limits for temperature, magnetic field and current density below which a material is in the superconducting state. The critical surfaces of the Nb-Ti, Nb$_3$Sn and ReBCO materials are shown in Figure 1.3a and 1.3b [14]. In addition, other parameters influence these three parameters as well, for example magnetic field orientation, strain and radiation load.

Type-II superconductors are traditionally subclassified into low-temperature superconductors (LTS) and high-temperature superconductors (HTS), depending whether T_c exceeds the boiling temperature of liquid nitrogen at 77 K. The difference between the operational temperature of superconductors and T_c determines a enthalpy margin which is beneficial against thermal perturbations. The most commonly used 'workhorse' is the type-II superconductor Nb-Ti. This material is ductile and can be manufactured in multifilamentary twisted wires, referred at as strands in the following, of length up to several kilometers. In the LHC, the main bending dipole magnets are wound using a fully-transposed cable, known as Rutherford cable, which is composed of Nb-Ti strands. The critical surface of Nb-Ti limits the magnetic field for practical applications to about 9 T [1]. Therefore, to exceed this field in the next generation accelerators the use of Nb$_3$Sn is foreseen. However, this material is brittle, complicating the manufacturing of superconducting coils. The filaments of Nb and Sn are initially separated in the coil, forming the compound only after several days of reaction at relatively high temperatures, up to over 900 K, in a technological process called wind-and-react, see for example [15]. After the heat treatment, the coil is usually impregnated using an epoxy resin to protect the brittle superconductor. In the context of FCC, the main bending dipole magnets are expected to be constructed with Nb$_3$Sn, with an intended magnetic field up to 16 T [9].

(a) Nb-Ti *and* Nb$_3$Sn *materials.*   (b) ReBCO *material.*
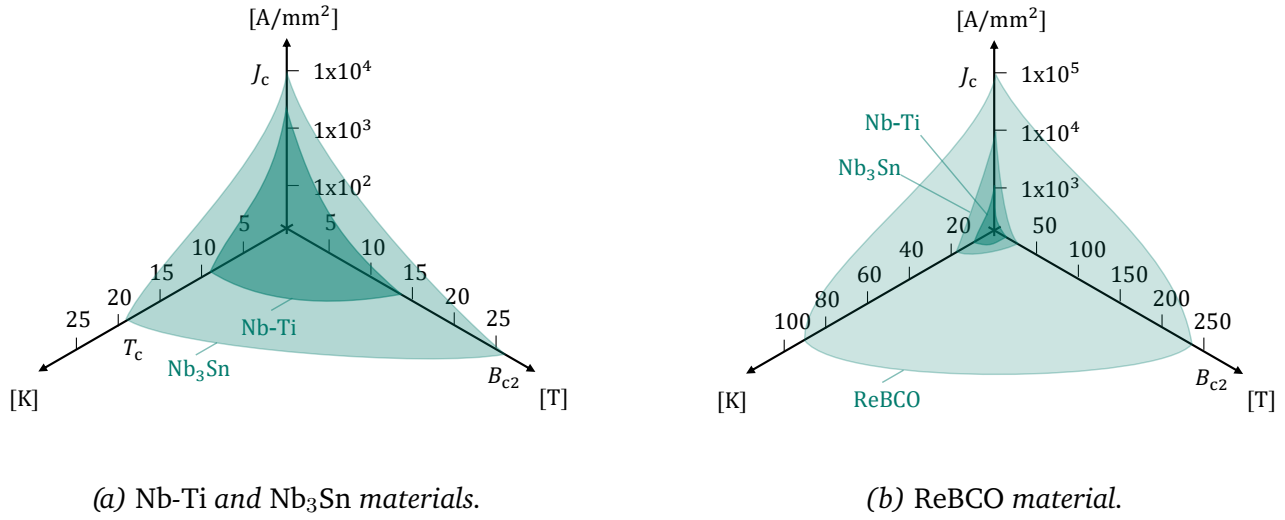
Figure 1.3. Comparison of the critical surfaces of Nb-Ti *and* Nb$_3$Sn*, and* ReBCO *materials.*

1.2 High-Temperature Superconductors

To date, a possibility for exceeding the magnetic field limits posed by Nb$_3$Sn is given by high-temperature superconducting (HTS) materials. As an example, YBCO compounds which were discovered in 1986 have an estimated upper critical field of $140\,\mathrm{T}$ [16] and a critical temperature of $93\,\mathrm{K}$ (See Figure 1.3). Consequently, HTS materials can potentially be used in superconducting magnets for boosting magnetic fields beyond 20 T [17], and with enthalpy margins one order of magnitude above traditional LTS materials. As a consequence, and in view of possible future accelerator projects including FCC, the use of high-temperature superconductors in accelerator-type dipole magnets is under exploration; see [18] for an overview. A significant milestone was recently achieved within the EuCARD-2 [19] and ARIES [20] projects, which led to the construction of the HTS accelerator dipole insert-magnet Feather-M2.1-2 [21, 22]. This demonstrator magnet is designed to operate inside the aperture of the Nb$_3$Sn FRESCA2 dipole magnet [23, 24], producing a peak field of $5\,\mathrm{T}$ at a nominal current of $10\,\mathrm{kA}$, in a background field of $13\,\mathrm{T}$.

At present, two main HTS conductors are available and sufficiently mature for applications in demonstration magnets [18]. The first is based on the Bi-2212 compound which belongs to the family of bismuth strontium calcium copper oxides (BSCCO) [25, 26], and it is manufactured in the shape of a strand. The second belongs to the family of rare-earth barium copper oxides (ReBCO) [27], where the rare earth element Re can be yttrium, gadolinium, and others. ReBCO conductors are available in form of thin film deposited on a carrier inside a tape. In comparison with Bi-2212, ReBCO tapes do not require any heat treatment, are more resistant to mechanical stress, and typically allow for higher engineering critical current density, that is, the equivalent critical current density in the overall cross section of the conductor [28]. At the same time, the cost of raw materials for ReBCO is not the principal factor in determining the cost of conductor, leaving room for potential cost reductions thanks to mass production. Also, ReBCO conductors are generally considered for power applications, and are more commonly used.

ReBCO conductors are made of a multilayered composite structure, as shown in Figure 1.4. The substrate, made of either stainless steel or Hastelloy (e.g. C-276), contributes towards mechanical robustness and provides the surface for the growth of thin films. A series of thin buffer layers of up to $1\,\mathrm{\mu m}$ are applied to the

Copper: 20-40 μm

Silver: 1-2 μm

ReBCO: 1-3 μm

Buffer layers: ∼ 1 μm

Hastelloy (or steel): 30-100 μm
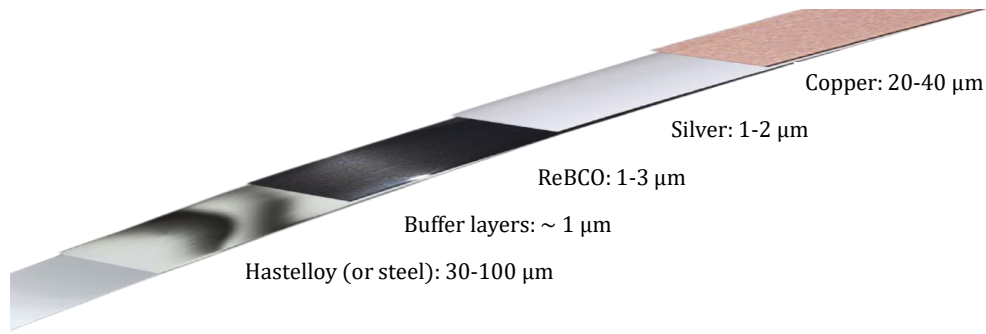
Figure 1.4. Material structure of a ReBCO tape, picture taken from [32].

surface, allowing the deposition of the ReBCO layer which is also in the order of $1\,\mu m$. A few μm thick layer of silver prevents chemical reactions between the ReBCO layer and the copper stabilizer coating the tape. As a result, the superconducting material is just a small fraction of the tape volume. The ReBCO behavior in magnetic fields is strongly anisotropic, differently from the LTS counterpart. The anisotropy is due to the crystalline structure of the superconducting layer whose crystallographic planes all have the same orientation. By applying a magnetic field perpendicular to these planes, the screening currents circulate within each plane but not between the planes, resulting in relatively weak flux line pinning. However, if magnetic fields are applied tangentially to the superconducting layer, they can penetrate between the crystallographic planes without destroying the superconducting state [29]. Consequently, superconducting tapes are highly influenced by perpendicular magnetic fields, but nearly unaffected by magnetic fields applied parallel to their wide surface. The anisotropy becomes more pronounced in high magnetic fields, at which the difference in critical current density between the parallel and perpendicular directions can be more than a factor of five, see for example [30, 31].

1.3 Quench

In superconducting devices, thermal perturbations can cause the temperature in the superconductor to locally exceed the current-sharing temperature $T_{cs} \leq T_c$, at which the superconductor can no longer carry the full current. The current in excess flows in the copper stabilizer, resulting in an effective low-resistance zone. If the heating due to Joule dissipation exceeds the thermal contribution from cooling, it leads to growth and propagation of the normal conducting zone, and eventually to a thermal runaway known as quench which can have potentially irreversible consequences for the superconductor. This can be prevented by detecting the thermal run-away on time, switching off the power converter, and dissipating the stored magnetic energy in the magnet in a controlled way, either internally or externally to the magnet.

In superconducting magnets, the quench detection may be achieved by means of several methods including secondary coils [33], acoustic detectors [34, 35], pick-up antennas [36], optic fibers [37, 38], superconducting quench detectors [39–41], and stray capacitance measurements [42]. Another method consists in measuring the voltage over the conductor [43] and compensating for inductive effects during dynamic phases. The presence of a voltage drop indicates an increase in temperature and a growing normal zone in the conductor. To date, voltage measurement is the most widespread detection method (see for example [44, 45]), because of its simplicity and robustness. Once the quench is detected, a protection strategy is triggered. For small cables and coils, switching off the power supply might be sufficient. However, for high energy-density

applications such as accelerator magnets, active protection strategies are necessarily put in place. A significant fraction of the coil may be heated up to normal state by means of quench heaters [46], thus spreading out the stored magnetic energy over a large volume. Another relatively new approach is based on the Coupling Loss Induced Quench (CLIQ) system [47], which heats up the superconductor by means of Joule losses produced by inter-filament coupling currents. Other concepts recently proposed include distributed energy extraction units (E3presso) [48], inductively coupled energy dissipaters [49], quench absorption coils [50], and CLIQ coupled to secondary coils [51]. A slightly different approach consists in using no-insulation (NI) coils [52, 53], such that in case of a quench the current redistributes between all the turns in the coil, bypassing the normal conducting zone. The main advantages consist in limiting the peak temperature and ensuring a homogeneous energy dissipation, at the price of inducing both large eddy currents increasing the ramp-up time, and possibly unbalanced Lorentz forces in the coil [54]. If several magnets are connected in series, it is crucial to separate the quenching magnet from the rest of the circuit and the energy stored therein. For the LHC, bypass elements such as diodes and resistors are put in place for each magnet composing the circuit, and a dump resistor can be connected in series with the magnet array for extracting the energy stored in the magnets.

Because of the high critical temperature, ReBCO coated conductors can easily be operated with significant enthalpy margin. At the same time, the heat capacity increases rapidly with temperature under cryogenic conditions, therefore the minimum quench energy can be up to three orders of magnitude higher than for LTS conductors. On the one hand, magnets constructed with ReBCO are expected to be very stable with respect to a thermal runaway. On the other hand, the energy required to propagate a possible normal zone is higher, leading to a propagation velocity which is about two orders of magnitude lower compared to LTS conductors [55, 56]. With respect to LTS materials, the voltage signal associated to the normal zone takes more time to reach prescribed thresholds for protection, providing a relatively late warning. The detection of and protection against a thermal runaway in HTS materials is an open challenge that is currently receiving significant attention, see for example [57] and the references therein.

1.4 Persistent Magnetization

Accelerator magnets must generate high-quality magnetic fields in their magnet aperture, because field imperfections can lead to particle-beam instabilities [58]. The field imperfections are typically limited to a few units of the main magnetic field within the area of 2/3 of the magnet aperture radius [3, 59], where a unit corresponds to 0.01% of the total magnetic field magnitude. The magnetic field quality is determined by magnet design criteria such as mechanical tolerances, and affected by material properties such as saturation and hysteresis of the iron yoke. High field quality is ensured by a precise control of the position and direction of the current inside the cable composing the coil of the magnet. As a consequence, tight construction tolerances and mechanical pre-stress are applied for suppressing the geometric field error. The magnet operational conditions also play a crucial role. Transient effects in the time domain such as mechanical deformation due to Lorentz forces, and magnetization due to eddy currents and screening currents in normal conducting and superconducting materials add a contribution on the magnetic field quality which is typically undesired.

Magnetic field quality is one of the concerns to be addressed for accelerator magnets based on ReBCO coils because the phenomenon of screening currents is of major relevance in HTS tapes. The magnetic behavior of the tapes is equivalent to wide and anisotropic mono-filaments, resulting in large screening currents. The related magnetization adds an undesired contribution which perturbs the magnetic field quality [60–66]

and vanishes with a time constant longer than the duty-cycle of the magnet. The field quality degradation is particularly severe at low currents, because screening currents are only limited by the superconducting current density, which is the highest when the applied magnetic field is low. For LTS stranded conductors, small filament sizes are adopted to reduce the field error due to the persistent magnetization from screening currents. For HTS tapes, a similar attempt was done by separating the HTS mono-filament into multifilaments by means of laser cutting, in a process called tape striation [67]. Unfortunately, the process does not allow for transposition of the obtained filaments, and the critical current density may be significantly degraded especially if small and localized defects are present before the cutting, as current redistribution is prevented. Another possibility is given by the tape-field alignment concept [68]. Within superconducting magnets, tapes can be aligned with the magnetic field lines, reducing the effective area of the mono-filament. Although this significantly suppresses the magnetization currents, the distribution of the transport current within the tapes cannot be enforced, posing a limit in the achievable field quality. Therefore, in addition to quench protection in ReBCO-based coils, the field quality is another significant challenge.

1.5 Simulations of Transient Effects in HTS Magnets

Numerical methods play a key role in the development of HTS-based applications, in particular they are crucial for analyzing the complex magnetothermal dynamics occurring within HTS high-field magnets. Numerical models, also referred to as digital twins, provide useful input during the design process of new magnets. Moreover, these models are valuable during magnet operations as they allow for analyzing the magnet performance, performing troubleshooting in case of faults, understanding and interpreting measurement data, and building new knowledge. The modeling of HTS magnets requires a suitable field formulation capturing the main physical phenomena related to persistent magnetization and quench dynamics, such that insights can be obtained on magnetic field quality and thermal stability. At the same time, the field formulation shall be implemented using a method suitable for domains of complex geometries, with the possibility of refining the accuracy of solution over specific sub-sets of the computational domain, for example the superconducting coil or the iron yoke.

Superconducting accelerator magnets are operated in connection to surrounding circuitry, and possibly to protection systems. Each domain represents several coupled physical phenomena which are characterized by a highly nonlinear behavior, with a wide range of time constants occurring at geometric scales spanning several orders of magnitude. Therefore, the simulation of transient effects in superconducting accelerator magnets is a multidomain, multiphysics, multirate, and multiscale problem. Consistent simulations require to account for the mutual influence between magnets, protection systems and the remainder of the circuit. As a consequence, care has to be taken as the field formulation shall allow for coupling with the external circuitry to exchange information.

In this work, the magnetothermal transients occurring in HTS accelerator magnets are formulated as an eddy-current problem in the time domain. The formulation is implemented in the finite element method, leading to high-resolution models exchanging information via field-circuit coupling cosimulation methods.

1.6 Related Work

Eddy-current problems in the time domain for normal conducting materials have been extensively studied with the use of both monolithic and mixed field formulations, see for example [69–71]. In particular, field

problems involving eddy currents in thin metallic structures have been discussed in [72–75]. After HTS materials were discovered, field formulations for eddy-current problems were progressively extended to this new class of materials. A magnetic-flux conforming formulation based on the magnetic vector potential was initially proposed in [76] and lately in [77, 78]. At the same time, magnetic-field conforming formulations [79–83] became increasingly popular. In particular, formulations based on the magnetic field strength vector are at the time of writing widely used, see for example [79, 84–86], and [87] for an overview. More recently, formulations based on the coupling of magnetic-flux and magnetic-field conforming vector fields have been developed, see [88] for an overview. Mixed-field formulations have been successfully implemented to simulate superconducting machines [89–91], superconducting tapes and cables [92–94], and superconducting and ferromagnetic materials [95]. Eddy-current problems in HTS materials have been treated also by means of volume integral formulations, leading to distributed models [96–98], as well as lumped models implemented as equivalent electrical networks [14, 99]. An exhaustive overview covering the numerical methods for the calculation of dynamic losses in HTS materials is given in [100].

Cosimulation methods can be applied to consistently couple various types of subsystems, such as circuits with controllers [101], as well as different physical models of the same device via mesh-mesh coupling [102]. Among other methods [103, 104], the waveform relaxation algorithm [105] has been used and studied for the cosimulation of field-circuit coupled systems [106, 107]. The convergence of the algorithm can be improved by means of optimized Schwarz methods [108, 109] which have been successfully applied to systems arising from both electric networks [110, 111] and field-circuit coupled systems [112, 113]. In the context of this work, the waveform relaxation method has been applied to the field-circuit coupled simulation of the LTS circuits of the LHC [114], High-Luminosity LHC upgrade [115–117], and FCC [118, 119] using the STEAM - *Simulation of transient effects in accelerator magnets* framework [120].

The mitigation of magnetic field errors is of central importance. Initial work in this direction led to magnetic cloaks for sensors [121, 122]. Subsequently, active shim coils were introduced for applications such as magnetic resonance imaging [123] and nuclear magnetic resonance [124]. Superconducting magnetic shields have been proposed for the septum magnets within the FCC project [125, 126]. The concept of selective shielding has been recently applied for field homogenization in solenoids [127]. More closely, screening-current shim coils were recently introduced as a conceptual solution for improving the field quality in accelerator magnets [14, 128].

1.7 Research Goals

This work deals with both the development of a numerical formulation for the simulation of HTS magnets in the time domain, and the development of a novel technology for improving the magnetic field quality in accelerator magnets. The goals of the thesis are:

1. to develop a magnetothermal field formulation for the simulation of HTS magnets in the time domain, and implement it in the finite element method;
2. to provide a field-circuit coupling interface which can be used in field-circuit cooperative simulations for analyzing the behavior in the time domain of circuits of HTS magnets;
3. to verify the implementation of the field formulation by means of numerical and analytical solutions, and validate it by comparison with measurements;
4. to provide the proof of concept of a technology based on HTS screens for the cancellation of static and dynamic field errors in accelerator magnets.
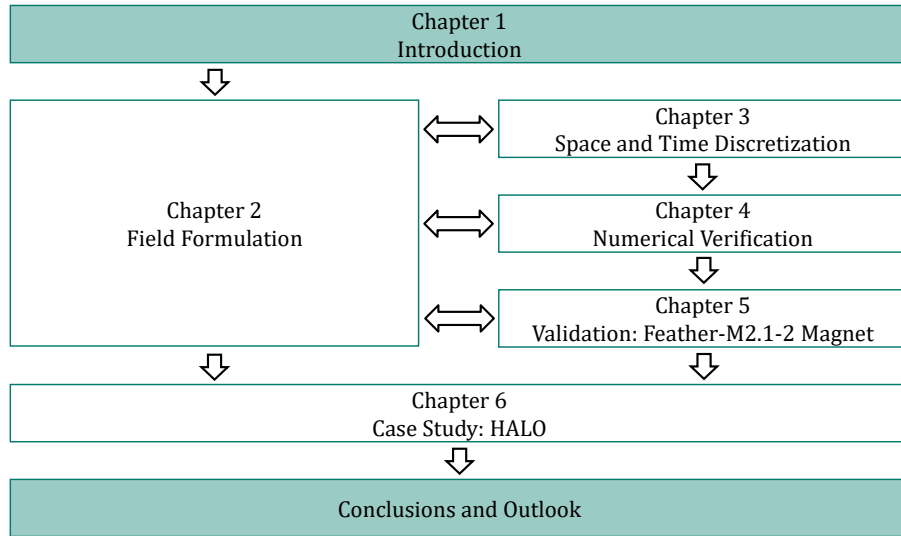
Figure 1.5. Flowchart showing the structure of the thesis.

1.8 Outline

The structure of this work is outlined here, and summarized in the flowchart shown in Figure 1.5. Chapter 2 introduces the theoretical fundamentals and the systems of equations used for describing the physical phenomena analyzed in the thesis. Electromagnetic fields are introduced with respect to Maxwell's equations and their different approximations. Next, stranded and solid conductor models are discussed, as they allow for coupling lumped quantities from circuit models whose theory is briefly recalled. Afterwards, the simulation of magnetothermal transients in superconducting accelerator magnets is formalized as an eddy-current problem in the time domain. A coupled field formulation and the related domain decomposition strategy is introduced to cope with the nonlinear electric behavior of superconducting materials, and the equations are given. Finally, the formulation is optimized for the cases of thin conducting domains such as HTS tapes, and multifilamentary stranded domains.

Chapter 3 starts by recalling the classic numerical methods that are used for simulating systems of partial differential equations arising from the coupled field formulation. First, the space discretization is discussed in terms of the Ritz-Galerkin finite element method. Second, classic time-integration theory and algorithms are recalled, and the waveform relaxation method is discussed with respect to field-circuit coupled problems. Afterwards, the weak and discrete formulation for the coupled field formulation is detailed for the 3D and 2D case, and the implications for thin conducting domains are discussed. As a key ingredient for the cosimulation, the field-circuit coupling interface is derived for the case of solid conductor models.

In Chapter 4, the implementation of the coupled field formulation in the finite element method is verified for models containing conducting domains represented as both bulks and thin shells. The verification is done for both reference solutions obtained with monolithic formulations, and available analytical solutions from literature. The test cases are designed such that they allow for analyzing the most relevant features of the formulation, whereas the geometric complexity is kept as low as possible. The field-circuit coupling interface

is tested against monolithic simulations for the field-circuit coupled magnetothermal simulation of a quench occurring in an HTS solenoid protected by quench heater strips.

In Chapter 5, the coupled field formulation is validated against field quality measurements in the HTS dipole insert magnet Feather-M2.1-2. The related numerical model is discussed, highlighting the key assumptions and simplifications. Simulations focus on the overall field quality in the magnet, and on the contribution from screening currents occurring in the HTS tapes composing the coil. The numerical results are compared with available magnetic measurements.

Chapter 6 presents a proof of concept of HTS screens based on superconducting tapes for the passive cancellation of the magnetic field error in accelerator magnets. This application is called HALO (harmonics-absorbing layered-object), and it is made of stacks of tapes aligned with the main field component, such that only the field imperfections are canceled out. Simulations are compared with experimental data, and then used to extrapolate the behavior of the screen for typical magnetic fields and operational temperatures of accelerator magnets. Results are discussed, and conclusions and recommendations for the design of future HTS screens are given. The thesis ends with a summary and outlook in Chapter 7.

The core of this work is constituted by the coupled field formulation and its application to systems containing HTS materials, in particular to the design and development of the HALO device. The contents of this work, including numerical models and source code, are available online [129].

2 Field Modeling

The physical phenomena occurring in superconducting materials that are relevant for this work are described by means of space- and time-dependent partial differential equations. This chapter presents the systems of equations which are used later on for the modeling of systems containing superconducting materials. The chapter starts from the general description of magnetic fields and heat propagation by means of Maxwell's equations and the heat balance equation, as both phenomena are relevant for modeling the magnetothermal dynamics in superconducting accelerator magnets. Then, the classical types of approximations in electromagnetism are presented. Subsequently, the most relevant field formulations are discussed under magnetoquasistatic assumptions, namely the $\vec{H} - \varphi$, $\vec{T} - \psi$ and $\vec{A} - \phi$ formulations. For each formulation, distribution functions are introduced for both stranded and solid conductor models which are of relevance for modeling cables based on low- and high-temperature superconductors. Moreover, distribution functions allow for coupling with lumped quantities belonging to external circuits. For this reason, the basic concepts of circuit simulation are detailed with respect to the method of modified nodal analysis.

The simulation of magnetothermal transients in superconducting accelerator magnets is formalized as an eddy-current problem in the time domain. Superconducting materials are firstly introduced with regards to their nonlinear electric behavior. Then, they are added to the general field problem by means of a coupled $\vec{A} - \vec{H}$ field formulation based on a domain decomposition strategy separating the superconducting source regions from the remaining regions. The set of equations representing the magnetothermal problem is given, and the interface conditions are discussed. This chapter closes by showing a further simplification of the coupled field formulation for thin conducting domains representing HTS tapes, and multifilamentary stranded domains representing BSCCO, Nb-Ti, and Nb$_3$Sn strands.

2.1 Maxwell's Equations

Electric and magnetic (EM) fields are described by Maxwell's equations [130, 131]. For a volume $\mathcal{V} \subset \mathbb{R}^3$ bounded by $\partial \mathcal{V}$ and facet $\mathcal{S} \subset \mathbb{R}^2$ bounded by $\partial \mathcal{S}$, the macroscopic description of EM fields reads

$$\int_{\partial \mathcal{S}} \vec{E} \cdot \mathrm{d}\vec{\mathcal{L}} = -\int_{\mathcal{S}} \partial_t \vec{B} \cdot \mathrm{d}\vec{\mathcal{S}}, \tag{2.1a}$$

$$\int_{\partial \mathcal{S}} \vec{H} \cdot \mathrm{d}\vec{\mathcal{L}} = \int_{\mathcal{S}} \left(\partial_t \vec{D} + \vec{J} \right) \cdot \mathrm{d}\vec{\mathcal{S}}, \tag{2.1b}$$

$$\int_{\partial \mathcal{V}} \vec{D} \cdot \mathrm{d}\vec{\mathcal{S}} = \int_{\mathcal{V}} \rho_{\mathrm{v}} \, \mathrm{d}\mathcal{V}, \tag{2.1c}$$

$$\int_{\partial \mathcal{V}} \vec{B} \cdot \mathrm{d}\vec{S} = 0, \tag{2.1d}$$

where the electric field strength $\vec{E}$, the magnetic flux density $\vec{B}$, the magnetic field strength $\vec{H}$, the electric flux density $\vec{D}$ and the electric current density $\vec{J}$ are vector fields $\mathbb{R}^3 \times \mathbb{R} \to \mathbb{R}^3$, and the electric charge density ρ_{v} is a scalar field $\mathbb{R}^3 \times \mathbb{R} \to \mathbb{R}$. The field quantities depend on space $\vec{r} \in \mathbb{R}^3$ and time $t \in \mathbb{R}$. The four relations in (2.1) correspond to Faraday's law, Ampère-Maxwell law, and Gauss's laws for electric and magnetic fields.

The differential formulation of Maxwell's equations is derived from (2.1) by applying Stokes' and Gauss's theorems, deriving a set of partial differential equations (e.g. [132]) which provide a mathematically equivalent representation, reading

$$\nabla \times \vec{E} = -\partial_t \vec{B}, \tag{2.2a}$$

$$\nabla \times \vec{H} = \partial_t \vec{D} + \vec{J}, \tag{2.2b}$$

$$\nabla \cdot \vec{D} = \rho_{\mathrm{v}}, \tag{2.2c}$$

$$\nabla \cdot \vec{B} = 0. \tag{2.2d}$$

The set of equations in (2.2) is typically extended by the current continuity equation which relates the space variation of the electric current density and the time variation of the electric charge density. The current continuity equation is derived by taking the divergence of (2.2b), inserting (2.2c) and noting that the left hand side is identically zero, obtaining

$$\nabla \cdot \vec{J} + \partial_t \rho_{\mathrm{v}} = 0. \tag{2.3}$$

2.2 Constitutive Laws

Constitutive laws define the electromagnetic properties for materials, and are appended to Maxwell's equations by introducing relations for the field quantities described by (2.2). In the general case, materials can be both field-dependent and anisotropic, resulting in nonlinear and tensor-valued material functions $\mathbb{R}^3 \times \mathbb{R} \to \mathbb{R}^{3 \times 3}$. In this work, constitutive laws are considered as possibly nonlinear and field-dependent scalar functions $\mathbb{R}^3 \times \mathbb{R} \to \mathbb{R}$. The dependency of materials from field quantities is explicitly mentioned, whereas for simplicity of notation the dependencies $(\vec{r}, t)$ from time and space in field and material quantities are omitted. The constitutive laws [131, 133] read

$$\vec{D} = \varepsilon_0 \vec{E} + \vec{P}, \tag{2.4a}$$

$$\vec{B} = \mu_0 \vec{H} + \mu_0 \vec{M}, \tag{2.4b}$$

$$\vec{J} = \sigma \vec{E} + \sigma \vec{E}_s. \tag{2.4c}$$

Here, the constants ε_0 and μ_0 are the electric permittivity and the magnetic permeability of vacuum, σ is the electrical conductivity [133], $\vec{P}$ is the electric polarization field, $\vec{M}$ is the magnetic polarization field or magnetization, and $\vec{E}_s$ is a source electric field independent of the rest of the fields. The electric and magnetic polarization fields are generated by electric charges bound in the material. These charges produce dielectric and magnetic dipoles on a molecular level, and can be represented by the polarization and magnetization current densities $\vec{J}_{\mathrm{p}}$ and $\vec{J}_{\mathrm{m}}$ as

$$\vec{J}_{\mathrm{p}} = \partial_t \vec{P}, \qquad \vec{J}_{\mathrm{m}} = \nabla \times \vec{M}, \tag{2.5}$$

with $\vec{J}_\mathrm{p}$ contributing to the displacement current density $\partial_t \vec{D}$ in (2.1b) as

$$\partial_t \vec{D} = \varepsilon_0 \partial_t \vec{E} + \vec{J}_\mathrm{p}. \tag{2.6}$$

The total current density $\vec{J}_\mathrm{tot}$ combines the contributions from bound and free charges. With the previous definitions, $\vec{J}_\mathrm{tot}$ reads

$$\vec{J}_\mathrm{tot} = \varepsilon_0 \partial_t \vec{E} + \vec{J}_\mathrm{p} + \vec{J}_\mathrm{m} + \vec{J}, \qquad \vec{J} = \vec{J}_\mathrm{c} + \vec{J}_\mathrm{v} + \vec{J}_\mathrm{s}, \tag{2.7}$$

where $\vec{J}_\mathrm{c} = \sigma \vec{E}$ is the conductive current density driven by the electric field strength, $\vec{J}_\mathrm{v} = \rho_\mathrm{v} \vec{v}$ is the convective current density determined by the motion of free charges at velocity $\vec{v}$, and $\vec{J}_\mathrm{s}$ is the source current density acting as an external source, independent of the rest of the fields. The source term $\vec{J}_\mathrm{s}$ can be imposed either directly as a current density, or indirectly as $\vec{J}_\mathrm{s} = \sigma \vec{E}_s$, thus by means of a source electric field strength. In this work, the convective contribution $\vec{J}_\mathrm{v}$ is disregarded, and no magnetization current density $\vec{J}_\mathrm{m}$ is considered, unless explicitly stated.

The simplest case is given by linear constitutive laws with constant σ and

$$\vec{P} = \varepsilon_0 \chi_\mathrm{d} \vec{E}, \qquad \vec{M} = \chi_\mathrm{m} \vec{H}, \tag{2.8}$$

where χ_d and χ_m are the dielectric and magnetic susceptibilities. The susceptibilities lead to the definition of the relative permittivity $\varepsilon_\mathrm{r} = 1 + \chi_\mathrm{d}$ and relative permeability $\mu_\mathrm{r} = 1 + \chi_\mathrm{m}$, with the conditions $\mu_\mathrm{r} < 1$, $\mu_\mathrm{r} > 1$ and $\mu_\mathrm{r} \gg 1$ referring to diamagnetic, paramagnetic and ferromagnetic materials. The material properties (2.4) can be rewritten in a more compact way by

$$\vec{D} = \varepsilon \vec{E}, \qquad \vec{B} = \mu \vec{H}, \qquad \vec{J}_c = \sigma \vec{E}, \tag{2.9}$$

with their inverse relations reading [131, 133]

$$\vec{H} = \nu \vec{B}, \qquad \vec{E} = \rho \vec{J}_c, \tag{2.10}$$

where $\varepsilon = \varepsilon_0 \varepsilon_\mathrm{r}$ is the electric permittivity, $\mu = \mu_0 \mu_\mathrm{r}$ is the magnetic permeability, ν is the magnetic reluctivity, and ρ the electric resistivity.

2.3 Electromagnetic Energy Balance

The energy balance relation for EM fields [131] is derived from the set of Maxwell's equations (2.2). The relation in (2.2b) is multiplied by $\vec{E}$ and then subtracted from the relation in (2.2a) multiplied by $\vec{H}$, reading

$$\vec{H} \cdot \nabla \times \vec{E} - \vec{E} \cdot \nabla \times \vec{H} = -\vec{H} \cdot \partial_t \vec{B} - \vec{E} \cdot \partial_t \vec{D} - \vec{E} \cdot \vec{J}. \tag{2.11}$$

The obtained equation is integrated over a volume $V \subset \mathbb{R}^3$ bounded by ∂V. Then Gauss's theorem is applied, and the power balance is obtained as

$$\int_\mathcal{V} \vec{E} \cdot \partial_t \vec{D} \, \mathrm{d}\mathcal{V} + \int_\mathcal{V} \vec{H} \cdot \partial_t \vec{B} \, \mathrm{d}\mathcal{V} + \int_\mathcal{V} \vec{E} \cdot \vec{J} \, \mathrm{d}\mathcal{V} + \int_{\partial \mathcal{V}} (\vec{E} \times \vec{H}) \cdot \mathrm{d}\vec{\mathcal{S}} = 0. \tag{2.12}$$

The first and the second volume integrals determine the rate of change of the energy associated to the electric and magnetic fields in the volume $\mathcal{V}$. Therefore, the two contributions are associated to the electric and magnetic losses. The third volume integral can be decomposed into two terms by replacing $\vec{E}$ with the relation in (2.4c), obtaining

$$\int_{\mathcal{V}} \vec{E} \cdot \vec{J} \, \mathrm{d}\mathcal{V} = \int_{\mathcal{V}} \rho \vec{J} \cdot \vec{J} \, \mathrm{d}\mathcal{V} - \int_{\mathcal{V}} \vec{E}_{\mathrm{s}} \cdot \vec{J} \, \mathrm{d}\mathcal{V}. \tag{2.13}$$

The first contribution represents a dissipation term associated to Joule losses, and the second contribution is the power supplied by means of an external source. The surface integral in (2.12) represents the energy flow through the boundary $\partial \mathcal{V}$ oriented by the normal unit vector $\vec{n}$. The energy flows according to the direction provided by the Poynting vector $\vec{S}$ defined as [131]

$$\vec{S} = \vec{E} \times \vec{H}. \tag{2.14}$$

With the previous definitions, the energy density function w is given for linear and isotropic materials as

$$w = \frac{1}{2}(\varepsilon|\vec{E}|^2 + \mu|\vec{H}|^2), \tag{2.15}$$

with $|\cdot|$ being the Euclidean norm in space. For nonlinear and anisotropic materials, the electric and magnetic energy densities are given by

$$w_{\mathrm{e}} = \int_0^{\vec{D}} \vec{E}(\vec{D}) \cdot \mathrm{d}\vec{D}, \qquad w_{\mathrm{m}} = \int_0^{\vec{B}} \vec{H}(\vec{B}) \cdot \mathrm{d}\vec{B}, \tag{2.16}$$

and depend on the characteristic of the material properties.

2.4 Boundary and Initial Conditions

Maxwell's equations in (2.2) are valid for EM fields existing in the whole domain $\mathbb{R}^3$ and for all time $\mathbb{R} > 0$. However, for the analysis of practical applications, simulations are typically solved for a truncated domain $\Omega \subset \mathbb{R}^3$, and for a time interval $t \in \mathcal{I} = [t_0,\ t_{\mathrm{end}})$, together with appropriate boundary conditions (BCs) and initial conditions (ICs).

The domain Ω bounded by $\Gamma = \partial\Omega$ is assumed to be composed of three types of sub-domains or regions, the conducting domain Ω_{c} where the source electric field $\vec{E}_s$ is imposed, the source domain Ω_{s} where the source current density $\vec{J}_s$ is imposed and the remainder Ω_0 which is source-free. The regions Ω_{c} and Ω_{s} are disjoint, that is, $\Omega_{\mathrm{c}} \cap \Omega_{\mathrm{s}} = \varnothing$. The partition of Ω is shown in Figure 2.1a. The conductivity σ and the resistivity ρ are positive-valued functions in Ω_{c}, and zero elsewhere. Consequently, $\vec{J}_s$ is divergence-free in Ω_{s}. The magnetic permeability μ (permittivity ν) and the electric permittivity ε are positive-valued functions in the entire domain Ω.

The truncation of space and time determines the need for BCs on the exterior boundary $\Gamma = \partial\Omega$, and for ICs for $t = t_0$. A unique solution for Maxwell's equations exists if the tangential component of either $\vec{H}$ or $\vec{E}$ is imposed on Γ [131]. In this way, the Poynting vector in (2.14) is uniquely determined, providing the energy exchange through Γ between Ω and the rest of the universe which is discarded by the space truncation. Although advanced BCs can be set, such as with geometry transformations representing the
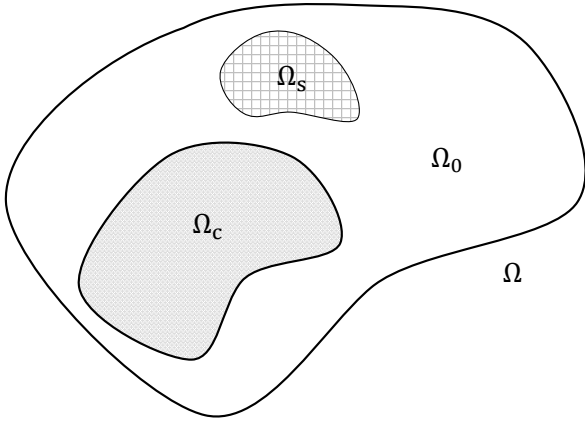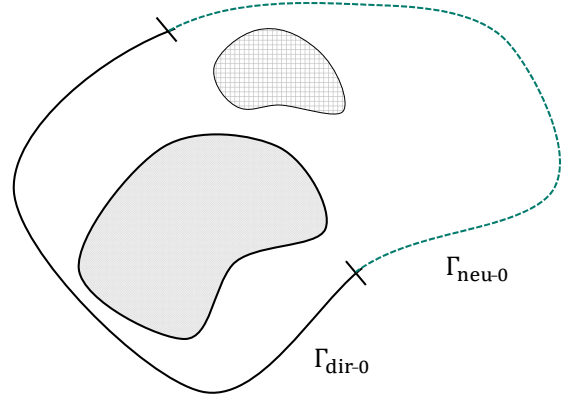
(a) Partition of the domain Ω.   *(b) Partition of the boundary Γ.*

Figure 2.1. Sketch of the domain Ω and boundary Γ partition.

infinite domain [134, 135], two principal conditions are considered in this work for the boundary Γ. The first consists in homogeneous electric boundary conditions [131] which assume perfect electric conductivity as $\sigma \to \infty$ on Γ_{ebc}, and the second consists in homogeneous magnetic boundary conditions [131] which consider perfect magnetic permeability as $\mu \to \infty$ on Γ_{mbc}. The boundary Γ is decomposed as $\Gamma = \Gamma_{\text{ebc}} \cup \Gamma_{\text{mbc}}$, with $\Gamma_{\text{ebc}} \cap \Gamma_{\text{mbc}} = \varnothing$, and equipped with the outward normal vector $\vec{n}$, such that the BCs are defined for all $t \in \mathcal{I}$ as

$$\begin{cases} \vec{E} \times \vec{n} = 0 & \text{on } \Gamma_{\text{ebc}}, \\ \vec{H} \times \vec{n} = 0 & \text{on } \Gamma_{\text{mbc}}. \end{cases} \tag{2.17}$$

The condition for Γ_{ebc} is also known as perfect electric conductor (PEC) which prevents any normal component of the magnetic flux. The condition for Γ_{mbc} is also known as perfect magnetic conductor (PMC) which prevents any normal component of the electric current density.

Alternatively, homogeneous Dirichlet and Neumann conditions can be defined for a given vector field $\vec{\zeta}$: $\Omega \times \mathcal{I} \to \mathbb{R}^3$ (scalar field $\varphi : \Omega \times \mathcal{I} \to \mathbb{R}$), on the boundaries $\Gamma_{\text{dir-0}}$ and $\Gamma_{\text{neu-0}}$, with $\Gamma = \Gamma_{\text{dir-0}} \cup \Gamma_{\text{neu-0}}$ and $\Gamma_{\text{dir-0}} \cap \Gamma_{\text{neu-0}} = \varnothing$ as shown in Figure 2.1b. The boundary conditions for $\vec{\zeta}$ read

$$\begin{cases} \vec{\zeta} \times \vec{n} = 0 & \text{on } \Gamma_{\text{dir-0}}, \\ (\nabla \times \vec{\zeta}) \times \vec{n} = 0 & \text{on } \Gamma_{\text{neu-0}}, \end{cases} \tag{2.18}$$

whereas the boundary conditions for φ are given by

$$\begin{cases} \varphi = 0 & \text{on } \Gamma_{\text{dir-0}}, \\ (\nabla \varphi) \cdot \vec{n} = 0 & \text{on } \Gamma_{\text{neu-0}}. \end{cases} \tag{2.19}$$

However, in the field of electrical engineering the terminology of electric and magnetic boundary conditions is typically preferred, as it can be immediately related to the physical behavior of the fields. The relation between the two terminologies is clarified later when necessary.

In addition to the spatial BCs, a consistent field distribution needs to be prescribed for the starting point t_0. ICs must comply with the imposed BCs, they are chosen for consistency as a solution of (2.2). In particular, homogeneous ICs prescribe the trivial null solution in Ω at $t = t_0$.

2.5 Interface Conditions

Interface conditions describe the behavior of EM fields at the interface of different materials, where a sharp transition in the material laws can occur [131, 133]. The interface $\Gamma_{1,2}$ is placed between two domains Ω_1 and Ω_2 with different material properties, and the normal unit vector $\vec{n}$ is conventionally oriented according to the outer direction of the first region. It is also convenient to split field quantities into their tangential and normal components at the interface (subscripts t and n). Interface conditions prescribe for the tangential component of the electric and magnetic fields $\vec{E}_t$ and $\vec{H}_t$ that

$$(\vec{E}_1 - \vec{E}_2) \times \vec{n} = 0, \qquad (\vec{H}_1 - \vec{H}_2) \times \vec{n} = \vec{K} \qquad \text{on } \Gamma_{1,2}, \tag{2.20}$$

and for the normal component of the electric flux, magnetic flux and electric current density fields $\vec{D}_n$, $\vec{B}_n$, and $\vec{J}_n$ that

$$(\vec{D}_1 - \vec{D}_2) \cdot \vec{n} = \rho_s, \qquad (\vec{B}_1 - \vec{B}_2) \cdot \vec{n} = 0, \qquad (\vec{J}_1 - \vec{J}_2) \cdot \vec{n} = \nabla \cdot \vec{K} \qquad \text{on } \Gamma_{1,2}, \tag{2.21}$$

where $\vec{K}$ is a surface current density and ρ_s a surface charge density, both located at $\Gamma_{1,2}$. The first relation in (2.20) corresponds to Faraday's law (2.2a) and prescribes the continuity of the tangential electric field. The second relation in (2.20) corresponds to Ampère-Maxwell's law (2.2b) and allows for a jump in the tangential component of the magnetic field equal to $\vec{K}$. The first relation in (2.21) enforces Gauss's law (2.2c) and allows for a jump in the normal component of the electric flux density equal to ρ_s. The second relation in (2.21) enforces Gauss's law (2.2d) by prescribing the continuity of the normal magnetic flux density. The third relation in (2.21) enforces the current continuity (2.3) by imposing the continuity of the normal component of the electric current density. If no surface current and no surface charge is present, then the normal component of the electric and magnetic fields $\vec{D}_n$ and $\vec{H}_n$ is also continuous. If the interface $\Gamma_{1,2}$ is moved to the boundary Γ of the domain, the following set of electric and magnetic boundary conditions can be defined

$$\vec{E} \times \vec{n} = 0, \qquad \vec{B} \cdot \vec{n} = 0, \qquad\qquad\qquad \text{on } \Gamma_{\text{ebc}}, \tag{2.22}$$

$$\vec{H} \times \vec{n} = 0, \qquad \vec{J} \cdot \vec{n} = 0, \qquad \vec{D} \cdot \vec{n} = 0, \qquad \text{on } \Gamma_{\text{mbc}}. \tag{2.23}$$

2.6 Thermodynamics

In general, EM fields cause electric, magnetic, and Joule losses, resulting in the generation of heat. The heat diffusion describes how the energy is stored within a domain and transported through its boundaries, affecting the temperature $T : \Omega \times \mathcal{I} \to \mathbb{R}$ of the domain [136, 137]. Heat transfer is always oriented according to the gradient of the temperature field, moving from higher to lower temperature regions. The mathematical description of heat diffusion and, therefore, the temperature evolution in time is provided by the heat balance equation

$$\rho_m C_p \partial_t T - \nabla \cdot (\kappa \nabla T) = P, \tag{2.24}$$

where ρ_m stands for the mass density, C_p is the heat capacity, κ is the thermal conductivity and the term $P : \Omega \times \mathcal{I} \to \mathbb{R}$ represents the impressed heat source due to dissipation phenomena in the domain. In particular, Joule losses are obtained as

$$P_J = (\rho \vec{J}) \cdot \vec{J}. \tag{2.25}$$

The temperature can be fixed to T_{dir} on the boundary Γ. Such constraint corresponds to a nonhomogeneous Dirichlet boundary condition for T, given by

$$T = T_{\text{dir}} \qquad \text{on } \Gamma. \tag{2.26}$$

Otherwise, adiabatic BCs can be imposed on Γ, such that no heat transfer occurs through the boundary. This constraint corresponds to a homogeneous Neumann boundary condition for T, given by

$$\kappa \nabla T \cdot \vec{n} = 0 \qquad \text{on } \Gamma. \tag{2.27}$$

Heat diffusion is of great importance for superconducting accelerator magnets. The heat capacity and the thermal conductivity of superconducting coils are both nonlinear and temperature-dependent. Moreover, the Joule losses P_{J} in the coils are influenced by the resistivity of superconducting and normal conducting materials which are again temperature-dependent. Also, the heat diffusion establishes the initiation and evolution of quench phenomena, the peak temperature, and the quench propagation velocity. In particular, the peak temperature is crucial as it determines the possible detrimental consequences for the magnet and, at the same time, the effectiveness of quench mitigation technologies.

2.7 Quasistatic and Static Fields

Maxwell's equations (2.2) provide a consistent description for three physical phenomena: electric, magnetic and Ohmic losses. However, for many practical applications parts of these effects are negligible with respect to the others, and can be discarded [138]. Therefore, it is possible to replace the full wave behavior described by Maxwell's equations with approximated behaviors still providing sufficient accuracy for the description of EM fields. In practice, a field propagates almost instantaneously for geometries much smaller than the EM wavelength, therefore propagation of waves and radiation effects can be neglected and a quasi-stationary assumption becomes appropriate. Moreover, in the limit-case where the change in time of fields is negligible, a further stationary assumption can be applied. The most relevant approximations, together with appropriate material laws and boundary and initial conditions, are given by (e.g. [139]):

(a) *Static*, where the time derivative of the electric and magnetic flux densities are disregarded, that is, $\partial_t \vec{D} = 0$ and $\partial_t \vec{B} = 0$. In this case, the electric and magnetic fields are decoupled, and can be studied separately. At the same time, the source current density $\vec{J_{\text{s}}}$ and the electric charge distribution ρ_{v} are assumed to be known. This leads to three distinct approximations, one for each loss contribution in Maxwell's equations.

(a1) The *current flow* (CF) case describes only Ohmic effects, solving for

$$\begin{cases} \nabla \times \vec{E} = 0, \\ \nabla \cdot \vec{J} = 0, \end{cases} \tag{2.28}$$

(a2) The *electrostatic* (ES) case describes only electric or capacitive effects, solving for

$$\begin{cases} \nabla \times \vec{E} = 0, \\ \nabla \cdot \vec{D} = \rho_{\text{v}}, \end{cases} \tag{2.29}$$

(a3) The *magnetostatic* (MS) case describes only magnetic effects, solving for

$$\begin{cases} \nabla \times \vec{H} = \vec{J}, \\ \nabla \cdot \vec{B} = 0, \end{cases} \tag{2.30}$$

(b) *Electroquasistatic* (EQS), where the inductive effects and the related magnetic losses are neglected by discarding the time derivative of the magnetic flux density in Faraday's law (2.2a), as $\partial_t \vec{B} = 0$. The governing equations read

$$\begin{cases} \nabla \times \vec{E} = 0, \\ \nabla \cdot (\partial_t \vec{D} + \vec{J}) = 0, \end{cases} \tag{2.31}$$

(c) *Magnetoquasistatic* (MQS), where the capacitive effects and the related electric losses are neglected by dropping the time derivative of the electric flux density as $\partial_t \vec{D} = 0$. The governing equations read

$$\begin{cases} \nabla \times \vec{E} = -\partial_t \vec{B}, \\ \nabla \times \vec{H} = \vec{J}, \end{cases} \tag{2.32}$$

(d) *Darwin* (DW) [140, 141], a less common approach which combines the EQS and MQS approximations for describing the electric, magnetic and ohmic loss effects, neglecting only the wave propagation. This is obtained by discarding the solenoidal component of the displacement current density (2.6) which is decomposed via the Helmholtz theorem [133].

(e) *Full Maxwell* (FM), where Maxwell's equations are considered without simplifications. Assuming that the initial conditions satisfy the divergence relations in (2.2c) and (2.2d), only Faraday's and Ampère-Maxwell's laws need to be considered [131]. Once the constitutive laws (2.9) are incorporated, the $\vec{E} - \vec{H}$ formulation [131] is obtained as

$$\begin{cases} \nabla \times \vec{E} = -\partial_t \vec{B}, \\ \nabla \times \vec{H} = \partial_t \vec{D} + \vec{J}, \end{cases} \tag{2.33}$$

where the BCs are set directly for $\vec{E}$ and $\vec{H}$ on Γ_{ebc} and Γ_{mbc} as detailed in (2.17).

The choice of the approximation depends on the given field problem and on its properties, such as the spatial dimension of the domain under study, the material properties, and the wavelength [142–144]. This work focuses on applications related to superconducting accelerator magnets. For such devices, wave propagation effects and capacitive effects are negligible. At the same time, inductive currents and Ohmic losses are of paramount importance, therefore they cannot be ignored. For this reason, the MQS assumption is adopted in the rest of this work.

2.8 Magnetoquasistatic Formulations

The MQS approximation (2.32) is applied to the set of Maxwell's equations which are then combined into a formulation. Potential fields are typically introduced [70, 71, 145, 146] for simplifying the mathematical treatment of Maxwell's equations. In this way, the solution of field problems is reduced to solving different classes of partial differential equations together with prescribed boundary conditions.

Several potential formulations are possible, each with advantages and drawbacks [70]. If a reduced magnetic scalar potential φ is used in the nonconducting region $\Omega_\text{s} \cup \Omega_0$, the $\vec{H} - \varphi$ formulation is obtained. Otherwise, two vector potentials can be used, either a electric vector potential $\vec{T}$ defined in the conducting region Ω_c, or a magnetic vector potential $\vec{A}$ defined in everywhere in Ω. Moreover, the potentials $\vec{T}$ and $\vec{A}$ can be coupled with scalar potentials defined everywhere in Ω. The cases detailed in the remaining of the section consider that $\vec{T}$ is coupled with the reduced magnetic scalar potential ψ, and $\vec{A}$ is coupled with the electric scalar potential ϕ.

2.8.1 $\vec{H} - \varphi$ formulation

The first approach is the $\vec{H} - \varphi$ formulation [147–149]. The magnetic field $\vec{H} : \Omega \times \mathcal{I} \to \mathbb{R}^3$ and a reduced magnetic scalar potential $\varphi : \Omega_\text{s} \cup \Omega_0 \times \mathcal{I} \to \mathbb{R}$ are defined such that

$$\begin{cases} \nabla \times \vec{H}_\text{s} = \vec{J}_\text{s}, & \text{in } \Omega_\text{s}, \\ \nabla \times \vec{H} = \vec{J}, & \text{in } \Omega_\text{c}, \\ \vec{H} = \vec{H}_\text{s} - \nabla\varphi, & \text{in } \Omega_\text{s} \cup \Omega_0, \end{cases} \tag{2.34}$$

where the field $\vec{H}_\text{s} : \Omega \times \mathcal{I} \to \mathbb{R}^3$ is an auxiliary source magnetic field strength related to the source current density $\vec{J}_\text{s}$ which is divergence-free in the source domain Ω_s, and φ is introduced by space-integration of Ampère's law (2.2b) in the region $\Omega_\text{s} \cup \Omega_0$. The choice of potentials immediately satisfies Ampère's law (2.2b) everywhere and Gauss's law (2.2d) in Ω_c, whereas Faraday's law (2.2a) and Gauss's law (2.2d) have to be explicitly prescribed in Ω_c and $\Omega_\text{s} \cup \Omega_0$, respectively. By combining Maxwell's equations for MQS and the material relations, the formulation reads

$$\begin{cases} \nabla \times \rho \nabla \times \vec{H} + \partial_t \mu \vec{H} = \nabla \times \vec{E}_s, & \text{in } \Omega_\text{c}, \\ \nabla \cdot \mu \nabla\varphi = \nabla \cdot \mu \vec{H}_s, & \text{in } \Omega_\text{s} \cup \Omega_0. \end{cases} \tag{2.35}$$

Since the magnetic scalar potential φ is defined only outside the conducting region Ω_c, interface conditions are required on $\Gamma_\text{c} = \partial\Omega_\text{c}$, reading

$$(\vec{H} + \nabla\varphi) \times \vec{n} = 0, \qquad \text{for } \vec{H}_t, \tag{2.36}$$

$$(\nabla \times \vec{H}) \cdot \vec{n} = 0, \qquad \text{for } \vec{J}_n, \tag{2.37}$$

$$(\mu_c(\vec{H} + \vec{H}_\text{s}) - \mu(\vec{H}_\text{s} - \nabla\varphi)) \cdot \vec{n} = 0, \qquad \text{for } \vec{B}_n, \tag{2.38}$$

with μ_c being the magnetic permeability in Ω_c.

The PEC boundary conditions lead to Neumann boundary conditions for the fields $\vec{H}$ and φ, given as

$$\begin{cases} (\rho \nabla \times \vec{H} - \vec{E}_s) \times \vec{n} = 0, \\ (\mu \nabla\varphi) \cdot \vec{n} = 0, \end{cases} \qquad \text{on } \Gamma_\text{ebc}. \tag{2.39}$$

The PMC boundary conditions lead to Dirichlet boundary conditions for the fields $\vec{H}$ and φ, given as

$$\begin{cases} \vec{H} \times \vec{n} = 0, \\ \nabla\varphi \times \vec{n} = 0, \qquad \Rightarrow \qquad \varphi = \varphi_0, \end{cases} \qquad \text{on } \Gamma_\text{mbc}. \tag{2.40}$$

2.8.2 $\vec{T} - \psi$ formulation

The second approach is the $\vec{T} - \psi$ formulation [147–149], also often referred to as the $\vec{T}$-Ω formulation. A current density vector potential $\vec{T} : \Omega_{\mathrm{c}} \times \mathcal{I} \to \mathbb{R}^3$ and a scalar magnetic potential $\psi : \Omega \times \mathcal{I} \to \mathbb{R}$ are defined such that

$$\begin{cases} \nabla \times \vec{H}_s = \vec{J}_{\mathrm{s}}, & \text{in } \Omega_{\mathrm{s}}, \\ \nabla \times \vec{T} = \vec{J}, & \text{in } \Omega_{\mathrm{c}}, \\ \vec{H} = \vec{T} + \vec{H}_{\mathrm{s}} - \nabla \psi, & \text{in } \Omega_{\mathrm{c}}, \\ \vec{H} = \vec{H}_{\mathrm{s}} - \nabla \psi, & \text{in } \Omega_{\mathrm{s}} \cup \Omega_0, \end{cases} \tag{2.41}$$

where $\vec{T}$ is related to the current density $\vec{J}$ which is divergence-free in the conducting domain Ω_{c}, and ψ is introduced by space-integration of Ampère's law (2.2b) in the region Ω. The choice of potentials immediately satisfies Ampère's law (2.2b) everywhere, whereas Faraday's law (2.2a) and Gauss's law (2.2d) have to be explicitly prescribed in Ω_{c} and Ω. By combining Maxwell's equations for MQS and the material relations, the formulation reads

$$\begin{cases} \nabla \times \rho \nabla \times \vec{T} + \partial_t \mu \vec{T} - \partial_t \mu \nabla \psi = -\partial_t \mu \vec{H}_s + \nabla \times \vec{E}_s, & \text{in } \Omega_{\mathrm{c}}, \\ \nabla \cdot (\mu \vec{T} - \mu \nabla \psi) = -\nabla \cdot \mu \vec{H}_s, & \text{in } \Omega_{\mathrm{c}}, \\ \nabla \cdot \mu \nabla \psi = \nabla \cdot \mu \vec{H}_s, & \text{in } \Omega_{\mathrm{s}} \cup \Omega_0. \end{cases} \tag{2.42}$$

Since $\vec{T}$ is defined only in the conducting region Ω_{c}, interface conditions are required on $\Gamma_{\mathrm{c}} = \partial \Omega_{\mathrm{c}}$, reading

$$\vec{T} \times \vec{n} = 0, \qquad \text{for } \vec{H}_t \text{ and } \vec{J}_n, \tag{2.43}$$

$$(\mu_c(\vec{T} + \vec{H}_{\mathrm{s}} - \nabla \psi) - \mu(\vec{H}_{\mathrm{s}} - \nabla \psi)) \cdot \vec{n} = 0, \qquad \text{for } \vec{B}_n. \tag{2.44}$$

The PEC boundary conditions lead to Neumann boundary conditions for the fields $\vec{T}$ and ψ, given as

$$\begin{cases} (\rho \nabla \times \vec{T} - \vec{E}_s) \times \vec{n} = 0, \\ (\mu \nabla \psi) \cdot \vec{n} = 0, \end{cases} \qquad \text{on } \Gamma_{\mathrm{ebc}}. \tag{2.45}$$

The PMC boundary conditions lead to Dirichlet boundary conditions for the fields $\vec{T}$ and ψ, given as

$$\begin{cases} \vec{T} \times \vec{n} = 0, \\ \nabla \psi \times \vec{n} = 0, \qquad \Rightarrow \qquad \psi = \psi_0, \end{cases} \qquad \text{on } \Gamma_{\mathrm{mbc}}. \tag{2.46}$$

The electric vector potential $\vec{T}$ determines $\vec{J}$ in the conducting region up to a gradient field [131]. Therefore, an additional gauging condition needs to be imposed on $\vec{T}$ to ensure the uniqueness of the solution.

The $\vec{T} - \psi$ and $\vec{H} - \varphi$ formulations differ only in the conducting domains, as $\vec{H}$ is decomposed in the former into a curl-free and a rotational component [133]. In the MQS setting, the formulations approximate the magnetic field in exactly the same way, thus leading to identical field solutions [148, 150]. However, the $\vec{H} - \varphi$ formulation is unstable in the magnetostatic limit, and shall be avoided [148].

2.8.3 $\vec{A} - \phi$ formulation

The third approach is the $\vec{A} - \phi$ formulation [71, 145, 151]. A magnetic vector potential $\vec{A} : \Omega \times \mathcal{I} \to \mathbb{R}^3$ and an electric scalar potential $\phi : \Omega \times \mathcal{I} \to \mathbb{R}$ are defined such that

$$\begin{cases} \vec{B} = \nabla \times \vec{A}, \\ \vec{E} = -\partial_t \vec{A} - \nabla \phi, \end{cases} \tag{2.47}$$

where $\vec{A}$ is related to the magnetic flux $\vec{B}$ which is divergence-free, and ϕ is introduced by space-integration of Faraday's law (2.2a) in the region Ω. Then, Ampère's law (2.2b) has to be explicitly prescribed. By combining Maxwell's equations for MQS and the material relations, and appending the current continuity equation (2.3), the formulation reads

$$\begin{cases} \nabla \times \mu^{-1} \nabla \times \vec{A} + \sigma \partial_t \vec{A} + \sigma \nabla \phi = \vec{J}_s, \\ \nabla \cdot (\sigma \partial_t \vec{A} + \sigma \nabla \phi) = 0, \end{cases} \quad \text{in } \Omega, \tag{2.48}$$

with the potentials defined everywhere in Ω, such that no further interface conditions are required.

The PEC boundary conditions lead to Dirichlet boundary conditions for the fields $\vec{A}$ and ϕ, given as

$$\begin{cases} \vec{A} \times \vec{n} = 0, \\ \nabla \phi \times \vec{n} = 0, \quad \Rightarrow \quad \phi = \phi_0, \end{cases} \quad \text{on } \Gamma_{\text{ebc}}. \tag{2.49}$$

The PMC boundary conditions lead to Neumann boundary conditions for the fields $\vec{A}$ and ϕ, given as

$$\begin{cases} (\mu^{-1} \nabla \times \vec{A}) \times \vec{n} = 0, \\ (\nabla \phi) \cdot \vec{n} = 0, \end{cases} \quad \text{on } \Gamma_{\text{mbc}}. \tag{2.50}$$

The magnetic vector potential determines the magnetic flux density $\vec{B}$ up to a gradient field [131]. Therefore, an additional gauging condition needs to be imposed on $\vec{A}$ for ensuring the uniqueness of the solution [145, 152, 153].

2.8.4 $\vec{A}^\star$ formulation

As the fourth approach, the $\vec{A}^\star$ formulation is derived from the $\vec{A} - \phi$ formulation. By exploiting the gauge freedom of $\vec{A}$, a specific magnetic vector potential can be chosen in order to reduce the degrees of freedom of the field problem [154, 155]. This is achieved by defining $\vec{A}^\star : \Omega \times \mathcal{I} \to \mathbb{R}^3$ as

$$\vec{A}^\star = \vec{A} - \int_{t^\star = t_0}^{t} \nabla \phi \, dt^\star. \tag{2.51}$$

The definition in (2.51) is inserted into (2.47), obtaining

$$\begin{cases} \vec{B} = \nabla \times \vec{A}^\star, \\ \vec{E} = -\partial_t \vec{A}^\star, \end{cases} \tag{2.52}$$

where the contribution from the scalar electric vector potential is incorportate into $\vec{A}$ and Gauss's law (2.2d) is immediately satisfied, however Ampère's law (2.2b) has to be solved explicitly. By combining Maxwell's equations for MQS and the material relations, the formulation reads

$$\nabla \times \mu_{-1} \nabla \times \vec{A}^\star + \sigma \partial_t \vec{A}^\star = \vec{J}_s \qquad \text{in } \Omega. \tag{2.53}$$

The boundary conditions for the reduced magnetic vector potential are analogous to the ones for the $\vec{A} - \phi$ formulation, given as

$$\begin{cases} \vec{A}^\star \times \vec{n} = 0 & \text{on } \Gamma_{\text{ebc}}, \\ (\mu_{-1} \nabla \times \vec{A}^\star) \times \vec{n} = 0 & \text{on } \Gamma_{\text{mbc}}. \end{cases} \tag{2.54}$$

The potential $\vec{A}^\star$ is uniquely determined in the conducting regions. However, in order to ensure the uniqueness of the solution, an additional gauging condition needs to be imposed on $\vec{A}^\star$ in the nonconducting region [70]. For simplicity of notation, from now on the symbol $\vec{A}$ is overloaded and it is used also for the reduced magnetic vector potential in the $\vec{A}^\star$ formulation.

2.9 Field Excitation Sources

The excitation source term $\vec{J}_s$ introduced in Section 2.8 is typically provided directly by currents $i_s : \mathcal{I} \to \mathbb{R}$ or indirectly by voltages $v_s : \mathcal{I} \to \mathbb{R}$ which belong to the external circuit powering the application under study. These functions are zero dimensional in space and need to be coupled to the three dimensional electric fields and current densities within the field formulations. The connection between lumped and distributed quantities is obtained by means of conductor models, whose coupling functions are voltage and current distribution functions $\vec{\chi} : \Omega \to \mathbb{R}^3$, or equivalently winding functions [156]. Conductor models do not intersect each other, that is, the distribution functions remain orthogonal [156, 157] as

$$\vec{\chi}^k \cdot \vec{\chi}^j = 0 \qquad \text{for } k \neq j. \tag{2.55}$$

Regions powered by external voltage and current sources must either connect to the boundary, or form a closed loop within the computational domain, otherwise the continuity of the current density may be violated. In the first case, the coupling of the external circuit occurs at the boundary, and it is straightforward. In the second case, the coupling occurs by means of a slit introduced in the loop.

In this work, only stranded and solid conductor models [103] are considered, although more elaborate models are available (e.g. the foil conductor model, see [158]). The distribution functions associated to stranded and solid conductor models are denoted as $\vec{\chi}_{\text{str}}$ and $\vec{\chi}_{\text{sol}}$. For three-dimensional problems, the distribution functions are assumed to have a three-dimensional support, that is, they are nonzero in the whole conductor volume, although functions with compact support are also possible [156]. Different methods can be found in literature on how to construct these distribution functions. One of the most common approaches, also followed here, consists in solving a Laplace-type problem restricted to either Ω_s for stranded conductors [156, 159–161], or to Ω_c for solid conductors [156, 159, 161].
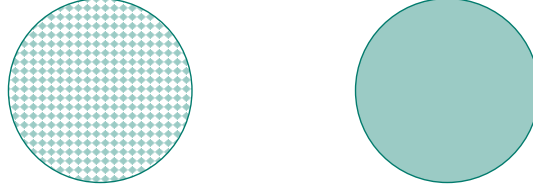
Figure 2.2. Sketch of cross sections for stranded (left) and solid (right) conductors.

2.9.1 Stranded conductor model

Stranded conductor models are suitable for strands containing thin filaments where the current density is assumed to be homogeneously distributed (see Figure 2.2a). This assumption neglects the individual filament insulation and implies that no eddy currents can occur as the filament diameter is below the skin depth [103, 156]. Therefore, stranded conductors $\vec{\chi}_{\mathrm{str}}$ exist only in the source domain Ω_{s}. Given N_{s} conductors in different source domains Ω_{s}^k, for $k = 1, 2, \ldots, N_{\mathrm{s}}$, each conductor is associated to a source current i_{s}^k. The source domains are disjoint, that is,

$$\Omega_{\mathrm{s}} = \bigcup_{k=1}^{N_{\mathrm{s}}} \Omega_{\mathrm{s}}^k, \qquad \Omega_{\mathrm{s}}^k \cap \Omega_{\mathrm{s}}^j = \varnothing, \qquad \text{for } k \neq j. \tag{2.56}$$

The distribution functions $\vec{\chi}_{\mathrm{str}}^k$ are defined such that

$$\vec{J}_{\mathrm{s}} = \sum_{k=1}^{N_{\mathrm{s}}} \vec{\chi}_{\mathrm{str}}^k i_{\mathrm{s}}^k = \boldsymbol{\chi}_{\mathrm{str}} \mathbf{i}_{\mathrm{s}}, \tag{2.57}$$

where $\boldsymbol{\chi}_{\mathrm{str}} : \Omega_{\mathrm{s}} \to \mathbb{R}^{3 \times N_{\mathrm{s}}}$ is a tensor field containing the N_{s} distribution functions and $\mathbf{i}_{\mathrm{s}} : \mathcal{I} \to \mathbb{R}^{N_{\mathrm{s}}}$ is a vector of functions containing all the current sources.

An important property of distribution functions for stranded conductors is that the surface integral over any cross sectional plane $\mathcal{S}_{\mathrm{str}}^j$ of the k-th stranded conductor is equal to the number of turns N_{t}^k in the cross section of the conductor [156], reading

$$\int_{\mathcal{S}_{\mathrm{str}}^j} \vec{\chi}_{\mathrm{str}}^k \cdot \mathrm{d}\vec{\mathcal{S}} = N_{\mathrm{t}}^k, \qquad \forall \mathcal{S}_{\mathrm{str}}^j. \tag{2.58}$$

In addition, a relation with the voltage drop v_{s}^k in the k-th source domain can be established as [156]

$$v_{\mathrm{s}}^k = -\int_{\Omega_{\mathrm{s}}^k} \vec{\chi}_{\mathrm{str}}^k \cdot \vec{E} \, \mathrm{d}\Omega, \tag{2.59}$$

such that the voltage can be calculated from the field solution. At the same time, an implicit relation between voltages and currents is established such that the field model can be coupled with the equations representing an external network model of a circuit [159].

The source current density $\vec{J}_\mathrm{s}$ can be formulated in terms of the auxiliary source magnetic field $\vec{H}_\mathrm{s}$ which was used in (2.34) and (2.41) for the $\vec{H} - \varphi$ and $\vec{T} - \psi$ formulations. Consequently, the distribution function $\vec{\zeta}_\mathrm{str}^k : \Omega_\mathrm{s}^k \to \mathbb{R}^3$ is introduced such that

$$\vec{H}_\mathrm{s} = \sum_{k=1}^{N_\mathrm{s}} \vec{\zeta}_\mathrm{str}^k i_\mathrm{s}^k = \boldsymbol{\zeta}_\mathrm{str} \mathbf{i}_\mathrm{s}, \tag{2.60}$$

where $\boldsymbol{\zeta}_\mathrm{str}$ is a tensor field $\Omega_\mathrm{s} \to \mathbb{R}^{3 \times N_\mathrm{s}}$ related to $\boldsymbol{\chi}_\mathrm{str}$ for the k-th source region by

$$\vec{\chi}_\mathrm{str}^k = \nabla \times \vec{\zeta}_\mathrm{str}^k. \tag{2.61}$$

The source voltage v_s^k is calculated for the k-th source domain as [162]

$$v_\mathrm{s}^k = - \int\limits_{\Omega_\mathrm{s}^k} \nabla \times \vec{\zeta}_\mathrm{str}^k \cdot \vec{E} \, \mathrm{d}\Omega = \int\limits_{\Omega_\mathrm{s}^k} \vec{\zeta}_\mathrm{str}^k \cdot \partial_t \vec{B} \, \mathrm{d}\Omega - \int\limits_{\Gamma_\mathrm{s}^k} (\vec{\zeta}_\mathrm{str}^k \times \vec{E}) \cdot \mathrm{d}\vec{\Gamma}, \tag{2.62}$$

where the relation is derived from (2.59) by first introducing the relation between the two distribution functions (2.61), and then by applying Gauss's theorem and Faraday's law (2.2a). The boundary term disappears in presence of electric boundary conditions applied to $\Gamma_\mathrm{s}^k = \partial \Omega_\mathrm{s}^k$.

2.9.2 Solid conductor model

Solid conductor models are useful for bulk, mono-filamentary conductors where the current density distribution is generally nonhomogeneous (see Figure 2.2b). For this reason, solid conductors are assumed to exist only in the conducting domain $\Omega_{\mathrm{c},\chi} \subseteq \Omega_\mathrm{c}$. In this work, solid conductors are linked to the external source circuit via electrodes located on the boundary of the computational domain. However, it is possible to use a compact support for the electrodes, positioning them within the cross section of the conductor, at an arbitrary intersection along the conductor length [156]. Given N_c conductors in different conducting domains $\Omega_{\mathrm{c},\chi}^k$, for $k = 1, 2, \dots, N_\mathrm{c}$, each conductor is associated to a source voltage v_s^k. The source domains are disjoint, that is,

$$\Omega_{\mathrm{c},\chi} = \bigcup_{k=1}^{N_\mathrm{c}} \Omega_{\mathrm{c},\chi}^k, \qquad \Omega_{\mathrm{c},\chi}^k \cap \Omega_{\mathrm{c},\chi}^j = \varnothing \qquad \text{for } k \neq j. \tag{2.63}$$

The distribution functions $\vec{\chi}_\mathrm{sol}^k$ are defined such that

$$\vec{E}_\mathrm{s} = \sum_{k=1}^{N_\mathrm{c}} \vec{\chi}_\mathrm{sol}^k v_\mathrm{s}^k = \boldsymbol{\chi}_\mathrm{sol} \mathbf{v}_\mathrm{s}, \tag{2.64}$$

where $\boldsymbol{\chi}_\mathrm{sol} : \Omega_{\mathrm{c},\chi} \to \mathbb{R}^{3 \times N_\mathrm{c}}$ is a tensor field containing the N_c distribution functions, and $\mathbf{v}_\mathrm{s} : \mathcal{I} \to \mathbb{R}^{N_\mathrm{c}}$ is a vector of functions containing all the source voltages. An important property of distribution functions for solid conductors is that the line integral along any path $\mathcal{L}_\mathrm{sol}$ between the electrodes of the k-th solid conductor is equal to the unity, reading

$$\int\limits_{\mathcal{L}_\mathrm{sol}} \chi_\mathrm{sol}^k \cdot \mathrm{d}\vec{\mathcal{L}} = 1, \qquad \forall \mathcal{L}_\mathrm{sol}. \tag{2.65}$$
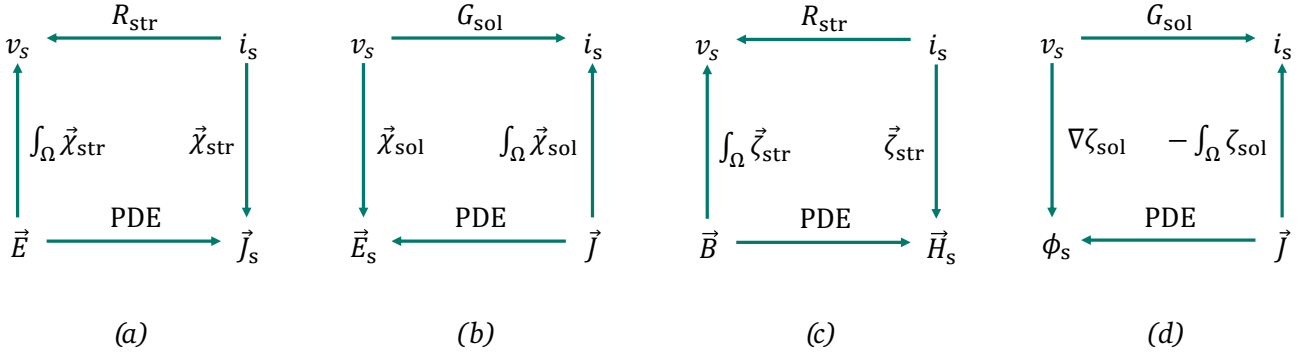
Figure 2.3. Schematic representation of the stranded and solid conductor coupling via distribution functions (a) $\vec{\chi}_{\text{str}}$ and (b) $\vec{\chi}_{\text{sol}}$, and their potentials (c) $\vec{\zeta}_{\text{str}}$ and (d) ζ_{sol}.

In addition, a relation with the current in the k-th source domain can be established [156], as

$$i_{\text{s}}^k = \int\limits_{\Omega_{\text{c},\chi}^k} \vec{\chi}_{\text{sol}}^k \cdot \vec{J} \, \mathrm{d}\Omega, \tag{2.66}$$

such that the current can be calculated from the field solution. At the same time, an implicit relation between voltages and currents is established such that the field model can be coupled with the equations of an external lumped circuit [159].

The source electric field $\vec{E}_{\text{s}}$ can be formulated in terms of an auxiliary source scalar potential ϕ_{s}, such that $\vec{E}_{\text{s}} = -\nabla\phi_{\text{s}}$. Consequently, the distribution function $\zeta_{\text{sol}}^k : \Omega_{\text{c},\chi}^k \to \mathbb{R}$ is introduced such that

$$\phi_{\text{s}} = \sum_{k=1}^{N_{\text{c}}} \zeta_{\text{sol}}^k v_{\text{s}}^k = \boldsymbol{\zeta}_{\text{sol}} \mathbf{v}_{\text{s}} \tag{2.67}$$

where $\boldsymbol{\zeta}_{\text{sol}}$ is a tensor field $\Omega_{\text{c},\chi} \to \mathbb{R}^{N_{\text{s}}}$ related to $\boldsymbol{\chi}_{\text{sol}}$ in the k-th source region by

$$\vec{\chi}_{\text{sol}}^k = -\nabla\zeta_{\text{sol}}^k. \tag{2.68}$$

The source current i_{s}^k is calculated for the k-th source domain as [161]

$$i_{\text{s}}^k = -\int\limits_{\Omega_{\text{c},\chi}^k} \nabla\zeta_{\text{sol}}^k \cdot \vec{J} \, \mathrm{d}\Omega = -\int\limits_{\Gamma_{\text{c},\chi}^k} \zeta_{\text{sol}}^k \vec{J} \cdot \mathrm{d}\vec{\Gamma}, \tag{2.69}$$

where the relation is derived from (2.66) by introducing the relation (2.68), and then by applying Gauss' theorem and observing that $\vec{J}$ is divergence-free in the MQS approximation. The resulting boundary term in (2.69) is applied on $\Gamma_{\text{c},\chi}^k = \partial\Omega_{\text{c},\chi}^k$.

2.9.3 Circuit coupling

In case of stranded conductors, the voltage drop along the k-th conductor consists of a resistive and an inductive voltage contribution. The field-circuit coupling equation is derived for the $\vec{H} - \varphi$, $\vec{T} - \psi$ and $\vec{A}$

formulations, for $k = 1, \ldots, N_\text{s}$, as [162, 163]

$$v_\text{s}^k = R_\text{str}^k i_\text{s}^k + \int\limits_{\Omega_\text{s}^k} \vec{\zeta}_\text{str}^k \cdot \partial_t \mu (\vec{H} + \vec{\zeta}_\text{str}^k i_\text{s}^k) \, \mathrm{d}\Omega, \tag{2.70a}$$

$$v_\text{s}^k = R_\text{str}^k i_\text{s}^k + \int\limits_{\Omega_\text{s}^k} \vec{\zeta}_\text{str}^k \cdot \partial_t \mu (\vec{T} - \nabla\psi + \vec{\zeta}_\text{str}^k i_\text{s}^k) \, \mathrm{d}\Omega, \tag{2.70b}$$

$$v_\text{s}^k = R_\text{str}^k i_\text{s}^k + \int\limits_{\Omega_\text{s}^k} \vec{\chi}_\text{str}^k \cdot \partial_t \vec{A} \, \mathrm{d}\Omega. \tag{2.70c}$$

The stranded conductor resistance R_str^k corresponds to the DC resistance in the stationary case, and it is given by

$$R_\text{str}^k = \int\limits_{\Omega_\text{s}^k} \overline{\rho}_\text{str} \vec{\chi}_\text{str}^k \cdot \vec{\chi}_\text{str}^k \, \mathrm{d}\Omega, \tag{2.71}$$

where $\overline{\rho}_\text{str}$ is the physical resistivity of the material composing the stranded conductor. From (2.70), stranded conductor models are coupled to the external circuit as current-driven voltage sources.

In case of solid conductors, the current through the k-th conductor is obtained from the $\vec{H}$, $\vec{T} - \psi$ and $\vec{A}$ formulation, for $k = 1, \ldots, N_\text{c}$ as [156]

$$i_\text{s}^k = \int\limits_{\Omega_{\text{c},\chi}^k} \vec{\chi}_\text{sol}^k \cdot \nabla \times \vec{H} \, \mathrm{d}\Omega, \tag{2.72a}$$

$$i_\text{s}^k = \int\limits_{\Omega_{\text{c},\chi}^k} \vec{\chi}_\text{sol}^k \cdot \nabla \times \vec{T} \, \mathrm{d}\Omega, \tag{2.72b}$$

$$i_\text{s}^k = G_\text{sol}^k v_\text{s}^k - \int\limits_{\Omega_{\text{c},\chi}^k} \sigma \vec{\chi}_\text{sol}^k \cdot \partial_t \vec{A} \, \mathrm{d}\Omega. \tag{2.72c}$$

where the conductance G_sol^k corresponds to the DC conductance in the stationary case, and it is given by

$$G_\text{sol}^k = \int\limits_{\Omega_{\text{c},\chi}^k} \sigma \vec{\chi}_\text{sol}^k \cdot \vec{\chi}_\text{sol}^k \, \mathrm{d}\Omega. \tag{2.73}$$

From (2.72), solid conductor models are coupled to the external circuit as voltage-driven current sources. The stranded and solid conductor couplings are schematically shown in Figure 2.3, both in terms of distribution functions $\vec{\chi}$ and their potentials.

2.10 Circuit Theory

In traditional circuit theory, electrical circuits are represented by means of oriented graphs. The graphs determine interconnections between the different circuit components representing the devices in the network.
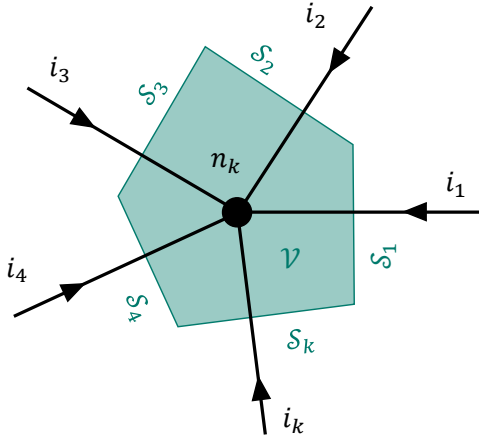
(a) Currents entering a node.
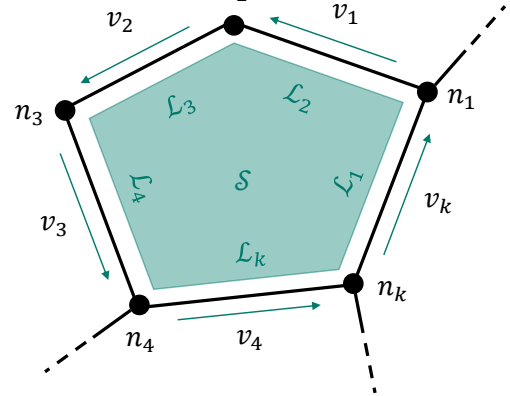
(b) Voltages around a closed loop.

Figure 2.4. Sketch of the circuit layout for the Kirchhoff's current and voltage laws.

The electrical behavior of each component is described using lumped element models which provide a mathematical relation (algebraic or differential) for the voltages and the currents associated to the branch where the component is located. Moreover, currents and voltages are not independent, instead they depend on the topology of the graph describing the circuit, and their relation is formulated by means of Kirchhoff's voltage (KVL) and current (KCL) laws. Nowadays, most modern circuit simulations are performed by means of SPICE-like programs [164] (Simulation Program with Integrated Circuit Emphasis). The description of voltages and currents in a circuit can be obtained by means of the modified nodal analysis (MNA) [165, 166] which extends the standard nodal analysis approach [165]. Specifically, the method allows including as degrees of freedom not only the node potentials, but also some of the branch currents. In this way, it is possible to include a broader range of components, like the ones featuring a current dependency, and to obtain an easier treatment of voltage sources. The combination of the circuit topology equations provided by the KVL and KCL, and the typology equations provided by the lumped element models of the components, leads to a system of equations which can be integrated in time for determining the electrical behavior of the circuit.

2.10.1 Kirchhoff's laws

Kirchhoff's laws are derived assuming time-invariant geometries for the circuits. To obtain KCL, the current continuity equation is applied to a volume $\mathcal{V}$ containing an arbitrary circuit node n_k, see Figure 2.4a. By assuming static conditions and by applying Gauss's theorem, the following relation is obtained

$$\int_{\mathcal{V}} \nabla \cdot \vec{J} \mathrm{d}\mathcal{V} = \int_{\partial \mathcal{V}} \vec{J} \cdot \mathrm{d}\vec{\mathcal{S}} = 0. \tag{2.74}$$

If the surface $\mathcal{S}$ around the node n_k is composed of n conductors each carrying the current i_k, then the KCL is obtained as

$$\sum_{k=1}^{n} \int_{\partial \mathcal{V}_k} \vec{J} \cdot \mathrm{d}\vec{\mathcal{S}} = \sum_{k=1}^{n} \pm i_k = 0, \tag{2.75}$$

27

where the sign of the currents depends on the orientation of conductors with respect to the surface integrals.

To obtain KVL, Faraday's law is applied to an arbitrary surface $\mathcal{S}$, see Figure 2.4b. By assuming static conditions and by applying Stokes' theorem, the following relation is obtained

$$\int_{\mathcal{S}} \nabla \times \vec{E} \cdot \mathrm{d}\vec{\mathcal{S}} = \int_{\partial \mathcal{S}} \vec{E} \cdot \mathrm{d}\vec{\mathcal{L}} = 0. \tag{2.76}$$

If the edge $\partial \mathcal{S}$ is composed of a loop of n circuit branches with voltages v_k, $k = 1, \ldots, n$, then KVL is obtained as

$$\sum_{k=1}^{n} \int_{\partial \mathcal{S}_k} \vec{E} \cdot \mathrm{d}\vec{\mathcal{L}} = \sum_{k=1}^{n} \pm v_k = 0, \tag{2.77}$$

where the voltage sign depends on the orientation of conductors with respect to the line integrals. As a consequence of the irrotationality of $\vec{E}$, the voltages across the circuit branches can be represented by means of an electric scalar potential ϕ. The related node potentials e_k represent the value of ϕ at the circuit node n_k, with $k = 1, \ldots, N_n$, and N_n is the number of nodes in the circuit. The voltage-potential relation is given for the nodes n_k and n_{k+1} as

$$v_k = \int_{\partial \mathcal{S}_k} \vec{E} \cdot \mathrm{d}\vec{\mathcal{L}} = -\int_{\partial \mathcal{S}_k} \nabla \phi \cdot \mathrm{d}\vec{\mathcal{L}} = \phi_{k+1} - \phi_k = e_{k+1} - e_k. \tag{2.78}$$

2.10.2 Modified nodal analysis

Let b_j one of the N_b oriented branches in the circuit. The topology of the circuit is described by the incidence matrix $\mathbf{A}^\star$ with

$$\mathbf{A}^\star_{k,j} = \begin{cases} 1 & \text{if branch } b_j \text{ leaves node } k, \\ -1 & \text{if branch } b_j \text{ enters node } k, \\ 0 & \text{otherwise.} \end{cases} \tag{2.79}$$

As $\mathbf{A}^\star$ has linearly dependent rows, regularization is needed. Therefore, an arbitrary ground node n_0 is chosen, and a reference potential ϕ_0 is provided to the circuit. The reduced incidence matrix $\mathbf{A}$ is obtained by eliminating from $\mathbf{A}^\star$ the row j_0 associated to the reference potential.

With the previous definition, it is possible to enforce KCL and KVL as

$$\mathbf{A}\mathbf{i} = 0, \tag{2.80}$$

$$\mathbf{A}^\top \mathbf{e} = \mathbf{v}, \tag{2.81}$$

where $\mathbf{i} : \mathcal{I} \to \mathbb{R}^{N_b}$ is the vector of all branch currents, $\mathbf{e} : \mathcal{I} \to \mathbb{R}^{N_n - 1}$ is the vector of node potentials excluding the ground node, and $\mathbf{v} : \mathcal{I} \to \mathbb{R}^{N_b}$ is the vector of voltages across all branches. For each circuit branch, the voltage-current relation is determined by the constitutive equations associated to the lumped elements. In the simple case of linear elements, the constitutive equations are combined into the conductance, capacitance and inductance matrices $\mathbf{G}$, $\mathbf{C}$ and $\mathbf{L}$, as

$$\mathbf{i}_G = \mathbf{G}\mathbf{v}_G, \qquad \mathbf{v}_L = \mathbf{L}\frac{\mathrm{d}}{\mathrm{d}t}\mathbf{i}_L, \qquad \mathbf{i}_C = \mathbf{C}\frac{\mathrm{d}}{\mathrm{d}t}\mathbf{v}_C, \tag{2.82}$$

whereas the branches containing source voltages $\mathbf{v}_s$ and source currents $\mathbf{i}_s$ are given by

$$\mathbf{v}_V = \mathbf{v}_s, \qquad \mathbf{i}_I = \mathbf{i}_s. \tag{2.83}$$

The currents and voltages related to resistance, inductance, capacitance, and source elements (subscripts C, G, L, V, I) are related such that

$$
\begin{aligned}
\mathbf{i}^\top &= [\mathbf{i}_G^\top, \ \mathbf{i}_C^\top, \ \mathbf{i}_L^\top, \ \mathbf{i}_V^\top, \ \mathbf{i}_I^\top], \\
\mathbf{v}^\top &= [\mathbf{v}_G^\top, \ \mathbf{v}_C^\top, \ \mathbf{v}_L^\top, \ \mathbf{v}_V^\top, \ \mathbf{v}_I^\top].
\end{aligned}
\tag{2.84}
$$

By combining the previous definitions, the MNA formulation reads

$$
\begin{aligned}
\mathbf{A}_C \mathbf{C} \mathbf{A}_C^\top \frac{\mathrm{d}}{\mathrm{d}t} \mathbf{e} + \mathbf{A}_G \mathbf{G} \mathbf{A}_G^\top \mathbf{e} + \mathbf{A}_L \mathbf{i}_L + \mathbf{A}_V \mathbf{i}_V + \mathbf{A}_I \mathbf{i}_s &= 0 \\
\mathbf{L} \frac{\mathrm{d}}{\mathrm{d}t} \mathbf{i}_L - \mathbf{A}_L^\top \mathbf{e} &= 0 \\
\mathbf{A}_V^\top \mathbf{e} - \mathbf{v}_s &= 0
\end{aligned}
\tag{2.85}
$$

where $\mathbf{A}_\star$ represents the columns of the incidence matrix associated to branches which contain specific devices, such that $\mathbf{A} = [\mathbf{A}_C, \ \mathbf{A}_G, \ \mathbf{A}_L, \ \mathbf{A}_V, \ \mathbf{A}_I]$. The equation system (2.85) can be solved for the time interval $t \in \mathcal{I} = (t_0, t_{\mathrm{end}})$ using time stepping schemes based for example on the trapezoidal rule or the backward differentiation formula, see Section 3.3 for a general overview. The generalization to elements featuring nonlinear constitutive equations is discussed in [167] and the references therein.

2.11 Field-Circuit Coupled Magnetothermal Problem

A convenient way for visualizing the different field quantities and potentials introduced for Maxwell's equations and their magnetoquasistatic approximation, including the constitutive laws, is shown in Figure 2.5, left. This schematic representation is known as Maxwell's house [168] or Tonti's diagram [169]. The potentials for the $\vec{A} - \phi$ (or $\vec{A}^\star$) formulation and the fields $\vec{E}$ and $\vec{B}$ are located on the primal complex (left side), and the potentials for the $\vec{T} - \psi$ (or $\vec{H} - \varphi$) formulation and the fields $\vec{D}$ and $\vec{J}$ are located on the dual complex (right side) of the diagram.

The representation in Figure 2.5 is completed by the thermal house on the top right, and a circuit model of arbitrary complexity on the bottom right. The two houses include vertical and planar links. The vertical links represent differential operators, the planar links are rendered as bold and dashed arrows, representing time derivatives and constitutive laws. The Maxwell house is extended by the distribution functions for stranded and solid conductors which allow connecting the external circuit via source voltages and currents. The electromagnetic coupling links the two houses by means of Joule and magnetic losses, and magnetic field-dependency in the heat capacity and heat transfer coefficients. The thermal coupling occurs via the temperature-dependent electrical conductivity. The circuit is coupled to both the houses via the field-dependent properties characterizing the lumped parameters. The three problems are tightly coupled, determining a field-circuit coupled problem which is intrinsically multiphysical. At the same time, the subsystems included in the problem typically show physical phenomena characterized by time rates which might differ up to several orders of magnitude. This is a challenge for any time-integration method, as solving the dynamics of different subsystems leads to a multirate problem. Moreover, subsystems may have very different spatial dimensions, and may require different level of spatial resolution in order to capture the most relevant physical phenomena, leading to a multiscale problem.
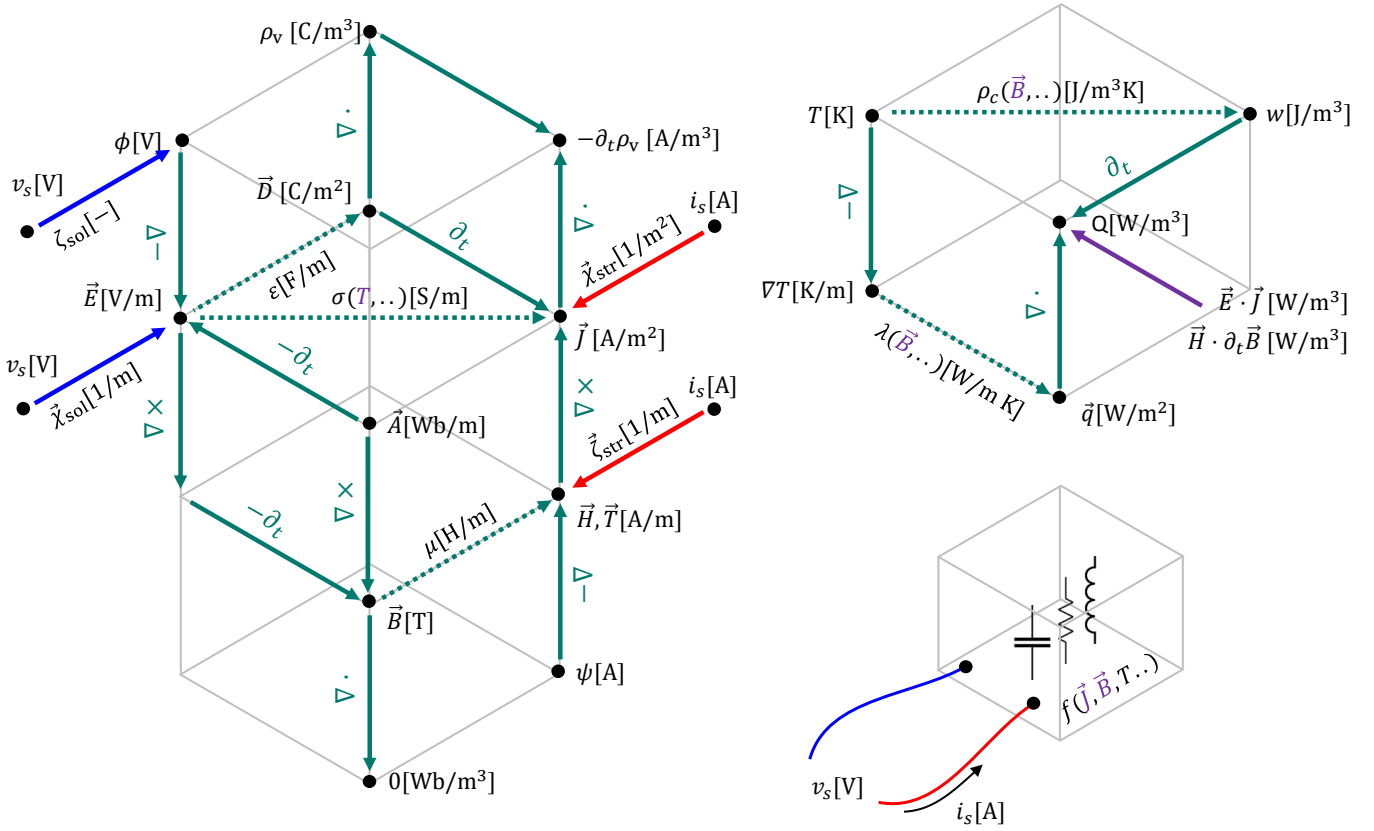
Figure 2.5. Left: Maxwell's house from [168], extended with the distribution functions. Right: thermal house and arbitrary electrical circuit. The vertical links represent differential operators, whereas the planar links are either time derivatives, or constitutive laws. The two houses are linked by the Joule and magnetic losses, the magnetic field-dependent mass density and heat transmission coefficient, and by the temperature-dependent conductivity. The houses are linked to the circuit via both distribution functions, and field-dependencies in the lumped parameters.

2.12 Modeling Of Superconducting Magnets

Superconducting materials such as Nb-Ti, Nb$_3$Sn and ReBCO and exhibit a highly nonlinear electric field strength-current density relation (e.g. [27]). The majority of models available in literature propose the use of continuous and smooth power-law relations as $|\vec{E}| \propto |\vec{J}|^n$, where the index n determines the steepness. Such relations are phenomenological and include fitting parameters which are commonly quantified by means of measurements.

2.12.1 Superconducting materials

A widely common approach in modeling the resistivity ρ of superconducting materials consists in using a phenomenological percolation-depinning law proposed in [170]. The law gives a lower limit for the current
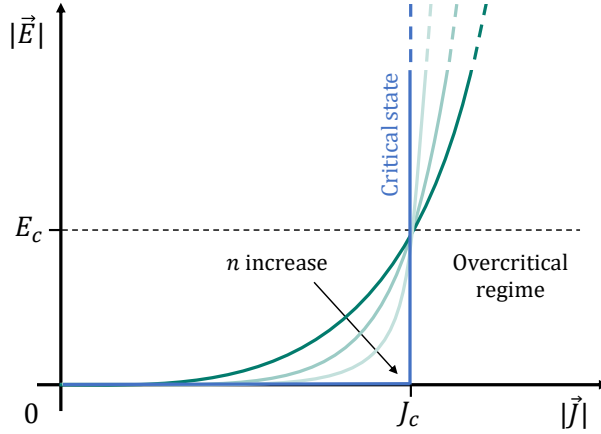
Figure 2.6. Sketch of the qualitative electric behavior in superconductors. The critical current density J_c and the corresponding critical field E_c are highlighted. The parametrization by the power-law index shows that by increasing the n-value, steeper curves and sharper transitions are obtained.

density, below which the magnetic field is frozen in the superconductor and no flux creep [1, 170] can occur. However, the current density values and the magnetic fields used in practical applications are typically much higher than the lower limit considered in the percolation-depinning law. Therefore, a further simplification into a power law [171] is sufficient, as shown in [172], and is also adopted in this work. The resistivity ρ in superconductors reads

$$\rho(|\vec{J}|, \vec{B}, T) = \frac{E_c}{J_c(\vec{B}, T)} \left(\frac{|\vec{J}|}{J_c(\vec{B}, T)} \right)^{n(\vec{B},T)-1} = \frac{E_c}{J_c(\vec{B}, T)} \left(\frac{|\vec{E}|}{E_c} \right)^{1-\frac{1}{n(\vec{B},T)}}, \tag{2.86}$$

where $\vec{J}$ is the current density, E_c is the critical electric field strength, set to $1 \times 10^{-4}\,\mathrm{V\,m^{-1}}$ [173], and the material- and field-dependent parameters J_c and n are the critical current density and the power-law index, respectively. The behavior of J_c can be represented for example by means of fitting functions (see Appendix A), or lookup tables. Typical values for the n-value are found between 40 and 50 for LTS materials [174], and between 25 and 35 for the HTS counterpart [175]. The qualitative behavior of the power law is shown in Figure 2.6. In case of $n \to 0$, the power law approximates the behavior of normal conducting materials. In case of $n \to \infty$, the power law can be further approximated by the critical state model [176, 177]. For a comparison of the percolation-depinning law with its power-law and critical-state approximations, see Appendix B.

Care has to be taken in the use of (2.86), see for example the discussion in [178] regarding continuity properties of material functions. Both the power law and its derivative vanish at low current density and are unbounded, that is,

$$\lim_{|\vec{J}|\to 0^+} \rho(|\vec{J}|, \vec{B}, T) = 0, \qquad \lim_{|\vec{J}|\to 0^+} \frac{\partial}{\partial|\vec{J}|}\rho(|\vec{J}|, \vec{B}, T) = 0, \tag{2.87a}$$

$$\lim_{|\vec{J}|\to +\infty} \rho(|\vec{J}|, \vec{B}, T) = +\infty, \qquad \lim_{|\vec{J}|\to +\infty} \frac{\partial}{\partial|\vec{J}|}\rho(|\vec{J}|, \vec{B}, T) = +\infty. \tag{2.87b}$$

To overcome these issues, a common approach consists in introducing lower and upper saturation thresholds in (2.86), see for example [78, 88, 179]. In this case, the magnitude for the lower threshold has to be carefully

chosen as it introduces an artificial resistivity potentially affecting the dynamics of the screening currents in the superconducting material. Another possibility consists in discarding the power law in favor of functions fulfilling the necessary continuity properties, for example hyperbolic tangent functions [76, 77]. Recently, a mathematical model based on empirical measurements was proposed in [180] for improving the power-law behavior in the overcritical regime, that is, $|\vec{J}| \geq J_{\mathrm{c}}$ (see Figure 2.6). For the simple case where the field dependency is discarded, J_{c} and n are constant, and the constitutive law $\vec{E}(\vec{J}) = \rho(|\vec{J}|)\vec{J}$ can be linearized as a Taylor series expansion around $|\vec{J_0}|$ truncated to the first order, reading

$$\vec{E}(\vec{J}) \approx \vec{E}(\vec{J_0}) + \frac{\partial}{\partial|\vec{J}|}\rho(|\vec{J_0}|)(|\vec{J}| - |\vec{J_0}|) \tag{2.88}$$

The parameter $|\vec{J_0}|$ should be chosen as $|\vec{J_0}| \gg J_{\mathrm{c}}$, such that the linearization does not affect that the field solution in the overcritical regime (see Figure 2.6).

2.12.2 Monolithic formulations

The power-law behavior of superconducting materials poses a challenge to the formulation of the field problem. At low currents, that is, $|\vec{J}| \to 0$, the resistivity in (2.86) vanishes or, conversely, the conductivity tends to infinity. In case that normal-conducting and insulating materials are also considered in the field problem, monolithic formulations show important drawbacks.

One possibility is given by conductivity-based monolithic formulations, such as the (reduced) magnetic vector potential $\vec{A}$, the difference in the conductivity of the different domains leads to numerical instabilities once the field problem is discretized, as it has been observed for example in [76, 95, 181]. Possible solutions consist in applying iterative schemes for the power-law calculation [78] and fine-tuning of numerical solvers via damping factors [95]. However, such solutions are sensitive to the model characteristics and in principle cannot guarantee the convergence of the numerical solution [95]. Another possibility is given by resistivity-based monolithic formulations, such as the widely-used $\vec{H}$ formulation [79, 84, 86, 87] which is derived from the $\vec{H} - \varphi$ formulation (see Section 2.8.1). The $\vec{H}$ formulation is derived by solving for the unknown $\vec{H}$ field everywhere in the computational domain, thus avoiding the scalar field φ. To do so, a finite resistivity ρ is introduced in the nonconducting fraction of the computational domain. The first drawback is the introduction of unnecessary degrees of freedom in the nonconducting domains, increasing the consequent computational cost [182]. The second and most relevant drawback is that the choice of the conductivity is usually based on empirical knowledge achieved through numerical experiments, see for example [182], and it directly affects the stability and accuracy of the solver. On the one hand, reducing ρ leads to a non-negligible and non-physical current density in the nonconducting region (e.g. [81]). On the other hand, increasing ρ might lead to issues in the robustness of the numerical time-stepping scheme [182]. Despite these important shortcomings, the $\vec{H}$ formulation is, at the time of writing, the most widely spread formulation for the simulation of high-temperature superconductors, most likely due to its simplicity.

2.12.3 Mixed-field formulations

A third possibility is given by the use of mixed field formulations, such that resistivity- and conductivity-based formulations are combined. In this case, the computational domain is decomposed into sub-domains or regions, and distinct formulations can be assigned region-wise, according to the electrical behavior of the regions. As a consequence, several possibilities arise due to the freedom in the domain decomposition

scheme, and the choice of the unknown field quantity in each region. For computational domains containing eddy-current regions, the formulations of interest can be subdivided into mixed vector-scalar and mixed vector-vector field formulations. Examples belonging to the mixed vector-scalar formulations group are the $\vec{H}$-oriented formulations, such as the $\vec{H} - \varphi$ and the $\vec{T} - \psi$ formulations detailed in Sections 2.8.1 and 2.8.2. These formulations have been successfully used for simulating bulk superconductors (e.g. [82]) as well as superconducting cables [182, 183]. However, the main drawback of a vector-scalar approach is the increased complexity deriving from the introduction of cohomology basis functions representing the net currents in the source regions, in case of non-trivial topology for the computational domain [95, 182]. A detailed comparison of the $\vec{H} - \varphi$ and $\vec{T} - \psi$ formulations in eddy-current problems is given in [184]. Concerning mixed vector-vector formulations, an example is provided by the $\vec{H} - \vec{E}$ formulation used for solving the full set of Maxwell's equations [131].

In this work, the coupled $\vec{A} - \vec{H}$ field formulation belonging to the mixed vector-vector class is chosen for modeling field problems in terms of $\vec{H}$ in the conducting domains containing superconducting materials, and in terms of $\vec{A}$ in the nonconducting and ferromagnetic materials. While the use of $\vec{H}$ for superconductors is a common choice [79], the introduction of $\vec{A}$ brings several advantages. In particular, the magnetic vector potential deals with multiply connected domains without the need of cohomology basis functions, does not require the introduction of an artificial resistivity in the nonconducting domains, and is more efficient for modeling ferromagnetic materials with respect to a monolithic $\vec{H}$ formulation [95]. The coupled $\vec{A} - \vec{H}$ formulation has been successfully used in the simulation of rotating electrical machines with superconducting windings [89], systems containing both superconducting and ferromagnetic materials in [95], and superconducting magnets in [185, 186].

2.13 Coupled $\vec{A} - \vec{H}$ Field Formulation

The field problem is defined under MQS assumptions by means of a coupled $\vec{A} - \vec{H}$ field formulation. A domain decomposition strategy is applied to the computational domain Ω, such that the field problem is solved for the (reduced) magnetic vector potential $\vec{A}$ in the region Ω_{A} containing only nonconducting and normal conducting materials, and for the magnetic field strength $\vec{H}$ in the conducting region Ω_{H} which includes all the superconducting materials. In this way, the formulation is resistivity-based in the superconducting domains, and conductivity-based in non-conducting domains, such that the material properties remain finite. The field variables are restricted as $\vec{A} = \vec{A}|_{\Omega_{\mathrm{A}}}$ and $\vec{H} = \vec{H}|_{\Omega_{\mathrm{H}}}$ to avoid ambiguity with the magnetic field strength vector in Ω_{A}. The domain decomposition strategy and the formulation of the coupled field formulation is detailed in the following.

2.13.1 Domain decomposition strategy

The domain decomposition is formalized by assuming that domains and boundaries include also their closure depending on the situation, for the simplicity of notation. The strategy is based on the separation of the conducting domain containing the superconducting materials from the remainder of the computational domain. The decomposition strategy is applied to the typical structure of an accelerator magnet where superconducting materials are typically used for the coil. The latter is powered by an external circuit and carries a current acting as the source for the magnetic field. For the general case, the coil is assumed to be composed of N_{r} windings which are electrically independent, that is, independent currents can be prescribed. The remainder of the domain represents the rest of the magnet containing the iron yoke, the mechanical supports and the

(a) Domain partition.   *(b) Boundary partition.*
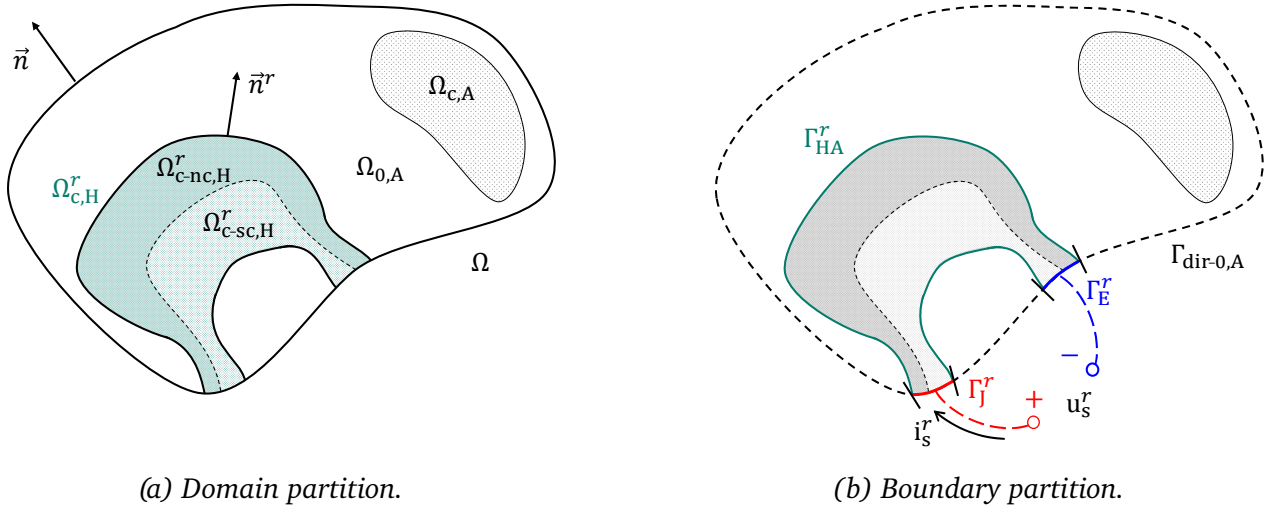
Figure 2.7. *Decomposition of the domain Ω. (a) The regions $\Omega^r_{\text{c-sc,H}}$ and $\Omega^r_{\text{c-nc,H}}$ account for superconducting and normal-conducting materials, whereas the regions $\Omega_{\text{c,A}}$ and $\Omega_{\text{0,A}}$ refer to normal conducting and insulating materials. (b) The boundary $\Gamma^r_{\text{c,H}}$ includes the interface Γ^r_{HA} and the electrical ports Γ^r_{E} and Γ^r_{J}, used for imposing the source voltages v^r_{s} and currents i^r_{s}. The electrical ports are excluded from the exterior boundary $\Gamma_{\text{dir-0,A}}$.*

air regions. The electrical insulation of the coil ensures the electrical separation between the two domains. As a consequence, the coil and the iron yoke are not in contact.

2.13.1.1 Partition of the domain

The domain $\Omega \subset \mathbb{R}^3$ bounded by $\Gamma = \partial\Omega$ is decomposed into the domain Ω_{H} bounded by Γ_{H}, and the domain Ω_{A} bounded by Γ_{A}, such that

$$\Omega = \Omega_{\text{H}} \cup \Omega_{\text{A}}, \qquad \Omega_{\text{H}} \cap \Omega_{\text{A}} = \Gamma_{\text{HA}}, \tag{2.89}$$

where Γ_{HA} is the interface between Ω_{H} and Ω_{A}. No source domain Ω_{s} is considered for Ω. The domain Ω_{H} is conducting, and is further subdivided into N_{r} independent and non-intersecting domains $\Omega^r_{\text{c,H}}$. These domains represent the windings composing the coil, as

$$\Omega_{\text{H}} = \bigcup_{r=1}^{N_{\text{r}}} \Omega^r_{\text{c,H}}, \qquad \Omega^r_{\text{c,H}} \cap \Omega^j_{\text{c,H}} = \varnothing \qquad \text{for } r \neq j. \tag{2.90}$$

Moreover, each r-th domain may contain both, superconducting and normal conducting regions, represented by $\Omega^r_{\text{c-sc,H}}$ and $\Omega^r_{\text{c-nc,H}}$, accounting for the superconducting and normal conducting fraction of the coil. The domain Ω_{A} may contain both, normal conducting and insulating domains, represented by $\Omega_{\text{c,A}}$ and $\Omega_{\text{0,A}}$, such that $\Omega_{\text{A}} = \Omega_{\text{c,A}} \cup \Omega_{\text{0,A}}$. The domain $\Omega_{\text{c,A}}$ is assumed to represent only the iron yoke, however the inclusion of other (normal conducting) structural components is straightforward. The magnetic permeability μ determining the magnetic constitutive law is assumed as field-independent in the domains $\Omega_{\text{c,H}}$ and $\Omega_{\text{0,A}}$, whereas a nonlinear field dependency $\mu(|\vec{B}|) : \Omega_{\text{c,A}} \to \mathbb{R}$ is assumed for the iron yoke. The domain decomposition strategy is shown in Figure 2.7a. For the sake of clarity, only the r-th conducting domain is represented.

2.13.1.2 Partition of the boundary

Each domain $\Omega_{c,H}^r$ is oriented with the outward normal vector $\vec{n}^r$ and it is contoured by $\Gamma_{c,H}^r$ such that

$$\Gamma_{c,H} = \bigcup_{r=1}^{N_r} \Gamma_{c,H}^r, \qquad \Gamma_{c,H}^r \cap \Gamma_{c,H}^j = \varnothing \qquad \text{for } r \neq j. \tag{2.91}$$

Each of the boundaries $\Gamma_{c,H}^r$ is further decomposed into three distinct contributions as

$$\Gamma_{c,H}^r = \Gamma_{HA}^r \cup \Gamma_E^r \cup \Gamma_J^r, \tag{2.92}$$

where Γ_{HA}^r is the boundary at the interface between $\Omega_{c,H}^r$ and Ω_A^r, and Γ_E^r and Γ_J^r are two electrical ports which are provided to each winding for imposing the field sources in terms of either voltages u_s^r or currents i_s^r. The cumulative boundaries are defined as

$$\Gamma_{HA} = \bigcup_{r=1}^{N_r} \Gamma_{HA}^r, \qquad \Gamma_E = \bigcup_{r=1}^{N_r} \Gamma_E^r, \qquad \Gamma_J = \bigcup_{r=1}^{N_r} \Gamma_J^r. \tag{2.93}$$

The domain Ω_A is oriented with the outward normal vector $\vec{n}$, and it is contoured by

$$\Gamma_A = \Gamma_{\text{dir-0,A}} \cup \Gamma_{HA}, \tag{2.94}$$

where $\Gamma_{\text{dir-0,A}} = \Gamma \backslash (\Gamma_E \cup \Gamma_J)$ is the exterior boundary without the electrical ports. The domains Ω_A and $\Omega_{c,H}^r$ are oriented such that $\vec{n}$ and $\vec{n}^r$ have opposite sign at the interface Γ_{HA}^r, for all $\forall r$. The boundary decomposition strategy is shown in Figure 2.7b. Once again, only the r-th source domain is shown.

2.13.2 Excitation sources

The N_r windings of the coil are assumed to be solid conductors, as in the case of cables made of HTS ReBCO tapes. For this reason, the excitation of the domains $\Omega_{c,H}^r$ representing the N_r windings of the coil is done by introducing a distribution function for solid conductors $\vec{\chi}_{\text{sol}}^r$ for each corresponding domain $\Omega_{c,H}^r$ (see Section 2.9.2). In this way, each winding can be powered by an independent source voltage v_s^r and can carry an independent source current i_s^r. With the previous observations, the voltages, currents and distribution functions are given by the vectors

$$\mathbf{v}_s = [v_s^1, \dots, v_s^{N_r}]^\top, \qquad \mathbf{i}_s = [i_s^1, \dots, i_s^{N_r}]^\top, \qquad \boldsymbol{\chi}_{\text{sol}} = [\vec{\chi}_{\text{sol}}^1, \dots, \vec{\chi}_{\text{sol}}^{N_r}]^\top. \tag{2.95}$$

Each distribution function allows linking the source electric field $\vec{E}_s^r$ in the r-th winding to the related source voltage v_s^r. For $r = 1, \dots, N_r$ the electric field strength reads

$$\vec{E}^r = \rho \vec{J}^r - \vec{E}_s^r = \rho \nabla \times \vec{H}^r - \vec{\chi}_{\text{sol}}^r v_s^r. \tag{2.96}$$

Alternatively, if the source current $\vec{i}_s^r$ is prescribed, the relation in (2.66) is used. In this case, the source voltage becomes an algebraic unknown, and one constraint equation is added for each of the independent currents in $\mathbf{i}_s$, as

$$i_s^r = \int_{\Omega_{c,H}^r} \vec{\chi}_{\text{sol}}^r \cdot (\nabla \times \vec{H}^r) \, d\Omega, \qquad k = 1, \dots, N_r. \tag{2.97}$$

serving as a Lagrange multiplier for the determination of the source voltage v_{s}^r. The domain decomposition strategy described in (2.89) and (2.90) leads to multiply connected domains with disconnected boundaries. As a consequence, the field quantities in Ω_{H} are defined independently for each domain $\Omega_{\mathrm{c,H}}^r$, and are given as the sum of the contributions from all the windings in the coil, reading

$$\vec{H} = \sum_{r=1}^{N_{\mathrm{r}}} \vec{H}^r, \qquad \vec{E} = \sum_{r=1}^{N_{\mathrm{r}}} \vec{E}^r, \qquad \vec{E}_{\mathrm{s}} = \sum_{r=1}^{N_{\mathrm{r}}} \vec{E}_{\mathrm{s}}^r. \tag{2.98}$$

2.13.3 Distribution functions

The distribution functions in (2.95) are independent from the field formulation applied in Ω, therefore they can be calculated separately. From (2.68), each $\vec{\chi}_{\mathrm{sol}}^r$ is given by a gradient field in $\Omega_{\mathrm{c,H}}^r$, and it is zero elsewhere, that is, $\vec{\chi}_{\mathrm{sol}}^r = 0$ in Ω_{A}. The potential is obtained by solving a unitary current-flow problem for each of the windings composing the coil [161]. The field problem is formalized for $r = 1, ..., N_{\mathrm{r}}$ as

$$\begin{cases} \nabla \cdot \sigma_\chi \nabla \xi^r = 0, & \text{in } \Omega_{\mathrm{c,H}}^r, & \text{(2.99a)} \\ \xi^r = 1, & \text{on } \Gamma_{\mathrm{J}}^r, & \text{(2.99b)} \\ \xi^r = 0, & \text{on } \Gamma_{\mathrm{E}}^r, & \text{(2.99c)} \\ (\sigma_\chi \nabla \xi^r) \cdot \vec{n}^r = 0, & \text{on } \Gamma_{\mathrm{HA}}^r, & \text{(2.99d)} \end{cases}$$

where $\sigma_\chi > 0$ is an arbitrary nonzero conductivity. With this definition, $\vec{\chi}_{\mathrm{sol}}^r$ can be interpreted as a per-unit source electric field strength.

2.13.4 Magnetoquasistatic formulation

The formulation of the field problem is composed of the $\vec{A}$ formulation in Ω_{A}, and the $\vec{H}$ formulation for each winding $\Omega_{\mathrm{c,H}}^r$. The field excitation is obtained by means of either voltage and/or current sources. In the first case, distribution functions apply the source voltage by means of an electric field source term, whereas in the second case the source current is enforced by means of integral constraints. Homogeneous Dirichlet boundary conditions are imposed to $\vec{A}$ on $\Gamma_{\mathrm{dir}\text{-}0,\mathrm{A}}$, and homogeneous Neumann boundary conditions are imposed for $r = 1, ..., N_{\mathrm{r}}$ to $\vec{H}^r$ on the electrical ports Γ_{J}^r and Γ_{J}^r, corresponding to electric boundary conditions for both the vector fields. With the previous observations, the formulation of the field problem reads: find $\vec{A}$, $\vec{H}^r$ and v_{s}^r, for $r = 1, ..., N_{\mathrm{r}}$, such that

$$\begin{cases} \nabla \times \mu^{-1} \nabla \times \vec{A} + \sigma \partial_t \vec{A} = 0, & \text{in } \Omega_{\mathrm{A}}, & \text{(2.100a)} \\ \nabla \times \rho \nabla \times \vec{H}^r + \partial_t \mu \vec{H}^r - \nabla \times \vec{\chi}_{\mathrm{sol}}^r v_{\mathrm{s}}^r = 0, & \text{in } \Omega_{\mathrm{c,H}}^r, & \text{(2.100b)} \\ \displaystyle\int_{\Omega_{\mathrm{c,H}}^r} \vec{\chi}_{\mathrm{sol}}^r \cdot (\nabla \times \vec{H}^r)\, \mathrm{d}\Omega = i_{\mathrm{s}}^r, & \text{for } r = 1, ..., N_{\mathrm{r}}, & \text{(2.100c)} \\ \vec{A} \times \vec{n} = 0, & \text{on } \Gamma_{\mathrm{dir}\text{-}0,\mathrm{A}}, & \text{(2.100d)} \\ (\rho \nabla \times \vec{H}^r - \vec{E}_{\mathrm{s}}^r) \times \vec{n}^r = 0, & \text{on } \Gamma_{\mathrm{E}}^r,\ \Gamma_{\mathrm{J}}^r. & \text{(2.100e)} \end{cases}$$

To ensure the consistency of the overall solution, the fields $\vec{A}$ and $\vec{H}$ are linked by appropriate interface conditions at Γ_{HA}^r. In detail, the continuity of the tangential components of $\vec{H}$ and $\vec{E}$, and the normal

components of $\vec{J}$ and $\vec{B}$ must be ensured. The interface conditions are given on Γ_{HA}^r for $r = 1, ..., N_{\mathrm{r}}$, as

$$(\mu^{-1}\nabla \times \vec{A} - \vec{H}^r) \times \vec{n}^r = 0, \qquad \text{for } \vec{H}_{\mathrm{t}}, \tag{2.101}$$

$$(\partial_t \vec{A} + \rho\nabla \times \vec{H}^r - \chi^r v_{\mathrm{s}}^r) \times \vec{n}^r = 0, \qquad \text{for } \vec{E}_{\mathrm{t}}, \tag{2.102}$$

$$(\sigma\partial_t \vec{A} + \nabla \times \vec{H}^r) \cdot \vec{n}^r = 0, \qquad \text{for } \vec{J}_{\mathrm{n}}, \tag{2.103}$$

$$(\nabla \times \vec{A} - \mu\vec{H}^r) \cdot \vec{n}^r = 0, \qquad \text{for } \vec{B}_{\mathrm{n}}. \tag{2.104}$$

2.13.5 Heat balance equation

The materials typically used in superconducting devices show magnetic- and temperature-dependent physical properties. In particular, the temperature T influences both the critical current density of the superconducting materials, and the resistivity of the normal conducting materials. This, in turn, determines the Joule losses P_{J} occurring in the conducting domains, and acting as the main heat source term. The temperature dependency requires characterizing the thermodynamics of the system by adding the heat balance equation, with suitable boundary and initial conditions, to the MQS problem described by (2.100a)−(2.100c). The temperature is obtained by solving the heat balance equation

$$\begin{cases} \rho_{\mathrm{m}} C_{\mathrm{p}}\partial_t T - \nabla \cdot (\kappa\nabla T) = P_{\mathrm{J}}, & \text{in } \Omega, \tag{2.105a} \\ \kappa\nabla T \cdot \vec{n} = 0, & \text{on } \Gamma. \tag{2.105b} \end{cases}$$

If the domain of interest is limited to the superconducting coil, as in case of a quench, and the adiabatic approximation is reasonable, then the Neumann boundary condition can be moved to $\Gamma_{\mathrm{c,H}}$, thereby reducing the model complexity.

2.14 Thin-Shell Approximation

High-temperature superconducting tapes feature a layered structure of composite materials. The tape structure is shown in Figure 2.8a. The generic tape $\Omega_{\mathrm{c,H}}^r$ of thickness δ_{t}^r is composed of one superconducting layer $\Omega_{\mathrm{c\text{-}sc,H}}^r$ of thickness $\delta_{\mathrm{t_{sc}}}^r$, and a normal conducting layer $\Omega_{\mathrm{c\text{-}nc,H}}^r$ of thickness $\delta_{\mathrm{t_{nc}}}^r$, which is made of composite materials and provides mechanical and thermal support. Tapes are typically characterized by a high aspect ratio between their width and thickness, up to two orders of magnitude for the overall cross section of the tape, and up to three orders of magnitude if only the superconducting layer is considered. Such high aspect ratios justify to represent the domain $\Omega_{\mathrm{c,H}}^r$ as a thin shell, neglecting its thickness δ_{t}^r. In this way, tapes can be represented by means of a thin-shell approximation [75]. Therefore, the tapes are reduced to an equivalent surface $\Gamma_{\mathrm{c,H}}^r$ (see Figure 2.8b) where the material properties are homogenized. In particular, the current sharing between the conducting layers is resolved via an equivalent resistivity ρ_{eq}^r which is formalized in Section 3.7.

The volume associated to the original shape of the conducting domain $\Omega_{\mathrm{c,H}}^r$ is preserved as an insulating structural element (dashed line, Figure 2.8b), and it is accounted for in Ω_{A}. In this way, the thermal contacts are preserved for the thermal problem in (2.105). The implications on the coupled field formulation are discussed in the following.
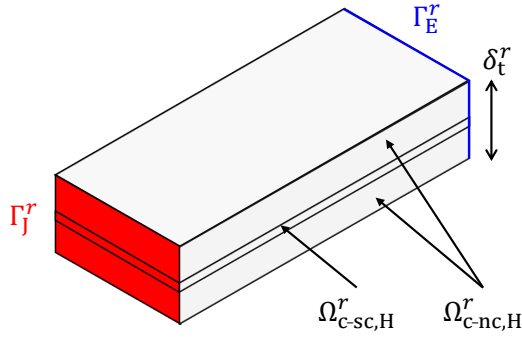
(a) Bulk tape, 3D setting. *(b) Thin-shell tape, 3D setting.*
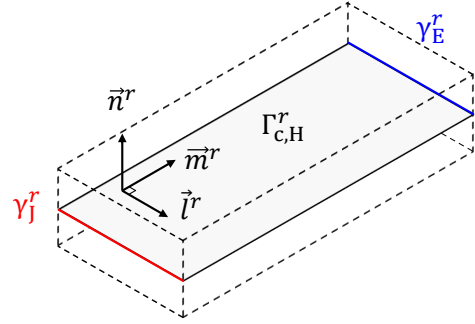
Figure 2.8. Thin-shell approximation. (a) Superconducting tape of thickness δ_{t}^r, featuring superconducting and normal conducting domains $\Omega_{\mathrm{c\text{-}sc,H}}^r$ and $\Omega_{\mathrm{c\text{-}nc,H}}^r$. (b) Equivalent thin-shell approximation $\Gamma_{\mathrm{c,H}}^r$. The electrical ports Γ_{E}^r and Γ_{J}^r are reduced to the edges γ_{E}^r and γ_{J}^r, respectively.

2.14.1 Electromagnetic behavior

The discussion of the electromagnetic behavior of the thin shell is discussed with respect to a local coordinate system $(\vec{l}^r, \vec{m}^r, \vec{n}^r)$ which is oriented according to the tangential ($\vec{l}^r$, $\vec{m}^r$) and normal ($\vec{n}^r$) directions of the r-th tape (see Figure 2.8b). With this definition, the differential operators and vectors $\vec{v}$ are decomposed into their tangential and normal components (subscripts t and n), such that

$$\nabla = \nabla_{\mathrm{t}} + \nabla_{\mathrm{n}}, \qquad \vec{v} = \vec{v}_{\mathrm{t}} + \vec{v}_{\mathrm{n}}. \tag{2.106}$$

Without loss of generality, the current density $\vec{J}^r$ within the r-th tape $\Omega_{\mathrm{c,H}}^r$ can be described by the contributions

$$\begin{aligned} \vec{J}^r &= \nabla \times \vec{H}^r \\ &= \nabla_{\mathrm{t}} \times \vec{H}_{\mathrm{t}}^r + \nabla_{\mathrm{t}} \times \vec{H}_{\mathrm{n}}^r + \nabla_{\mathrm{n}} \times \vec{H}_{\mathrm{t}}^r + \nabla_{\mathrm{n}} \times \vec{H}_{\mathrm{n}}^r \\ &= \nabla_{\mathrm{t}} \times \vec{H}_{\mathrm{n}}^r + \nabla_{\mathrm{n}} \times \vec{H}_{\mathrm{t}}^r, \end{aligned} \tag{2.107}$$

where the contributions $\nabla_{\mathrm{t}} \times \vec{H}_{\mathrm{t}}^r$ and $\nabla_{\mathrm{n}} \times \vec{H}_{\mathrm{n}}^r$ are identically zero. At this point, the thin-shell approximation is introduced by neglecting the physical thickness δ_{t}^r of the superconducting tape, collapsing its volume into a surface (or line, in the 2D setting). By doing so, the variation of all field quantities along the perpendicular direction of the tape $\vec{n}^r$ is forced to be zero, therefore

$$\nabla \cdot = (\nabla_{\mathrm{t}} \cdot, \nabla_{\mathrm{n}} \cdot) = (\nabla_{\mathrm{t}} \cdot, 0) \qquad \text{on } \Gamma_{\mathrm{c,H}}^r. \tag{2.108}$$

Since no variation of the current density can occur along the normal direction of the tape, the current density can be replaced by an equivalent surface current density term $\vec{K}^r$ in the thin shell as

$$\vec{K}^r = \delta_{\mathrm{t}}^r \vec{J}^r = \delta_{\mathrm{t}}^r \nabla_{\mathrm{t}} \times \vec{H}_{\mathrm{n}}^r \qquad \text{on } \Gamma_{\mathrm{c,H}}^r, \tag{2.109}$$

where the last step in (2.109) is obtained by incorporating the property in (2.108) into (2.107). Following (2.109) the quantity $\vec{K}^r$ is determined only by the normal component $\vec{H}_{\mathrm{n}}^r$ of the magnetic field strength within the thin shell.

2.14.2 Magnetoquasistatic formulation

The description of the magnetic field dynamics within the thin-shell approximation is obtained by projecting the $\vec{H}$ formulation in (2.100b) along the $\vec{n}^r$ component of the thin shell, that is $\vec{H}_{\mathrm{n}}^r = H^r \vec{n}^r$, obtaining for $r = 1, ..., N_{\mathrm{r}}$

$$\nabla \times \rho \nabla \times (H^r \vec{n}^r) + \partial_t \mu (H^r \vec{n}^r) - \nabla \times \vec{\chi}_{\mathrm{sol}}^r v_{\mathrm{s}}^r = 0 \qquad \text{on } \Gamma_{\mathrm{c,H}}^r, \tag{2.110}$$

where the differential operator is intended as in (2.108), and $\vec{\chi}_{\mathrm{sol}}^r$ is adapted for solid conductors represented by a thin-shell approximation, that is, the current flow problem (2.99) is solved for a surface domain where the electrical ports are represented by lines (see Figure 2.8b). The interface conditions introduced in (2.101)-(2.104) are modified to include the thin-shell surface, ensuring the consistency of the overall solution. The interface conditions are given with respect to the indexes 1 and 2 referring to the two sides of the surface $\Gamma_{\mathrm{s,H}}^r$, reading

$$\mu^{-1}(\nabla \times \vec{A}_1 - \nabla \times \vec{A}_2) \times \vec{n}^r = \vec{K}^r, \qquad \text{for } \vec{H}_{\mathrm{t}}, \tag{2.111}$$

$$(\partial_t \vec{A}_1 - \partial_t \vec{A}_2) \times \vec{n}^r = 0, \qquad \text{for } \vec{E}_{\mathrm{t}}, \tag{2.112}$$

$$\sigma(\partial_t \vec{A}_1 - \partial_t \vec{A}_2) \cdot \vec{n}^r = 0, \qquad \text{for } \vec{J}_{\mathrm{n}}, \tag{2.113}$$

$$(\nabla \times \vec{A}_1 - \nabla \times \vec{A}_2) \cdot \vec{n}^r = 0, \qquad \text{for } \vec{B}_{\mathrm{n}}, \tag{2.114}$$

with $\vec{K}^r$ introducing a discontinuity of the tangential magnetic field strength in Ω_{A}. The magnetic permeability is assumed identical on the two sides, as the source domains are assumed to be surrounded by an insulating material. As a consequence, the tangential continuity of $\vec{E}$ and the normal continuity of $\vec{B}$ and $\vec{J}$ are automatically satisfied across $\Gamma_{\mathrm{c,H}}^r$.

2.14.3 Equivalence of the $\vec{A} - \vec{H}$ and $\vec{T} - \vec{A}$ formulations

A widespread choice for modeling superconducting tapes by means of the thin-shell approximation is given by the $\vec{T} - \vec{A}$ formulation [92]. At the time of writing, the formulation has been successfully used for modeling 3D complex cable architectures such as CORC® [93] and Roebel [187], high-field solenoids [94], fault-current limiters [188] and rotating electrical machines [91].

For the thin-shell approximation, the $\vec{A} - \vec{H}$ and $\vec{T} - \vec{A}$ formulations cannot be distinguished anymore as they lead to the same field equations (cf. (2.110) with e.g. [189]). Here, it is recalled that the electric vector potential $\vec{T}$ introduced in Section 2.8.2 is defined up to a gradient function $\nabla \alpha$. A possibility for gauging $\vec{T}$ in the thin-shell approximation is provided by choosing $\vec{T}$ as a single-component vector field, that is, $\vec{T} = T \vec{n}$ (see [189]). At the same time, the same result is obtained for the $\vec{A} - \vec{H}$ formulation, see Section 2.14.2. On the one hand, the tangential component of $\vec{T}$ is irrotational, and can be represented by $\nabla \alpha$. On the other hand, the tangential component of $\vec{H}$ does not contribute to the description of the current density in the thin shell, therefore it is also irrotational. It is concluded that the single-component vector potential corresponds to the normal component of the magnetic field strength within the thin shell, and that the formulations are equivalent.

(a) Cross section of the cable.

(b) Characteristic strand loops.
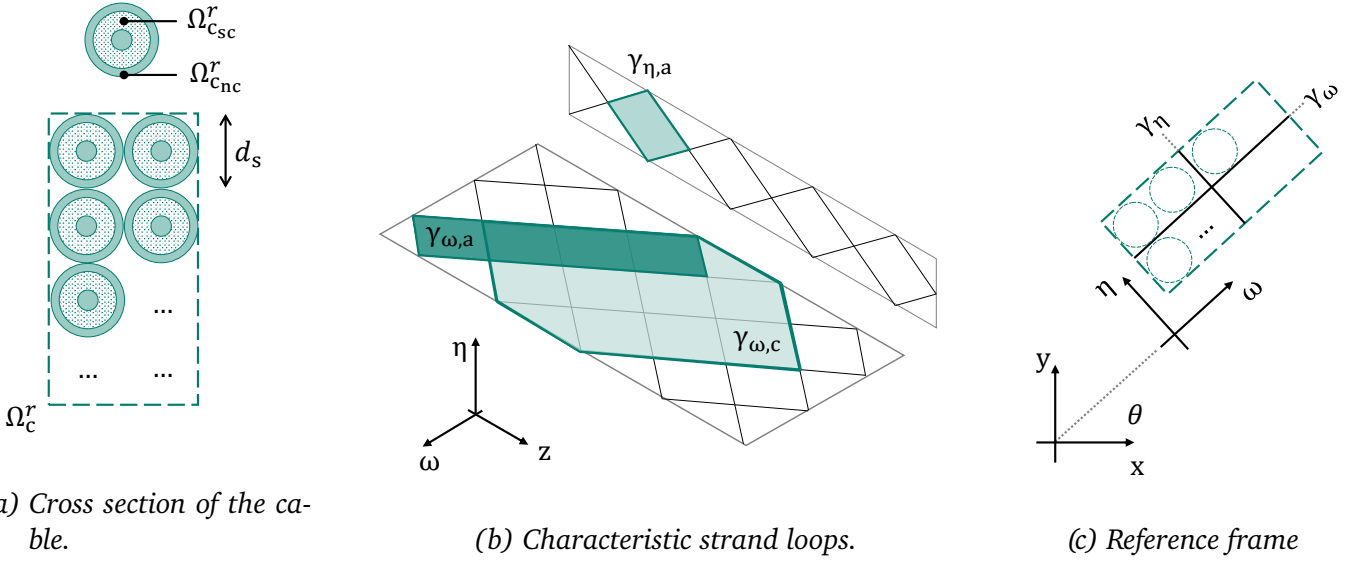
(c) Reference frame

Figure 2.9. Main geometric features of a fully transposed cable. (a) The strands in the cable Ω_c^r, composed of the superconducting filaments and the conducting matrix $\Omega_{c\text{-sc}}^r$ and $\Omega_{c\text{-nc}}^r$; (b) Characteristic strand loops $\gamma_{\omega,a}$, $\gamma_{\omega,c}$ and $\gamma_{\eta,a}$. (c) Local reference frame in the 2D setting for the cable Ω_c^r.

2.15 Equivalent Magnetization Approximation

The coupled $\vec{A} - \vec{H}$ field formulation is extended to stranded conductor models which is of relevance for HTS (e.g. BSCCO), as well as LTS (e.g. Nb-Ti, Nb$_3$Sn) materials. A practical example is given by the LHC dipole magnets which are made of fully-transposed cables, also known as Rutherford cables, whose strands are essentially superconducting filamentary compounds embedded in a copper matrix [1]. The cross section of a typical cable is shown in Figure 2.9a. The cross section Ω_c^r is made of strands which feature a superconducting region $\Omega_{c\text{-sc}}^r$ containing the filamentary structure, and a normal conducting region $\Omega_{c\text{-nc}}^r$ associated to the normal conducting matrix. The voids in the cable are nonconducting and may be filled by the coolant, or impregnated for example with an epoxy resin.

Computing the distribution of eddy currents within such cables would require a geometric resolution down to the micrometric scale of the filaments, while a magnet has a typical dimension of a meter in the cross section and up to ten meters in the longitudinal direction. As a consequence, solving this magnetoquasistatic problem would lead to an unacceptable computational cost. Therefore, a homogenization method is illustrated for modeling eddy-current phenomena in stranded LTS cables for the 2D setting with translational symmetry, assuming a coil made of N_c turns in the cross section. In the remainder of the section, the geometric entities and the vector field quantities are to be interpreted as two-dimensional.

2.15.1 Magnetization contributions

Three principal contributions from eddy currents are identified in superconducting Rutherford cables [1]. The first contribution is given by inter-filament coupling currents (IFCC) within a strand. These currents form loops which follow the twisted superconducting filaments, and close through the copper matrix embedding the filaments. The second contribution is given by inter-strand coupling currents (ISCC) which are

inherently related to the Rutherford architecture. In this case, these parasitic currents form loops along the twisted strands, and close through the contact resistances where the strands touch each other. The third contribution is given by screening currents circulating in loops entirely contained in the filaments composing the strands. For this last contribution, the currents remain within a superconducting material, therefore decay with a time constant which can be orders of magnitude longer than the IFCCs and ISCCs, and produce a persistent magnetization which affects the steady-state magnetic field in superconducting magnets [1, 59].

The magnetic contribution of inter-filament and inter-strand coupling currents is accounted for by means of an equivalent magnetization formulation applied to the cable model [114, 190, 191]. The formulation combines Faraday's and Ampère-Maxwell's laws, relating the magnetization of the cable with the derivative of the magnetic flux density through an equivalent time constant [191]. This time constant can be explicitly calculated if the paths of the coupling currents are known a-priori. The magnetic contribution of screening currents is formulated following [1, 59], assuming a critical-state behavior for the superconducting material [177], neglecting the hysteresis behavior. The equivalent magnetization $\vec{M}_{\text{eq}}$ associated to eddy currents reads

$$\vec{M}_{\text{eq}} = \vec{M}_{\text{ifcc}} + \vec{M}_{\text{iscc}} + \vec{M}_{\text{pers}}, \tag{2.115}$$

where $\vec{M}_{\text{ifcc}}$ and $\vec{M}_{\text{iscc}}$ are the contributions from coupling currents, and $\vec{M}_{\text{pers}}$ is given by screening currents. The contributions are calculated in the cross section of each strand, without resolving the superconducting and normal conducting contributions, thus assuming homogenized material properties.

2.15.1.1 Inter-filament coupling currents

Following [1, 47, 190], the magnetization term $\vec{M}_{\text{ifcc}}$ due to inter-filament coupling currents is formulated as

$$\vec{M}_{\text{ifcc}} = -\frac{1}{\mu_0} \tau_{\text{ifcc}}(|\vec{B}|, T) \partial_t \vec{B}, \tag{2.116}$$

with $\tau_{\text{ifcc}}(|\vec{B}|, T) : \Omega_{\text{c}} \to \mathbb{R}$ being the equivalent cable time constant which depends on the geometry and material of the strands, the magnetic field magnitude $|\vec{B}|$ and the temperature T. The time constant is given by [1]

$$\tau_{\text{ifcc}}(|\vec{B}|, T) = \frac{\mu_0}{2} \left(\frac{l_{\text{f}}}{2\pi} \right)^2 \frac{1}{\rho_{\text{nc}}(|\vec{B}|, T) f_{\text{eff}}}, \tag{2.117}$$

where l_{f} is the filament twist pitch, $\rho_{\text{nc}}(|\vec{B}|, T)$ is the resistivity of the material used for the normal conducting matrix in the strand and f_{eff} is a parameter which depends on the fraction of superconductor in the matrix, on the contact resistance between filaments and matrix, and on the distribution of the filaments within the cross section [192]. Care has to be taken in the use of (2.116).

Care has to be taken with the use of (2.116). The formulation is derived by assuming an externally applied magnetic field, therefore neglecting the magnetization due to the self magnetic field of the strand (see [193]). However, the formulation has been satisfactorily used for the simulation of practical applications (see e.g. [24, 114]).

2.15.1.2 Inter-strand coupling currents

The ISCC magnetization features three distinct contributions [190], which reflect the three characteristic strand loops $\gamma_{\omega,a}$, $\gamma_{\omega,c}$ and $\gamma_{\eta,a}$ associated to the ISCCs paths in fully transposed cables, as shown in Figure 2.9b. Each of the three ISCCs contributions is homogenized over the unit length of the cable and then linked to the equivalent time constants $\tau_{\omega,c}$, $\tau_{\omega,a}$ and $\tau_{\eta,c}$ [190, Chapter 4].

In the 2D setting, the three characteristic strand loops are replaced by two equivalent loops γ_ω and γ_η which are aligned with the wide and narrow faces of the cable, and located in the two mid-planes of the cable. The traces of the equivalent loops are shown in Figure 2.9c. In a local reference frame (ω, η) oriented according to the cable, the tensor of the equivalent time constants $\boldsymbol{\tau}_{\text{iscc}} : \Omega_c \to \mathbb{R}^{2 \times 2}$ reads

$$\boldsymbol{\tau}_{\text{iscc}} = \begin{bmatrix} \tau_{\omega,c} + \tau_{\omega,a} & 0 \\ 0 & \tau_{\eta,a} \end{bmatrix}. \tag{2.118}$$

The magnetization due to inter-strand coupling currents is given, for $r = 1, ..., N_c$, by

$$\vec{M}_{\text{iscc}}^r = -\frac{1}{\mu_0} \boldsymbol{\tau}_{\text{iscc},\theta}^r \partial_t \vec{B}_\theta^r, \tag{2.119}$$

with the quantities $\boldsymbol{\tau}_{\text{iscc},\theta}^r$ and $\vec{B}_\theta^r$ defined as

$$\boldsymbol{\tau}_{\text{iscc},\theta}^r = \mathbf{F}_{\text{rot}}(-\theta^r) \boldsymbol{\tau}_{\text{iscc}} \mathbf{F}_{\text{rot}}(\theta^r), \qquad \vec{B}_\theta^r = \mathbf{F}_{\text{rot}}(-\theta^r) \mathbf{F}_{\text{avg}}(\gamma_{\omega,\eta}) \mathbf{F}_{\text{rot}}(\theta^r) \vec{B}, \tag{2.120}$$

where θ^r is the rotation angle of the cable, $\mathbf{F}_{\text{rot}}(\cdot) : \mathbb{R}^2 \to \mathbb{R}^{2 \times 2}$ is a rotation matrix, positive definite for a counterclockwise rotation of the 2-D Euclidean space and $\mathbf{F}_{\text{avg}}(\cdot) : \Omega_c \to \mathbb{R}^2$ is an operator calculating the averaged normal components of $\vec{B}$ along γ_ω and γ_η.

2.15.1.3 Screening currents

Following [59], the persistent magnetization due to screening currents is given by

$$\vec{M}_{\text{pers}} = -\frac{2}{3\pi} d_f \lambda_{\text{sc}} J_c(\vec{B}, T) \left(1 - \frac{|\vec{J}|^2}{(\lambda_{\text{sc}} J_c(\vec{B}, T))^2} \right) \frac{\vec{B}}{|\vec{B}|}, \tag{2.121}$$

where d_f is the diameter of the superconducting filaments, and λ_{sc} is the fraction of superconductor in the strand. For LTS materials such as Nb-Ti or Nb_3Sn, the critical current density in (2.121) shows an isotropic field dependency. The filament size in accelerator magnets should be as small as possible, such that the contribution $\vec{M}_{\text{pers}}$ decays rapidly with the increase of the source current, being negligible during high-field operations [59].

2.15.2 Heat sources

The heat losses P in coils made of Rutherford cables are modeled as two distinct contributions P_M and P_J associated to the Joule losses due to eddy currents and the transport current. The first contribution P_M is calculated as the variation of the associated magnetic energy density function [194], reading

$$P_M = \vec{M}_{\text{ifcc}} \cdot \partial_t \vec{B} + \sum_{r=1}^{N_c} \vec{M}_{\text{iscc}}^r \cdot \partial_t \vec{B}_\theta^r + \vec{M}_{\text{pers}} \cdot \partial_t \vec{B}. \tag{2.122}$$

(a) Current sharing with Stekly approximation.

(b) Quench state variable.
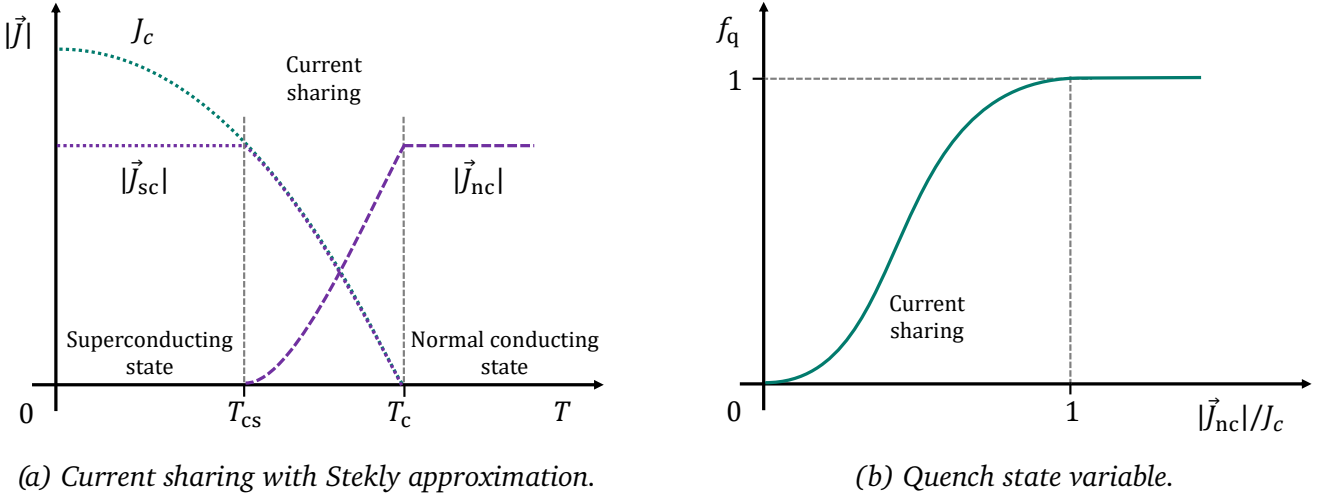
Figure 2.10. Sketch of the quench transition in an LTS strand.

As for HTS materials, the second contribution P_J is governed by the power-law behavior defined in (2.86). However, for strands made of LTS materials, that is, with high n value and steep power law, the Stekly approximation is typically sufficient [59, 195]. This approximation assumes that whenever the current density in the superconducting fraction of the cable exceeds the critical current density, only the current in excess flows into the normal conducting fraction. this behavior is shown in Figure 2.10a, where $\vec{J} = \vec{J}_{sc} + \vec{J}_{nc}$ with $\vec{J}_{sc}$ and $\vec{J}_{nc}$ flowing in the superconducting and normal conducting fraction of the cable. For the sake of simplicity, the two fractions are assumed as identical. For $T \leq T_{cs}$, that is, in the superconducting state, being $|\vec{J}_{sc}| = |\vec{J}|$ and $|\vec{J}_{nc}| = 0$. Once the temperature enters the current sharing regime $T_{cs} < T \leq T_c$, $|\vec{J}_{sc}| = \vec{J}_c$ and $|\vec{J}_{nc}| = |\vec{J}| - \vec{J}_c$. Once $T > T_c$, that is, the critical temperature is exceeded, then $\vec{J}_c = 0$ and $|\vec{J}_{nc}| = |\vec{J}|$ and the transition to the normal conducting state is complete. The Stekly approximation is implemented by means of the state variable $f_q(\vec{J}, \vec{B}, T) : \Omega \to \mathbb{R}$, shown in Figure 2.10b. The function relies on third-order polynomial function for the range $[0, 1]$, and assumes nonzero values only if $|\vec{J}| \geq J_c$. The Joule loss contribution is given by

$$P_J = f_q(\vec{J}, \vec{B}, T)\rho_{nc}\vec{J} \cdot \vec{J}, \tag{2.123}$$

where ρ_{nc} is a homogenized conductivity taking into account the fraction of normal conducting material in the cable.

2.15.3 Magnetoquasistatic formulation

Within filamentary strands, the current density distribution is assumed as homogeneous. At the same time, eddy currents are modeled by means of an equivalent magnetization model introduced in Section 2.15.1. Therefore, the solid conductor model is discarded for the superconducting coils in favor of the stranded conductor model (see Section 2.9.1). The coil region, previously introduced as $\Omega_{c,H}$ in the coupled $\vec{A} - \vec{H}$ field formulation, is modeled as a nonconducting source domain Ω_s which includes all the superconducting materials. A known source current density $\vec{J}_s^r$, $r = 1, ..., N_r$, is imposed in each of the N_r independent windings composing the coil. The external source currents i_s^r are coupled to the field model by means of distribution functions for stranded conductors $\vec{\chi}_{str}^r$ as $\vec{J}_s^r = \vec{\chi}_{str}^r i_s^r$. Consequently, the coupled field formulation (2.100)

can be simplified by solving the field problem only with respect to the (reduced) magnetic vector potential $\vec{A}$. The formulation is derived under MQS assumptions, reading

$$
\begin{cases}
\nabla \times \mu^{-1} \nabla \times \vec{A} + \nabla \times \vec{M}_{\text{eq}} + \sigma \partial_t \vec{A} = \displaystyle\sum_{r=1}^{N_{\text{r}}} \vec{\chi}_{\text{str}}^{r} i_{\text{s}}^{r}, & \text{on } \Omega, & \text{(2.124a)} \\[2ex]
\rho_{\text{m}} C_{\text{p}} \partial_t T - \nabla \cdot (\kappa \nabla T) = P_{\text{M}} + P_{\text{J}}, & \text{on } \Omega, & \text{(2.124b)} \\[2ex]
\vec{A} \times \vec{n} = 0, & \text{on } \Gamma_{\text{dir-0}}, & \text{(2.124c)} \\[2ex]
\kappa \nabla T \cdot \vec{n} = 0, & \text{on } \Gamma, & \text{(2.124d)}
\end{cases}
$$

where the heat equation is solved for the full computational domain Ω. The formulation is implemented and used for example in [196] for the simulation of the inner triplet quadrupole magnets of the High-Luminosity LHC upgrade.

2.16 Summary

The magnetothermal simulation of superconducting magnets requires suitable models. The most relevant formulations for the eddy-current field problem are derived from Maxwell's equations, under magnetoquasistatic approximations. As magnets are part of circuits, distribution functions for both stranded and solid conductors are implemented for the various formulations, such that the field models can be coupled with external circuits. The circuit dynamics is also of interest as there is a mutual influence on the magnet behavior. Therefore, the generally applied method for circuit simulation, known as the modified nodal analysis (MNA), is recalled.

The analysis of magnetothermal phenomena in accelerator magnets is formulated as an eddy-current problem in the time domain. The electrical behavior of high-temperature superconductors is introduced by means of a phenomenological power law. Then, a coupled $\vec{A} - \vec{H}$ field formulation combined with a domain decomposition strategy is proposed. The general formulation for magnetothermal problems in the time domain is derived with respect to solid conductors, and equations are given. Afterwards, the general formulation is also approximated for two cases of practical importance: a convenient thin-shell approximation is introduced for superconducting tapes, and an equivalent magnetization approximation is presented for coils made of stranded cables. The formulation of the coupled field formulation and its thin-shell approximation are discretized in Chapter 3 by means of the Finite Element Method, verified in Chapter 4 against theoretical references, and applied to the analysis of full scale applications in Chapter 5 and 6.

3 Space and Time Discretization

The systems of differential equations derived from the set of Maxwell's equations in Chapter 2 are both space-dependent boundary value problems as well as time-dependent initial value problems. The solution of these two types of problems is approximated by means of numerical methods. In Section 3.2, the boundary value problems arising from Maxwell's equations are discretized in space by means of the Ritz-Galerkin finite element method. The obtained initial value problems are treated by means of time discretization methods, and the most common time-integration methods are discussed in Section 3.3. In particular, the cooperative simulation of field-circuit coupled problems is introduced in Section 3.4 with respect to the waveform relaxation method. Afterwards, in Section 3.5 the weak and discrete formulation for the coupled $\vec{A} - \vec{H}$ field problem is detailed for the 3D and 2D settings, and the implications of thin-shell approximation are discussed in Section 3.7. As a key ingredient for the cosimulation, the field-circuit coupling interface is derived for the case of solid conductor models.

3.1 Partial Differential Equations

A boundary value problem (BVP) is given by a differential equation together with a set of additional constraints, that is, the boundary conditions. Partial differential equations (PDEs) are introduced following [197, Chapter 1]. They are defined as differential equations containing derivatives of the unknown function with respect to both time- and space-dependent variables. By denoting with $\vec{u} : \Omega \times \mathcal{I} \to \mathbb{R}^3$ the unknown function, x_i the independent variables with $i = 1, \ldots, n$, and t the time, the generic PDE $P(\vec{u}, \vec{g})$ is denoted as

$$F\left(x_1, \ldots, x_n, t, \vec{u}, \frac{\partial \vec{u}}{\partial x_1}, ..., \frac{\partial \vec{u}}{\partial x_n}, ..., \frac{\partial^{p_1 + \cdots + p_n + p_t} \vec{u}}{\partial x_1^{p_1} \ldots \partial x_n^{p_n} \partial t^{p_t}}\right) - \vec{g} = 0, \tag{3.1}$$

where $\vec{g} : \Omega \times \mathcal{I} \to \mathbb{R}^3$ is the excitation term (right-hand term) on which the PDE depends, p_1, p_n $p_t \in \mathbb{N}_0$, and $q = p_1 + \cdots + p_n + p_t$ is the maximal order of partial derivatives appearing in the equation.

Solving a boundary value problem requires finding a solution which satisfies both the differential equation and the boundary conditions. In general, available analytical integration methods (such as separation of variables) show limited applicability. Therefore, it is generally not possible to obtain an exact solution for BVPs containing partial differential equations. From a theoretical point of view, the analysis of a given PDE is limited to the investigation of the existence, uniqueness, and, if possible, the regularity of its solutions. In general finding a closed-form solution is not possible. Therefore, numerical methods are of importance because they allow to find an approximation $\vec{u}_N$ of the exact solution $\vec{u}$, and to estimate the approximation error $\vec{u}_N - \vec{u}$ by means of a suitable norm. Here, N is a positive integer indicating the finite dimension of the approximate problem. This can be schematically represented by

$$P(\vec{u}, \vec{g}) = 0 \xrightarrow[\text{method}]{\text{numerical}} P_N(\vec{u}_N, \vec{g}_N) = 0,$$

where P_N is the approximate problem, and $\vec{g}_N$ the approximation of the excitation term on which the PDE is dependent. The correctness of numerical methods depends on several properties. The most important are [198]:

1. *Consistency*. A numerical method is consistent if $P_N(\vec{u}, \vec{g}) \to 0$ for $N \to \infty$, and strongly consistent if $P_N(\vec{u}, \vec{g}) \to 0 \; \forall N \geq 1$. This property shows that the approximate PDE tends to the exact one as the dimension of the approximate problem is increased.
2. *Stability*. A numerical method is stable if a small perturbation in the right-hand term $\vec{\delta}_g$ leads to a small perturbation in the solution $\vec{\delta}_u$, such that $P_N(\vec{u}_N + \vec{\delta}_u, \vec{g}_N + \vec{\delta}_g) = 0 \; \forall N \geq 1$, where $\vec{u}_N + \vec{\delta}_u$ is the solution of the perturbed problem.
3. *Convergence*. A numerical method is convergent if $|\vec{u}_N - \vec{u}| \to 0$ for $N \to \infty$. In other words, the numerical solution tends to the analytical solution as the dimension N of the numerical problem is increased. A direct verification of the convergence of a numerical method might not be easy to be demonstrated. However, a fundamental result known as the Lax-Richtmyer equivalence theorem [71] states that if a method is consistent, then it is convergent if and only if it is stable.

Assuming that the method is consistent, stable, and converged, other fundamental properties influence the choice of a numerical method. The most relevant are the convergence rate, that is, the order with which the numerical error tends to zero with respect to $1/N$, and the computational cost which determines the amount of time and hardware resources required to utilize a given numerical method (CPU, memory, etc.).

The search for an approximate solution $\vec{u}_N$ requires first to identify the space to which the exact solution belongs, second to define the space of the approximate solutions, and third to measure the error introduced by the numerical approximation.

3.2 Space Discretization with the Finite Element Method

Electromagnetic field problems typically contain regions in the computational domain with heterogeneous material properties, such as ferromagnetic and nonmagnetic regions, and field sources at the region interfaces, such as surface current densities. Tangent- and normal-continuous vector fields may have jump discontinuities in their normal and tangent direction, respectively. Scalar fields such as scalar potentials show kinks in their equipotential lines on the material boundaries, and tangent-continuous vector fields such as vector potentials show similar kinks in their tangent component, and may have jump discontinuities in their normal component. Therefore, electromagnetic fields are in general not differentiable on the whole domain.

The consistency of the overall solution can be ensured by splitting the field problem into sub-problems where the each of the fields is sufficiently differentiable, and enforce continuity conditions at the interface between the sub-domains. However, a more elegant way for the treatment of EM field problems consists in weighing the strong formulation with appropriate test functions, and integrating it over the computational domain. In this way, the weak formulation of the field problem is obtained, [71]. Using weak formulations has several advantages, see for example [199] for a theoretical analysis. The weak formulation turns a generic PDE into an integral equation, and PDEs are no longer required to hold everywhere (and this is not even well defined), but only with respect to a set of test functions. Instead of trying to solve the BVP for every point in the computational domain, it is required that the differential equations are fulfilled only in a weak sense over the integration domain. Moreover, the application of Gauss's theorem and the consequent integration of

the weak formulation by parts leads to a reduced differentiation order, such that the weak solution requires less smoothness, and no differentiability for material properties. At the same time, it also provides a natural way to specify interface and boundary conditions by choosing appropriate function spaces for the test functions. It can be shown that solutions of the strong formulation satisfy also the weak formulation [71, Chapter 2].

3.2.1 Function spaces

Finding the solution of the weak form of a BVP consists in finding within a suitable function space the element satisfying both the governing equations and the boundary conditions of the BVP [197]. The function spaces are defined such that the solution fulfills some properties which are discussed in the following. First, the Hilbert spaces (i.e. function spaces with scalar product) of square-integrable scalar and vector functions $L^2(\Omega)$ and $\mathbf{L}^2(\Omega)$ are introduced as

$$L^2(\Omega) := \{f \in L^2(\Omega) \Longleftrightarrow \int_\Omega |f|^2 \, d\Omega < +\infty\},$$

$$\mathbf{L}^2(\Omega) := \{\vec{f} \in \mathbf{L}^2(\Omega) \Longleftrightarrow \int_\Omega \vec{f} \cdot \vec{f} \, d\Omega < +\infty\}.$$

Second, the following Sobolev spaces are defined by

$$H^1(\Omega) := \{u \in L^2(\Omega); \ \nabla u \in \mathbf{L}^2(\Omega)\},$$

$$\mathbf{H}(\text{curl}; \Omega) := \{\vec{v} \in \mathbf{L}^2(\Omega); \ \nabla \times \vec{v} \in \mathbf{L}^2(\Omega)\},$$

$$\mathbf{H}(\text{div}; \Omega) := \{\vec{w} \in \mathbf{L}^2(\Omega); \ \nabla \cdot \vec{w} \in \mathbf{L}^2(\Omega)\},$$

where the gradient, curl and divergence operators $\nabla(\cdot)$, $\nabla \times (\cdot)$ and $\nabla \cdot (\cdot)$ are well defined in the weak sense (e.g. [71]). Fields in $H^1(\Omega)$ are (weakly) continuous and their weak gradient is also square-integrable. Vector fields in $\mathbf{H}(\text{curl}; \Omega)$ are (weakly) tangentially continuous whereas their normal component may exhibit jumps, and their weak curl is also square-integrable. Vector fields in $\mathbf{H}(\text{div}; \Omega)$ are (weakly) normal continuous whereas their tangential component may exhibit jumps, and their weak divergence is also square-integrable.

The Sobolev spaces are of great importance for Maxwell's equations since field solutions in terms of $\vec{E}$ and $\vec{H}$ belong to $\mathbf{H}(\text{curl}; \Omega)$, whereas the field solutions in terms of $\vec{D}$ and $\vec{B}$ belong to $\mathbf{H}(\text{div}; \Omega)$. The spaces, together with the differential operators, compose the de Rahm diagram [71]:

$$\mathbb{R} \longrightarrow H^1(\Omega) \xrightarrow{\text{grad}} \mathbf{H}(\text{curl}; \Omega) \xrightarrow{\text{curl}} \mathbf{H}(\text{div}; \Omega) \xrightarrow{\text{div}} \mathbf{L}^2(\Omega).$$

The boundary conditions prescribed by the BVP are incorporated in the function spaces by means of trace operators. These operators map the function spaces to their respective extensions on the boundary Γ. As an example, the Dirichlet trace of fields in $H^1(\Omega)$, $\mathbf{H}(\text{curl}; \Omega)$ and $\mathbf{H}(\text{div}; \Omega)$ are respectively continuous fields, tangential-continuous fields and piece-wise constant fields on the boundary Γ.
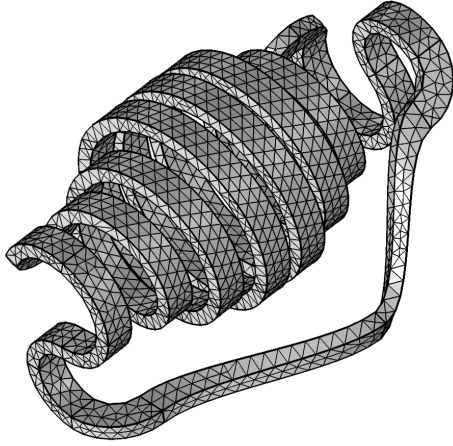
(a) Example of a mesh made of tetrahedra.
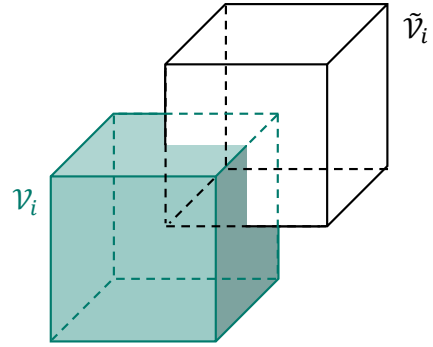
(b) Primal and dual mesh elements.

Figure 3.1. Discretization of the computational domain.

3.2.1.1 Discrete function spaces

The aim of numerical methods is to find an approximate solution within a finite-dimensional subspace of the respective function space. In other words, the solution is built from a finite number of basis functions which retain the main features of the complete function space but define only a finite subset of it. Moreover, a process of refinement exists to make the method convergent to the exact solution.

The domain Ω containing the field problem is subdivided into n_{V} elements $\mathcal{V}_i$, $i = 1, \ldots, n_{\mathrm{V}}$. The elements compose an oriented simplicial complex G, commonly referred to as the mesh, which defines the discretized domain Ω_h. Examples of finite elements are triangles and quadrangles for 2D geometries, or tetrahedra and hexahedra in the 3D space. Figure 3.1a shows an example of discretization obtained for an arbitrary 3D domain by means of tetrahedral elements. The field quantities described by Maxwell's equations are dual to each other and are linked by material properties, as shown by Maxwell's house in Figure 2.5. The left side of the house is known as the primal complex (Faraday's fields), whereas the right side is the dual complex (Ampère-Maxwell's fields). Consequently, a consistent description of Maxwell's equations requires not only the mesh G where primal quantities are described, but also a dual mesh $\tilde{G}$, shown in Figure 3.1b. In the FEM, this dual mesh is constructed implicitly [71].

The computational domain Ω is discretized into Ω_h by means of the mesh G into volumes $\mathcal{V}_i$ and their corresponding facets $\mathcal{S}_i$, edges $\mathcal{L}_i$ and points $\mathcal{P}_i$. In this context, h gives a measure of the degree of refinement of the mesh G by corresponding for example to the diameter of a sphere which contains exactly the largest element in the mesh. The geometrical entities in the mesh provide the support to different basis functions. Volume s_i, face $\vec{\omega}_i$, edge $\vec{\nu}_i$, and node u_i basis functions are connected to the n_{V} volumes, n_{S} facets, n_{L} edges and n_{P} nodes in the mesh. The basis functions are defined such that they generate discrete spaces which inherit the properties of their continuous counterpart. This leads to an exact de Rahm sequence also on the discrete set, given by

$$\mathbb{R} \longrightarrow \mathrm{U}_h \xrightarrow{\mathrm{grad}} \mathbf{V}_h \xrightarrow{\mathrm{curl}} \mathbf{W}_h \xrightarrow{\mathrm{div}} \mathrm{S}_h.$$
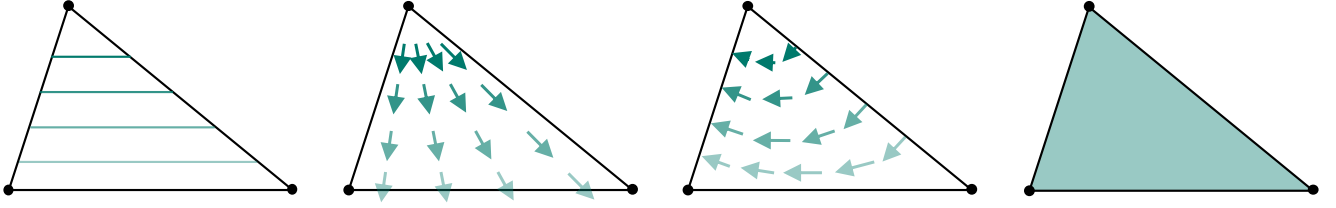
Figure 3.2. Lowest-order Whitney shape functions, in the 2D setting. From left to right: Lagrange, Nedéléc, Raviart-Thomas and piecewise-constant shape functions. Lagrange, Nedéléc and piecewise-constant functions may be also interpreted as the traces of the 3D Lagrange, Nedéléc and Raviart-Thomas functions on one facet of a tetrahedron.

where the discrete subspaces are defined such that

$$\mathrm{U}_h := \{f \in \mathrm{L}^2(\Omega); \; f = \sum_{i=1}^{n_{\mathrm{P}}} \alpha_i u_i, \; \alpha_i \in \mathbb{R}\} \subseteq \mathrm{H}^1(\Omega),$$

$$\mathbf{V}_h := \{\vec{f} \in \mathbf{L}^2(\Omega); \; \vec{f} = \sum_{i=1}^{n_{\mathrm{L}}} \alpha_i \vec{\nu}_i, \; \alpha_i \in \mathbb{R}\} \subseteq \mathbf{H}(\mathrm{curl}; \Omega),$$

$$\mathbf{W}_h := \{\vec{f} \in \mathbf{L}^2(\Omega); \; \vec{f} = \sum_{i=1}^{n_{\mathrm{A}}} \alpha_i \vec{\omega}_i, \; \alpha_i \in \mathbb{R}\} \subseteq \mathbf{H}(\mathrm{div}; \Omega),$$

$$\mathrm{S}_h := \{f \in \mathrm{L}^2(\Omega); \; f = \sum_{i=1}^{n_{\mathrm{V}}} \alpha_i s_i, \; \alpha_i \in \mathbb{R}\} \subseteq \mathrm{L}^2(\Omega),$$

Scalar fields belonging $\mathrm{H}^1(\Omega)$ are modeled by means of Lagrange shape functions, also known as hat or nodal shape functions. Vector fields belong either to $\mathbf{H}(\mathrm{curl}; \Omega)$ or $\mathbf{H}(\mathrm{div}; \Omega)$, depending if they are evaluated along curves or across surfaces. As a consequence, there are two types of vector shape functions. Nedéléc or edge shape functions discretize tangential-continuous fields, whereas Raviart-Thomas or face functions discretize normal-continuous fields. Lastly, scalar fields belonging to $\mathrm{L}^2(\Omega)$ are discretized by means of volume shape functions. The four classes of shape functions are also called Whitney basis functions, and are shown in Figure 3.2. The coefficients associated to the basis functions are the degrees of freedom for the approximation of the exact solution. The coefficients represent the values of scalar fields in $\mathrm{U}_h(\Omega_h)$ over the nodes of a mesh, the integration of tangential-continuous fields in $\mathbf{V}_h(\Omega_h)$ along the edges of a mesh, the integration of normal-continuous fields in $\mathbf{W}_h(\Omega_h)$ across the faces of a mesh, and the integration over volumes for scalar fields in $\mathrm{S}_h(\Omega_h)$.

3.2.2 Ritz-Galerkin method

The most widely-used method for the numerical solution of BVPs containing time-dependent PDEs is the method of lines. Following this approach, the PDEs arising from Maxwell's equations are firstly discretized in space over a computational grid or mesh. The space discretization is achieved by means of the Ritz-Galerkin finite element method (FEM) [71, 197, 200], using appropriate basis functions.

The Ritz-Galerkin method consists in approximating the exact function spaces containing the solutions of PDEs by their discrete counterpart. The solution fields in the weak formulation are approximated by the shape functions defined on the mesh G, reducing the dimension of the function space. At the same time, the test functions are chosen to be the same basis functions which are used for approximating the solution fields. Consequently, the weak formulation needs to be verified on the discrete setting only for the finite number of basis functions composing the subspace. The basis functions can be chosen such that the space they incorporate Dirichlet boundary conditions (essential conditions). The Neumann conditions are instead

incorporated into the weak formulation (natural conditions). The key property of the Galerkin approach is that the error due to the discrete approximation is minimized with respect to the chosen subspaces, that is, the difference in the solutions of the weak and Galerkin problems is orthogonal to the subspace defined by the basis functions used for the field approximation [71].

The accuracy of solution obtained by FEM can be increased in three ways. The first way is the h-FEM and consists in increasing the number of finite elements, therefore decreasing the element size. The second way is to increase the degree of polynomials building up a shape function. This is the p-FEM, and the high-order shape functions must still fulfill the continuity, tangential continuity and normal continuity of the discretized spaces. The combination of the h-FEM and the p-FEM leads to the hp-FEM, for which an exponential convergence rate of the Euclidean norm of the error in the field solution can be obtained by refining the mesh with a suitable combination of h-refinements and p-refinements [201]. Each element in the mesh can be hp-refined in many different ways since once the element is subdivided, there are many combinations for the polynomial degrees on the sub-elements. As a consequence, it is desirable to obtain optimality conditions for the mesh via an automatic hp-adaptivity. However, dedicated error indicators are needed (e.g. [202]) as standard FEM error estimates providing only one constant number per element are not enough to guide automatic hp-adaptivity [203].

The next section introduces the most common time-integration methods, with emphasis on the waveform relaxation technique. Subsequently, the weak and discrete Ritz-Galerkin formulation for the coupled $\vec{A} - \vec{H}$ field formulation presented in Chapter 2 is discussed.

3.3 Time Discretization

The numerical solution of PDEs requires to adopt discretization schemes, for both space and time. The application of the method of lines, for example as in the finite element method, reduces a time-dependent PDE to a system of ordinary differential equations (ODEs) or differential algebraic equations (DAEs). DAEs are systems of equations where a set of ordinary differential equations is combined with algebraic constraints. The methods for solving ODEs and DAEs are referred to as time integration methods which are discussed for example in [198, 204–206]. In this context, the most common approaches are briefly recalled, with emphasis on the backward differentiation formula which provides the backbone for the solution of the field problems described in this work.

Classic time discretization schemes are not immediately applicable to arbitrary DAEs [204]. For this reason, the discussion is restricted to quasilinear DAEs which arise frequently in problems in science and engineering, including eddy-current problems [207]. The initial value problem (IVP), with the potentially singular matrix $\mathbf{M}(\mathbf{x}, t)$ and consistent initial conditions $\mathbf{x}_0$, is defined as

$$\mathbf{M}(\mathbf{x}, t)\frac{\mathrm{d}\mathbf{x}}{\mathrm{d}t} = \mathbf{b}(\mathbf{x}, t), \tag{3.2a}$$

$$\mathbf{x}(t_0) = \mathbf{x}_0, \tag{3.2b}$$

for $t \in \mathcal{I} = [t_0, t_{\mathrm{end}})$ and with $\mathbf{x} \in \mathbb{R}^{n_{\mathrm{dof}}}$, where n_{dof} is the number of degrees of freedom. The time evolution of the IVP is obtained by firstly subdividing the time interval $\mathcal{I}$ into $n_{\mathrm{t}} + 1$ sub-intervals $[t_n, t_{n+1})$ with $n = 0, \ldots, n_{\mathrm{t}}$, of size $\Delta t_{n+1} = t_{n+1} - t_n$, then by calculating approximate solutions $\{\mathbf{x}_0, \ldots, \mathbf{x}_{n_{\mathrm{t}}}\}$ for the given points $\{\mathrm{t}_0, \ldots, \mathrm{t}_{n_{\mathrm{t}}}\}$ by means of a time-integration method. In case of $\mathbf{M}(\mathbf{x}, t) = \mathbf{I}$, the IVP in (3.2) is reduced to a system of ODEs.
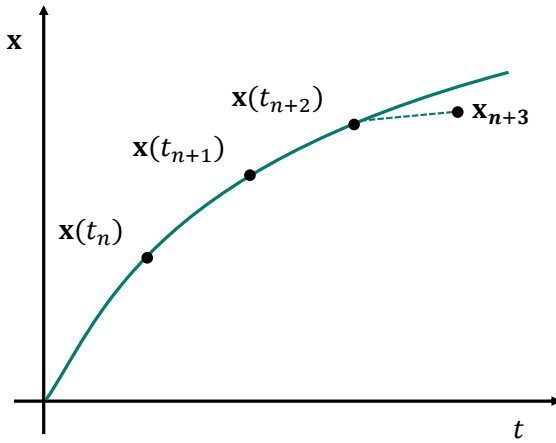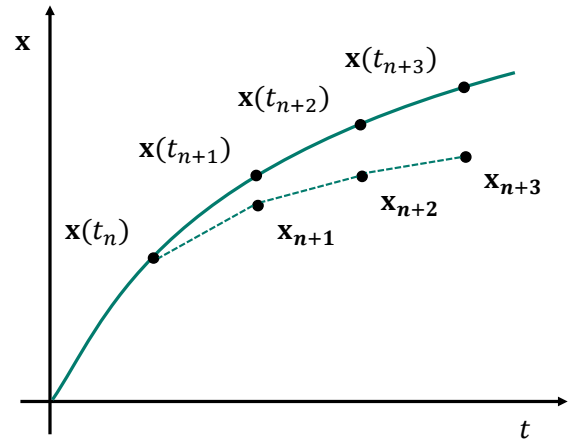
(a) Local truncation error *(b) Local truncation error propagation*

Figure 3.3. Sketch of the propagation of the local truncation error in the global error. Figures taken from [204].

The choice of the time step size Δt_{n+1} is crucial. On the one hand, the total number of time steps determines the overall computational cost. On the other hand, the size of the individual time step influences the accuracy and the stability of the time-integration method. A flexible compromise is provided by adaptive time stepping schemes, which are crucial for practical applications and allow to increase or reduce the time step size and, at the same time, keep the error under control by means of estimators [198].

Consistency, stability and convergence are key properties also for time-integration methods. Due to the fact that ODEs are solved numerically, the exact solution $\mathbf{x}(t_n)$ differs from its numerical approximation $\mathbf{x}_n$, introducing a local truncation error (LTE), see Figure 3.3a. The method is considered consistent if the LTE tends to zero whenever the time step tends to zero. At the same time, the LTE may propagate through the integration process, increasing the global error without control, see Figure 3.3b. If the stability of the solution is independent from the time step size, the method is said to be A-stable. Therefore, the time step size is not determined by the stability condition of the numerical method, but rather by the required accuracy and the dynamics of the equation. Consistent and stable methods are convergent to the exact solution, with their order p indicating how fast the LTE disappears with respect to the step size and/or the refinement of the discretization.

Stiff equations are a class of problems that pose a challenge for explicit time integration methods, unless the step size is extremely small. Although there is no formal definition, equations become stiff when they contain dynamic phenomena occurring at different time scales [208]. The fastest phenomenon limits the time step size for explicit methods, up to the point where the number of steps is too large for practical use [204]. Therefore, implicit time-integration methods are required for stiff equations [204].

3.3.1 Time-integration methods

Time integration methods can be classified into explicit and implicit schemes. Explicit schemes are simpler, providing an explicit formula for computing the solution at the next time step t_{n+1}. However, they are conditionally stable, as a criterion fixing the maximal allowed time step must be fulfilled in order to ensure the stability of the scheme [198]. Explicit methods are not applicable if the mass matrix in (3.2) is singular [209].

Instead, implicit schemes are more complex to be implemented, requiring to solve a possibly nonlinear system of equations at each time step t_n, with freedom in the choice of the maximal allowed time step. Time integration methods are also distinguished in one-step and multi-step schemes. The first category requires only the information from the most recent time step t_n for calculating the solution at the next time step t_{n+1}. Instead, the second category requires a combination of multiple solutions calculated at previous time steps in order to find the solution at the next time step.

3.3.1.1 θ-methods

An important class of one-step methods for the solution of ODEs is given by the Runge-Kutta schemes of which both explicit and implicit versions are available [205, 206]. The most popular is the classical Runge-Kutta method which is an explicit scheme with a convergence rate of the fourth order. Within the Runge-Kutta schemes, a relevant class is given by the θ-methods [197] which are defined by

$$\mathbf{x}_{n+1} = \mathbf{x}_n + \Delta t \left[\theta \mathbf{b}(\mathbf{x}_{n+1}, t_{n+1}) + (1 - \theta) \mathbf{b}(\mathbf{x}_n, t_n) \right] \tag{3.3}$$

whit Δt being the time step size, and $0 \leq \theta \leq 1$. By choosing $\theta = 0$, the explicit or forward Euler scheme is obtained, whereas $\theta = 1$ leads to the implicit or backward Euler scheme, with both the methods being linearly convergent. The explicit and implicit Euler schemes are conditionally stable and A-stable, respectively. The case $\theta = 1/2$ corresponds to the implicit trapezoidal rule, derived from integrating the differential equation in the IVP (3.2) from t_n to t_{n+1} obtaining

$$
\begin{aligned}
\mathbf{x}(t_{n+1}) &= \mathbf{x}(t_n) + \int_{t_n}^{t_{n+1}} \mathbf{b}(\mathbf{x}, t) \, \mathrm{d}t \\
&\approx \mathbf{x}(t_n) + \frac{t_{n+1} - t_n}{2} \left[\mathbf{b}(\mathbf{x}_{n+1}, t_{n+1}) + \mathbf{b}(\mathbf{x}_n, t_n) \right].
\end{aligned}
\tag{3.4}
$$

The method can be extended to IVPs composed of systems of quasilinear DAEs with constant mass matrix $\mathbf{M}$ (see [204]), as

$$\mathbf{M}(\mathbf{x}(t_{n+1}) - \mathbf{x}(t_n)) \approx \frac{t_{n+1} - t_n}{2} \left[\mathbf{b}(\mathbf{x}_{n+1}, t_{n+1}) + \mathbf{b}(\mathbf{x}_n, t_n) \right]. \tag{3.5}$$

The method features second order convergence in time [210], and it is equivalent to the implicit midpoint rule in case of linear equations.

3.3.1.2 Backward differentiation formula

An implicit multi-step method for integrating the quasilinear DAE IVP in (3.2) is provided by the backward differentiation formula of order k (BDF-k) [211, 212], which approximates the solution $\mathbf{x}_{n+1}$ by using the known $\mathbf{x}_{n+1-k}, \ldots, \mathbf{x}_n$ solutions. The method is of relevance as it is used for the numerical simulation of the applications discussed in this work. The method is formalized as

$$\mathbf{M}(\mathbf{x}_{n+1}, t_{n+1}) \frac{1}{t_{n+1} - t_n} \sum_{i=0}^{k} \alpha_{n+1,j} \mathbf{x}_{n+1-j} = \mathbf{b}(\mathbf{x}_{n+1}, t_{n+1}), \tag{3.6}$$

where the coefficients $\alpha_{n+1,j}$ are determined by the Lagrange interpolation polynomial $\mathbf{q}(t)$ for the points $(t_{n+1-j}, \mathbf{x}_{n+1-j})$ for $j = 0, \ldots, k$, with a time derivative $\partial_t \mathbf{q}(t)$ such that $\partial_t \mathbf{q}(t_{n+1}) = \mathbf{f}(\mathbf{x}_{n+1}, t_{n+1})$.

Methods based on BDF-1 (order 1) and BDF-2 (order 2) are both A-stable, with BDF-1 corresponding to the backward Euler method [198], and BDF-2 showing a quadratic convergence rate [209]. BDFs with $k = 3, 4, 5, 6$ are progressively less stable [204], up to $k \geq 7$ which are unstable [204]. The main advantage of the BDF is that their convergence accuracy is achieved by an efficient re-use of the solutions calculated for the previous time step. This does not happen in case of high-order, implicit Runge-Kutta methods: although accuracy is achieved by calculating within each time step several solution points, these solutions are discarded in the next time step.

3.3.2 Solution of systems of equations

Implicit time-integration methods lead, in case of nonlinear differential equations, to nonlinear systems of equations that have to be solved. The solution is sought by means of root-finding algorithms, mostly based on iterative methods which solve at each step a linearized version of the original nonlinear system. Widely used algorithms are the Picard method [198] which belongs to fixed point methods, and the Newton-Raphson method [213] which provides a linearization of the original nonlinear system by means of a Taylor series expansion limited to the first order.

On the one hand, fixed points iteration schemes may only achieve an acceptable convergence rate when a relaxation scheme is used, that is, $\tilde{x}_{n+1} = \alpha \mathbf{x}_{n+1} + (1 - \alpha)\mathbf{x}_n$ where the relaxation factor $\alpha \in (0, 2]$ can be tuned for achieving ($\alpha < 1$) or accelerating ($\alpha > 1$) convergence. On the other hand, the Newton-Raphson method may be particularly convenient due to its second-order convergence rate. As an example, the classic Newton method applied for solving ODEs with an implicit Euler scheme reads in its $k + 1$ iteration

$$\left[\mathbf{I} - \frac{t_{n+1} - t_n}{2} \mathbf{J}_\mathrm{b}(\mathbf{x}_{n+1}^k, t_{n+1}) \right] \Delta \mathbf{x}_{n+1} = - \left[\mathbf{x}_{n+1}^k - \mathbf{x}_n - \frac{t_{n+1} - t_n}{2} \left(\mathbf{b}(\mathbf{x}_n, t_n) + \mathbf{b}(\mathbf{x}_{n+1}^k, t_{n+1}) \right) \right], \quad (3.7)$$

where $\Delta \mathbf{x}_{n+1} = \mathbf{x}_{n+1}^{k+1} - \mathbf{x}_{n+1}^k$, $\mathbf{x}_{n+1}^{k+1}$ is the vector of unknowns, and $\mathbf{J}_\mathrm{b}(\mathbf{x}_{n+1}^k, t_{n+1})$ corresponds to the Jacobian of $\mathbf{b}(\mathbf{x}, t)$ in $\mathbf{x}$ evaluated at $(\mathbf{x}_{n+1}^k, t_{n+1})$. The solution update which is obtained for each iteration of the Newton method would require to calculate the inverse of a term containing the Jacobian. This is not computed, as it would be computationally too expensive. Instead, numerical methods for the solution of systems of linear equations are adopted, as briefly discussed in the next section.

3.3.2.1 Linear Systems

Root finding algorithms for the time-integration of nonlinear differential algebraic equations, such as the Newton method, require solving at each iteration a system of linear equation in the form of

$$\mathbf{A}\mathbf{x} = \mathbf{b} \quad (3.8)$$

where $\mathbf{A} \in \mathbb{R}^{N \times N}$ is a matrix of size N, and $\mathbf{x}$ and $\mathbf{b}$ are vectors of size N representing the unknown field and the right-hand term. The computational effort which is required for solving (3.8) depends mostly on the magnitude of N, and possibly on the condition number $\kappa(\mathbf{A})$ of $\mathbf{A}$ if iterative solvers are used. For a normal matrix $\mathbf{A}$ in the Euclidean space, the condition number is defined as [214, 215]

$$\kappa(\mathbf{A}) = \frac{|\lambda_{\mathrm{max}}(\mathbf{A})|}{|\lambda_{\mathrm{min}}(\mathbf{A})|} \quad (3.9)$$

where $\lambda_{\min}(\mathbf{A})$ and $\lambda_{\max}(\mathbf{A})$ are the minimum and maximum absolute eigenvalues of $\mathbf{A}$. A low condition number leads to well-conditioned systems, whereas a high condition number (e.g. due to high differences in material properties) leads to ill-conditioned systems which possibly lead to inaccurate solutions, regardless of the numerical method.

The methods for the solution of linear systems of type $\mathbf{Ax} = \mathbf{b}$ can be classified in direct and iterative [215, 216]. Especially when using iterative methods, the exact solution of (3.8) is typically not available, leading to an approximate solution $\bar{\mathbf{x}}$. The condition number gives a bound on the accuracy of $\bar{\mathbf{x}}$ with respect to the exact solution $\mathbf{x}$. The quality of the approximate solution is measured by the relative error $\varepsilon_{\mathrm{LS}}$ defined by [214]

$$\varepsilon_{\mathrm{LS}} = \frac{|\mathbf{x} - \bar{\mathbf{x}}|}{|\mathbf{x}|} \leq \kappa(\mathbf{A}) \frac{|\bar{\mathbf{r}}|}{|\mathbf{A}||\bar{\mathbf{x}}|} \tag{3.10}$$

where $|\cdot|$ denotes the spectral norm for matrices (Euclidean norm for vectors), and $\bar{\mathbf{r}} = \mathbf{A}\bar{\mathbf{x}} - \mathbf{b}$ is the residual associated to the approximate solution.

3.3.2.2 Solution Methods

An extensive description of direct and iterative methods, together with a historical overview is available in [214]. Direct methods rely on algorithms specialized in solving (3.8) exactly (up to roundoff errors) by factorizing $\mathbf{A}$. Widely used algorithms include (sparse) Gaussian elimination, lower-upper (LU) decomposition, and Cholesky factorization [215, 217]. For large linear systems which are likely to occur in modeling complex 3D applications, the construction of any factorization of $\mathbf{A}$ might become prohibitive due to memory constraints. Iterative methods start by guessing the initial solution, then refining it until the prescribed accuracy is obtained. These methods are further split into stationary and non-stationary methods. The first group include the Jacobi, Gauss-Seidel and successive over-relaxation (SOR) methods [215, 216], are easier to implement but do not always guarantee convergence or may converge slowly. The second group is more complex to be implemented, but can be very effective if coupled with an appropriate preconditioner. The most important are the Krylov subspace methods, of which the generalized minimal residual (GMRES) and the conjugate gradient (CG) are examples [215, 216]. Extensions of the CG for non-symmetric matrices are given by biconjugate gradient (BiCG), quasi minimal residual (QMR), and the stabilized biconjugate gradient (BiCGStab) [215, 216]. For a comparison of the methods about reliability, robustness and ease of implementation, see [214].

The convergence of iterative, non-stationary methods can be improved by the use of preconditioners which provide an approximate inverse of the matrix $\mathbf{A}$. The underlying idea is that the original linear system can be simplified by means of a multiplication with a preconditoner, such that the obtained system has a lower condition number and, therefore, the iterative solver converges faster. The choice of a preconditioner might be more crucial than the choice of the solver itself, however the preconditioner is problem-dependent. Well-known preconditioners are the Jacobi preconditoner, the Gauss-Seidel preconditoner, the incomplete LU decomposition, the incomplete Cholesky factorization, or the symmetric SOR [215]. Nowadays, the most efficient preconditoners are commonly considered to be the domain decomposition methods [218] and the class of multi-grid (MG) methods [219–221], further subdivided into geometric and algebraic MG methods.
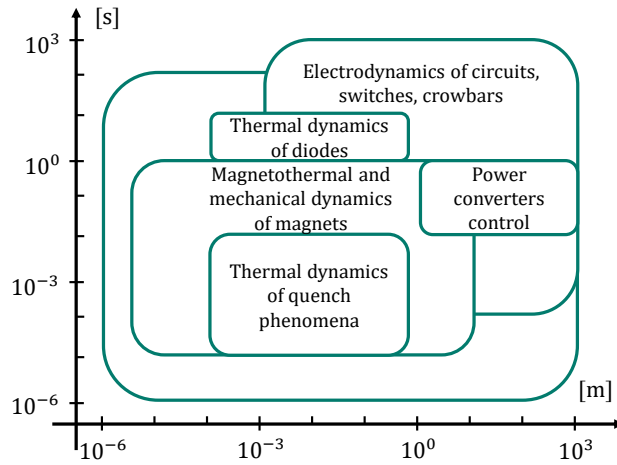
Figure 3.4. Multiscale and multirate behavior of the quench simulation problem in the LHC [222].

3.4 Cooperative Simulation

The simulation of multiphysical coupled problems [223] of large size, such as circuits of superconducting accelerator magnets, leads to considerable challenges. These challenges arise from the different mathematical properties, time rates and sizes shown by the different equations representing the coupled system (see the example in Figure 3.4). Simulations can be carried out either in a monolithic way, where the equations representing the different physics are coupled together in one system which is very large, or they can be cosimulated. Although tackling the problem by solving the equations system in a monolithic way may appear as the easiest approach, it can quickly lead to unacceptable computational efforts. In particular, special care has to be taken when considering space discretized methods such as FEM where the overall system can become very large and expensive to solve. Available simulation software tends to be specialized in one type of physics or technology. This is a consequence of the differences in the mathematical properties of the equations which require different time-integration methods and linear solvers. As example, electric circuits are simulated by means of SPICE-like solvers, whereas problems which require space-discretization of PDEs such as magnetothermal field problems, can be simulated using specialized software such as COMSOL [224] or GetDP [225].

To avoid monolithic simulations a possible solution consists in using cosimulation methods [226]. These methods allow solving the systems separately while they exchange information, such that the overall behavior of the system is captured in a consistent way. Different coupling schemes are available, namely one-way coupling, strong coupling, weak coupling and the waveform relaxation method (e.g. [227, Chapter 3]). Here, focus is given to the waveform relaxation (WR) method [228, 229] which performs the information exchange in an iterative way. These cosimulation methods are implemented in the STEAM cosimulation framework [222, 227] which applies the WR method within a hierarchical cosimulation structure based on deterministic finite automaton (state machine) for the management of the models representing the coupled multiphysical problem (see [227, Chapter 4]). The framework has been used mostly for coupling the different physics involved in the simulation of quench effects in accelerator magnets [24, 51, 117–119, 230–232]. However, the WR method can be applied to a variety of subsystems such as for example controller-circuit coupling [233].
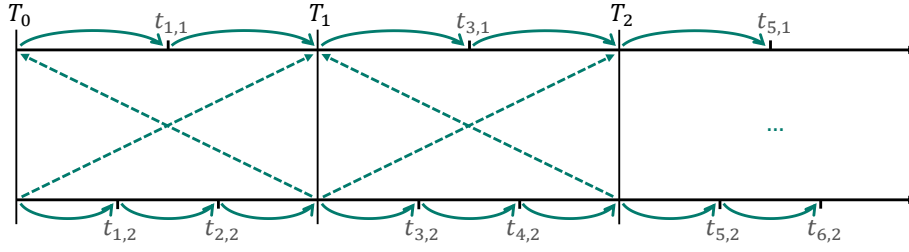
Figure 3.5. Schematic representation of the waveform relaxation method, for two subsystems and windowing.

3.4.1 Waveform relaxation method

The WR method was initially introduced for the simulation of large electric networks [228]. For an initial value problem on time $t \in \mathcal{I}$, for $t \in \mathcal{I} = [t_0,\ t_{\text{end}})$, where $\mathcal{I}$ is the time window of interest, the method consists in dividing the original monolithic system into N_{m} subsystems which are solved separately, each with an appropriate time stepping scheme. The initial value problem for a fully implicit DAE system $\mathbf{F}$ with consistent initial condition is split, for $k = 1, \ldots, N_{\text{m}}$, as

$$\mathbf{F}_k \left(\frac{\mathrm{d}\mathbf{x}_k}{\mathrm{d}t}, \mathbf{x}_k, \mathbf{u}_k, t \right) = 0 \tag{3.11a}$$

$$\mathbf{x}_k(t_0) = \mathbf{x}_{k,0}, \tag{3.11b}$$

with the degrees of freedom $\mathbf{x}_k$ and input $\mathbf{u}_k(\mathbf{x}_1, \ldots, \mathbf{x}_{k-1}, \mathbf{x}_{k+1}, \ldots, \mathbf{x}_{N_{\text{m}}})$ for each subsystem. This is a suitable choice for multirate coupled systems, since distinct time stepping schemes can be applied per each model, as well as for multiscale and multiphysics coupled systems when conversion between models is impractical.

Subsequently, information is exchanged between the subsystems which receive an update at each iteration. If the iterative process is convergent, it leads for a well-posed problem to a solution that satisfies tolerances of all the m subsystems and corresponds to the monolithical solution. Detailed convergence studies are found for systems of ODEs in [226], and systems of DAEs [234–236].

This method is traditionally combined with a windowing of the time span $\mathcal{I}$ which is subdivided into N_{wr} sub-windows $\mathcal{I}_n = [t_{n-1}, t_n)$ with $n = 1, \ldots, N_{\text{wr}}$, and the iteration is performed for each window, until convergence is reached. The windowing is advised for non-linear problems, where the size of $\mathcal{I}_n$ can be exploited for adapting the WR method to the dynamics of the system under study, improving the convergence speed [237]. The WR scheme and the windowing process is schematically represented for two subsystems in Figure 3.5. The optimal choice of $\mathcal{I}_n$ is an open research topic (see for example [238]).

3.4.1.1 Optimized Schwarz waveform relaxation method

Classical iterative Schwarz methods [109] solve Dirichlet boundary value problems in space by subdividing the computational domain into smaller, partially overlapping domains. The field problem is solved separately for each of the subdomains which exchange information in an iterative way, until the solution converges to the one of the original problem.

Optimized Schwarz methods are obtained by means of expanding the iterative process such that the sub-division of the computational domain is done by means of non-overlapping domains. The convergence of the iterations can be still ensured by improving the exchange of information, also known as transmission condition [111, 112]. The optimization consists in finding the optimized transmission conditions such that the iteration process converges faster. The optimized Schwarz WR method can be seen as a Schwarz domain decomposition method where the subdivision is done in the time domain. Moreover, if this subdivision is applied to coupled systems composed of different models, this leads to the heterogeneous domain decomposition method [239]. The information exchange can be optimized between circuit subsystems but also for field-circuit coupled problems, which is of relevance for the modeling of circuits of superconducting accelerator magnets.

The work in [113] shows the application of optimized Schwarz WR method applied to field-circuit coupled systems arising from the 2D eddy-current problem (2.124) for inter-filament coupling currents in stranded superconducting coils, whose formulation is detailed in Section 2.15.3. The optimization is detailed in [240, Chapter 5], and moves from linearizing the original system of equations and rewriting it in the frequency domain [110, 111], to a field model representation on the circuit side by means of the equivalent impedance $\mathbf{Z}(\omega)$. The impedance is typically not explicitly computable in time domain and needs to be approximated, thus simplifying the computation of the transmission condition and applies also in case of nonlinear problems. For the eddy-current problem, this can be done by means of a Taylor series expansion of $\mathbf{Z}(\omega)$, truncated to the first order. This leads to the optimized transmission condition for the n-th WR iteration

$$\mathbf{v}_{\mathrm{c}}^{n} = \frac{\mathrm{d}}{\mathrm{d}t}\mathbf{L}\mathbf{i}_{\mathrm{c}}^{n} - \frac{\mathrm{d}}{\mathrm{d}t}\mathbf{L}\mathbf{i}_{\mathrm{f}}^{n-1} + \mathbf{v}_{\mathrm{f}}^{n-1} \tag{3.12}$$

where $\mathbf{L}$ is the inductace matrix, and the subscripts correspond to the field (f) and circuit (c) models. The field model is represented by means of an inductance and a correction term on the circuit [113] and corresponds to the engineering intuition in [241, 242]. This transmission condition has been adopted by the STEAM framework for models of superconducting magnets solving the MQS field problem for stranded conductors in (2.124). In this work, the STEAM framework has been extended by an optimized Schwarz transmission condition derived in Section 3.5.7 for field-circuit coupled problems implementing a coupled $\vec{A} - \vec{H}$ field formulation on the field side.

3.4.2 STEAM cosimulation framework

The STEAM cosimulation framework applies a hierarchical cosimulation approach to the simulation of circuits of superconducting accelerator magnets, formulated as field-circuit coupled problems. The computational complexity is reduced by decomposing the original system into simpler subsystems, each of them modeled by means of specialized models. At the same time, the mutual dependencies between the subsystems are resolved by applying the WR method with the following algorithm:

1. The overall simulation time is subdivided into smaller windows;
2. Within each window, the models representing the system under study are solved, then the transmission conditions are applied by exchanging information following a Gauss-Seidel scheme [226];
3. The previous point is repeated for the same window until the waveforms belonging to two consecutive iterations differ by less than a prescribed tolerance, then the algorithm moves to the next window. The convergence of the algorithm for every window ensures the consistency of the overall solution [243].

For a fully-detailed description of the algorithm and its implementation, see [227], Chapters III and IV.
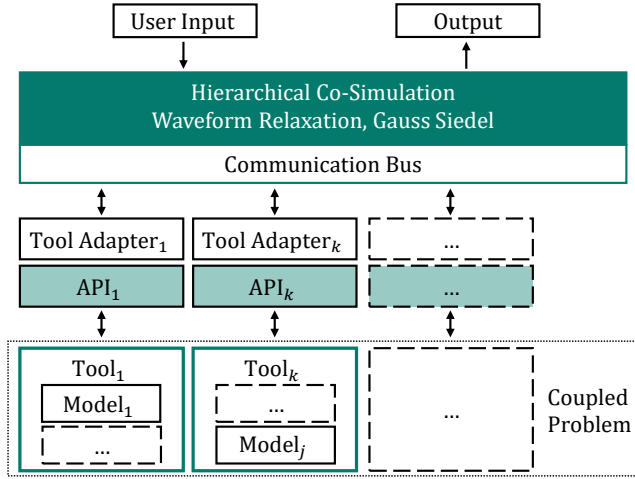
(a) Framework architecture.   (b) Hierarchy of models.
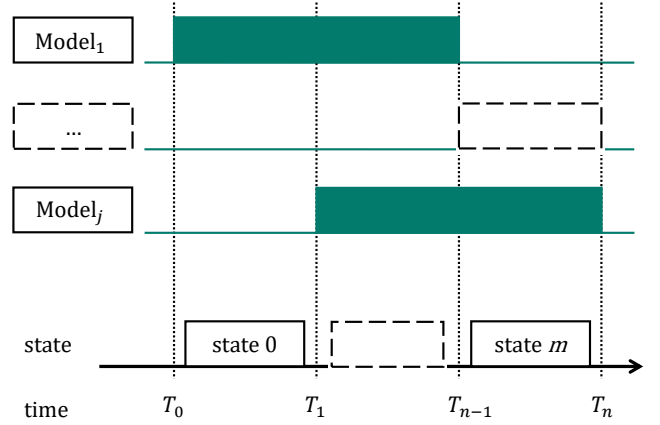
Figure 3.6. Architecture of the STEAM cosimulation framework [222]. (a) The j models representing a generic multiphysical problem are implemented by means of k different tools. (b) The models participate to simulations according to a hierarchy composed of m states.

3.4.2.1 Architecture

The STEAM framework is developed on a three-layer, scalable and expandable structure (see Figure 3.6a). The top layer features the hierarchical cosimulation algorithm which implements the optimal Schwarz WR method. The top layer provides the necessary input/output interfaces for the user, manages the execution of the models over the simulation time windows, and checks the convergence criteria for the WR algorithm. The middle layer handles the iterative information exchange between the models included in the cosimulation, for each time window. The layer is composed of a communication bus which enforces a communication protocol which is common to all the models. Moreover, the bus can handle both time- and space-dependent signals. For the latter ones, the MpCCI [244] mesh-based interpolation tool is in use [245]. The bottom layer features a modular structure, composed of blocks called tool adapters. Each tool adapter handles the waveform exchange between the communication bus and the models belonging to a tool via a suitable Application Programming Interface (API), which is tool-dependent. In this way, different models developed within the same tool can reuse the same tool adapter. At the same time, the architecture is fully expandable and scalable. By developing dedicated tool adapters, new simulation tools can be interfaced with the framework and included in the iterative solution of the coupled problem.

3.4.2.2 Hierarchy

In general, the transient phenomena potentially occurring in a circuit of accelerator magnets might happen at different times, and with different time constants. Whenever these phenomena are distributed among separated multiphysical models, then not all the models might be necessary in each time window. This observation leads to the introduction of a hierarchical state-machine algorithm for the management of the models. Referring to Figure 3.6b, the user has the possibility of defining both the states and the transitions of the overall system. After the simulation time is windowed, each window is associated to a state which determines the models which are required in each time window. A transition can be determined by a fixed time, or a

conditional expression which depends on information exchanged among the models. The benefit is two-fold, as the input of the state-machine explicitly determines the causality relations between the models, and the overall computational cost is reduced by an efficient use of the models.

3.5 Discretization of the Coupled Field Formulation

The $\vec{A} - \vec{H}$ coupled field formulation introduced in Section 2.13 is derived by first stating the weak formulation for the $\vec{A}$ and $\vec{H}$ formulations separately. Subsequently, the formulations are linked by means of interface conditions, and the system of equations is discretized in space with the Ritz-Galerkin approach. To couple the field problem to an external circuit, an optimized Schwarz field-circuit interface is derived from the semi-discrete system of equations.

3.5.1 Weak formulation for magnetic vector potential $\vec{A}$

The magnetoquasistatic curl-curl PDE given by the strong $\vec{A}$ formulation in (2.100a) is weighted with the edge functions $\vec{\nu}$. The weak formulation requires to find for the domain Ω_A the vector field $\vec{A}$ within the solution space $\mathbf{H}(\mathrm{curl};\Omega)$ such that, for all $\mathbf{H}(\mathrm{curl})$-conforming test functions $\vec{\nu} \in \mathbf{H}(\mathrm{curl};\Omega)$,

$$
\int_{\Omega_A} \nabla \times (\mu^{-1}\nabla \times \vec{A}) \cdot \vec{\nu}\,\mathrm{d}\Omega + \int_{\Omega_A} (\sigma \partial_t \vec{A}) \cdot \vec{\nu}\,\mathrm{d}\Omega = 0. \tag{3.13}
$$

The Gauss's theorem is applied to the first volume integral in (3.13), obtaining

$$
\int_{\Omega_A} (\mu^{-1}\nabla \times \vec{A}) \cdot \nabla \times \vec{\nu}\,\mathrm{d}\Omega + \int_{\Omega_A} (\sigma \partial_t \vec{A}) \cdot \vec{\nu}\,\mathrm{d}\Omega + \int_{\partial\Omega_A} (\mu^{-1}\nabla \times \vec{A}) \times \vec{\nu} \cdot \mathrm{d}\vec{\Gamma} = 0. \tag{3.14}
$$

The surface integral in (3.14) is composed of the exterior boundary Γ_A where boundary conditions are imposed, and the interior interface Γ_{HA} related to the domain decomposition for the mixed field formulation, such that $\partial\Omega_A = \Gamma_A \cup \Gamma_{HA}$. The magnetic vector potential and the test functions are chosen such that they fulfill on the exterior boundary the homogeneous Dirichlet and Neumann conditions for $\vec{A}$, corresponding to electric and magnetic boundary conditions in (2.54). The boundary integral on Γ_A reads

$$
\int_{\Gamma_A} (\mu^{-1}\nabla \times \vec{A}) \times \vec{\nu} \cdot \mathrm{d}\vec{\Gamma} = \int_{\Gamma_{\mathrm{ebc,A}}} (\vec{\nu} \times \vec{n}) \cdot \mu^{-1}\nabla \times \vec{A}\,\mathrm{d}\Gamma + \int_{\Gamma_{\mathrm{mbc,A}}} (\vec{n} \times \mu^{-1}\nabla \times \vec{A}) \cdot \vec{\nu}\,\mathrm{d}\Gamma = 0, \tag{3.15}
$$

with $\mathrm{d}\vec{\Gamma} = \vec{n}\,\mathrm{d}\Gamma$ and $\vec{n}$ being the normal unit vector. The integrals in (3.15) are zero due to the incorporation of electric and magnetic boundary conditions. Therefore, the surface integral on $\partial\Omega_A$ is reduced to

$$
\int_{\partial\Omega_A} (\mu^{-1}\nabla \times \vec{A}) \times \vec{\nu} \cdot \mathrm{d}\vec{\Gamma} = -\int_{\Gamma_{HA}} (\vec{n} \times \mu^{-1}\nabla \times \vec{A}) \cdot \vec{\nu}\,\mathrm{d}\Gamma, \tag{3.16}
$$

where the minus sign is due to the opposite orientation of the source domain Ω_H with respect to the interior boundary of the domain Ω_A.

3.5.2 Weak formulation for magnetic field strength $\vec{H}$

The magnetoquasistatic curl-curl PDE given by the strong $\vec{H}$ formulation in (2.100b) is weighted with the edge functions $\vec{v}^{r}$. The weak formulation requires to find for each source domain $\Omega_{\mathrm{c,H}}^{r}$, with $r = 1, \ldots, N_{\mathrm{r}}$, the vector fields $\vec{H}^{r}$ within the solution space $\mathbf{H}(\mathrm{curl};\Omega)$ such that, for all $\mathbf{H}(\mathrm{curl})$-conforming test functions $\vec{v}^{r} \in \mathbf{H}(\mathrm{curl};\Omega)$,

$$\int_{\Omega_{\mathrm{c,H}}^{r}} \nabla \times (\rho \nabla \times \vec{H}^{r}) \cdot \vec{v}^{r} \, \mathrm{d}\Omega + \int_{\Omega_{\mathrm{c,H}}^{r}} (\partial_{t} \mu \vec{H}^{r}) \cdot \vec{v}^{r} \, \mathrm{d}\Omega - v_{\mathrm{s}}^{r} \int_{\Omega_{\mathrm{c,H}}^{r}} (\nabla \times \vec{\chi}_{\mathrm{sol}}^{r}) \cdot \vec{v}^{r} \, \mathrm{d}\Omega = 0. \tag{3.17}$$

Gauss's theorem is applied to the first and the third volume integral in (3.17), obtaining

$$\int_{\Omega_{\mathrm{c,H}}^{r}} (\rho \nabla \times \vec{H}^{r}) \cdot \nabla \times \vec{v}^{r} \, \mathrm{d}\Omega + \int_{\Omega_{\mathrm{c,H}}^{r}} (\partial_{t} \mu \vec{H}^{r}) \cdot \vec{v}^{r} \, \mathrm{d}\Omega - v_{\mathrm{s}}^{r} \int_{\Omega_{\mathrm{c,H}}^{r}} \vec{\chi}_{\mathrm{sol}}^{r} \cdot \nabla \times \vec{v}^{r} \, \mathrm{d}\Omega$$
$$+ \int_{\partial \Omega_{\mathrm{c,H}}^{r}} (\vec{E}^{r} \times \vec{v}^{r}) \cdot \mathrm{d}\vec{\Gamma} = 0, \tag{3.18}$$

where the electric field $\vec{E}^{r}$ in the surface integral is defined in (2.96).

The surface integral in (3.18) is composed of the exterior boundary $\Gamma_{\mathrm{J}}^{r} \cup \Gamma_{\mathrm{E}}^{r}$ where boundary conditions are imposed, and the interior interface Γ_{HA}^{r} related to the domain decomposition for the mixed field formulation, such that $\partial \Omega_{\mathrm{c,H}}^{r} = \Gamma_{\mathrm{J}}^{r} \cup \Gamma_{\mathrm{E}}^{r} \cup \Gamma_{\mathrm{HA}}^{r}$. The magnetic field strength and the test functions are chosen such that they fulfill on the exterior boundary the homogeneous Dirichlet and Neumann conditions for $\vec{H}$, corresponding to magnetic and electric boundary conditions in (2.40) and (2.39). The boundary integral on $\Gamma_{\mathrm{J}}^{r} \cup \Gamma_{\mathrm{E}}^{r}$ reads

$$\int_{\Gamma_{\mathrm{J}}^{r} \cup \Gamma_{\mathrm{E}}^{r}} (\vec{E}^{r} \times \vec{v}^{r}) \cdot \mathrm{d}\vec{\Gamma} = \int_{\Gamma_{\mathrm{mbc,H}}^{r}} (\vec{v}^{r} \times \vec{n}) \cdot \vec{E}^{r} \, \mathrm{d}\Gamma + \int_{\Gamma_{\mathrm{ebc,H}}^{r}} (\vec{n} \times \vec{E}^{r}) \cdot \vec{v}_{p}^{r} \, \mathrm{d}\Gamma = 0, \tag{3.19}$$

with $\mathrm{d}\vec{\Gamma} = \vec{n}^{r} \, \mathrm{d}\Gamma$ and $\vec{n}^{r}$ being the outer normal vector of the domain $\Omega_{\mathrm{c,H}}^{r}$. The integrals in (3.19) are zero due to the incorporation of magnetic and electric boundary conditions. Therefore, the surface integral is reduced to

$$\int_{\partial \Omega_{\mathrm{c,H}}^{r}} (\vec{E}^{r} \times \vec{v}^{r}) \cdot \mathrm{d}\vec{\Gamma} = \int_{\Gamma_{\mathrm{HA}}^{r}} (\vec{n}^{r} \times \vec{E}^{r}) \cdot \vec{v}^{r} \, \mathrm{d}\Gamma. \tag{3.20}$$

The constraint condition for the current in (2.100c) is equivalent to a boundary condition for the normal component of the current density on Γ_{J}^{r}. This is shown by first rewriting the distribution function in terms of its corresponding scalar potential (2.68), then by applying Gauss's theorem to the current constraint,

as

$$\int\limits_{\Omega_{\mathrm{c,H}}^{r}} \vec{\chi}_{\mathrm{sol}}^{r} \cdot \nabla \times \vec{H}^{r}\, \mathrm{d}\Omega = -\int\limits_{\Omega_{\mathrm{c,H}}^{r}} \nabla \zeta_{\mathrm{sol}}^{r} \cdot \nabla \times \vec{H}^{r}\, \mathrm{d}\Omega$$

$$= -\int\limits_{\Omega_{\mathrm{c,H}}^{r}} \nabla \cdot (\zeta_{\mathrm{sol}}^{r} \nabla \times \vec{H}^{r})\, \mathrm{d}\Omega + \int\limits_{\Omega_{\mathrm{c,H}}^{r}} \zeta_{\mathrm{sol}}^{r} \nabla \cdot (\nabla \times \vec{H}^{r})\, \mathrm{d}\Omega$$

$$= -\int\limits_{\Gamma_{\mathrm{HA}}^{r}} \zeta_{\mathrm{sol}}^{r} \nabla \times \vec{H}^{r} \cdot \mathrm{d}\vec{\Gamma} - \int\limits_{\Gamma_{\mathrm{J}}^{r}} \zeta_{\mathrm{sol}}^{r} \nabla \times \vec{H}^{r} \cdot \mathrm{d}\vec{\Gamma} - \int\limits_{\Gamma_{\mathrm{E}}^{r}} \zeta_{\mathrm{sol}}^{r} \nabla \times \vec{H}^{r} \cdot \mathrm{d}\vec{\Gamma}$$

$$= -\int\limits_{\Gamma_{\mathrm{J}}^{r}} \nabla \times \vec{H}^{r} \cdot \mathrm{d}\vec{\Gamma}, \tag{3.21}$$

where $\nabla \cdot (\nabla \times \vec{H}^{r}) = 0$ is a known vector identity, and for the last step it is observed that $\nabla \times \vec{H}^{r} \cdot \vec{n}^{r} = 0$ on Γ_{HA}^{r}, and $\zeta_{\mathrm{sol}}^{r} = 0$ on Γ_{E}^{r} as prescribed by (2.99).

3.5.2.1 Equivalence of distribution functions and boundary conditions

The third volume integral in (3.18) can be further simplified by replacing $\vec{\chi}_{\mathrm{sol}}^{r}$ with its corresponding scalar potential (2.68) and applying Gauss's theorem, obtaining

$$v_{\mathrm{s}}^{r} \int\limits_{\Omega_{\mathrm{c,H}}^{r}} \nabla \zeta_{\mathrm{sol}}^{r} \cdot \nabla \times \vec{v}^{r}\, \mathrm{d}\Omega = v_{\mathrm{s}}^{r} \int\limits_{\Omega_{\mathrm{c,H}}^{r}} \nabla \cdot (\zeta_{\mathrm{sol}}^{r} \nabla \times \vec{v}^{r})\, \mathrm{d}\Omega - v_{\mathrm{s}}^{r} \int\limits_{\Omega_{\mathrm{c,H}}^{r}} \zeta_{\mathrm{sol}}^{r} \nabla \cdot (\nabla \times \vec{v}^{r})\, \mathrm{d}\Omega$$

$$= v_{\mathrm{s}}^{r} \int\limits_{\Gamma_{\mathrm{HA}}^{r}} \zeta_{\mathrm{sol}}^{r} \nabla \times \vec{v}^{r} \cdot \mathrm{d}\vec{\Gamma} + v_{\mathrm{s}}^{r} \int\limits_{\Gamma_{\mathrm{J}}^{r}} \zeta_{\mathrm{sol}}^{r} \nabla \times \vec{v}^{r} \cdot \mathrm{d}\vec{\Gamma} + v_{\mathrm{s}}^{r} \int\limits_{\Gamma_{\mathrm{E}}^{r}} \zeta_{\mathrm{sol}}^{r} \nabla \times \vec{v}^{r} \cdot \mathrm{d}\vec{\Gamma}$$

$$= v_{\mathrm{s}}^{r} \int\limits_{\Gamma_{\mathrm{J}}^{r}} \nabla \times \vec{v}^{r} \cdot \mathrm{d}\vec{\Gamma},$$

where $\nabla \cdot (\nabla \times \vec{v}^{r}) = 0$ is a known vector identity, and for the last step it is observed that $\nabla \times \vec{v}^{r} \cdot \vec{n}^{r} = 0$ on Γ_{HA}^{r}, and $\zeta_{\mathrm{sol}}^{r} = 0$ on Γ_{E}^{r} as prescribed by (2.99).

3.5.3 Weak formulation for temperature T

The heat balance div-grad PDE given by the strong formulation (2.105) is weighted with the scalar functions u. The weak formulation requires to find for the domain Ω the scalar field T within the solution space $\mathrm{H}(\mathrm{grad}; \Omega)$ such that, for all H(grad)-conforming test functions $u \in \mathrm{H}(\mathrm{grad}; \Omega)$,

$$\int\limits_{\Omega} \nabla \cdot (\kappa \nabla T) u\, \mathrm{d}\Omega + \int\limits_{\Omega} (\rho_{\mathrm{m}} C_{\mathrm{p}} \partial_{t} T) u\, \mathrm{d}\Omega = \int\limits_{\Omega} P_{\mathrm{J}} u\, \mathrm{d}\Omega. \tag{3.23}$$

Gauss's theorem is applied to the first volume integral in (3.23), obtaining

$$\int\limits_{\Omega} (\kappa \nabla T) \cdot \nabla u\, \mathrm{d}\Omega + \int\limits_{\Omega} (\rho_{\mathrm{m}} C_{\mathrm{p}} \partial_{t} T) u\, \mathrm{d}\Omega + \int\limits_{\Gamma} (-\kappa \nabla T) u \cdot \mathrm{d}\vec{\Gamma} = \int\limits_{\Omega} P_{\mathrm{J}} u\, \mathrm{d}\Omega. \tag{3.24}$$

The temperature and the test functions are chosen such that they fulfill on the exterior boundary the homogeneous Dirichlet conditions. The Neumann conditions are imposed in a natural way by means of the surface integral in (3.24).

3.5.4 Coupling conditions

The $\vec{A}$ and $\vec{H}$ formulations are coupled along the interface Γ_{HA}. The field $\vec{H}$ is coupled to $\vec{A}$ by means of the tangential continuity of the magnetic field strength. By applying the continuity condition in (2.101) to the surface integral (3.16), the coupling reads

$$\int_{\Gamma_{\mathrm{HA}}^r} (\vec{n} \times \mu^{-1}\nabla \times \vec{A}) \cdot \vec{\nu}\, \mathrm{d}\Gamma = \int_{\Gamma_{\mathrm{HA}}^r} (\vec{n} \times \vec{H}^r) \cdot \vec{\nu}\, \mathrm{d}\Gamma \qquad r = 1,\dots,N_{\mathrm{r}}. \tag{3.25}$$

The field $\vec{A}$ is coupled to $\vec{H}$ by means of the tangential continuity of the electric field strength. By applying the continuity condition in (2.102) to the surface integral (3.20), the coupling reads

$$\int_{\Gamma_{\mathrm{HA}}^r} (\vec{n} \times \vec{E}^r) \cdot \vec{v}^r\, \mathrm{d}\Gamma = -\int_{\Gamma_{\mathrm{HA}}^r} (\vec{n} \times \partial_t \vec{A}) \cdot \vec{v}^r\, \mathrm{d}\Gamma \qquad r = 1,\dots,N_{\mathrm{r}}. \tag{3.26}$$

The temperature field T is coupled to both $\vec{A}$ and $\vec{H}$ by means of the Joule loss term appearing on the right-hand side of (3.23). The coupling reads

$$\int_{\Omega} P_{\mathrm{J}} u\, \mathrm{d}\Omega = \int_{\Omega_{\mathrm{c,H}}^r} \rho(\nabla \times \vec{H}^r \cdot \nabla \times \vec{H}^r) u\, \mathrm{d}\Omega + \int_{\Omega_{\mathrm{A}}} \sigma(\partial_t \vec{A} \cdot \partial_t \vec{A}) u\, \mathrm{d}\Omega \qquad r = 1,\dots,N_{\mathrm{r}}. \tag{3.27}$$

For compactness of notation, the coupling term is given as

$$\int_{\Omega} P_{\mathrm{J}} u\, \mathrm{d}\Omega = \int_{\Omega} q(\cdot) u\, \mathrm{d}\Omega, \tag{3.28}$$

where $q(\vec{A}, \vec{H})$ represents the nonlinear operator providing the Joule loss contribution.

3.5.5 Semidiscrete formulation

The fields $\vec{A}$ and $\vec{H}^r$ are approximated for $r = 1,\dots,N_{\mathrm{r}}$ by a finite set of Nedéléc-type shape functions $\vec{\nu}_j$ and $\vec{v}_q^r$ which are **H**(curl)-conforming, and define the discrete solution space $\mathbf{V}_h$ (the discrete counterpart of **H**(curl; Ω)). Different discretization orders need to be chosen for $\vec{A}$ and $\vec{H}$, this to avoid potential stability issues [189]. The field approximation reads

$$\vec{A} \approx \sum_{j=1}^{n_{\mathrm{L,A}}} \vec{w}_j a_j, \qquad \vec{H}^r \approx \sum_{q=1}^{n_{\mathrm{L,H}}^r} \vec{v}_q^r h_q^r, \tag{3.29}$$

where $n_{\mathrm{L,A}}$ and $n_{\mathrm{L,H}}^r$ are the number of mesh edges in Ω_{A} and $\Omega_{\mathrm{c,H}}^r$. The voltage distribution function $\vec{\chi}_{\mathrm{sol}}^r$ which is calculated a-priori (see Section 2.13.3) is approximated for $r = 1,\dots,N_{\mathrm{r}}$ by nodal shape functions

N_p^r which are H(grad)-conforming, and define the solution space U_h (the discrete counterpart of $H^1(\Omega)$). The approximation reads

$$\vec{\chi}_{\text{sol}}^r \approx -\sum_{p=1}^{n_{\text{P,H}}^r} \nabla N_p^r \xi_p^r, \tag{3.30}$$

where $n_{\text{P,H}}^r$ is the number of mesh nodes in $\Omega_{\text{c,H}}^r$. The temperature field T is also discretized by nodal shape functions N_n, as

$$T \approx \sum_{n=1}^{n_{\text{P}}} N_n t_n. \tag{3.31}$$

where n_{p} is the number of mesh nodes in Ω. The unknowns a_j, h_q^r and t_n are the degrees of freedom for $\vec{A}$, $\vec{H}^r$ and T, respectively. The unknown field $\mathbf{h}$ is given by the composition of the N_{r} source domains in Ω_{H} and is therefore represented as

$$\mathbf{h}^\top = [(\mathbf{h}^1)^\top, \dots, (\mathbf{h}^{N_{\text{r}}})^\top]. \tag{3.32}$$

The fields given by the weak formulations (3.14), (3.18), (3.24) and the current constraint in (3.21) are replaced with their finite dimensional counterparts. The field interface conditions (3.25) and (3.26), and the coupling (3.27) are explicitly imposed. The continuity of the normal component of the current density and magnetic flux density, given respectively by (2.103) and (2.104), is satisfied by choosing suitable discretization functions based on Whitney edge elements [246]. The following discrete problem is obtained:

$$\begin{bmatrix} \mathbf{K}^\nu + \mathbf{M}^\sigma \frac{\text{d}}{\text{dt}} & -\mathbf{Q} & \mathbf{0} & \mathbf{0} \\ \mathbf{Q}^\top \frac{\text{d}}{\text{dt}} & \mathbf{K}^\rho + \mathbf{M}^\mu \frac{\text{d}}{\text{dt}} & -\mathbf{X} & \mathbf{0} \\ \mathbf{0} & \mathbf{X}^\top & \mathbf{0} & \mathbf{0} \\ \mathbf{0} & \mathbf{0} & \mathbf{0} & \mathbf{K}^\kappa + \mathbf{M}^\rho \frac{\text{d}}{\text{dt}} \end{bmatrix} \begin{bmatrix} \mathbf{a} \\ \mathbf{h} \\ \mathbf{u}_{\text{s}} \\ \mathbf{t} \end{bmatrix} = \begin{bmatrix} \mathbf{0} \\ \mathbf{0} \\ \mathbf{i}_{\text{s}} \\ \mathbf{q}(\cdot) \end{bmatrix}. \tag{3.33}$$

In detail, $\mathbf{K}^\star$ and $\mathbf{M}^\star$ represent the discrete counterparts of the differential operators and material matrices, $\mathbf{X}$ is the discrete representation of $\vec{\chi}_{\text{sol}}$ and $\mathbf{q}(\mathbf{a}, \mathbf{h})$ is the nonlinear discrete operator providing the Joule loss contribution.

The coefficients of the matrices of reluctance $\mathbf{K}^\nu$, conductance $\mathbf{M}^\sigma$, interface coupling $\mathbf{Q}$, resistance $\mathbf{K}^\rho$, permeance $\mathbf{M}^\mu$ and voltage coupling $\mathbf{X}$ are given for $r = 1, ..., N_{\text{r}}$ as

$$(K^\nu)_{i,j} = \int_{\Omega_{\text{A}}} (\mu^{-1} \nabla \times \vec{w}_j) \cdot \nabla \times \vec{w}_i \, \text{d}\Omega, \tag{3.34}$$

$$(M^\sigma)_{i,j} = \int_{\Omega_{\text{A}}} (\sigma \vec{w}_j) \cdot \vec{w}_i \, \text{d}\Omega, \tag{3.35}$$

$$(Q)_{i,q}^r = \int_{\Gamma_{\text{HA}}^r} (\vec{v}_q^r \times \vec{w}_i) \cdot \text{d}\vec{\Gamma}, \tag{3.36}$$

$$(K^\rho)^r_{p,q} = \int\limits_{\Omega^r_{c,H}} (\rho \nabla \times \vec{v}^r_q) \cdot \nabla \times \vec{v}^r_p \, \mathrm{d}\Omega \,, \tag{3.37}$$

$$(M^\mu)^r_{p,q} = \int\limits_{\Omega^r_{c,H}} (\mu \vec{v}^r_q) \cdot \vec{v}^r_p \, \mathrm{d}\Omega \,, \tag{3.38}$$

$$(X)^r_p = \int\limits_{\Omega^r_{c,H}} \vec{x}^r_p \cdot (\nabla \times \vec{v}^r_p) \, \mathrm{d}\Omega = - \int\limits_{\Gamma^r_J} (\nabla \times \vec{v}^r_p) \cdot \mathrm{d}\vec{\Gamma} \,. \tag{3.39}$$

The matrix coefficients of heat diffusion $\mathbf{K}^\kappa$ and heat capacitance $\mathbf{M}^\rho$, and the vector coefficients in Joule loss contribution $\mathbf{q}(\cdot)$ are given as

$$(K^\kappa)_{m,n} = \int\limits_{\Omega} (\kappa \nabla N_n) \cdot \nabla N_m \, \mathrm{d}\Omega \,, \tag{3.40}$$

$$(M^\rho)_{m,n} = \int\limits_{\Omega} (\rho_m C_p N_n) N_m \, \mathrm{d}\Omega \,, \tag{3.41}$$

$$(q(\cdot))_m = \int\limits_{\Omega} q(\cdot) N_m \, \mathrm{d}\Omega \,. \tag{3.42}$$

3.5.6 Discrete gauging

The field problem presented in (2.100) is not uniquely solvable, due to the gauge freedom of $\vec{A}$ for the nonconducting parts of the domain, where the magnetic vector potential is defined up to a gradient field. This property is inherited by the semidiscrete counterpart (3.33) which remains not uniquely solvable even after the incorporation of the boundary and initial conditions. A possibility to overcome this impasse is given by discrete gauging.

Gauging conditions can be applied in several ways. As an example, the original field problem can be changed in the nonconducting regions by introducing a constant artificial conductivity, leading to a system of stiff ODEs [247]. However, the approach introduces unecessary degrees of freedom and increases the effective condition number of the problem. An alternative method consists in adding an additional term describing the gauging condition, either to the original field problem [145], or to the semidiscrete counterpart [247]. Another possibility is using specific iterative solvers, such as the conjugate gradient method [248], as they implicitly gauge the system and thus provide a valid solution without the need of an explicit gauging condition [249]. Another method consists in using a tree-cotree gauge [70, 250]. This method modifies the semidiscrete set of equations by deleting the degrees of freedom that define divergence fields, retaining only the unknowns describing a divergence-free solution.

Once suitable gauging conditions are applied, and if initial conditions and voltages $\mathbf{v}_s$ (currents $\mathbf{i}_s$) are prescribed, then the semi-discrete system (3.33) is ready to be solved by a time-stepping algorithm, for example the backward differentiation formula (see Section 3.3.1.2). However, if the voltages (currents) depend on a surrounding circuitry (e.g. [222]), then further derivations are necessary.

3.5.7 Field-circuit coupling

Each source domain $\Omega_{c,H}^r$ is equipped with two electrical ports Γ_E^r and Γ_J^r, providing the source terms to the field model. If an external electrical network is present, the electrical ports can be exploited to apply the source terms determined by the network. For this reason, a field-circuit coupling interface is introduced, allowing to connect the electric field strength and current density in each source domain to the voltages and currents of an external circuit model. Among the possible coupling schemes, the field-circuit coupled simulation with the WR method [106, 242] is suitable for analyzing the magnetothermal transients in high-field accelerator magnets [114].

The field-circuit coupling interface is derived as a Schwarz transmission condition for a linearized system [251] which optimizes cosimulation schemes, promising faster convergence of the cosimulation algorithm [113]. The coupling interface can be formalized as a voltage-current relation $\mathbf{u}_s = \mathbf{Z}\mathbf{i}_s$ for a multi-port electrical device, where the impedance $\mathbf{Z}$ is a $N_r \times N_r$ dimensional matrix. The expression for $\mathbf{Z}$ is obtained in the frequency domain, with ω being the angular frequency. The discrete counterpart of the magnetic vector potential $\mathbf{a}$ is assumed to be gauged in Ω_A, such that the matrix $\mathbf{K}^\nu + j\omega\mathbf{M}^\sigma$ is positive-definite, thus invertible. Moreover, $\mathbf{K}^\rho$ is positive semidefinite, $\mathbf{M}^\mu$ is positive-definite, and $\mathbf{Q}$ and $\mathbf{X}$ have full-column rank. Thus, it is possible to use the Schur complement in (3.33) to derive the voltage-current relation, leading to the following equations

$$\mathbf{a} = [\mathbf{K}^\nu + j\omega\mathbf{M}^\sigma]^{-1}\mathbf{Q}\mathbf{h}, \tag{3.43a}$$

$$\mathbf{h} = [\mathbf{K}^\rho + j\omega[\mathbf{M}^\mu + \mathbf{Q}^\top[\mathbf{K}^\nu + j\omega\mathbf{M}^\sigma]^{-1}\mathbf{Q}]]^{-1}\mathbf{X}\mathbf{v}, \tag{3.43b}$$

$$\mathbf{i} = \mathbf{X}^\top\mathbf{h}. \tag{3.43c}$$

By eliminating $\mathbf{a}$ and $\mathbf{h}$ in (3.43) the impedance is derived, obtaining the following expression

$$\mathbf{Z}(j\omega) = [\mathbf{X}^\top[\mathbf{M}^z]^{-1}\mathbf{X}]^{-1}, \tag{3.44}$$

where the impedance matrix $\mathbf{M}^z$ and reluctance matrix $\mathbf{K}^\varphi$ are defined as

$$\mathbf{M}^z = \mathbf{K}^\rho + j\omega\mathbf{K}^\varphi, \tag{3.45}$$

$$\mathbf{K}^\varphi = \mathbf{M}^\mu + \mathbf{Q}^\top[\mathbf{K}^\nu + j\omega\mathbf{M}^\sigma]^{-1}\mathbf{Q}. \tag{3.46}$$

In the frequency domain, the impedance in (3.44) is immediately computable, providing an optimized transmission condition. However, when dealing with nonlinear systems in the time domain, the time derivatives contained in $\mathbf{Z}$ must be approximated. This is achieved by following [113], that is, $\mathbf{Z}$ is approximated by a Taylor series expansion truncated to the first order, as

$$\mathbf{Z}(j\omega) \approx \mathbf{Z}(0) + j\omega \left. \frac{\partial}{\partial j\omega}\mathbf{Z}(j\omega)\right|_{\omega=0}. \tag{3.47}$$

By using (3.44) into (3.47), the first term is expanded as

$$\mathbf{Z}(0) = [\mathbf{X}^\top[\mathbf{K}^\rho]^+\mathbf{X}]^{-1}, \tag{3.48}$$

and second term is expanded as

$$\begin{aligned} j\omega \left. \frac{\partial}{\partial j\omega}\mathbf{Z}(j\omega)\right|_{\omega=0} &= j\omega\mathbf{Z}(0)\mathbf{X}^\top[\mathbf{M}^z(0)]^{-1}\left. \frac{\partial}{\partial j\omega}\mathbf{M}^z\right|_{\omega=0}[\mathbf{M}^z(0)]^{-1}\mathbf{X}\mathbf{Z}(0) \\ &= j\omega\mathbf{Z}(0)\mathbf{X}^\top[\mathbf{K}^\rho]^+[\mathbf{M}^\mu + \mathbf{Q}^\top[\mathbf{K}^\nu]^+\mathbf{Q}][\mathbf{K}^\rho]^+\mathbf{X}\mathbf{Z}(0). \end{aligned} \tag{3.49}$$

where $[\mathbf{K}^\rho]^+$ and $[\mathbf{K}^\nu]^+$ are the (Moore-Penrose) pseudo-inverse matrices of $[\mathbf{K}^\rho]$ and $[\mathbf{K}^\nu]$ (see e.g. [217]). Using the results (3.48) and (3.49) in (3.47), the voltage-current relation reads in time domain

$$\mathbf{u}_{\mathrm{s}}(t) \approx \mathbf{R}\mathbf{i}_{\mathrm{s}}(t) + \mathbf{L}\frac{\mathrm{d}}{\mathrm{dt}}\mathbf{i}_{\mathrm{s}}(t), \tag{3.50}$$

where $\mathbf{R}$ and $\mathbf{L}$ represent equivalent resistance and inductance matrices, respectively. The matrices are defined as

$$\mathbf{R} = \mathbf{Z}(0) = [\mathbf{X}^\top[\mathbf{K}^\rho]^+\mathbf{X}]^{-1}, \tag{3.51}$$
$$\mathbf{L} = \mathbf{R}\mathbf{X}^\top[\mathbf{K}^\rho]^+[\mathbf{M}^\mu + \mathbf{Q}^\top[\mathbf{K}^\nu]^+\mathbf{Q}][\mathbf{K}^\rho]^+\mathbf{X}\mathbf{R}, \tag{3.52}$$

and may be used to approximate the finite element model in the circuital counterpart, as an RL-series component. The low-order model introduced by (3.47) disregards several effects, in particular the contribution of the eddy currents $\mathbf{M}^\sigma$ occurring in the domains outside the source region. As the Taylor series is expanded around $j\omega = 0$, the approximation should only be used for low frequencies.

3.5.8 2D approximation

For field problems featuring translational symmetry, it is possible to limit the discretization of the field problem to a two-dimensional cut plane. Given a Cartesian reference frame (x,y,z), the symmetry is assumed to occur along the z-direction for geometry, material properties and excitation sources, thereby bounding the field problem to the x-y plane. Therefore, $\vec{A} = (0, 0, A_{\mathrm{z}}(x, y))$, $\vec{H} = (H_{\mathrm{x}}(x, y), H_{\mathrm{y}}(x, y), 0)$ and $T = T(x, y)$. As a consequence, $\vec{A}$ does not need an explicit gauge since $\nabla \cdot \vec{A} = 0$ is automatically satisfied. The orientation and position dependency of $\vec{A}$ is encoded using dedicated shape functions based on nodal elements, whereas classical Nedéléc-type shape functions are used for $\vec{H}$.

The distribution function $\vec{\chi}_{\mathrm{sol}}^r$ is given in the 2D Cartesian case as [156, 252]

$$\vec{\chi}_{\mathrm{sol}}^r = \pm\frac{\vec{z}}{\delta_{\mathrm{z}}} \qquad \text{for } r = 1, ..., N_{\mathrm{r}}, \tag{3.53}$$

where the sign in (3.53) depends on the direction of the current in the conducting domain, δ_{z} is the depth of the field problem in the direction of the translational symmetry. With these definitions, the system entries introduced in (3.33) read

$$(K^\nu)_{i,j} = \int_{\Omega_{\mathrm{A}}} \mu^{-1}(\partial_x N_j \partial_x N_i + \partial_y N_j \partial_y N_i) \, \mathrm{d}\Omega, \tag{3.54}$$

$$(M^\sigma)_{i,j} = \int_{\Omega_{\mathrm{A}}} (\sigma N_j) N_i \, \mathrm{d}\Omega, \tag{3.55}$$

$$(Q)_{i,q}^r = \int_{\Gamma_{\mathrm{HA}}^r} (v_{q,y}^r n_x - v_{q,x}^r n_y) N_i \, \mathrm{d}\Gamma, \tag{3.56}$$

$$(K^\rho)_{p,q}^r = \int_{\Omega_{\mathrm{c,H}}^r} \rho(\partial_x v_{q,y}^r - \partial_y v_{q,x}^r)(\partial_x v_{p,y}^r - \partial_y v_{p,x}^r) \, \mathrm{d}\Omega, \tag{3.57}$$

$$(X)_p^r = \pm \frac{1}{\delta_z} \int\limits_{\Omega_{c,H}^r} (\partial_x v_{p,y}^r - \partial_y v_{p,x}^r) \, d\Omega, \tag{3.58}$$

$$(K^k)_{m,n} = \int\limits_{\Omega} k(\partial_x N_m \partial_x N_n + \partial_y N_m \partial_y N_n) \, d\Omega, \tag{3.59}$$

$$(M^\rho)_{n,m} = \int\limits_{\Omega} (\rho_m C_p N_n) N_m \, d\Omega, \tag{3.60}$$

where the integrals over the domains $\Omega_\star$ and $\Gamma_\star$ are 2D and 1D integrals.

3.6 Discretization of the Thin-Shell Approximation

The field problem is formulated with respect to the general weak formulation described by (3.14), (3.18) and (3.24), taking into account the properties of the thin-shell approximation described in Section 2.14. Instead of modeling the tape as the volume $\Omega_{c,H}^r$, the geometry is collapsed to the surface $\Gamma_{c,H}^r$. As a consequence, the domain $\Gamma_{c,H}^r$ reduces to the interface Γ_{HA}^r.

3.6.1 Weak formulation

The weak formulation for the vector field $\vec{A}$ in the domain Ω_A is determined as illustrated in Section 3.5.1, up to the surface integral in (3.16) which is rewritten as

$$\int\limits_{\partial\Omega_A} (\mu^{-1} \nabla \times \vec{A}) \times \vec{\nu} \cdot d\vec{\Gamma} = -\int\limits_{\Gamma_{HA}} [\vec{n} \times \mu^{-1}(\nabla \times \vec{A}_1 - \nabla \times \vec{A}_2)] \cdot \vec{\nu} \, d\Gamma = -\sum_{r=1}^{N_r} \int\limits_{\Gamma_{HA}^r} \vec{K}^r \cdot \vec{\nu} \, d\Gamma, \tag{3.61}$$

where the subscripts 1 and 2 refer to the field components on the two sides of the tapes, and from (2.111) the tangential discontinuity of the magnetic field strength in Ω_A is associated to the surface current $\vec{K}^r$ for each of the N_r tapes.

The weak formulation for the vector field $\vec{H}$ in the thin-shell domain $\Gamma_{c,H}$ is determined by following the same formalism as in Section 3.5.2, but integrating the strong formulation provided by (2.110) over a thin-shell instead of a domain. The obtained weak formulation reads

$$\delta_t^r \int\limits_{\Gamma_{c,H}^r} (\rho \nabla \times H^r \vec{n}^r) \cdot \nabla \times \vec{v}^r \, d\Gamma + \delta_t^r \int\limits_{\Gamma_{c,H}^r} (\partial_t \mu H^r \vec{n}^r) \cdot \vec{v}^r \, d\Gamma - v_s^r \delta_t^r \int\limits_{\Gamma_{c,H}^r} \vec{\chi}_{sol}^r \cdot \nabla \times \vec{v}^r \, d\Gamma$$

$$+ \delta_t^r \int\limits_{\partial\Gamma_{c,H}^r} (\vec{E}^r \times \vec{v}^r) \cdot d\vec{\gamma} = 0. \tag{3.62}$$

The second surface integral is further developed, and the continuity condition of the normal component of the magnetic field given in (2.114) is incorporated, leading to

$$
\delta_{\mathrm{t}}^{r} \int_{\Gamma_{\mathrm{c,H}}^{r}} (\partial_{t}\mu H^{r}\vec{n}^{r}) \cdot \vec{v}^{r}\, \mathrm{d}\Gamma = \delta_{\mathrm{t}}^{r} \int_{\Gamma_{\mathrm{c,H}}^{r}} (\partial_{t}\nabla \times \vec{A}) \cdot \vec{v}^{r}\, \mathrm{d}\Gamma
$$

$$
= \delta_{\mathrm{t}}^{r} \int_{\Gamma_{\mathrm{c,H}}^{r}} (\partial_{t}\vec{A}) \cdot \nabla \times \vec{v}^{r}\, \mathrm{d}\Gamma + \delta_{\mathrm{t}}^{r} \int_{\partial\Gamma_{\mathrm{c,H}}^{r}} (\partial_{t}\vec{A} \times \vec{v}^{r}) \cdot \mathrm{d}\vec{\gamma}.
\tag{3.63}
$$

The surface integral in (3.63) provides the interface condition for $\vec{A}$, and the line integrals in (3.62) and (3.63) are combined and disappear, due to the tangential continuity condition (2.102) on the electric field strength.

The volume of the tape is preserved for the thermal problem, with the exception of the heat source term which follows the thin-shell approximation. In detail, the source term in the heat balance equation in (3.24) is transformed into a surface integral in $\Gamma_{\mathrm{c,H}}$, weighted with the tape thickness δ_{t}^{r}. The source term reads for $r = 1, \ldots, N_{\mathrm{r}}$

$$
\int_{\Omega_{\mathrm{c,H}}^{r}} P_{\mathrm{J}}u\, \mathrm{d}\Omega = \delta_{\mathrm{t}}^{r} \int_{\Gamma_{\mathrm{c,H}}^{r}} P_{\mathrm{J}}u\, \mathrm{d}\Gamma = \delta_{\mathrm{t}}^{r} \int_{\Gamma_{\mathrm{c,H}}^{r}} (\rho_{\mathrm{eq}}^{r}\vec{J}^{r} \cdot \vec{J}^{r})u\, \mathrm{d}\Gamma,
\tag{3.64}
$$

where ρ_{eq}^{r} is the equivalent tape resistivity which is detailed in Section 3.7.

3.6.2 Semidiscrete formulation

The fields $\vec{A}$ and T are discretized as in Section 3.5.5. The field $\vec{H}^{r} = H^{r}\vec{n}^{r}$ is discretized for $r = 1, \ldots, N_{\mathrm{r}}$ by defining a suitable set of edge functions $\vec{v}_{q}^{r}$ which read

$$
\vec{H}^{r} = \sum_{q=1}^{n_{\mathrm{P,H}}^{r}} \vec{v}_{q}^{r}h_{q}^{r}, \qquad \vec{v}_{q}^{r} = \frac{N_{q}^{r}}{\delta_{\mathrm{t}}^{r}}\vec{n}^{r},
\tag{3.65}
$$

where $n_{\mathrm{P,H}}^{r}$ is the number of mesh nodes in $\Gamma_{\mathrm{c,H}}^{r}$, and N_{q}^{r} represents a set of nodal basis functions defined at the surface of the thin shell, and zero elsewhere. Again, different discretization orders are used for $\vec{A}$ and $\vec{H}^{r}$, $r = 1, \ldots, N_{\mathrm{r}}$, avoiding potential stability issues [189]. Once all the field variables are replaced with their discrete counterparts and boundary conditions are considered, the following discrete problem is obtained:

$$
\begin{bmatrix}
\mathbf{K}^{\nu} + \mathbf{M}^{\sigma}\frac{\mathrm{d}}{\mathrm{dt}} & -\overline{\mathbf{Q}} & \mathbf{0} & \mathbf{0} \\
\overline{\mathbf{Q}}^{\top}\frac{\mathrm{d}}{\mathrm{dt}} & \overline{\mathbf{K}}^{\rho} & -\overline{\mathbf{X}} & \mathbf{0} \\
\mathbf{0} & \overline{\mathbf{X}}^{\top} & \mathbf{0} & \mathbf{0} \\
\mathbf{0} & \mathbf{0} & \mathbf{0} & \mathbf{K}^{\kappa} + \mathbf{M}^{\rho}\frac{\mathrm{d}}{\mathrm{dt}}
\end{bmatrix}
\begin{bmatrix}
\mathbf{a} \\
\mathbf{h} \\
\mathbf{u}_{\mathrm{s}} \\
\mathbf{t}
\end{bmatrix}
=
\begin{bmatrix}
\mathbf{0} \\
\mathbf{0} \\
\mathbf{i}_{\mathrm{s}} \\
\overline{\mathbf{q}}(\cdot)
\end{bmatrix}.
\tag{3.66}
$$

The coefficients in (3.66) differing from those in (3.33) are given for $r = 1, ..., N_{\mathrm{r}}$ as

$$
(\overline{Q})_{i,q}^{r} = \delta_{\mathrm{t}}^{r} \int_{\Gamma_{\mathrm{c,H}}^{r}} (\nabla \times \vec{v}_{q}^{r}) \cdot \vec{w}_{i}\, \mathrm{d}\Gamma,
\tag{3.67}
$$

$$(\overline{K}^{\rho})_{p,q}^r = \delta_{\mathrm{t}}^r \int\limits_{\Gamma_{\mathrm{c,H}}^r} (\rho_{\mathrm{eq}}^r \nabla \times \vec{v}_q^r) \cdot \nabla \times \vec{v}_p^r \, \mathrm{d}\Gamma, \qquad (3.68)$$

$$(\overline{X})_p^r = \delta_{\mathrm{t}}^r \int\limits_{\Gamma_{\mathrm{c,H}}^r} \vec{x}_p^r \cdot (\nabla \times \vec{v}_p^r) \, \mathrm{d}\Gamma, \qquad (3.69)$$

$$(\overline{q}(\cdot))_m = \delta_{\mathrm{t}}^r \int\limits_{\Gamma_{\mathrm{c,H}}^r} q(\cdot) N_m \, \mathrm{d}\Gamma, \qquad (3.70)$$

where the integrals over the domains $\Gamma_\star$ are 1D integrals. The elements composing the heat source $\overline{\mathbf{q}}(\cdot)$ in the right-hand side of (3.66) are given by the sum of (3.42) and (3.70), the second term occurring only in the thin shell.

3.6.3 Field-circuit coupling

For the field-circuit coupling, the interface is derived following a procedure formally identical to the one in Section 3.5.7, but applied to (3.66). The obtained interface reads

$$\mathbf{u}_{\mathrm{s}}(t) \approx \mathbf{R}_\Gamma \mathbf{i}_{\mathrm{s}}(t) + \mathbf{L}_\Gamma \frac{\mathrm{d}}{\mathrm{d}t} \mathbf{i}_{\mathrm{s}}(t), \qquad (3.71)$$

where $\mathbf{R}_\Gamma$ and $\mathbf{L}_\Gamma$ represent equivalent resistance and inductance matrices related to the thin-shell approximation. The matrices are defined as

$$\mathbf{R}_\Gamma = [\overline{\mathbf{X}}^\top [\overline{\mathbf{K}}^\rho]^{-1} \overline{\mathbf{X}}]^{-1}, \qquad (3.72)$$

$$\mathbf{L}_\Gamma = \mathbf{R}_\Gamma \overline{\mathbf{X}}^\top [\overline{\mathbf{K}}^\rho]^+ [\overline{\mathbf{Q}}^\top [\mathbf{K}^\nu]^+ \overline{\mathbf{Q}}] [\overline{\mathbf{K}}^\rho]^{-1} \overline{\mathbf{X}} \mathbf{R}_\Gamma, \qquad (3.73)$$

where $\overline{\mathbf{K}}^\rho$ is positive-definite in the thin-shell approximation, thus invertible. The relation (3.73) can be used to approximate the finite element model in the circuital counterpart, as an RL-series component.
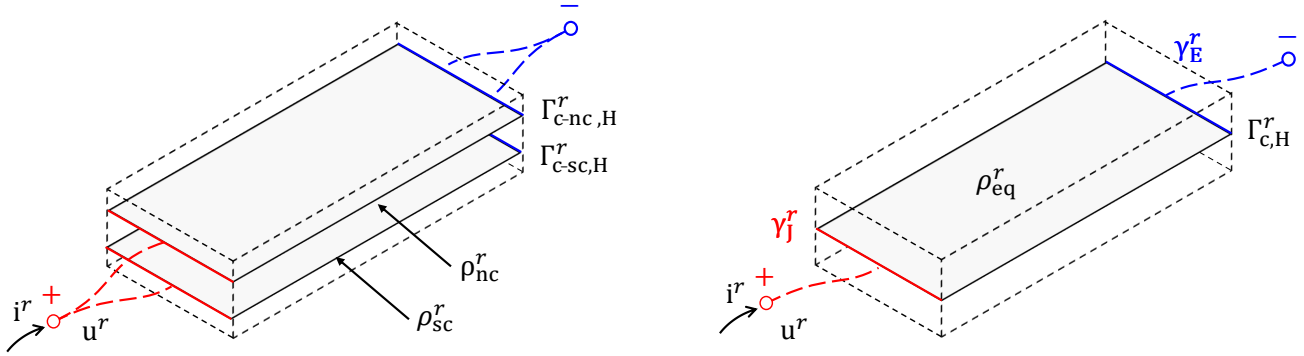
3.6.4 2D approximation

For field problems which show translational symmetry, source domains $\Gamma_{\mathrm{c,H}}^r$ are represented by 1D curves $\gamma_{\mathrm{c,H}}^r$, for $r = 1, \ldots, N_{\mathrm{r}}$. With respect to a local reference frame (l^r, n^r, z^r) oriented according to the tangential l^r and normal n^r directions of $\gamma_{\mathrm{c,H}}^r$, the magnetic field strength $\vec{H}^r$ in each thin shell is given as $\vec{H}^r = (0, H^r, 0)$, and discretized with the edge functions defined in (3.65). The treatment of the fields $\vec{A}$ and T, and the distribution function χ_{sol}^r is analogous as in Section 3.5.8. With the previous observations, the system entries introduced in (3.66) differing from those in Section 3.5.8 read

$$(\overline{Q})_{i,q}^r = \int\limits_{\gamma_{\mathrm{HA}}^r} (\partial_l N_q^r) N_i \, \mathrm{d}\gamma, \qquad (3.74)$$

$$(\overline{K}^\rho)_{p,q}^r = \frac{1}{\delta_{\mathrm{t}}^r} \int\limits_{\gamma_{\mathrm{c,H}}^r} \rho (\partial_l N_q^r)(\partial_l N_p^r) \, \mathrm{d}\gamma, \qquad (3.75)$$

$$(\overline{X})_p^r = \pm \frac{1}{\delta_{\mathrm{z}}} \int\limits_{\gamma_{\mathrm{c,H}}^r} \partial_l N_q^r \, \mathrm{d}\gamma = \frac{\vec{z}}{\delta_{\mathrm{z}}} (N_{q,2}^r - N_{q,1}^r), \qquad (3.76)$$

(a) Thin-shell approximation for each layer.   *(b) Layers homogenization.*

Figure 3.7. Sketch of the electrical behavior of the thin-shell approximation. (a) The two paths $\Gamma^r_{\text{c-sc,H}}$ and $\Gamma^r_{\text{c-nc,H}}$ representing the superconducting layer and the normal conducting layer, are homogenized into (b) the equivalent path $\Gamma^r_{\text{c,H}}$.

where the indices 1 and 2 refer to the nodes at the two edges of $\gamma^r_{\text{c,H}}$, and the sign in (3.76) depends from the orientation of the current in $\gamma^r_{\text{c,H}}$. This simplification is crucial, since the line integrals are replaced by Dirichlet boundary conditions for each tape. This brings a major advantage in modeling applications containing up to several thousand turns, such as accelerator magnets.

3.7 Current Sharing in the Thin-Shell Approximation

The layered structure of superconducting tapes provides electrical paths in parallel connection, such that the source current can redistribute between all the conducting layers. The current sharing occurs when the superconducting layer cannot carry anymore all the transport current. This situation can be caused either by an increase of the transport current beyond the critical current of the tape into the overcritical regime, or by a temperature increase which reduces the critical current, leading to a quench regime.

The electrical behavior of the thin-shell approximation for a generic HTS tape is discussed with respect to two conducting paths arranged in a parallel connection, as shown in Figure 3.7a. The first path $\Gamma^r_{\text{c-sc,H}}$ is associated to the superconducting layer, the second path $\Gamma^r_{\text{c-nc,H}}$ to a shell homogenization of the remaining N_{nc} normal conducting layers, that is, the stabilizer, the substrate, the buffer layers and the silver coating (see Section 1.2). The two paths are then homogenized into an equivalent shell $\Gamma^r_{\text{c,H}}$, as shown in Figure 3.7b. The equivalent shell $\Gamma^r_{\text{c,H}}$ carries the surface current density $\vec{K}^r$ defined in (2.109). The magnitude of the surface current density depends on the equivalent resistivity ρ^r_{eq} obtained from the homogenization of the resistivities ρ^r_{sc} and ρ^r_{nc} related to the superconducting and normal conducting layers. From the relation (2.86), ρ^r_{sc} shows a current density dependency and therefore the current sharing needs to be resolved to obtain the equivalent resistivity ρ^r_{eq}.

Since $\Gamma^r_{\text{c-sc,H}}$ and $\Gamma^r_{\text{c-nc,H}}$ are assumed to be geometrically identical, Kirchhoff's current (KCL) and voltage (KVL) laws hold true also in their differential formulation. On the one hand, KCL allows to introduce the
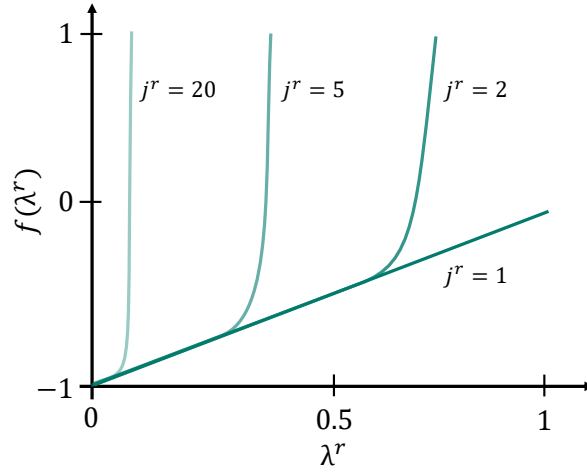
Figure 3.8. Sketch of the polynomial associated to the zero-finding problem, as a function of the current-sharing index λ^r in the superconducting layer. The curves are parametrized by the surface current density saturation index r^r in the tape.

current-sharing index $\lambda^r \in [0,1]$. The index relates $\vec{K}^r$ to the current densities $\vec{J}^r_{sc}$ and $\vec{J}^r_{sc}$ in the superconducting and the normal-conducting layers, as

$$
\vec{J}^r_{sc} = \lambda^r \frac{\vec{K}^r}{\delta^r_{sc}}, \qquad \vec{J}^r_{nc} = (1 - \lambda^r)\frac{\vec{K}^r}{\delta^r_{nc}}, \tag{3.77}
$$

where δ^r_{sc} and δ^r_{nc} are the thicknesses of the superconducting and the normal-conducting layers, such that $\delta^r_t = \delta^r_{sc} + \delta^r_{nc}$. On the other hand, KVL allows to formulate the electric field balance of the superconducting and normal conducting layers as

$$
\rho^r_{sc}\vec{J}^r_{sc} - \rho^r_{nc}\vec{J}^r_{nc} = 0, \tag{3.78}
$$

which can be further developed by using (3.77), obtaining

$$
\lambda^r \rho^r_{sc} \frac{\vec{K}^r}{\delta^r_{sc}} - (1 - \lambda^r)\rho^r_{nc} \frac{\vec{K}^r}{\delta^r_{nc}} = 0. \tag{3.79}
$$

The superconducting and normal conducting resistivities are given by

$$
\rho^r_{sc}(\lambda^r, |\vec{J}^r|) = \frac{E_c}{J_c}(\lambda^r j^r)^{n-1}, \qquad j^r = \frac{|\vec{J}^r|}{J_c}, \tag{3.80}
$$

and

$$
\rho^r_{nc} = \delta^r_{nc} \left(\sum_{k=1}^{N_{nc}} \frac{\delta^{r,k}_{nc}}{\rho^{r,k}_{nc}} \right)^{-1}, \tag{3.81}
$$

where j^r is the current density saturation index. The determination of λ^r is done by substituting (3.80)

and (3.81) into (3.77). The root-finding problem is formulated, for $r = 1, \ldots, N_{\mathrm{r}}$, as

$$
\begin{cases}
\text{find } \lambda^r \in [0, 1] : \begin{cases} f(\alpha^r, \lambda^r) = 0, \\ \alpha^r \geq 0, \end{cases} \\
\text{with } f(\alpha^r, \lambda^r) = \alpha^r (\lambda^r)^n + \lambda^r - 1, \\
\qquad \alpha^r = \left. \frac{\delta^r_{\mathrm{nc}}}{\delta^r_{\mathrm{sc}}} \; \frac{\rho^r_{\mathrm{sc}}(\lambda^r, |\vec{J}^r|)}{\rho^r_{\mathrm{nc}}} \right|_{\lambda^r = 1} .
\end{cases} \tag{3.82}
$$

The problem in (3.82) cannot be solved analytically, due to the circular dependency on the current density $|\vec{J}^r|$. However, the continuity property of the polynomial and the intermediate zero theorem ensure that for $\alpha^r > 0$, $f(\alpha^r, \lambda^r) = 0$ admits at least one real root in the interval $[0, 1]$. Moreover, applying Descartes' rule of signs [253] to the polynomial $f(\alpha^r, \lambda^r)$ guarantees the existence of only one real and positive root, at most.

It is worth observing that the behavior of the polynomial derivative $f'(\alpha^r, \lambda^r)$ strongly depends on the current density saturation. The behavior is shown in Figure 3.8, for different j^r. For low saturation $j^r \to 0$, then $f'(\alpha^r, \lambda^r) = 1$, whereas for saturation in the overcritical regime $j^r \to +\infty$, then $f'(\alpha^r, \lambda^r) = +\infty$. This behavior is shown in Figure 3.7 for increasing values of the saturation index. From the previous observations, the scalar root-finding problem (3.82) is solved using the bisection method (e.g. [254]) which guarantees linear convergence independently of the saturation index. The current-sharing algorithm is implemented as an inner loop within the time-stepping algorithm. Once λ^r is found, it is used in (3.80) such that the equivalent surface resistivity ρ^r_{eq} can be calculated as

$$
\rho^r_{\mathrm{eq}} = (\delta^r_{\mathrm{sc}} + \delta^r_{\mathrm{nc}}) \left(\frac{\delta^r_{\mathrm{sc}}}{\rho^r_{\mathrm{sc}}} + \frac{\delta^r_{\mathrm{nc}}}{\rho^r_{\mathrm{nc}}} \right)^{-1} . \tag{3.83}
$$

3.8 Summary

The solution of the multiphysical field problems requires finding a solution of boundary value and time-dependent initial-value problems composed of partial differential equations. In general, such equations do not allow to determine the exact solution, therefore numerical methods are needed. Approximate solutions are sought for in finite subspaces of the function spaces of the exact solution, where the subspaces are defined by means of suitable basis functions. The partial differential equations are reduced to a system of either ordinary differential or differential algebraic equations, and the most common time-integration methods are discussed.

The weak formulation of the coupled $\vec{A} - \vec{H}$ field problem is obtained by means of the Ritz-Galerkin method. The semi-discrete system of equations is presented for the 3D and 2D settings, and the implications of the thin-shell approximation are detailed. Then, the field-circuit coupling interface is derived as an optimized Schwarz transmission condition. The obtained set of equations are implemented in a numerical solver which relies on the finite element method. The implementation of the coupled $\vec{A} - \vec{H}$ field formulation is verified in Chapter 4 and validated in Chapter 5. To deal with field-circuit coupled problems, the optimized Schwarz waveform relaxation method is discussed, as it allows decomposing the coupled problems into a set of independent models, solved in an iterative way. This method is implemented in the STEAM cosimulation framework, allowing for the hierarchical cosimulation of field-circuit coupled problems of circuits containing superconducting accelerator magnets. The framework is used in Chapter 4.

4 Numerical Verification

In this chapter, the coupled $\vec{A} - \vec{H}$ field formulation is implemented with the finite-element method, using the proprietary software COMSOL, and it is verified by means of test cases. The formulation is first verified in Section 4.1 against the $\vec{A}$ formulation for both the bulk and shell implementations of a single tape in the 3D and 2D setting, assuming constant material properties. The influence of the tape thickness is assessed with respect to the shell approximation. Subsequently, in Section 4.2 the electric nonlinear behavior of superconducting materials is introduced by means of the power law discussed in Chapter 2, and it is verified against the $\vec{H}$ formulation for superconducting blocks and stacks in the 3D setting.

In Section 4.3, the shell implementation of a single superconducting tape is verified in the 2D setting against analytical solutions from literature. Subsequently, in Section 4.4 the single tape model is extended to the geometry of a superconducting coil in the 2D setting. The formulation is verified for different connection schemes, for both the bulk and shell representation of the tapes. In Section 4.5, the field-circuit coupling interface derived in Chapter 3 is verified within the waveform relaxation method. In detail, a quench event occurring in an HTS solenoid protected by quench heater strips is cosimulated, and the results are compared with the monolithic solution.

4.1 Normal Conducting Tape

This section provides the verification for the implementation of the coupled $\vec{A} - \vec{H}$ field formulation for both the bulk and shell representations of tapes. The model geometry is kept simple and the material properties are chosen as constant, such that focus is given to the verification of the implementation of the formulation. The calculated quantities of interest are compared with the solution provided by the monolithic $\vec{A}$ formulation.

4.1.1 Problem setting

The model is composed of one normal conducting tape represented as a 3D bulk object surrounded by air, as shown in Figure 4.1a. The computational domain Ω is decomposed into the source region $\Omega_{c,H}$ containing the tape, and the passive and nonconducting region $\Omega_{0,A}$. The field problems is solved in $\Omega_{c,H}$ for the magnetic field strength $\vec{H}$, and in $\Omega_{0,A}$ for the (reduced) magnetic vector potential $\vec{A}$. The interface Γ_{HA} between the two regions corresponds to the four lateral faces of the tape, as the tape ends touch the exterior boundary. The red and blue arrows show the positive orientation of the current in the tape. The 3D bulk tape is first simplified into a 3D shell tape by neglecting its thickness, as shown by Figure 4.1b where $\Omega_{c,H}$ is collapsed into the surface $\Gamma_{c,H}$. Subsequently, the 3D bulk and shell models are further simplified by exploiting their translational symmetry into the 2D bulk and shell models shown in Figure 4.1c and 4.1d. The relevant geometric
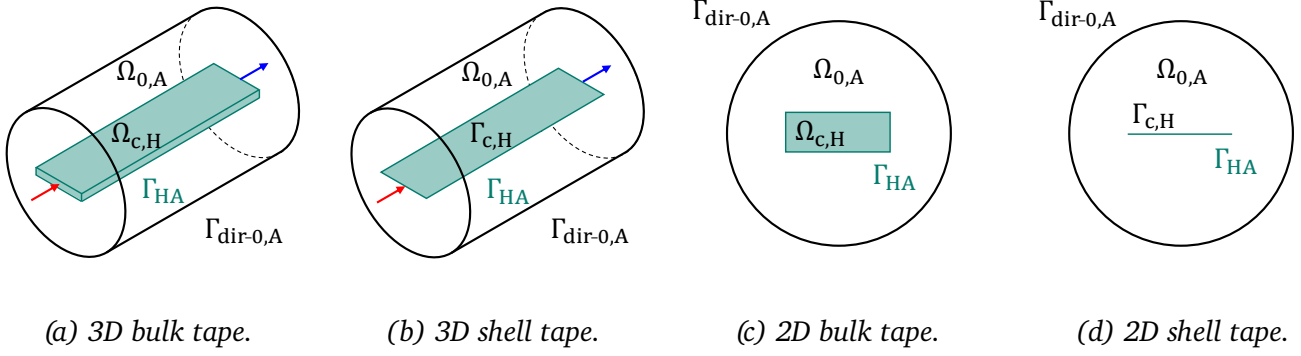
(a) 3D bulk tape.   (b) 3D shell tape.   (c) 2D bulk tape.   (d) 2D shell tape.

Figure 4.1. Numerical models for bulk and shell tapes, in the 3D and 2D setting.

Parameter	Unit	Value	Description
δ_w	mm	10	Tape width
δ_t	mm	0.5	Tape thickness
δ_l	mm	100	Tape length
ρ	$n\Omega\,m$	10	Tape resistivity

Table 4.1. Tape specifications.

and material properties are given in Table 4.1. For the 3D models, homogeneous Dirichlet boundary conditions are applied to $\vec{A}$ on $\Gamma_{\text{dir-0,A}}$, the exterior boundary of $\Omega_{0,A}$, whereas homogeneous Neumann boundary conditions are applied to $\vec{H}$ on the tape ends. In the 2D setting, only homogeneous Dirichlet boundary conditions are imposed to $\vec{A}$ on the exterior boundary $\Gamma_{\text{dir-0,A}}$. Homogeneous boundary conditions are justified by considering the exterior boundary sufficiently far from the tapes.

All four models are powered by means of a voltage source which follows the general source signal $v_s(t)$ shown in Figure 4.2, parametrized with the DC and AC contributions Y_{dc} and Y_{ac}, and the frequency f. The curve $y_s(t)$ is defined as

$$y_s(t) = \begin{cases} Y_{\text{dc}} f t & \text{if } t \in [0, 0.9)/f \\ p_{\text{dc}}(t) & \text{if } t \in [0.9, 1.1)/f \\ Y_{\text{dc}} & \text{if } t \in [1.1, 2.9)/f \\ p_{\text{ac}}(t) & \text{if } t \in [2.9, 3.1)/f \\ Y_{\text{dc}} + Y_{\text{ac}} \sin{(2\pi f t)} & \text{if } t \in [3.1, 5.0]/f, \end{cases} \tag{4.1}$$

where $p_{\text{dc}}(t)$ and $p_{\text{ac}}(t)$ denote fifth-order polynomial functions which ensure that $y_s(t)$ is derivable twice, hence C^2 continuous at the two transitions. For the case under study, the source signal parameters are chosen as $Y_{\text{dc}} = 1\,\text{mV}$, $Y_{\text{ac}} = 0.5\,\text{mV}$, and $f = 10\,\text{Hz}$. The problem setting is the same for the four models with respect to the source signal and initial and boundary conditions, leading to the same field problem.
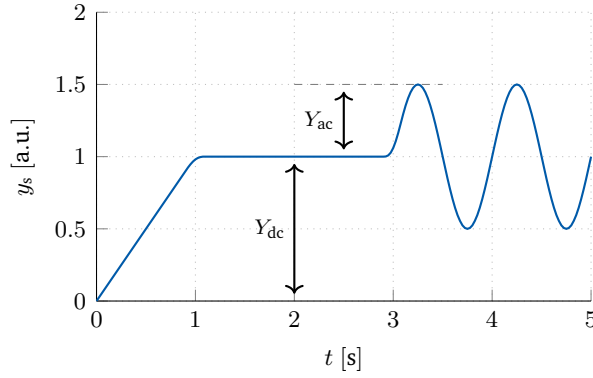
Figure 4.2. Source signal, for $f = 1\,\mathrm{Hz}$.

4.1.2 Simulation setup

For each of the four models, the field problem is solved by using the coupled field formulation, adapted to the geometry and the representation of the tape. The reference solution is obtained for the 3D models with bulk and shell tapes by using the monolithic $\vec{A}$ formulation which is provided by COMSOL. The comparison of results is done consistently with the tape geometry. A set of quantities of interest $q(t)$ are extracted from each of the simulations and then compared as

$$\Delta q(t) = \frac{|q_{\mathrm{A}}(t)| - |q_{\mathrm{AH}}(t)|}{|q_{\mathrm{A}}(t)|}, \tag{4.2}$$

where the subscripts A and AH refer to the two formulations used for computing the field solution, and $\Delta q(t)$ is the relative difference. For bulk tapes in the 3D setting, the quantities of interest are defined by

$$i_{\mathrm{s}} = \int_{\Omega_{\mathrm{c,H}}} \vec{\chi} \cdot \vec{J}\,\mathrm{d}\Omega \qquad [\mathrm{A}] \qquad \text{Source current,} \tag{4.3a}$$

$$R_{\mathrm{DC}} = \left(\int_{\Omega_{\mathrm{c,H}}} \frac{1}{\rho}\vec{\chi} \cdot \vec{\chi}\,\mathrm{d}\Omega \right)^{-1} \qquad [\Omega] \qquad \text{DC resistance,} \tag{4.3b}$$

$$P_{\mathrm{s}} = v_{\mathrm{s}} i_{\mathrm{s}} \qquad [\mathrm{W}] \qquad \text{Source power,} \tag{4.3c}$$

$$P_{\mathrm{J}} = \int_{\Omega_{\mathrm{c,H}}} \rho \vec{J} \cdot \vec{J}\,\mathrm{d}\Omega \qquad [\mathrm{W}] \qquad \text{Joule power,} \tag{4.3d}$$

$$W_{\mathrm{s}} = \int_{0}^{t} P_{\mathrm{s}}\,\mathrm{d}t \qquad [\mathrm{J}] \qquad \text{Source energy,} \tag{4.3e}$$

$$W_{\mathrm{J}} = \frac{1}{2} \int_{\Omega} \vec{B} \cdot \vec{H}\,\mathrm{d}\Omega \qquad [\mathrm{J}] \qquad \text{Magnetic energy.} \tag{4.3f}$$

The quantities of interest are chosen such that both electric and magnetic phenomena are compared. The definitions given in (4.3) can be adapted for bulk tapes in the 2D setting by replacing the volume integrals with surface integrals weighted with the tape length δ_{l}. For the thin-shell approximation, volume and surface integrals for bulk tapes in the 3D and 2D settings are replaced by surface and line integrals, weighted with the tape thickness δ_{t}.
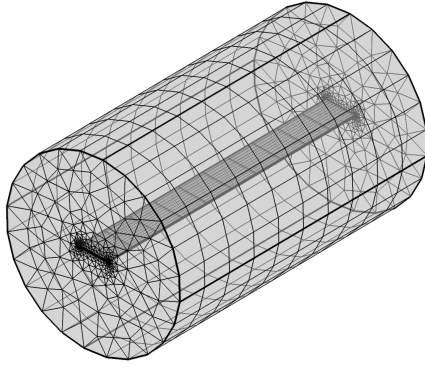
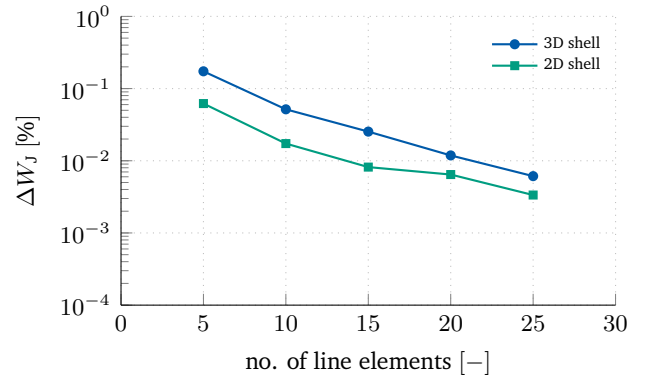*(a) Mesh of the 3D bulk tape.*
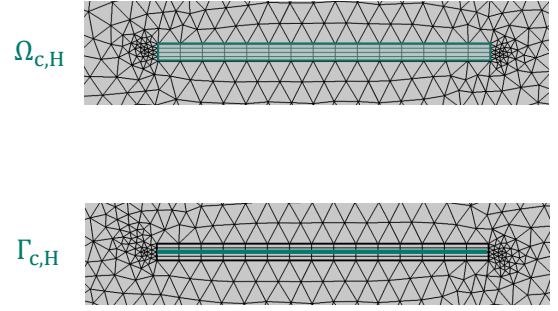
(b) Mesh detail.

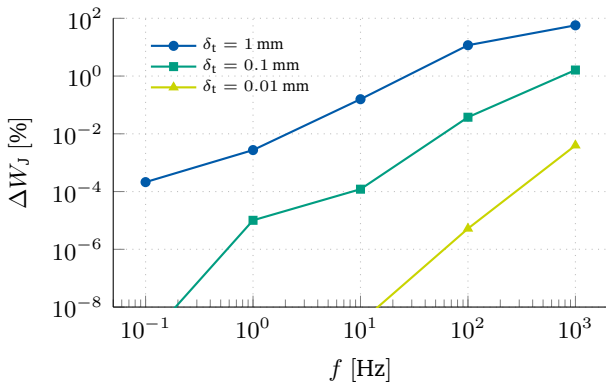*Figure 4.3. (a) Mesh of the 3D bulk tape. (b) From top to bottom, detail of the bulk and shell tape.*
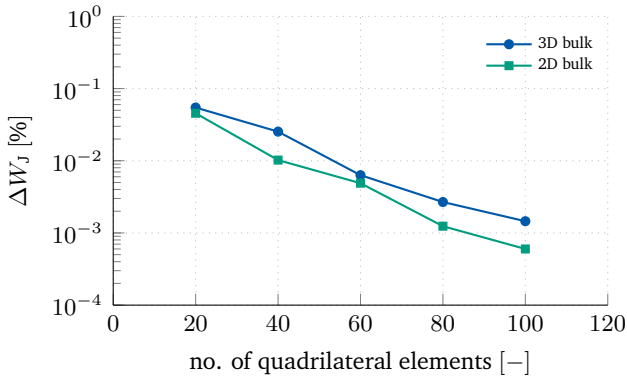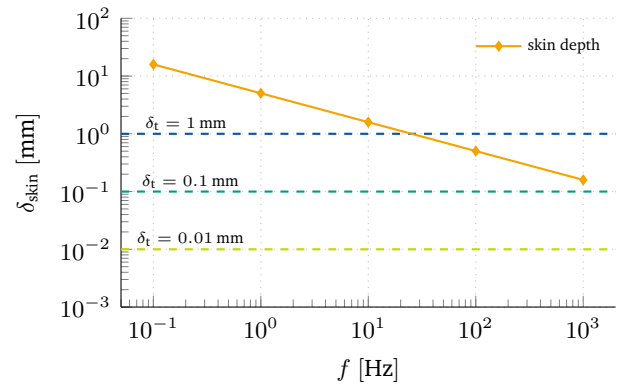

(a) Bulk tape.

(b) Shell tape.

Figure 4.4. Relative difference ΔW_{J} between the $\vec{A}$ and $\vec{A} - \vec{H}$ formulation. Results are given for (a) bulk and (b) shell tape models, in dependency of the number of mesh elements in the cross section of the tape.

(a) Relative difference of ΔW_{J}.

(b) Skin depth.

Figure 4.5. Relation between the skin depth and the thin-shell approximation. (a) Relative difference ΔW_{J} between 3D bulk and shell tapes. (b) Skin depth, as a function of the frequency.

The mesh used for the 3D bulk tape is shown in Figure 4.3a. The cross section of the bulk tape is discretized by a structured grid of quadrilateral elements, using 15 elements in the width and 4 elements in the thickness, whereas for the thin-shell approximation the structured grid is replaced with 15 line elements evenly distributed along the tape width (Figure 4.3b, top and bottom). The cross section of the nonconducting air is discretized with triangular elements, and the mesh is propagated along the tape length for the 3D models using $10\,\mathrm{mm}$ long hexahedra. The models with 3D bulk and shell tapes use a mesh first-order elements. The models with 2D bulk and shell tapes use a mesh of first-order elements in $\Omega_{\mathrm{c,H}}$ and $\Gamma_{\mathrm{c,H}}$, and second-order elements in $\Omega_{\mathrm{0,A}}$.

4.1.3 Numerical convergence analysis

The accuracy of the numerical solution provided by the $\vec{A} - \vec{H}$ formulation is investigated for the four models. The Joule energy W_{J} is calculated for increasingly refined meshes in the cross section of the tape, and compared with the results obtained with the $\vec{A}$ formulation and a highly refined mesh. The results for the bulk tape in both 3D and 2D settings are shown in Figure 4.4a where the reference solution is obtained with 500 elements in the cross section. The results for the shell tape in both 3D and 2D settings are shown in Figure 4.4b where the reference solution is obtained with 125 elements in the cross section. For all the four models, the relative difference in the Joule energy ΔW_{J} shows a monotonic decrease with the number of elements, indicating that the solution converges to the exact solution.

4.1.4 Thickness analysis

The shell model introduces an approximation which depends on the thickness of the tape in comparison to the skin penetration depth of eddy currents. In general, the thin-shell approximation produces reliable results only if the thickness is significantly smaller than the skin penetration depth. In quasistatic regimes, the skin depth δ_{skin} is defined by the approximate expression [255]

$$\delta_{\mathrm{skin}} = \left(\frac{\rho}{\pi f \mu} \right)^{1/2} . \tag{4.4}$$

The approximation is quantified by comparing the results obtained from the 2D models with bulk and shell tapes. The results are shown in Figure 4.5, parametrized by the tape thickness and the frequency. The relative difference of the Joule energy ΔW_{J} between the bulk and the shell model for the tape is shown in Figure 4.5a, as a function of the frequency and parametrized by the thickness of the tape δ_{t}. The difference shows a monotonic increase, with higher values for thicker tapes. This behavior can be explained with respect to Figure 4.5b showing a comparison of the skin depth of the tape with respect to the thicknesses considered for the bulk-shell comparison. For frequencies above $10\,\mathrm{Hz}$, the skin depth is smaller than $1\,\mathrm{mm}$, therefore the equivalent shell model shows a difference which quickly increases above $1\,\%$. In the other two cases, the tape thickness is below the skin depth, and the difference remains below $1\,\%$ for almost all the frequency spectrum. For the case under study, that is, a $1\,\mathrm{mm}$ thick tape and $f = 10\,\mathrm{Hz}$, the skin depth is about a factor five thicker than the tape. The case under study assumes a frequency of $f = 10\,\mathrm{Hz}$, where the skin depth is about five times greater than the total tape thickness of $1\,\mathrm{mm}$.

Geometry	Source	y_{dc}	y_{ac}	f	$\varepsilon_{\mathrm{rel}}$	$\varepsilon_{\mathrm{abs}}$	Time stepping	Δt_{max}
Bulk Shell	v_{s}	1 mV	0.5 mV	10	1×10^{-4}	1×10^{-3}	adaptive BDF-5	$(100f)^{-1}$

Table 4.2. Main solver settings.
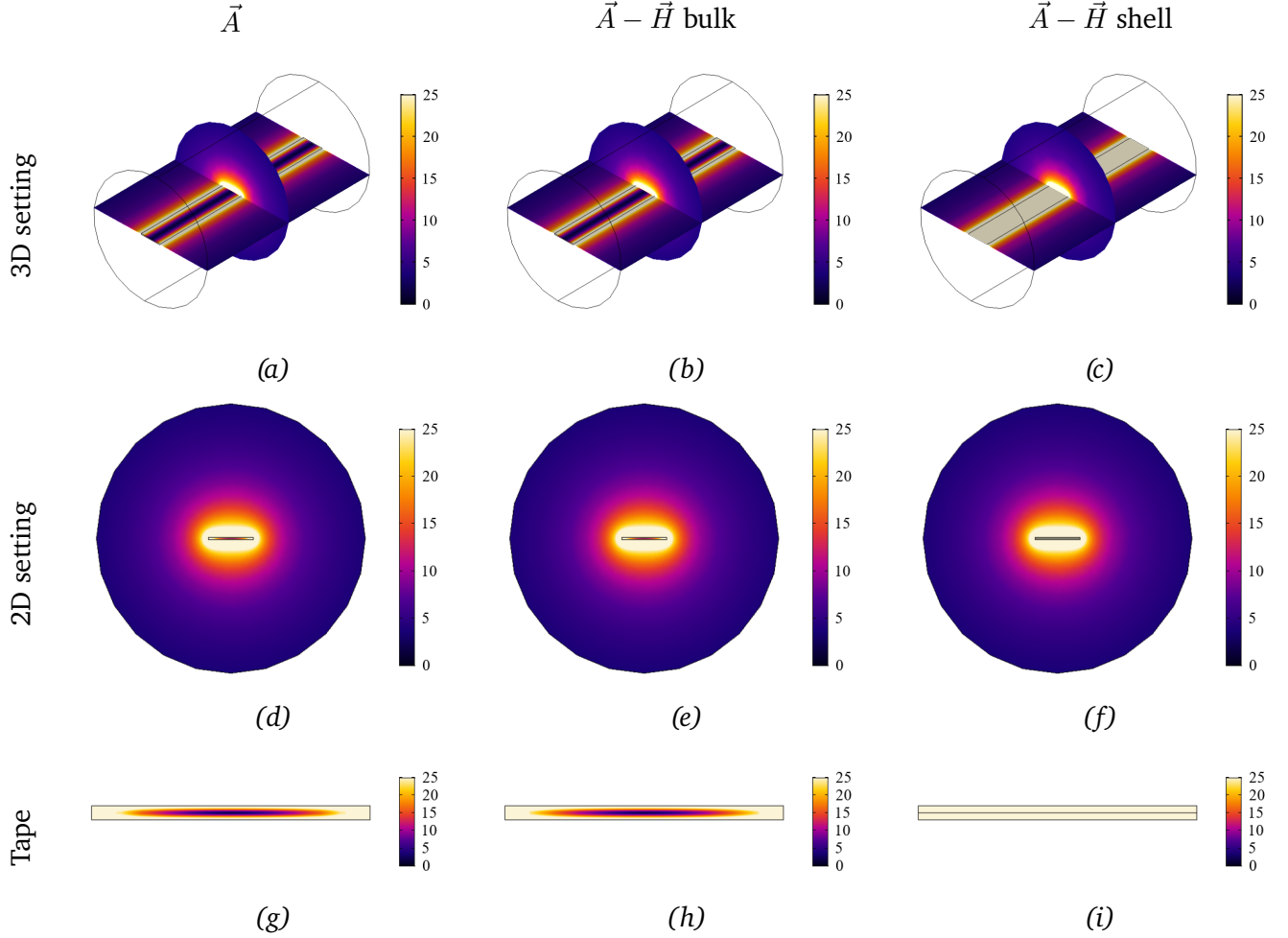
Figure 4.6. Comparison of the numerical solutions for the magnetic flux density in mT *at* $t = 0.425$ s*, obtained with the $\vec{A}$ formulation (first column), and the $\vec{A} - \vec{H}$ formulation with both bulk (second column) and shell tapes (third column). Simulations are done for voltage driven models. The first and second rows in the figure refer to models in the 3D and 2D settings. The third row shows the magnetic flux density in the cross section of the tape.*

4.1.5 Numerical results

The time stepping scheme is implicit and based on the adaptive BDF-5 (of order 1-5), using an adaptive time step limited to a maximum size of $\Delta t = (100f)^{-1}$, for both the bulk and shell tape simulations. The most relevant solver-setting parameters adopted in the simulations are given in Table 4.2. The field solution for the magnetic flux density is shown in Figure 4.6. The results are organized in columns corresponding respectively
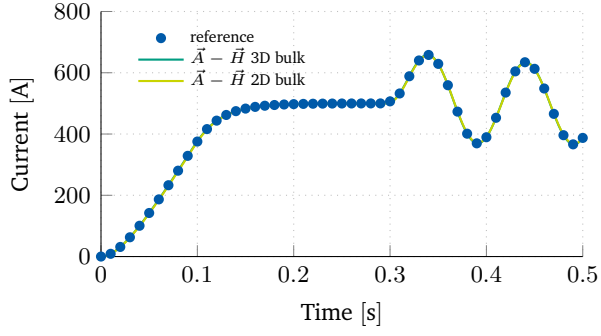
(a) Source current i_s.
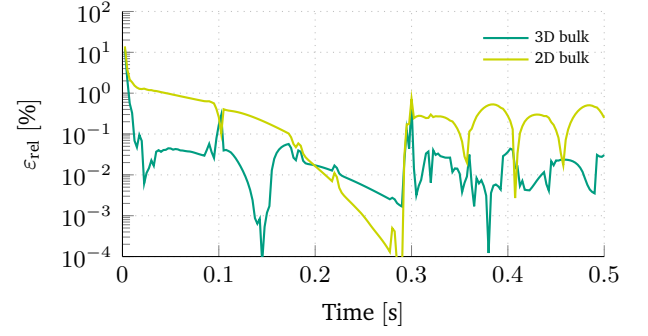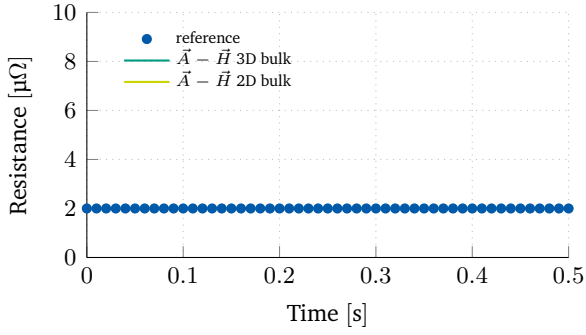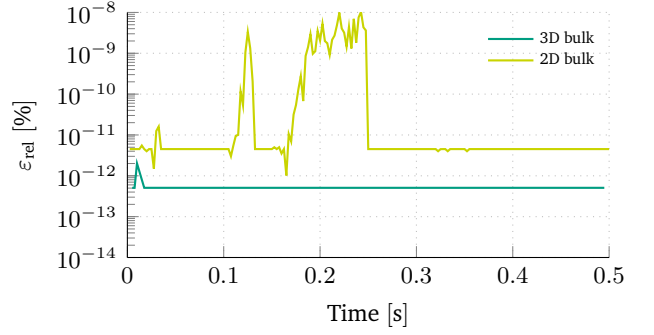
(b) Relative difference of i_s.

(c) DC resistance R_DC.

(d) Relative difference of R_DC.
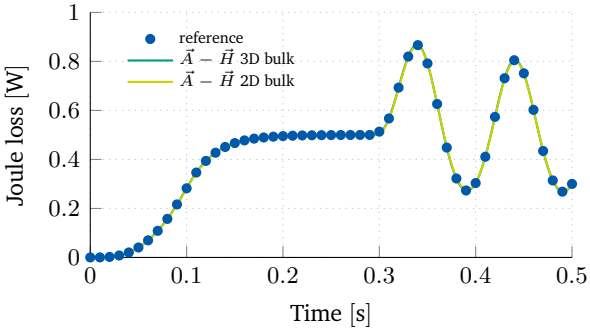
(e) Joule losses P_J.
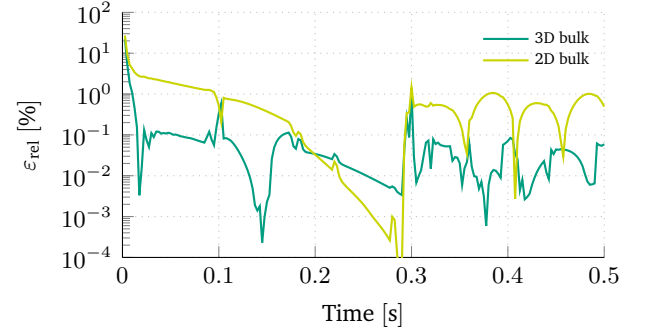
(f) Relative difference of P_J.
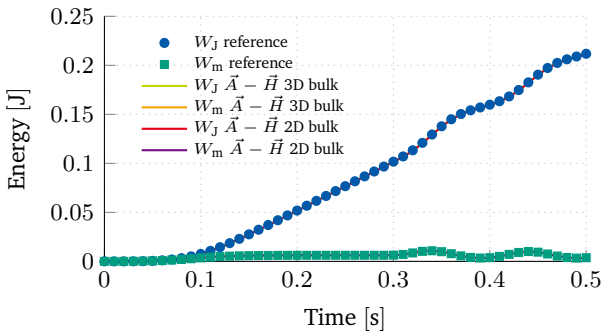
(g) Joule and magnetic energies W_J and W_m.
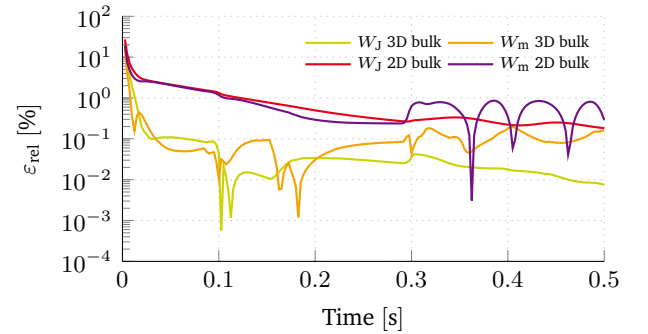
(h) Relative difference of W_J and W_m.

Figure 4.7. Results comparison for the voltage-driven model of a bulk tape in 3D and 2D setting. The reference results are obtained by means of the $\vec{A}$ formulation.
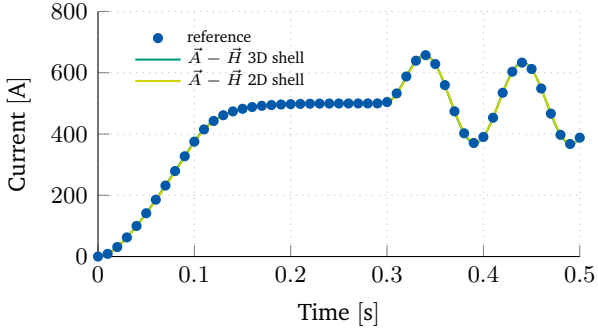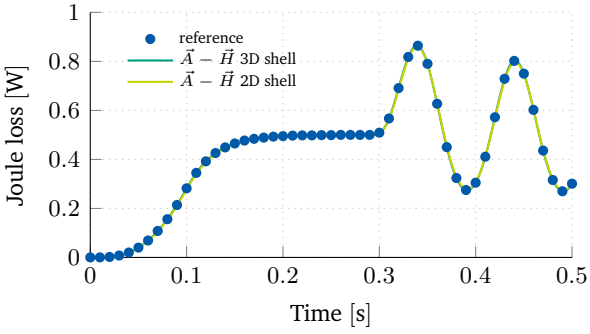
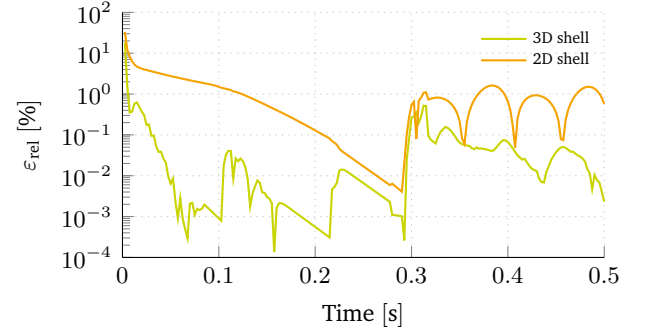*(a) Source current i_s.*
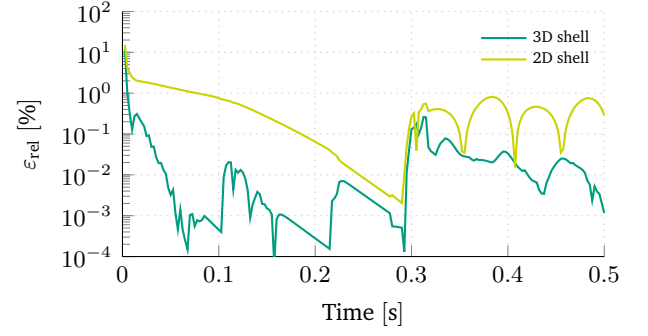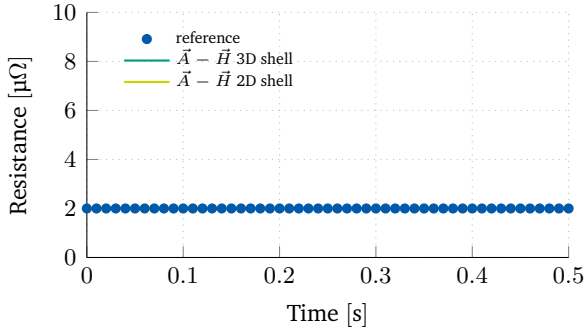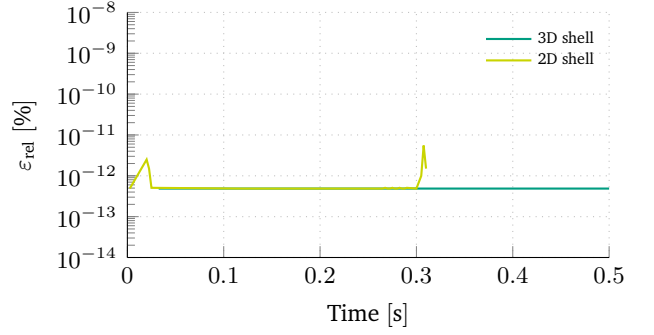
(b) Relative difference of i_s.
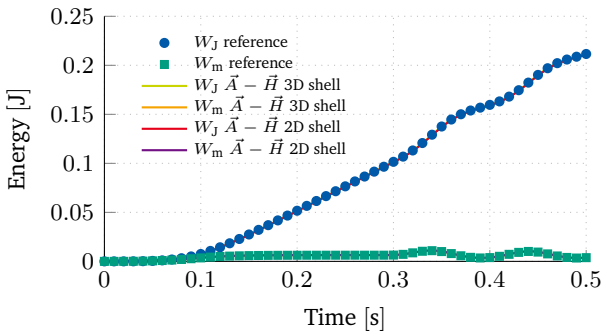

(c) DC resistance R_{DC}.
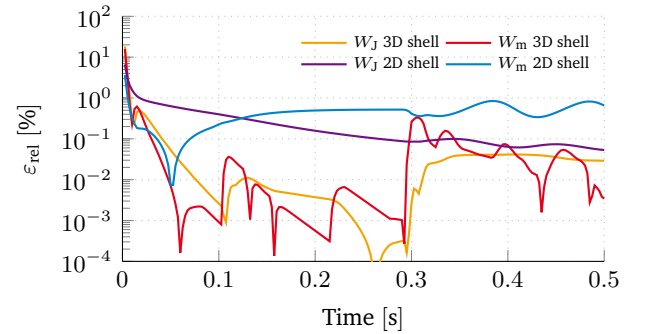

(d) Relative difference of R_{DC}.

(e) Joule losses P_J.

(f) Relative difference of P_J.

(g) Joule and magnetic energies W_J and W_m.

(h) Relative difference of W_J and W_m.

Figure 4.8. Results comparison for the voltage-driven model of a shell tape in 3D and 2D setting. The reference results are obtained by means of the $\vec{A}$ formulation.

to the $\vec{A}$, bulk $\vec{A} - \vec{H}$ and shell $\vec{A} - \vec{H}$ formulations. The first and the second rows give the field solution for the 3D and 2D setting, whereas the last row highlights the cross section of the tape, showing that the 2D field distribution within the tape is neglected by the shell approximation.

The results of the comparison for the bulk tape model are shown in Figure 4.7. The left and right columns show the quantities of interest and the relative differences. The results are in quantitative agreement, showing relative differences which remain below 1% for most of the time steps. The differences tend to be higher at the beginning of the simulations, showing values above 10%. The difference tends to increase whenever the quantities of interest tend to zero, as a consequence of the relative error definition, because for quantities $|x| \to 0$, small absolute errors $|\Delta x|$ can still lead to relevant relative errors. The results of the comparison for the shell tape model are shown in Figure 4.8, with the same layout as for the bulk tape. The results are again in quantitative agreement. Relative differences are found below 1% for most of the time steps, with higher discrepancies in the order of 10% difference at the beginning of the simulations. Overall, results obtained for a normal conducting tape powered via a voltage source with the $\vec{A} - \vec{H}$ formulation are consistent with the $\vec{A}$ formulation.
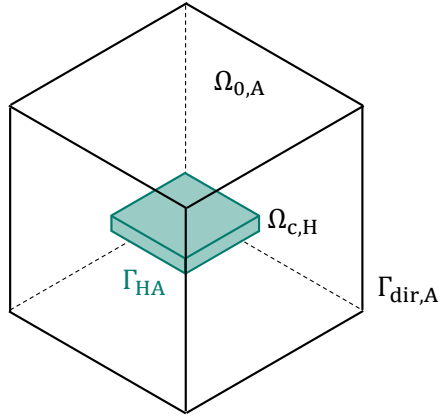
4.2 Superconducting Block

With respect to the previous section, the verification of the implementation of the $\vec{A} - \vec{H}$ field formulation is extended to passive and conducting domains made of superconducting materials. A superconducting block exposed to a time-varying magnetic field is modeled by means of both a bulk and an equivalent stack representation, the latter using the thin-shell approximation. The Joule losses in the block are calculated for the two models, and compared with the solution provided by the monolithic $\vec{H}$ formulation. The problem setting and the simulation setup closely follow the work in [256].

4.2.1 Problem setting

The 3D model is composed of a block made of superconducting material surrounded by air, as shown in Figure 4.9a. The superconducting bulk has a square base of $10\,\mathrm{mm}$ and a thickness of $1\,\mathrm{mm}$. The material parameters related to the superconducting properties of the bulk are chosen as $J_\mathrm{c} = 1 \times 10^8\,\mathrm{A\,m^{-2}}$ and $n = 25$ [256]. The computational domain is decomposed into the conducting region $\Omega_\mathrm{c,H}$ representing the block solved for $\vec{H}$, and the passive region $\Omega_\mathrm{0,A}$ solved for $\vec{A}$. The interface Γ_HA between the two regions corresponds to the outer surface of the block. A second model, shown in Figure 4.9b, is obtained by approximating the bulk geometry of the block by means of a stack of layers implementing the thin-shell approximation. In this way, the geometric thickness of the bulk is neglected, and the domain $\Omega_\mathrm{c,H}$ is replaced by the stack of thin shells $\Gamma_\mathrm{c,H}^r$, with $r = 1, \ldots, N_\mathrm{t}$, each of them representing $1/N_\mathrm{t}$ of the thickness of the block. The value of N_t is set to five, as a compromise between the accuracy of the approximation and the computational cost. The two models do not feature any actively powered domains, therefore distribution functions are not required.

Nonhomogeneous Dirichlet boundary conditions are applied to $\vec{A}$ on the exterior boundary $\Gamma_\mathrm{dir,A}$, imposing the magnetic field $B_\mathrm{s}(t) = B_\mathrm{p} \sin{(2\pi f t)}$ as an external source. Consequently, the source region corresponds for this case to the exterior boundary. Two simulation scenarios are investigated [256]. In the first scenario the magnetic field is applied with parameters $B_\mathrm{p} = 200\,\mathrm{mT}$ and $f = 50\,\mathrm{Hz}$, with an angle of $30°$ with respect to the wide surface of the block. In this way, the currents induced in the superconducting bulk show components
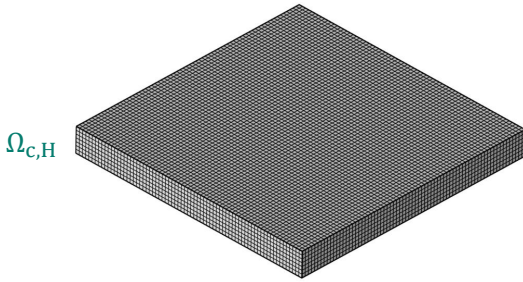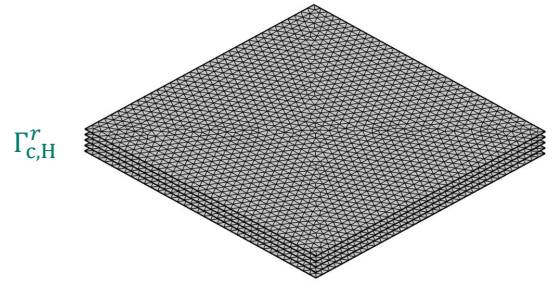
(a) Block, 3D setting.
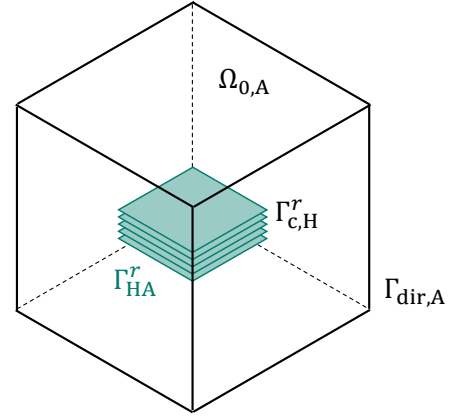
(b) Stack, 3D setting.

Figure 4.9. Models for the superconducting block and stack, in the 3D setting.

(a) Mesh for the bulk representation.

(b) Mesh for the shell representation.

Figure 4.10. Mesh of the superconducting block, for (a) bulk and (b) shell representations.

in all the three dimensions, intrinsically requiring a bulk model. In the second scenario, the magnetic field is applied with parameters $B_{\mathrm{p}} = 100\,\mathrm{mT}$ and $f = 50\,\mathrm{Hz}$, perpendicularly to the wide surface of the block. Here, the induced currents have only in-plane components, therefore the results from block and stack models can be compared.

4.2.2 Simulation setup

The field problem is solved by using the coupled $\vec{A} - \vec{H}$ field formulation for bulk and shell geometries in the 3D setting. The reference solution is obtained for the model with bulk geometry by using the monolithic $\vec{H}$ formulation which is provided by COMSOL. The quantities of interest $q(t)$ are compared as

$$\Delta q(t) = \frac{|q_{\mathrm{H}}(t)| - |q_{\mathrm{AH}}(t)|}{|q_{\mathrm{H}}(t)|}, \tag{4.5}$$

where the subscripts H and AH refer to the two formulations used for computing the field solution, and $\Delta q(t)$ is the relative difference. The quantities of interest are limited for this case to the Joule losses P_{J} occurring

Geometry	Source	Value	f	ε_{rel}	ε_{abs}	Time stepping	Δt_{max}
Block Stack	B_{p}	100 mT-200 mT	50	1×10^{-6}	1×10^{-4}	adaptive BDF-5	$(100f)^{-1}$

Table 4.3. Main solver settings.
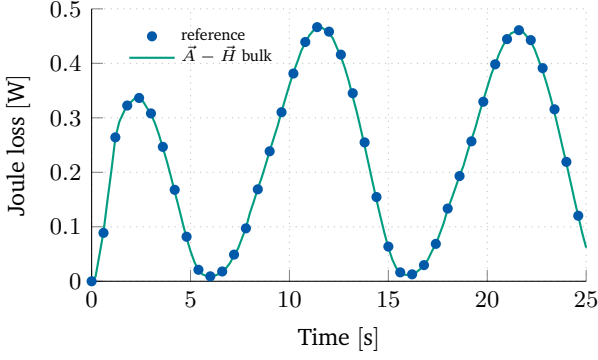
(a) Joule losses P_{J}.
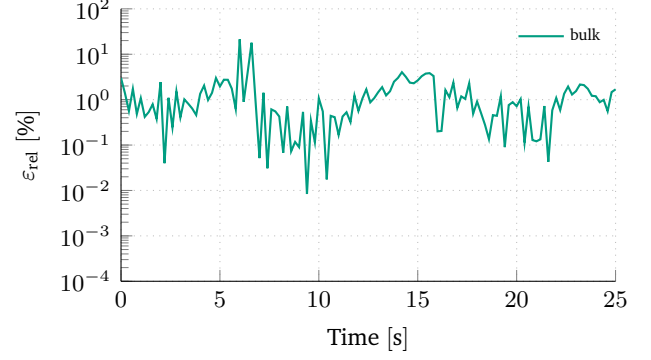
(b) Relative difference of P_{J}.
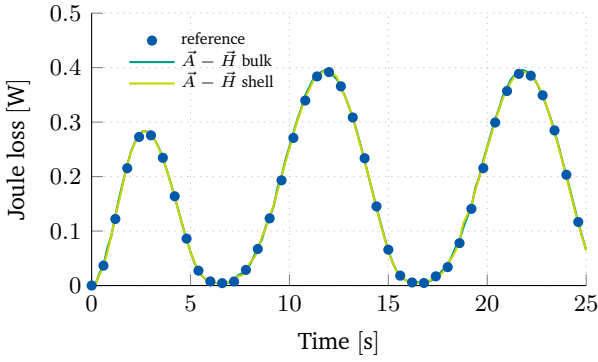
(c) Joule losses P_{J}.
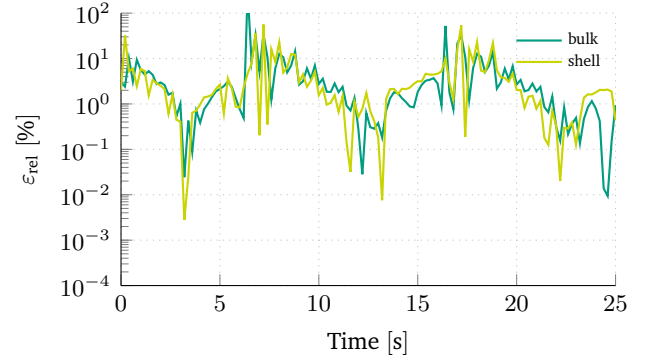
(d) Relative difference of P_{J}.

Figure 4.11. Results comparison for a superconducting block in the bulk and shell representation. The reference results are obtained by means of the $\vec{H}$ formulation.

in the superconducting material, and are given by

$$P_{\text{J,block}} = \int_{\Omega_{\text{c,H}}} \rho \vec{J} \cdot \vec{J} \, \mathrm{d}\Omega \qquad [\text{W}] \qquad \text{Joule power,} \qquad (4.6a)$$

$$P_{\text{J,stack}} = \sum_{r=1}^{N_{\text{t}}} \delta_{\text{t}}^r \int_{\Gamma_{\text{c,H}}^r} \rho \vec{J}^r \cdot \vec{J}^r \, \mathrm{d}\Gamma \qquad [\text{W}] \qquad \text{Joule power,} \qquad (4.6b)$$

where for the thin-shell approximation the volume integral is replaced by a sum of N_{t} surface integrals, one per each shell in the stack.

The mesh used for the 3D block is shown in Figure 4.10. The block is discretized with hexahedra using 45×45 elements on the basis and 7 elements in the thickness (Figure 4.10a). For the thin-shell approximation, each layer in the stack is discretized using a structured grid of 45×45 quadrilateral elements
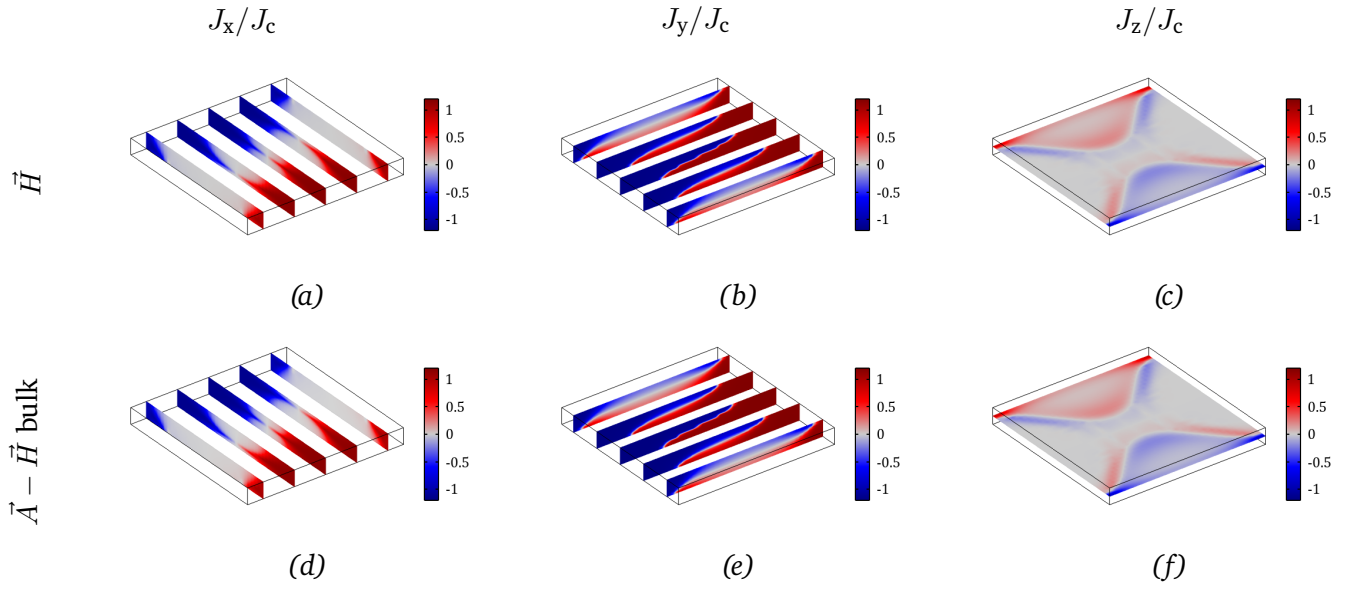
Figure 4.12. Normalized current density in the superconducting block, modeled as a bulk, for a field incidence angle of $30°$ with respect to the wide surface of the block.
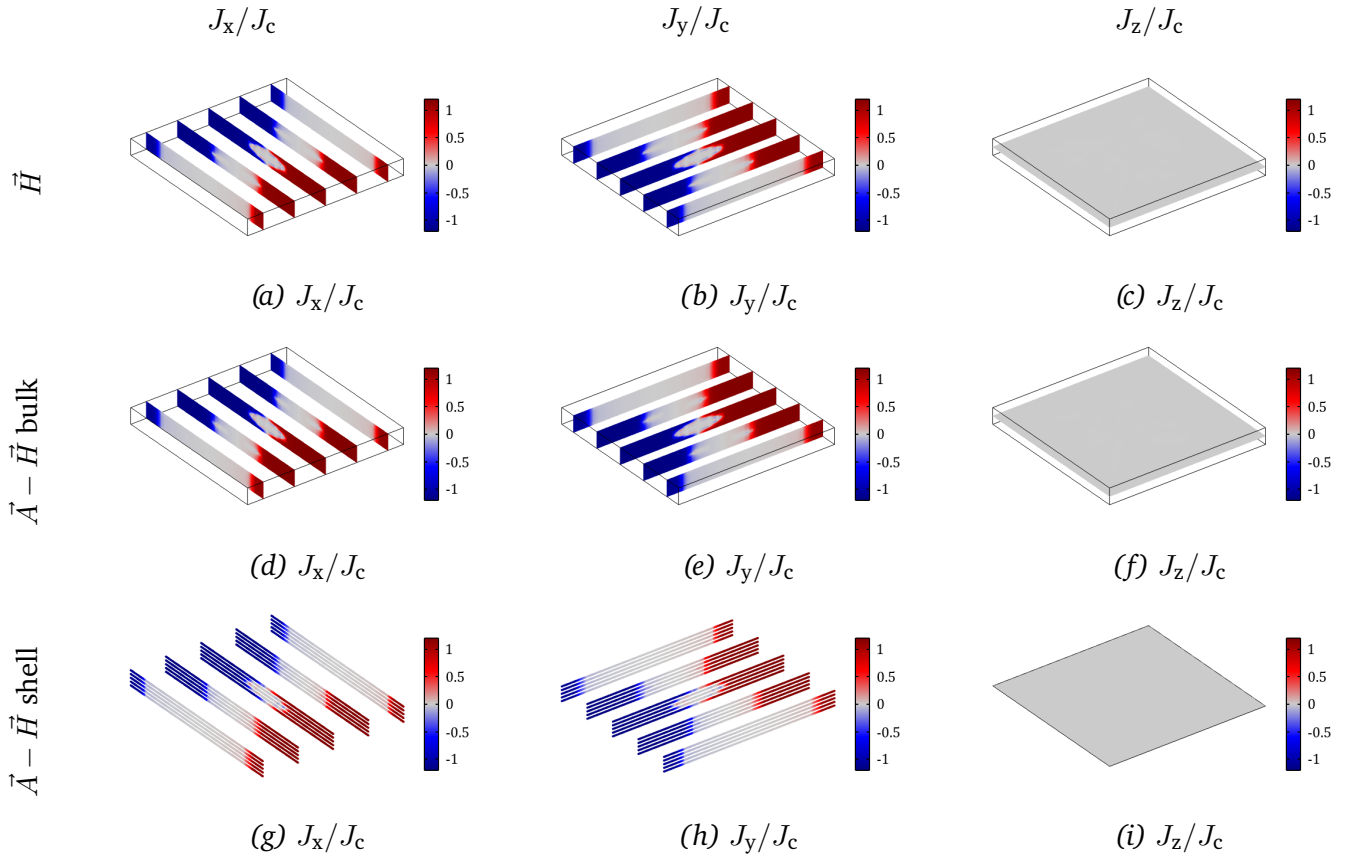

Figure 4.13. Normalized current density in the superconducting block, modeled both as a bulk and a stack of shells, for a field incidence angle of $0°$ with respect to the wide surface of the block.

(Figure 4.10b). The models implementing bulk and stack geometries use a mesh of first-order elements everywhere.

4.2.3 Numerical results

The time stepping scheme is implicit and based on the second-order BDF, using an adaptive time step limited to a maximum size of $\Delta t = (100f)^{-1}$, for both the bulk and shell tape simulations. The most relevant solver-setting parameters adopted in the simulations are given in Table 4.3. Simulations are carried out for two and a half periods of the sinusoidal field source. The results of the comparison for the block and stack models are shown in Figure 4.11. The left and right columns show the Joule losses and the relative differences between the different formulations. The results are in agreement, showing relative differences which are below 1% for most of the time steps. The difference tends to increase whenever the quantities of interest tend to zero. Figure 4.12 shows the three spatial components of the current density distribution in the bulk, normalized by the critical current density and given with respect to a local reference frame (x, y, z) oriented along the superconducting block. Results are shown for the bulk representation in the $\vec{H}$ and $\vec{A} - \vec{H}$ formulations, for the case where the source field has a $30°$ incidence angle. Figure 4.13 shows the same field quantities as Figure 4.12, but for the $\vec{H}$ formulation and the $\vec{A} - \vec{H}$ formulations for bulk and shell geometries, for the case where the source field is perpendicular to the wide surface of the superconducting domain. Overall, the implementation of the $\vec{A} - \vec{H}$ formulation for a superconducting block powered via an external field source delivers results for both bulk and shell representations which are consistent to the $\vec{H}$ formulation.

4.3 Superconducting Tape

This section provides the verification for the implementation of the coupled $\vec{A} - \vec{H}$ field formulation for HTS tapes represented by means of the thin-shell approximation, as described in Section 2.14. The dynamic behavior of a single HTS tape is investigated while exposed to an externally applied field and in self-field. These two cases are chosen since analytical solutions from existing literature are available for the verification of the numerical results. A third case investigates the influence of the thin-shell approximation in the case of normal conducting coating added to the tape, analyzing the result in comparison to a bulk tape model solved for $\vec{H}$, where the layers are explicitly meshed.

4.3.1 Problem setting

The reference model shows translational symmetry, therefore is represented in the 2D setting. It is composed of one superconducting tape represented by the 1D line $\Gamma_{c,H}$ surrounded by air, as shown in Figure 4.1d. The decomposition of the computational domain has already been discussed in Section 4.1.1 for the 2D shell approximation case. The specifications for the superconducting tape are given in Table 4.4. Two scenarios are considered, differing in the source quantity applied to the model. In the first scenario, a zero net current is imposed to the tape, and an external magnetic field $B_s = B_p \sin(2\pi ft)$ is applied in the y-direction, perpendicularly to the tape, by means of nonhomogeneous Dirichlet boundary conditions imposed to $\vec{A}$ on the exterior boundary of $\Omega_{0,A}$. In the second scenario, an external source current $i_s = I_p \sin(2\pi ft)$ is applied to the tape, and homogeneous Dirichlet conditions are applied to $\vec{A}$ on the exterior boundary. In this
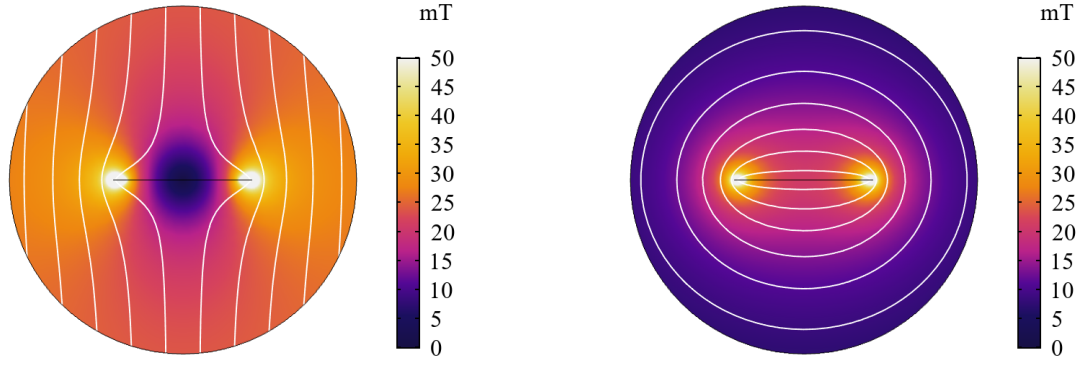
(a) Magnetic field distribution at 1.25 s.   (b) Magnetic field distribution at 1.25 s.

Figure 4.14. Magnetic field produced by a superconducting tape with n-value of 20, powered by (a) an external sinusoidal field of 25 mT and frequency of 1 Hz, and (b) a sinusoidal current of 500 A and frequency of 1 Hz.

Name	Unit	Value	Description
δ_{w}	mm	10	Tape width
δ_{t}	μm	1	Tape thickness
δ_{l}	mm	100	Tape length
J_{c}	kA mm^{-2}	100	Critical current density
I_{c}	kA	1	Current density
n	-	$\{5, 20, 40\}$	Power law index

Table 4.4. Tape specifications.

case, the tape is said to be in self-field. The magnetic field distribution is shown for the two scenarios in Figure 4.14.

4.3.2 Simulation setup

The quantity of interest is given by the specific Joule losses w_{J} occurring in the tape within a sinusoidal cycle, and it is defined as

$$w_{\mathrm{J}} = \frac{1}{\delta_{\mathrm{w}}\delta_{\mathrm{t}}\delta_{\mathrm{l}}} \int\limits_{\tau}^{2\tau} \delta_{\mathrm{t}}\delta_{\mathrm{l}} \int\limits_{\Gamma_{\mathrm{c,H}}} \rho \vec{J} \cdot \vec{J} \, \mathrm{d}\Gamma \, \mathrm{d}t, \tag{4.7}$$

where δ_{w}, δ_{t} and δ_{l} are the width, thickness and length of the tape, and $\tau = 1/f$. In the calculation of w_{J}, the first period of the sinusoidal cycle is discarded since it corresponds to the first magnetization cycle which is not representative of the specific Joule losses occurring in sinusoidal regime. The numerical model of the HTS tape is used over a frequency range of several orders of magnitude. For this reason, the mesh distribution is adapted to the magnitude of the current in the tape. The mesh elements are denser at the tape edges, with their size following an exponential distribution such that the ratio between the biggest and the smallest

Geometry	Source	Value	f	$\varepsilon_{\mathrm{rel}}$	$\varepsilon_{\mathrm{abs}}$	Time stepping	Δt_{max}
Shell	B_{p}	1 mT-10 T	1 mHz-100 Hz	1×10^{-6}	1×10^{-4}	adaptive BDF-5	$(100f)^{-1}$
Shell	I_{p}	10 A-1.2 kA					

Table 4.5. Main solver settings.

(a) Fine mesh.	*(b) Coarse mesh.*

Figure 4.15. Mesh of the HTS tape, represented as a thin shell in the 2D setting. (a) Fine and (b) coarse mesh, for the low- and high-field and current scenarios.

element is 25 (see Figure 4.15a). This allows for resolving the highly-nonlinear current density distribution in the tape. About 500 elements are used for the simulations at low field and current, whereas about 20 elements are used for a saturated tape (see Figure 4.15b), in accordance with the relaxation of the magnetic field within the tape. The model uses a mesh of first-order elements in $\Gamma_{\mathrm{c,H}}$, and second-order elements in $\Omega_{0,\mathrm{A}}$. The maximum time step size is given as $\Delta t = (100f)^{-1}$, where f is the frequency of the source quantity in the model.

4.3.3 Numerical results: external field

In this scenario, a single HTS tape with no supply current is exposed to a time-dependent, sinusoidal field applied perpendicularly to the wide face of the tape. The layout of the simulated scenario is shown in the box of Figure 4.16a. The source term is provided by the magnetic field $B_s = B_p \sin(2\pi f t)$, with $f = 1\,\mathrm{Hz}$. The specific loss per cycle w_{J} is calculated as a function of the peak field B_p, and parametrized for the power-law index values $n = 5$, 20 and 40. The case with $n = \infty$ corresponds to critical state model [176, 177], and it is calculated analytically. In detail, the theory of infinitely thin films with finite width and one dimensional current distribution in a perpendicular field [100, 257, 258] provides an analytical expression for w_{J} as

$$w_{\mathrm{J}} = \delta_{\mathrm{w}} J_{\mathrm{c}} B_{\mathrm{c}} \left(\frac{2}{b_{\mathrm{p}}} \ln(\cosh b_{\mathrm{p}}) - \tanh b_{\mathrm{p}} \right), \tag{4.8}$$

where the normalized magnetic field b_{p} and critical magnetic field B_{c} are given by

$$b_{\mathrm{p}} = \frac{B_{\mathrm{p}}}{B_{\mathrm{c}}}, \qquad \text{and} \qquad B_{\mathrm{c}} = \mu_0 \frac{\delta_{\mathrm{t}} J_{\mathrm{c}}}{\pi}. \tag{4.9}$$

The specific losses w_{J} are shown in Figure 4.16a and 4.16b as a function of B_{p} and f, showing that for increasing n-values of the power-law index, the losses converge to the theoretical solution in (4.8) [257]. Therefore, the numerical results meet the expectations given that the critical state model corresponds to (2.86) where n goes to infinity. For field values $B_{\mathrm{p}} \ll B_c$, the losses follow a quartic scaling law with respect to the magnetic field amplitude. Once the magnetic field exceeds B_{c}, it fully penetrates in the tape, and the distribution of
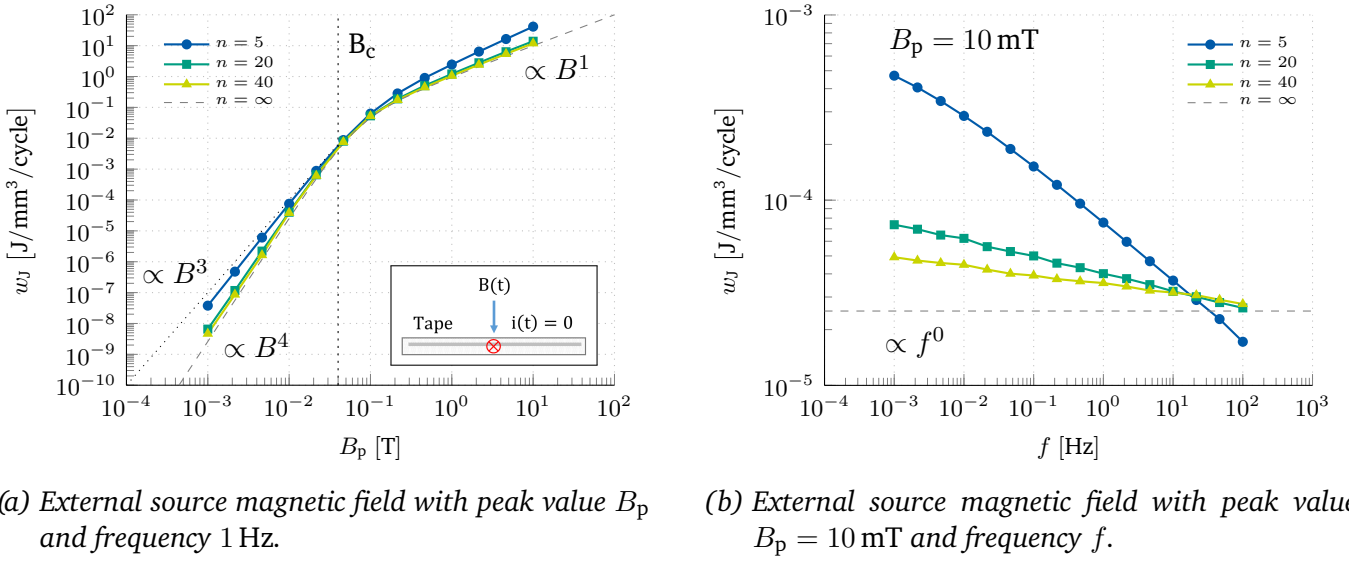
(a) External source magnetic field with peak value B_{p} and frequency $1\,\mathrm{Hz}$.

(b) External source magnetic field with peak value $B_{\mathrm{p}} = 10\,\mathrm{mT}$ and frequency f.

Figure 4.16. *Specific Joule losses per cycle in a single HTS tape of critical current $I_{\mathrm{c}} = 1\mathrm{kA}$. The numerical results are parametrized by $n = 5$, 20, 40, and compared with the analytical solution from literature where $n \to \infty$.*

screening currents relaxes into a homogeneous distribution. For field values $B_{\mathrm{p}} \gg B_c$ the specific losses grow proportionally with the amplitude B_{p}, as the model considers the critical current density to be constant and field-independent. For the sake of completeness, Figure 4.16a shows also a trend line for a cubic scaling law, which is found in models accounting for finite n-values and two dimensional current density distributions in the tape [14, 259, 260].

The specific losses shown in Figure 4.16b are obtained for a peak field of $10\,\mathrm{mT}$. The value for B_p is set below the penetration limit, such that the simulation results are determined by the field-screening behavior of the tape. For high n-values, the frequency dependency in the losses tends to vanish, as expected by the hysteresis-like behavior of screening currents, and w_{J} converges to the theoretical solution in [257] for $n \to \infty$.

4.3.4 Numerical results: self-field

In this scenario, a time-dependent, sinusoidal source current is imposed to a single HTS tape with no externally applied field. The layout of the simulated scenario is shown in the box of Figure 4.17a. The source term is provided by the external current $i_s = I_p \sin\left(2\pi f t\right)$, with $f = 1\,\mathrm{Hz}$. The specific loss per cycle w_{J} is calculated as a function of the peak current I_p, and parametrized for the power-law index $n = 5$, 20 and 40. The case with $n = \infty$ corresponds to the critical state model [176, 177], and is calculated analytically. In detail, the theory of infinitely thin films with finite width and one dimensional current distribution [100, 261] provides an analytical expression for w_{J} as

$$w_{\mathrm{J}} = \frac{\mu_0}{\delta_{\mathrm{w}}\delta_{\mathrm{h}}} I_{\mathrm{c}}^2 \frac{i_{\mathrm{p}}^4}{6\pi}, \tag{4.10}$$
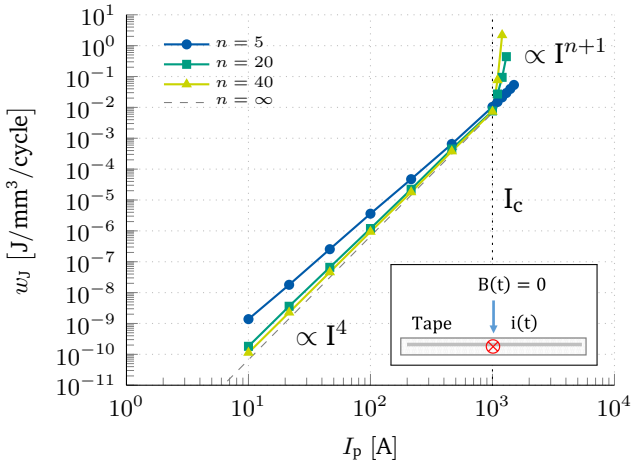
(a) External source current, with peak value I_p and frequency $1\,\mathrm{Hz}$.
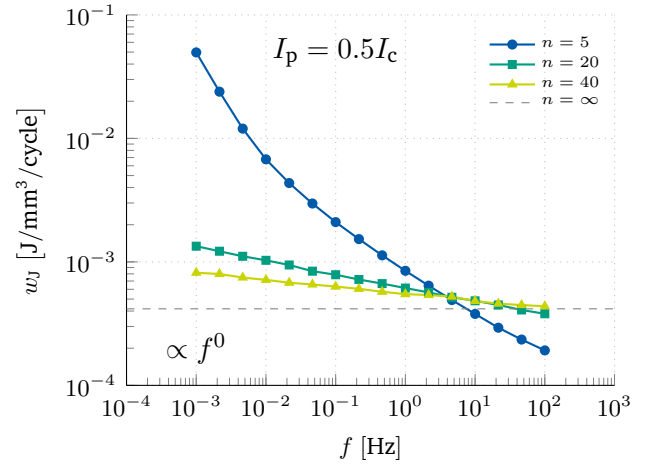
(b) External source current with peak value $I_\mathrm{p} = 0.5I_\mathrm{c}$ and frequency f.

Figure 4.17. Specific Joule losses per cycle in a single HTS tape of critical current $I_\mathrm{c} = 1\mathrm{kA}$. The numerical results are parametrized by $n = 5$, 20, 40, and compared with the analytical solution from literature where $n \to \infty$.

where I_c is the critical current of the tape and i_p is the normalized peak current given by

$$i_\mathrm{p} = \frac{I_\mathrm{p}}{I_\mathrm{c}}. \tag{4.11}$$

The specific losses w_J are shown in Figure 4.17a and 4.17b as a function of I_p and f, showing that for increasing n-values of the power-law index, the losses converge to the theoretical solution in (4.10) [257]. Therefore, the numerical results meet the expectations given that the critical state model corresponds to (2.86) where n goes to infinity. For current values $I_\mathrm{p} \ll I_c$, the losses follow a quartic scaling law with respect to the current amplitude. Once the supply current exceeds I_c, the current density distribution relaxes into a homogeneous distribution in the cross section of the tape. For current values $I_\mathrm{p} \gg I_c$, the specific losses grow proportionally to I^{n+1}, in accordance with the power-law behavior in (2.86).

The specific losses shown in Figure 4.17b are obtained for a current of $I_\mathrm{p} = 0.5I_\mathrm{c}$. The value for I_p is set below the penetration limit, such that the simulation results are determined by the field-screening behavior of the tape. For high n-values, the frequency dependency in the losses tends to vanish, as expected by the hysteresis-like behavior of screening currents, and w_J converges to the theoretical solution in [257] for $n \to \infty$.

### 4.3.5 Numerical results: thin-shell approximation

The $\vec{A}$-$\vec{H}$ formulation is applied in combination with the thin-shell approximation to an individual HTS tape in a transverse-field 2D configuration, as shown in Figure 4.1d. The model accounts for the current sharing by including the normal conducting part of the tape as discussed in Section 3.7. The reference results are obtained solving the field problem for the $\vec{H}$ formulation for bulk tapes, and compared with the results from the $\vec{A} - \vec{H}$ formulation for thin-shell tapes. The most relevant solver-setting parameters adopted in the simulations are given in Table 4.6. The superconducting layer has the same dimensions as in Table 4.4, a power-law

Geometry	Source	Value	f	ε_{rel}	ε_{abs}	Time stepping	Δt_{max}
Bulk Shell	I_{p}	$0.25I_{\text{c}}$-$2I_{\text{c}}$	1 Hz-1 kHz	1×10^{-6}	1×10^{-4}	adaptive BDF-5	$(100f)^{-1}$

Table 4.6. Main solver settings.
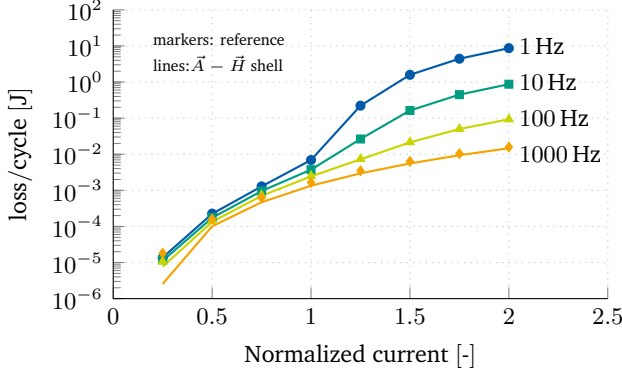
(a) Joule losses per cycle W_{J}.
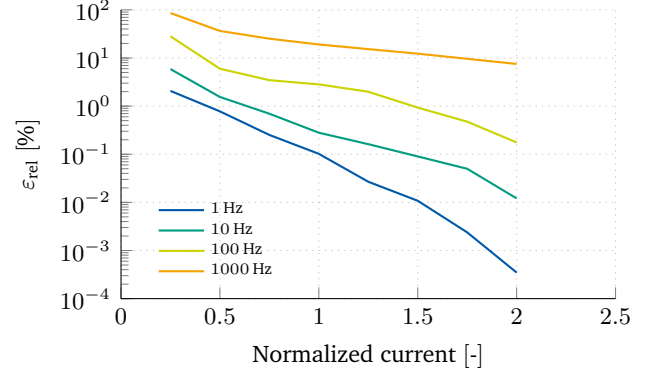
(b) Relative difference of W_{J}.

Figure 4.18. Joule losses per cycle in a single tape powered with a sinusoidal current, as a function of the current normalized by the critical current. The losses are parametrized by the frequency of the source current, and are given at 1, 10, 100, 1000 Hz.
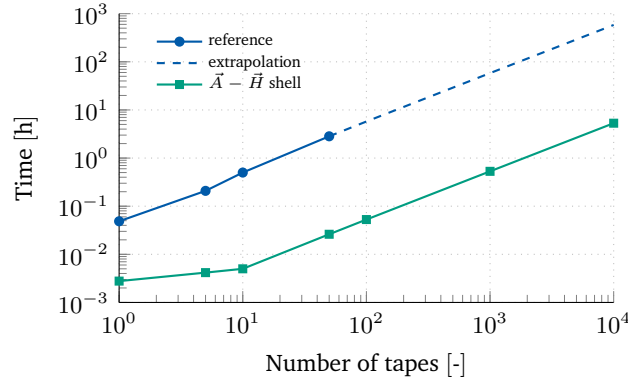

Figure 4.19. Computational time in hours, as function of the number of tapes included in the model. The reference model features 2D domains for the superconducting tapes, whereas the $\vec{A} - \vec{H}$ formulation relies on the thin-shell approximation.

index $n = 20$ and a critical current $I_{\text{c}} = 200\,\text{A}$. The normal conducting layer has a thickness $\delta_{\text{tnc}} = 100\,\mu\text{m}$ and a resistivity of $0.1\,\text{n}\Omega\,\text{m}$. The Joule losses are compared against the reference model, which used explicit 2D domains for the superconducting tapes. The tape is powered by a sinusoidal current $i_{\text{s}}(t) = I_0\sin(2\pi f t)$. Currents with frequencies 1, 10, 100, 1000 Hz are applied as source. The current amplitude I_0 ranges between $0.25I_{\text{crit}}$ and $2I_{\text{crit}}$, where $I_{\text{crit}} = 200$ A is the critical current of the tape. By increasing the frequency and the magnitude of the applied current, it is possible to quantify the approximations introduced by the shell geometry and the equivalent surface resistivity, respectively.
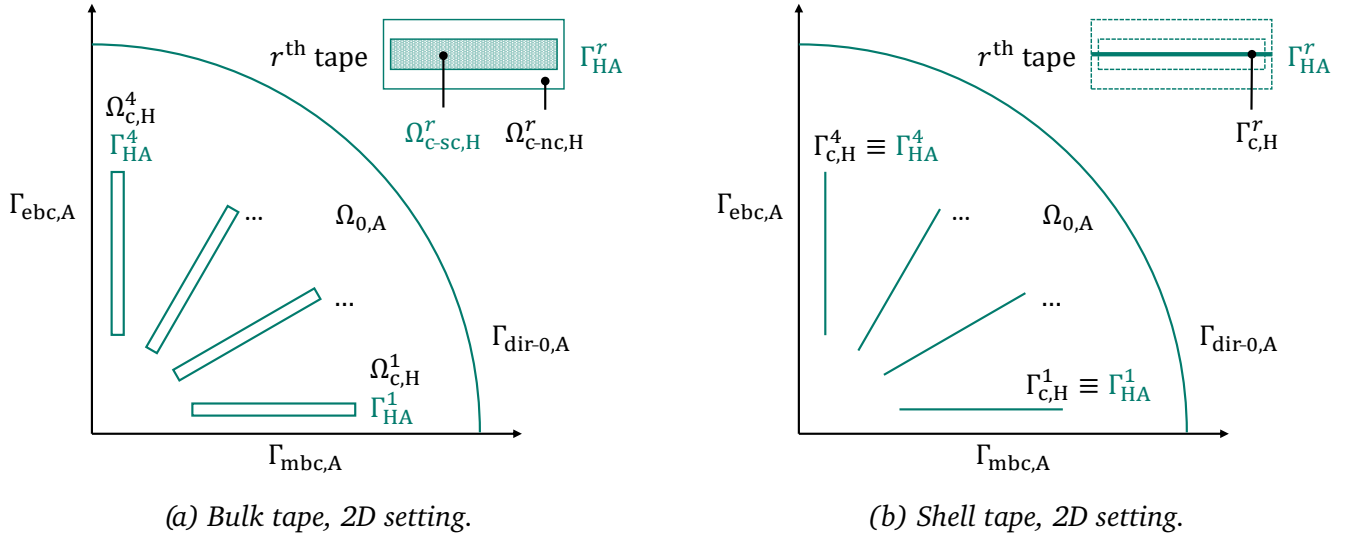
(a) *Bulk tape, 2D setting.* $\qquad$ (b) *Shell tape, 2D setting.*

Figure 4.20. Sketch of the superconducting coil model.

The time stepping scheme is implicit and based on the second-order BDF, using an adaptive time step limited to a maximum size of $\Delta t = (100 f)^{-1}$, for both the bulk and shell tape simulations. The Joule losses per cycle are reported in Fig. 4.18. For sub-critical currents ($I < I_c$), the difference of the curves decreases but does not vanish. The difference is due to a weak frequency dependency in the losses per cycle (see for example [262]). For over-critical currents ($I > I_c$), the losses are dominated by the contribution from the normal conducting part of the tape. This is reflected by the substantial frequency dependency in the curves. For currents above I_c and frequencies up to $100\,\mathrm{Hz}$ the relative error is below $5\,\%$

The gain on the computational time of the model due to the thin-shell approximation is shown in Fig. 4.19. In detail, the same equations have been solved for models featuring an increasing number of tapes, stacked on each other, for both the $\vec{H}$ and the $\vec{A}$-$\vec{H}$ formulations. The performance improvement achieved with the thin-shell approximation is about two orders of magnitude. For the most computationally-intensive model containing ten thousand tapes implementing the thin-shell approximation, the computational time was eight hours.

4.4 Superconducting Coil

This section provides the verification for the implementation of the coupled $\vec{A} - \vec{H}$ field formulation in case the tapes are electrically connected, composing a coil in the 2D setting. The tapes are composed of a superconducting layer coated with normal conducting material, and are represented as bulk and thin-shell conductors, in two distinct models. The electrical connections of the tapes implement the series, parallel and mixed connection schemes.

4.4.1 Problem setting

The reference model in this section shows translational symmetry and includes a simple coil surrounded by air, as shown in Figure 4.20a. The model exploits a four-quadrants symmetry and contains a coil of N_t HTS

tapes, with $N_t = 4$, with each tape made of a thin superconducting layer coated with a normal conducting material. The computational domain Ω is split into the conducting regions $\Omega^r_{c,H}$ with $k = 1, \cdots, N_t$ and solved for $\vec{H}$, and the passive region $\Omega_{0,A}$ solved for $\vec{A}$. The conducting region is further subdivided into the superconducting and normal conducting parts $\Omega^r_{c\text{-sc},H}$ and $\Omega^r_{c\text{-nc},H}$ referring to the superconducting layer and the coating of the tape.

The reference model is then simplified into a shell by neglecting the thickness of the tape, as shown in Figure 4.20b where $\Omega^r_{c,H}$ collapses into the surface $\Gamma^r_{c,H}$. As the tape is made of a composite material, the equivalent resistivity is obtained by means of the homogenization method detailed in Section 3.7. The relevant geometric and material properties are given in Table 4.7.

The tapes can be arranged following different connection schemes, namely the series, parallel and mixed connection schemes known in literature as *no coupling*, *all coupling* and *end coupling* schemes [263]. The different schemes are obtained by appending dedicated sets of algebraic constraints to the formulation of the field problem. The constraints are applied by introducing the coil voltage and current sources $v_{s,coil}$ and $i_{s,coil}$, reading for the different connection schemes

$$\text{series connection} \begin{cases} v_{s,coil} &= \sum_{r=1}^{N_t} v_s^r \\ i_{s,coil} &= i_s^r \qquad \text{with } i = 1, \cdots, N_t \end{cases} \tag{4.12}$$

$$\text{parallel connection} \begin{cases} v_{s,coil} &= v_s^r \qquad \text{with } i = 1, \cdots, N_t \\ i_{s,coil} &= \sum_{r=1}^{N_t} i_s^r \end{cases} \tag{4.13}$$

$$\text{mixed connection} \begin{cases} v_{s,coil} &= \sum_{r=1}^{2} v_s^r = \sum_{i=3}^{4} v_s^r \\ i_{s,coil} &= \sum_{r=1}^{2} i_s^{2r-1} = \sum_{r=1}^{2} i_s^{2r} \\ i_s^1 &= i_s^2 \\ i_s^3 &= i_s^4 \end{cases} \tag{4.14}$$

The voltage and current constraints in (4.12), (4.13) and (4.14) are scalable to arbitrary number of connections and tapes, and can be added to models in a programmatic way.

Homogeneous Dirichlet boundary conditions are imposed to $\vec{A}$ on the exterior boundary of $\Gamma_{dir\text{-}0,A}$. The models are powered using both a voltage and a current source derived from the general source signal $y_s(t)$ shown in Figure 4.2. The coil voltage source $v_{s,coil}$ is parametrized with $Y_{dc} = 10\,\text{mV}$, $Y_{ac} = 5\,\text{mV}$, and $f = 10\,\text{Hz}$, whereas $i_{s,coil}$ is parametrized with $Y_{dc} = 100\,\text{A}$, $Y_{ac} = 50\,\text{A}$, and $f = 10\,\text{Hz}$. The comparison has been carried out for all the connection schemes; here the focus is given to the mixed connection case since it contains features from both the series and parallel connection schemes.

4.4.2 Simulation setup

The field problem is solved by using the $\vec{A} - \vec{H}$ coupled field formulation, for both the bulk and the shell models and the three connection schemes detailed in (4.12)-(4.14). The reference solutions are obtained by using the monolithic $\vec{H}$ formulation which is provided by COMSOL. The quantities of interest are extracted from each of the simulations and then compared as in (4.5). The quantities of interest previously defined in (4.3) are further expanded, with the aim of separating the calculation of the Joule loss contributions $P_{J_{sc}}$ and $P_{J_{nc}}$ from the superconducting and normal conducting parts of the tapes. The losses in terms of power

Parameter	Unit	Value	Description
δ_{w}	mm	10	Tape width
δ_{t}	μm	500	Tape thickness
δ_{z}	m	10	Tape length
$\delta_{\text{w}_{\text{nc}}}$	mm	10	Normal conductor width
$\delta_{\text{t}_{\text{nc}}}$	μm	499	Normal conductor thickness
$\delta_{\text{w}_{\text{sc}}}$	mm	9.8	Superconductor width
$\delta_{\text{t}_{\text{sc}}}$	μm	1	Superconductor thickness
ρ_{nc}	nΩ m	10	Normal conductor resistivity
I_{c}	A	500	Critical current
n	–	20	Power-law index

Table 4.7. Tape specifications.

and energy are given for the coil made of bulk tapes as

$$P_{\text{J}_{\text{sc}}} = \sum_{r=1}^{N_{\text{t}}} \int_{\Omega_{\text{c-sc,H}}^r} \rho \vec{J}^r \cdot \vec{J}^r \, \mathrm{d}\Omega \qquad \text{[W]} \qquad \text{Superconducting Joule power,} \tag{4.15a}$$

$$P_{\text{J}_{\text{nc}}} = \sum_{r=1}^{N_{\text{t}}} \int_{\Omega_{\text{c-nc,H}}^r} \rho \vec{J}^r \cdot \vec{J}^r \, \mathrm{d}\Omega \qquad \text{[W]} \qquad \text{Normal conducting Joule power,} \tag{4.15b}$$

$$W_{\text{J}_{\text{sc}}} = \int_0^t P_{\text{J}_{\text{sc}}} \, \mathrm{d}t \qquad \text{[J]} \qquad \text{Superconducting Joule energy,} \tag{4.15c}$$

$$W_{\text{J}_{\text{sc}}} = \int_0^t P_{\text{J}_{\text{nc}}} \, \mathrm{d}t \qquad \text{[J]} \qquad \text{Normal conducting Joule energy.} \tag{4.15d}$$

In the case where the coil is made of shell tapes, the power losses are given as

$$P_{\text{J}_{\text{sc}}} = \frac{1}{\delta_{\text{t}}} \sum_{r=1}^{N_{\text{t}}} \int_{\Gamma_{\text{c,H}}^r} \lambda^r \rho_{\text{eq}}^r \vec{K}^r \cdot \vec{K}^r \, \mathrm{d}\Gamma \qquad \text{[W]} \qquad \text{Superconducting Joule power,} \tag{4.16a}$$

$$P_{\text{J}_{\text{nc}}} = \frac{1}{\delta_{\text{t}}} \sum_{r=1}^{N_{\text{t}}} \int_{\Gamma_{\text{c,H}}^r} (1 - \lambda^r) \rho_{\text{eq}} \vec{K}^r \cdot \vec{K}^r \, \mathrm{d}\Gamma \qquad \text{[W]} \qquad \text{Normal conducting Joule power,} \tag{4.16b}$$

whereas the energy losses follow the same definition given for the bulk tapes in (4.15).

The mesh used for the 2D coil is shown in Figure 4.21, for the (a) bulk and (b) shell representation. The cross section of the tape in the 2D setting is discretized by a structural grid of quadrilateral elements counting 15 elements in the width, and 1 and 4 elements in the thickness of the superconducting and normal conducting layers. The cross section of the air is discretized with triangular elements. For the shell approximation, the structural grid is replaced with line elements evenly distributed along the tape width. The models with 2D bulk and shell tapes use a mesh of first-order elements in $\Omega_{\text{c,H}}$ and $\Gamma_{\text{c,H}}$, and second-order elements in $\Omega_{\text{0,A}}$.

4.4.3 Comparison of results

The results for the model implementing the $\vec{H}$ formulation are compared with the $\vec{A} - \vec{H}$ formulation, for the bulk and shell representation for the tapes. Two cases are detailed, assuming end connection schemes
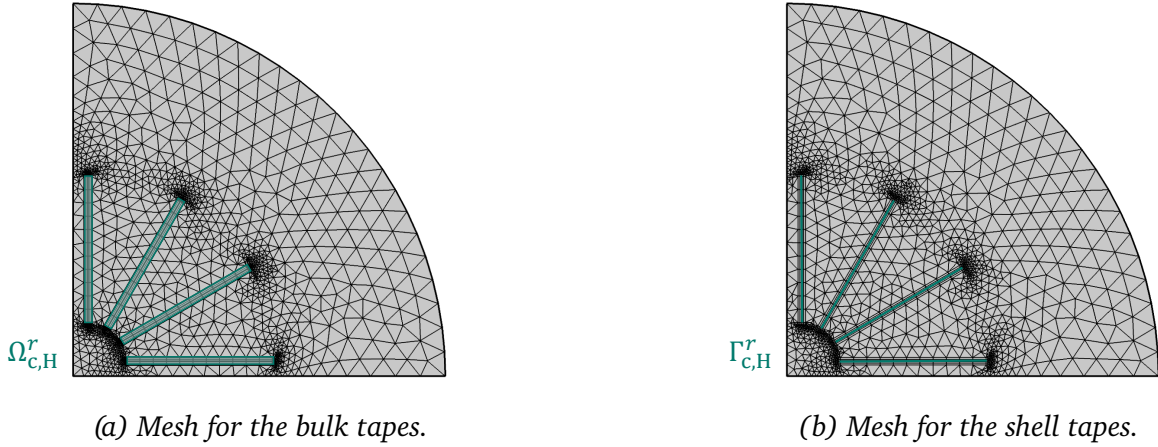
(a) Mesh for the bulk tapes.

(b) Mesh for the shell tapes.

Figure 4.21. Mesh of the HTS coil in the 2D setting, shown for the models with (a) bulk and (b) shell tapes.

Geometry	Source	y_{dc}	y_{ac}	f	ε_{rel}	ε_{abs}	Time stepping	Δt_{max}
Bulk	$v_{s,coil}$	10 mV	5 mV	10	1×10^{-6}	1×10^{-4}	adaptive BDF-5	1 ms
Shell	$v_{s,coil}$							
Bulk	$i_{s,coil}$	100 A	50 A	10	1×10^{-6}	1×10^{-4}	adaptive BDF-5	1 ms
Shell	$i_{s,coil}$							

Table 4.8. Main solver settings.

powered by means of voltage and current sources. All the connection schemes in (4.12)-(4.14) have been tested, but the results are particular cases of the end-connection scheme, and are omitted. Still, Figure 4.22 shows the magnetic flux density obtained for the three connection schemes with the $\vec{H}$ formulation and the $\vec{A} - \vec{H}$ formulation for bulk and shell tape models. Qualitative agreement is obtained for all the cases. The time stepping scheme is implicit and based on the second-order BDF, using an adaptive time step limited to a maximum size of $\Delta t = (100f)^{-1}$, for both the bulk and shell tape simulations. The most relevant solver-setting parameters adopted in the simulations are given in Table 4.8.

4.4.4 Voltage driven scenario

The results of the comparison for the voltage driven scenario are shown in Figure 4.23. The left and right columns show the quantities of interest and the relative errors. The results are in quantitative agreement, showing relative errors which are below 1% for most of the time steps, except for the Joule power losses which show differences above 1% at the beginning of the simulations. This is due to the relative difference criterion which is more sensitive to numerical errors for quantities which tend to zero. The differences are reduced as the current is increased to values which are more relevant for practical applications. The shell model provides a relative difference which tends to be higher than for the bulk model. These differences are in the range of 1% to 2% for the Joule power loss contribution in the normal conducting part of the coil. This discrepancy is expected, and it is explained by the fact that the shell model neglects the current dynamics due to the skin effect, as discussed in Section 4.1.4.
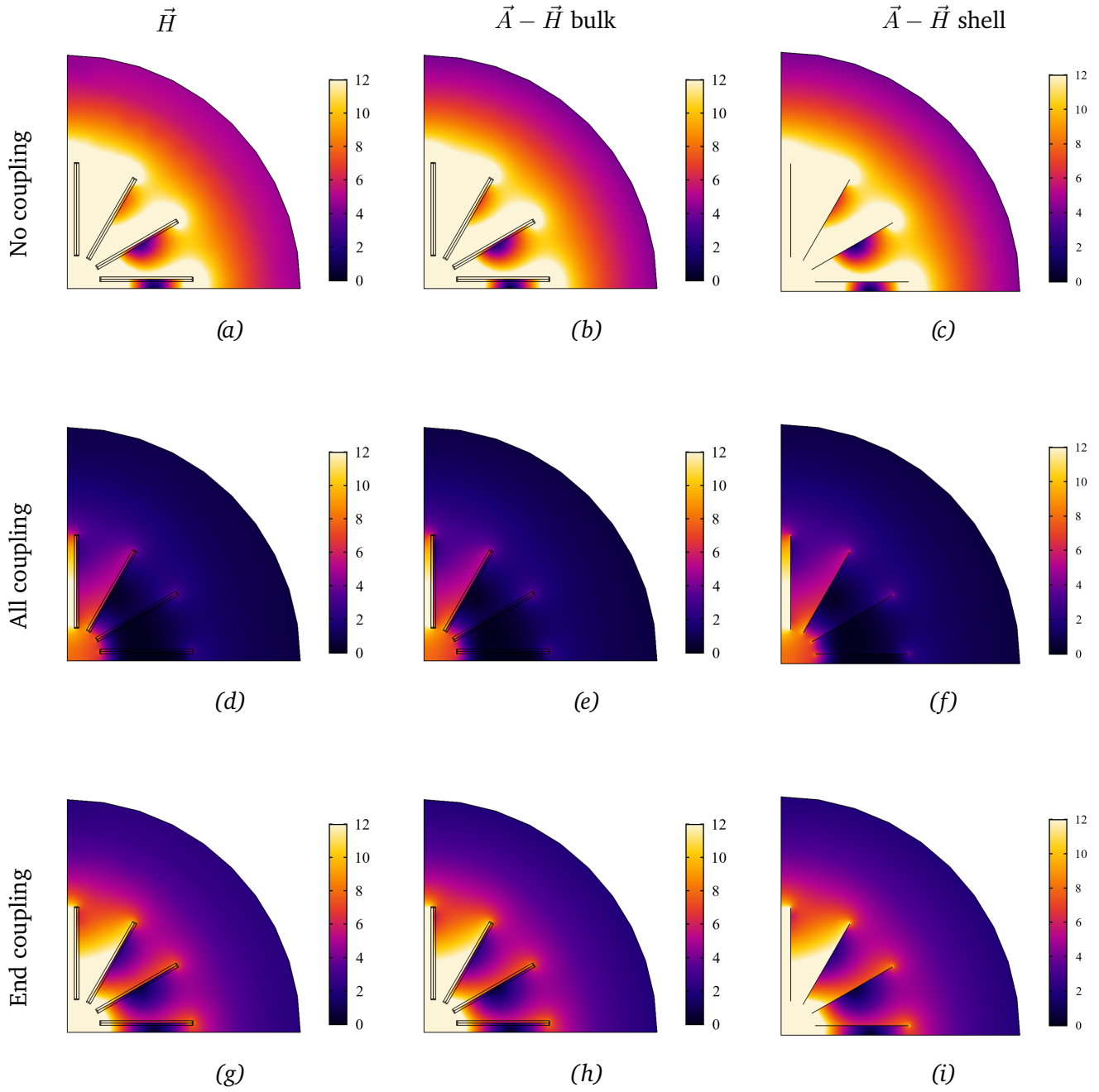
Figure 4.22. Comparison of the numerical solutions for the magnetic flux density at $t = 0.425$ s, obtained with the $\vec{H}$ formulation (first column), and the $\vec{A} - \vec{H}$ formulation with both bulk (second column) and shell tapes (third column). Simulations are done for current driven models. The three rows in figure refer to no-coupling, full-coupling and end-coupling connection schemes for the superconducting coil.
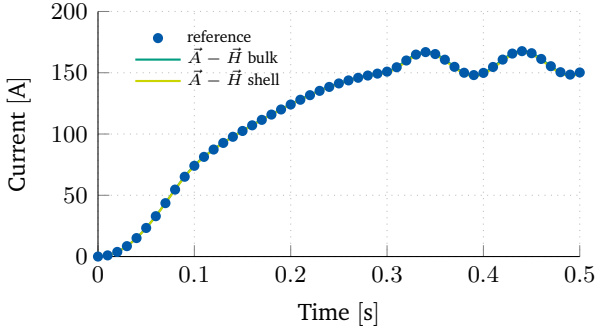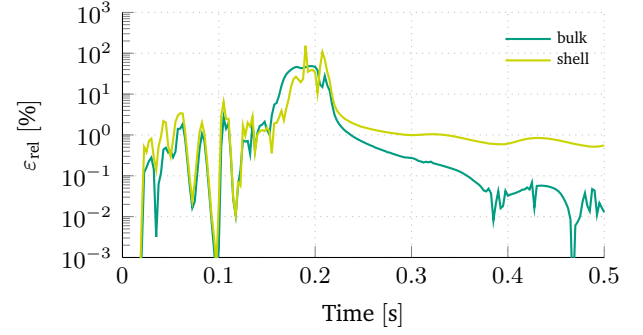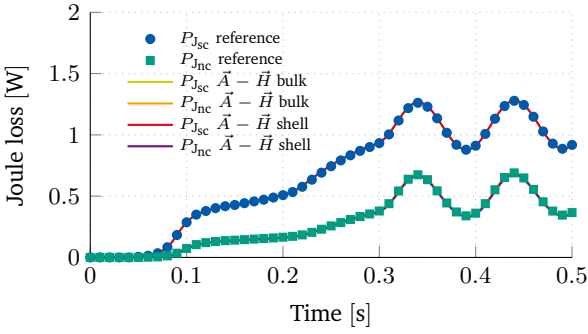
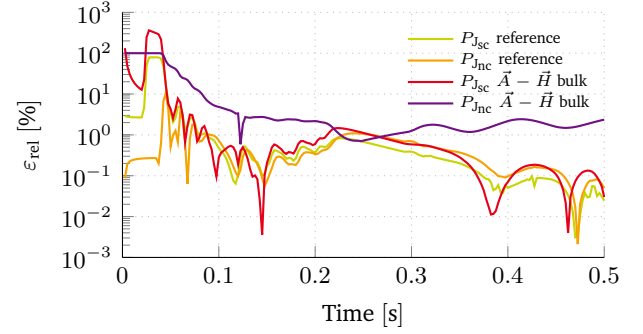(a) Current i_s.
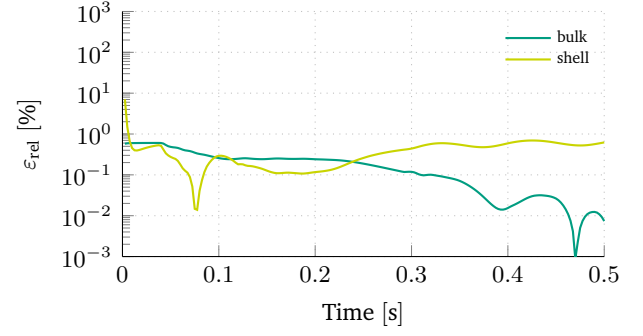
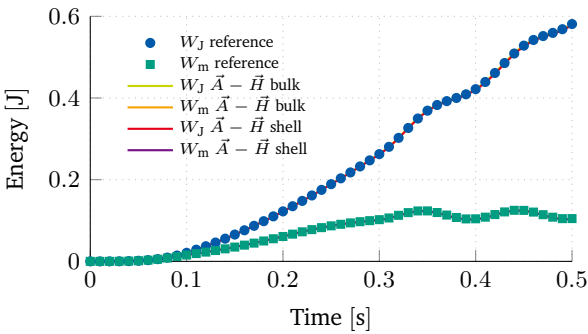(b) Relative difference of i_s.
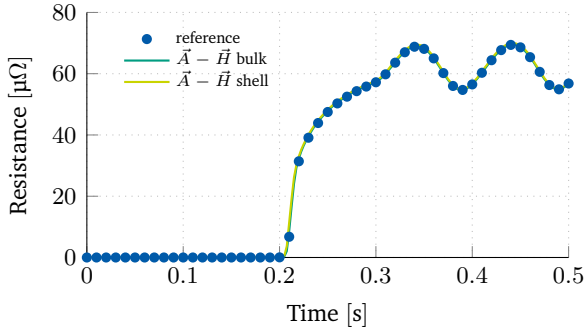
(c) DC resistance R_{DC}.

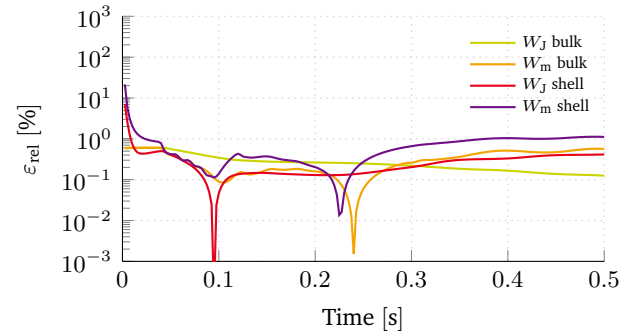(d) Relative difference of R_{DC}.

(e) Joule losses P_J.
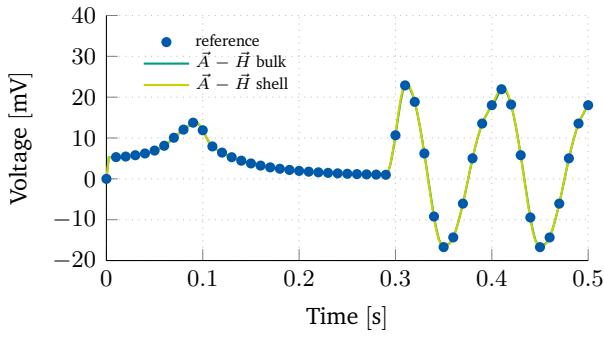
(f) Relative difference of P_J.

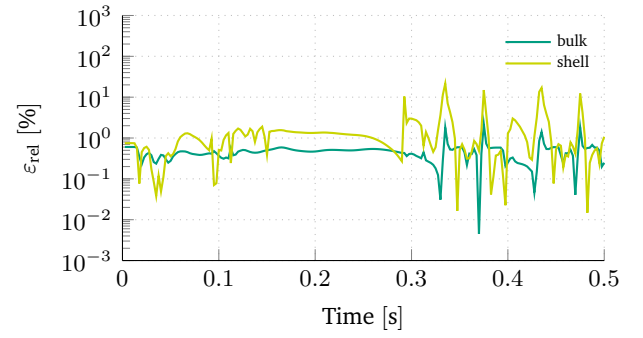(g) Joule and magnetic energies W_J and W_m.
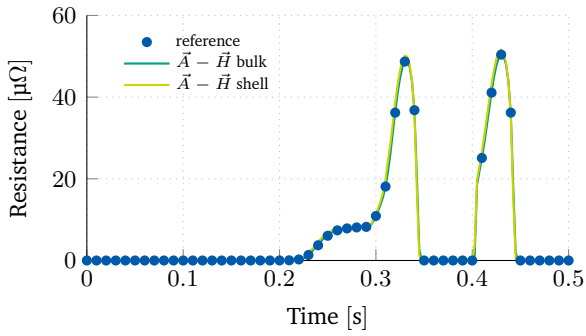
(h) Relative difference of W_J and W_m.

Figure 4.23. Results comparison for a coil implementing the end-connection scheme, powered using a voltage source. The reference results are obtained by means of the $\vec{H}$ formulation.

(a) Voltage v_s.

(b) Relative difference of v_s.

(c) DC resistance R_DC.
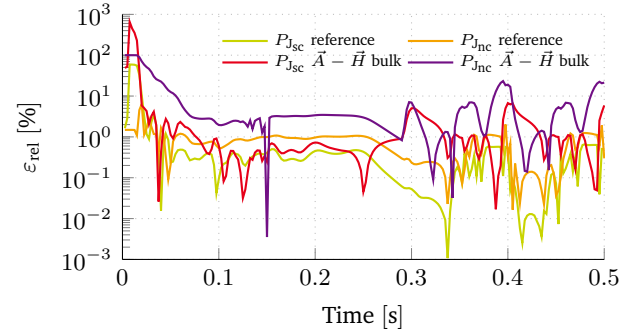
(d) Relative difference of R_DC.

(e) Joule losses P_J.

(f) Relative difference of P_J.
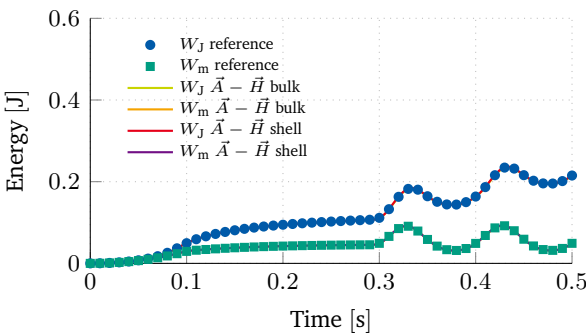
(g) Joule and magnetic energies W_J and W_m.
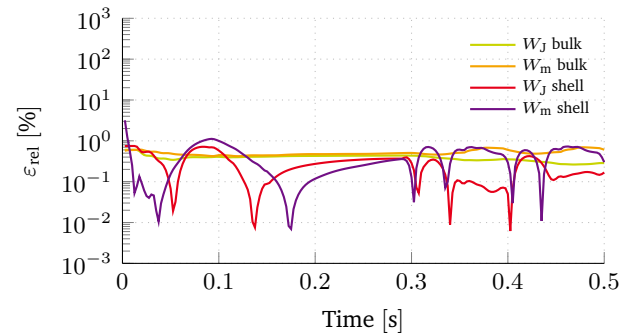
(h) Relative difference of W_J and W_m.

Figure 4.24. Results comparison for a coil implementing the end-connection scheme, powered using a current source. The reference results are obtained by means of the $\vec{H}$ formulation.
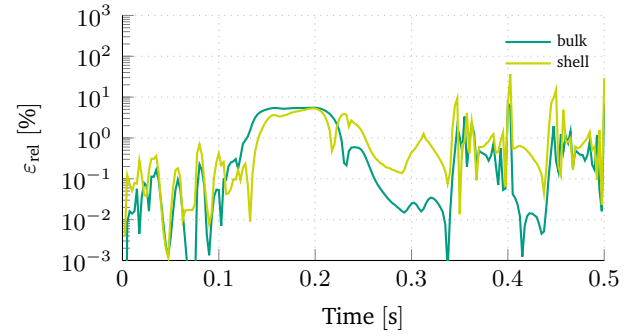
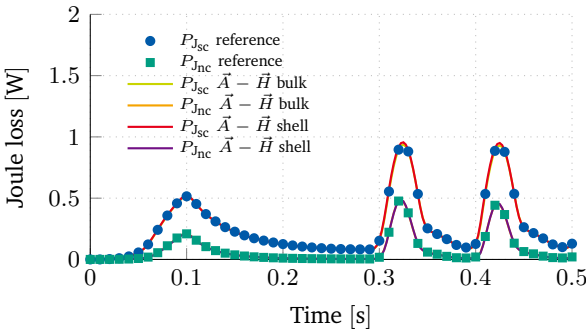### 4.4.5 Current driven scenario

The results of the comparison for the current driven scenario are shown in Figure 4.24. The left and right columns show the quantities of interest and the relative errors. The results are in quantitative agreement, showing relative errors which are below 1% for most of the time steps. It is possible to observe spikes in the relative differences of the voltage and resistance signals. The spikes occur for the time steps in which the quantities of interest tend to zero, and they are higher for the shell-tape model. This discrepancy is again justified with the behavior of the relative difference criterion. Similarly to the voltage driven scenario, the Joule power loss shows differences well above 1% at the beginning of the simulations. Again, the Joule power loss contribution in the normal conducting part of the coil shows a difference of 1-2% for the model with shell tapes. Overall the voltage and current models implementing the $\vec{A} - \vec{H}$ formulation are consistent with the $\vec{H}$ formulation.

4.5 Cosimulation of a Superconducting Solenoid

The model discussed in this section implements the magnetothermal formulation in (2.100)-(2.105) for bulk tapes, and is powered by an external circuit via the field-circuit coupling interface derived in (3.12). The STEAM cosimulation framework introduced in Section 3.4.2 is adopted for a field-circuit coupled simulation of an HTS solenoid, via the WR method. At the same time, the proposed model is sufficiently simple that a monolithic solution is also achieved, and used for comparison. Therefore, the purpose of the section is two-fold: 1. showing the implementation of the thermal part of the coupled $\vec{A} - \vec{H}$ formulation, and 2. verifying the field-circuit coupling interface for a simplified circuit example. Generally speaking, for such a simplified problem the complexity associated to the cosimulation approach may not be justified. However, this approach allows to tackle full-scale applications involving several field models implemented with different tools and complex circuits containing nonlinear elements (e.g. [116, 227]), which would be extremely difficult to be solved with high resolution in a monolithic simulation.

4.5.1 Problem setting

The solenoid is shown in Figure 4.25a and is composed, from the central axis to the outside, by a cylindrical core made of pure iron (Fe $> 99.8\%$), a nonconducting holder made of polymide which provides mechanical support to the superconducting coil, and $N_{\mathrm{hs}} = 2$ stainless steel strips. For the sake of clarity, parts of the insulating material have been removed from Figure 4.25a, such that the coil and the strips are visible. The coil is made of $N_{\mathrm{t}} = 30$ turns of an individually insulated HTS tape. The principal geometric parameters of the model and details of the superconducting tape are given in Table 4.9. Concerning the materials used in the model, the magnetothermal properties are taken for copper and polymide from [264], for Hastelloy from [265] and for silver from [266]. The nonlinear iron magnetization curve is taken from [267]. The relevant material parameters are also given in Table 4.9.

The strips work as quench heaters [3, 46], delivering heat to the coil via thermal conduction, heating up the superconducting material. The strips are powered only in case a quench is detected, for the purpose of increasing the volume of the normal conducting region, reducing the density of the energy dissipation and ultimately, limiting the peak temperature reached in the coil.
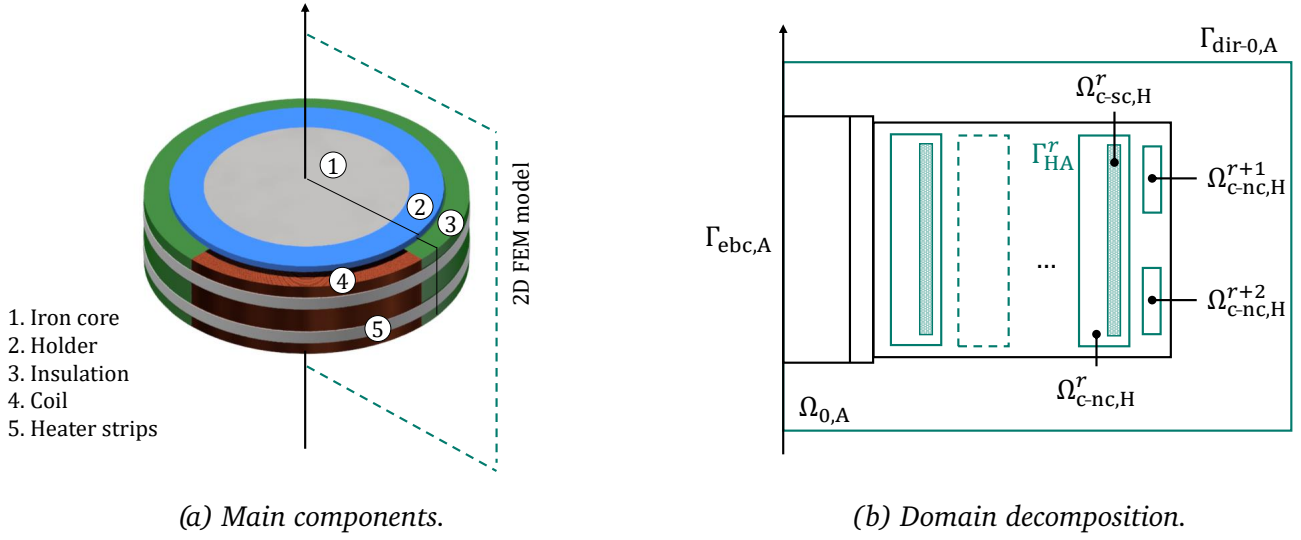
(a) Main components.   *(b) Domain decomposition.*

Figure 4.25. Model of a superconducting solenoid protected by quench heaters, in the 2D axial symmetric setting.

4.5.1.1 Field problem setting

The field problem is formulated for the 2D domain shown in Figure 4.25a by exploiting the axial symmetric geometry of the HTS solenoid. The field problem is shown in Figure 4.25b where the solenoid surrounded by air is decomposed into iron yoke, holder, coil and quench heaters regions. The tape composing the coil is made of a thin superconducting layer on a Hastelloy substrate, coated with two normal conducting layers made of silver and copper, respectively.

The computational domain Ω is split into conducting and passive regions. The conducting region $\Omega_{c,H}^r$ with $r = 1, \cdots, N_t + N_{hs}$ accounts for the coil and the quench heaters, and it is solved for $\vec{H}$. The passive region $\Omega_{0,A}$ accounts for the iron yoke, the holder, the insulating materials and the air region, and it is solved for $\vec{A}$. The conducting region is further subdivided into the superconducting and normal conducting parts $\Omega_{c\text{-sc},H}^r$ and $\Omega_{c\text{-nc},H}^r$ referring to the superconducting layer and the coating of the tape. As each tape is individually insulated, the interface Γ_{HA}^r between the conducting and passive regions is set on each of the boundaries of the conducting regions, namely the tapes and the quench heaters. Homogeneous Dirichlet boundary conditions are applied to $\vec{A}$ on the exterior boundary of $\Gamma_{\text{dir-0,A}}$.

The thermal domain Ω_T accounts for both the superconducting coils and the quench heaters, and their insulation. Therefore, the thermal domain corresponds to a subset of the overall computational domain. Homogeneous Neumann conditions are prescribed to T on the boundary Γ_T, therefore solving for adiabatic conditions which provide a conservative assumption in terms of the maximum temperature $T_{\max}$ reached in the coil.

The power law in (2.86) depends on the ratio $|\vec{J}|/J_c$ and may cause numerical instabilities in case of a transition from the superconducting to the normal conducting state, where both $|\vec{J}| \to 0$ and $J_c \to 0$. Several methods for stabilizing solvers based on the Newton's method are available in literature [268]. Here, the adopted strategy is similar to the *Gmin-stepping* homotopy method used in network solvers [269], and consists in adding a damping factor to the ratio $|\vec{J}|/J_c$ whose magnitude depends on the iteration index of the Newton's scheme.

Parameter	Unit	Value	Description
r_{iron}	mm	15	Iron radius
$r_{\text{coil,in}}$	mm	20	Coil inner radius
$r_{\text{coil,out}}$	mm	23.75	Coil outer radius
h_{iron}	mm	14	Iron height
h_{supp}	mm	14	Support height
h_{coil}	mm	12.25	Coil height
n_{turns}	–	30	Number of turns
δ_{w}	mm	12	Bare tape width
δ_{t}	mm	0.1	Bare tape thickness
$\delta_{\text{t}_{\text{i}}}$	µm	12.5	Insulation thickness
$\delta_{\text{t}_{\text{sc}}}$	µm	1	Superconductor thickness
$\delta_{\text{t}_{\text{ag}}}$	µm	2	Silver thickness
$\delta_{\text{t}_{\text{cu}}}$	µm	40	Copper thickness
$\delta_{\text{t}_{\text{hs}}}$	µm	57	Hastelloy thickness
RRR_{cu}	–	100	Copper residual resistivity ratio
RRR_{ag}	–	100	Silver residual resistivity ratio
I_{c}	kA	1.8	@ 10 K
$J_{\text{c}}(T)$	A mm^{-2}	fit	See Figure 4.27
n	-	25	Power-law index

Table 4.9. Model specifications.

4.5.1.2 Circuit problem setting

The HTS solenoid is powered via an external circuit whose schematics is shown in Figure 4.26. The superconducting coil is powered via the primary circuit on the left, by means of a current source generator representing the power converter. The generator can also be short-circuited by the switch S_{crow} in series with the resistor R_{crow}, in case a power-abort is required. The quench heaters are powered by the secondary circuit on the right by means of a capacitor. The capacitor is assumed to be charged, and can be series-connected to the quench heaters by means of the switch S_{qh}. The parameters $R_{\text{cir},i}$ and $L_{\text{cir},i}$ represent the parasitic resistances and inductances associated to the electrical connections between the power sources and the HTS solenoid.

The circuital representation of the field model is shown in the dashed box of Figure 4.26. The lumped parameters are chosen according to the Schwarz optimized transmission condition as in (3.12), with the field voltage represented by a resistor-inductor series as derived in (3.50). The inductors are mutually coupled due to the magnetic coupling of the coil and the quench heaters. The circuital parameters are given in Table 4.10.

4.5.1.3 Cosimulation setting

The field and circuit models are coupled by means of the cosimulation framework discussed in Section 3.4.2, adopting the WR method [270]. The simulation time interval $\mathcal{I} = [t_0, t_{\text{end}}]$, with $t_0 = 0$ ms and $t_{\text{end}} = 150$ ms is subdivided into nine time windows $\mathcal{I}_j = [t_0^j, t_{\text{end}}^j]$ of variable span Δt_j. For each of the time windows, the field and circuit solvers are executed independently, with prescribed maximum time steps. The size of time windows and the maximum time step for each solver are given in Table 4.11. Within the j-th window, k WR
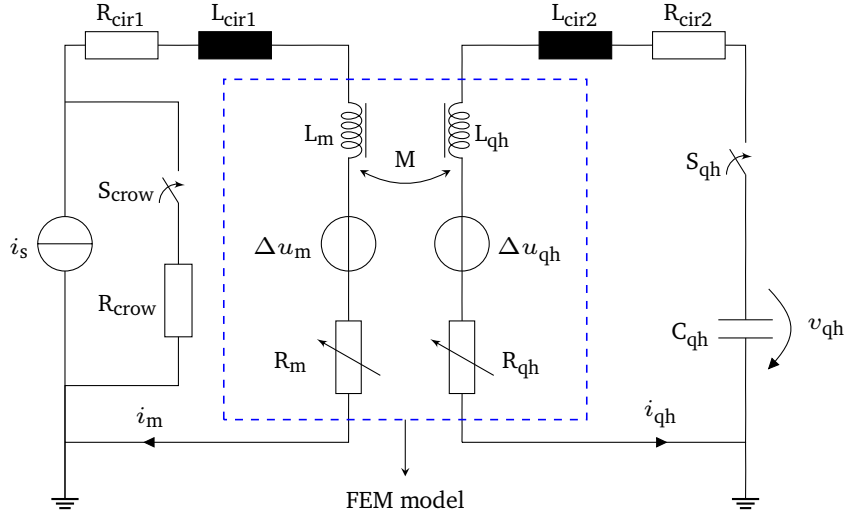
Figure 4.26. Circuit model.

Parameter	Unit	Value	Description
R_{crow}	$\mu\Omega$	100	Crowbar resistance
R_{cir1}	$m\Omega$	1	Circuit resistance
R_{cir2}	$m\Omega$	1	Circuit resistance
L_{cir1}	μF	10	Circuit Inductance
L_{cir2}	μF	10	Circuit Inductance
$R_m(T_{op})$	$n\Omega$	< 1	Coil resistance
$R_{qh}(T_{op})$	Ω	9	Quench heater resistance
$L_m(I_s)$	μH	50	Coil inductance
$L_{qh}(I_s)$	μH	0.5	Quench heater inductance
$M(I_s)$	μH	0.4	Mutual inductance

Table 4.10. Circuit parameters, for $I_s = 1.25$ kA and $T_{op} = 10$ K.

iterations are performed until the stopping criterion

$$F_{conv} = \begin{cases} 0 & \text{if } k < 3 \\ \epsilon_{wr,k} < 1 & \text{if } k \geq 3, \end{cases} \tag{4.17}$$

is fulfilled. A minimum of three iterations is enforced for each time window, before F_{conv} can be satisfied. The WR error $\epsilon_{wr,k}$ is defined for the k-th iteration as

$$\epsilon_{wr,k} = \max\left(\frac{|x_k - x_{k-1}|}{\epsilon_{abs} + |x_k|\epsilon_{rel}} \right), \tag{4.18}$$

where x_k and x_{k-1} are waveforms from two consecutive iterations belonging to the signal chosen as convergence variable, and $\epsilon_{abs} = 0.1$ and $\epsilon_{rel} = 0.001$ are two parameters prescribing the maximum absolute and relative errors for the WR method. The accuracy and the computational cost of the overall cosimulation is determined by the choice of ϵ_{abs} and ϵ_{rel}. Moreover, the size of the time windows can be adjusted for improving convergence, as shorter time windows should be used when significant changes occur in the system.

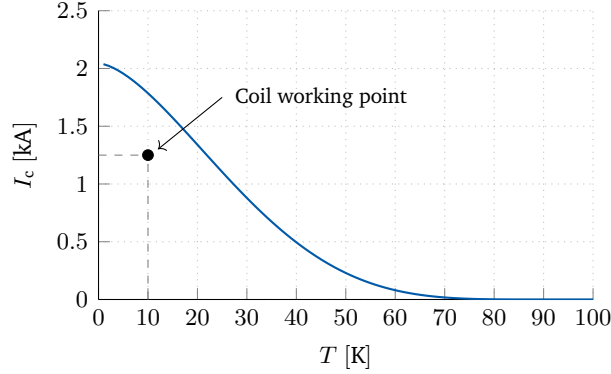| Parameter	Unit	$\mathcal{I}_1$	$\mathcal{I}_2$	$\mathcal{I}_3$	$\mathcal{I}_4$	$\mathcal{I}_5$	$\mathcal{I}_6$	$\mathcal{I}_7$	$\mathcal{I}_8$	$\mathcal{I}_9$
t_0^j	ms	0	5	15	30	45	60	75	90	120
t_{end}^j	ms	5	15	30	45	60	75	90	120	150
Δt_j	ms	5	10	15	15	10	15	15	30	30
Δt_{max} circuit	µs	10	10	50	50	50	50	50	100	100
Δt_{max} field	µs	200	200	500	500	500	500	500	1000	1000

Table 4.11. Cosimulation parameters.

Figure 4.27. Tape critical current I_{c}, as a function of the temperature.

For the problem under study, the current in the solenoid i_{s} is used as convergence variable, that is, the iterations are repeated until the maximum difference between two subsequent waveforms satisfies the stopping criterion in (4.17).

4.5.2 Simulation setup

The HTS solenoid is initially at stationary conditions, powered in series by the ideal current generator at the nominal current $I_{\mathrm{s}} = 1.25\,\mathrm{kA}$, and kept at a temperature of $10\,\mathrm{K}$. The working point of the superconducting tape is at 70% of the critical current which is shown in Figure 4.27 as a function of the temperature. The quench heaters capacitor is assumed to be charged with an initial voltage $V_{\mathrm{c}_0} = 50\,\mathrm{V}$. The quantities of interest are given by the currents $i_{\mathrm{s,m}}$ and $i_{\mathrm{s,qh}}$ in the coil and quench heaters, as well as the maximal temperatures therein. At the same time, the performance of the WR method is quantified in terms of iterations and computational time. Results are given in the next section. The cross section of the tape in the 2D setting is discretized by a structural grid of quadrilateral elements counting 15 elements in the width, and 1, 2 and 3 elements in the thickness of the superconducting, normal conducting, and insulating materials, respectively. The iron yoke, holder and air domain are discretized with triangular elements. The model uses a mesh of first-order elements in Ω_{c}, and second-order elements in $\Omega_{0,\mathrm{A}}$.

4.5.3 Numerical results

A quench is assumed to be detected at $t = 0\,\mathrm{ms}$, for the sake of simplicity. However, a dedicated quench detection model simulating the quench initiation and propagation can be also coupled to the cosimulation

(see [116]). After the detection, a power abort is subsequently triggered. The switch S_{crow} commutes at $t = 2.5\,\text{ms}$, bypassing the current source generator and inserting the resistor R_{crow} in series with the solenoid. At $t = 5\,\text{ms}$, the switch S_{qh} is also activated, transferring the energy stored in the capacitor into the quench heater as Ohmic losses.

The dynamics of the coil and quench heater currents is shown in Figure 4.28a, for both the monolithic and cosimulated models. The current $i_{s,m}$ in the coil shows an initial decay in the first two time windows $\mathcal{I}_1$ and $\mathcal{I}_2$, due to R_{crow}. At the same time, the quench heaters are powered by the current $i_{s,qh}$ which follows a double exponential profile with a fast rise time and a slower decay. The temperature rise in the coil increases its equivalent resistance, contributing to the current discharge in the primary circuit. The sharp variation in the derivative of the main current occurs in the time interval $\mathcal{I}_3$ as the coil starts to quench. The increase of the temperature due to the quench heaters reduces the critical current of the tape, eventually below the transport current. At this point, the current starts to flow in the stabilizer fraction of the tape, generating Joule losses which further increase the temperature. Although the time constant of the primary circuit is equal to $500\,\text{ms}$ in the absence of a quench, the resistive build-up in the superconducting coil leads to a complete discharge of the solenoid in less than $150\,\text{ms}$.

The evolution of the peak temperature in the quench heaters and in the coil, and the coil equivalent resistance, is shown in Figure 4.29a and 4.29b. For the simulated scenario, the peak temperature never exceeds $130\,\text{K}$. The temperature distribution in the cross section of the coil is shown for different times in Figure 4.30, highlighting the contributions from the quench heaters on the right side of the coil, the quench and the subsequent heat diffusion.

Once the dynamics of the current in the superconducting coil is known, the hotspot criterion is used for determining t the maximum detection time which is allowed in case of a quench. This criterion provides pessimistic but conservative results. The hotspot consists in a quench thermal model of spatial dimension zero used for calculating the temperature in the coil, assuming adiabatic conditions and neglecting heat diffusion phenomena. The energy deposited in the hotspot is defined by means of the Joule integral in $\text{MA}^2\,\text{s}$ units (MIITS), and is used in the zero dimensional model to obtain the maximum temperature T_{hotspot}. Results are shown in Figure 4.31a, parametrized by the residual resistivity ratio RRR_{Cu} of the copper stabilizer in the tape.

At this point, the MIITS associated to the coil current is calculated as

$$\text{MIITS}(t_{\text{delay}}) = I_{\text{m}}^2 t_{\text{delay}} + \int_{t_0}^{t_{\text{end}}} i_{\text{m}}^2 \, \mathrm{d}t, \tag{4.19}$$

where t_{delay} represents the time interval between the starting of the quench and its detection at t_0. By using $\text{MIITS}(t_{\text{delay}})$ into Figure 4.31a, the curve in Figure 4.31b is calculated for $RRR_{\text{Cu}} = 100$, correlating the delay in the quench detection time with the peak temperature in the coil. As an example, for a maximum temperature $T_{\text{max}} = 300\,\text{K}$, it is found that a maximum delay of about $15\,\text{ms}$ can be tolerated to ensure $T_{\text{hotspot}} \leq T_{\text{max}}$.

4.5.4 Cosimulation results

The convergence rate of the WR method is shown in Figure 4.32a, whereas the number of iterations per time window is shown in 4.32b. For $\mathcal{I}_1$-$\mathcal{I}_3$, the convergence criterion is already met after the minimum number of iterations has been performed. Starting from $\mathcal{I}_4$, the number of iterations is always ≥ 4, consequently to the quench transition in the coil which enforces a faster dynamics is the coil-circuit system. This, in turn, leads to
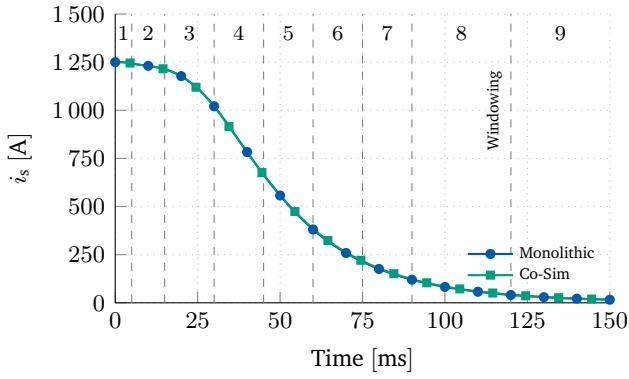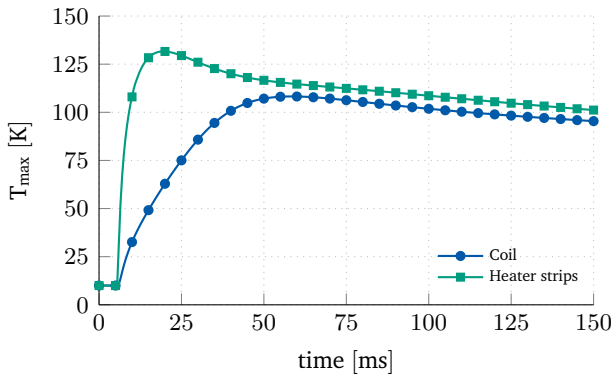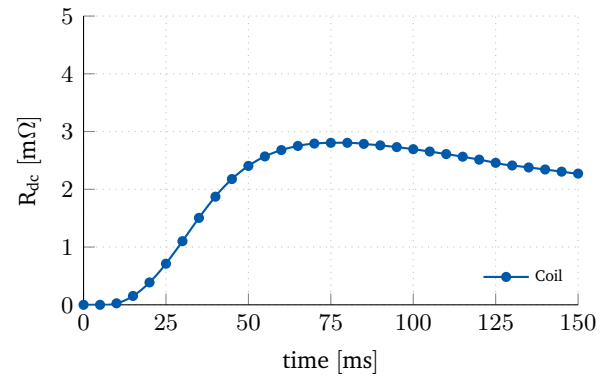
(a) Current in the coil.
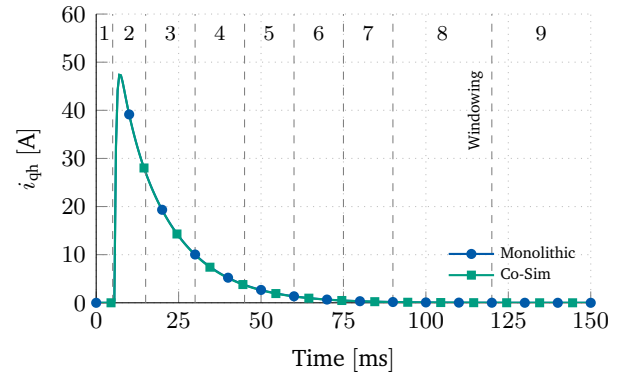
(b) Current in the heater strips.

Figure 4.28. Currents in the circuit, obtained by means of monolithic and cosimulation models.

(a) Peak temperatures.

(b) Coil resistance.

Figure 4.29. Quantities of interest in the solenoid.

(a) $t = 10$ ms.   *(b) $t = 20$ ms.*   *(c) $t = 30$ ms.*   *(d) $t = 50$ ms.*   *(e) $t = 100$ ms.*   *(f) $t = 150$ ms.*
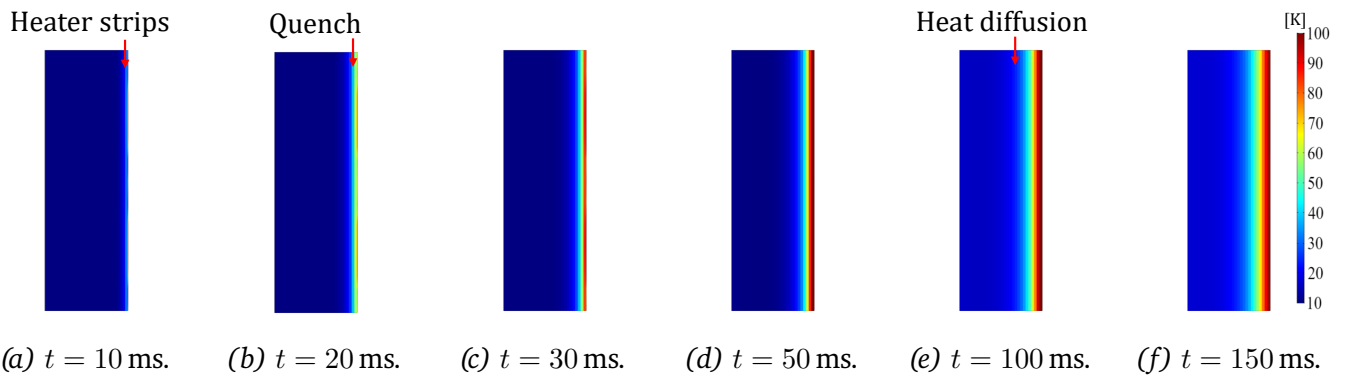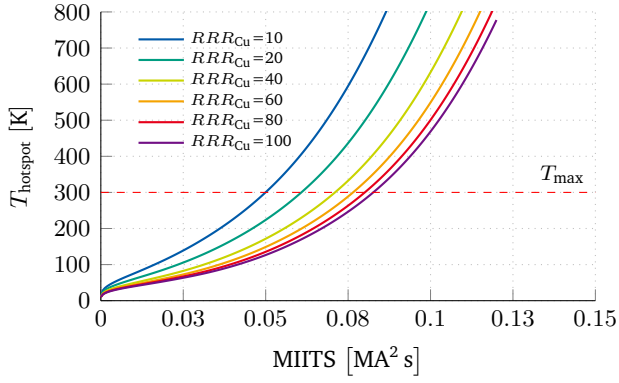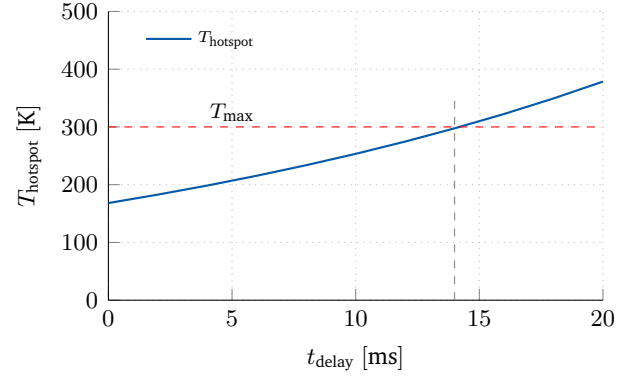
Figure 4.30. Temperature distribution in the coil, for six different times. The temperature dynamics is initially driven by the thermal contribution from the heater strips, subsequently by the quench contribution, and in the last part of the current discharge by heat diffusion phenomena.

(a) Hotspot temperature and MIITS.

(b) Maximum quench detection time.

Figure 4.31. Maximum quench detection time, obtained via an adiabatic coil approximation.
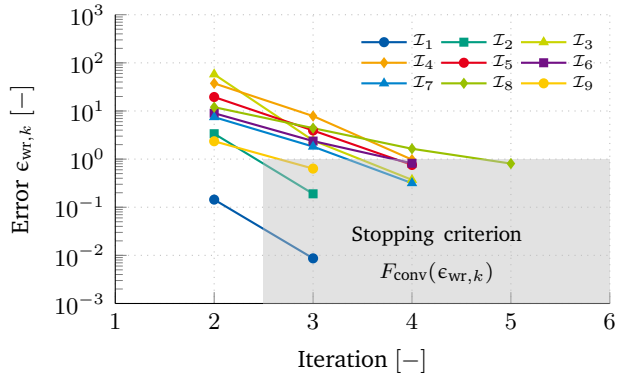
(a) Convergence rate.
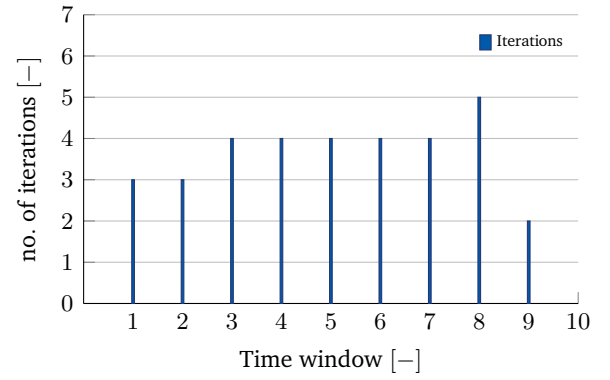
(b) Number of iterations per time window.

Figure 4.32. Performance of the waveform relaxation method. (a) Convergence rate of the stopping criterion for each time window. (b) Number of iterations per each time window.
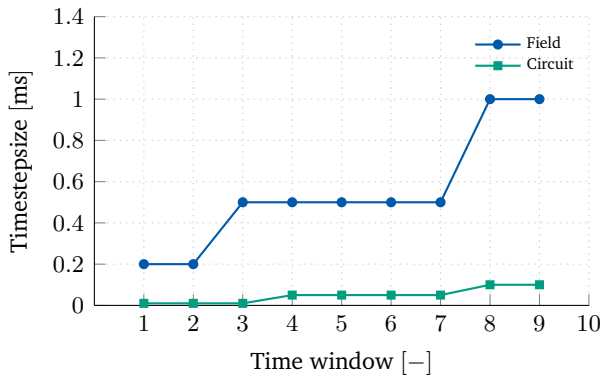
(a) Maximum step size.
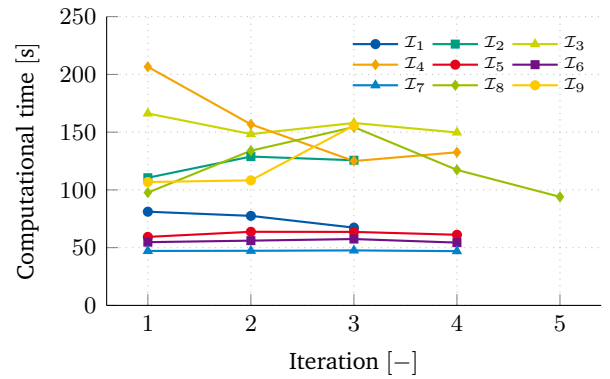
(b) Computational time.

Figure 4.33. Computational cost of the waveform relaxation method. (a) Maximum time step size for the field and circuit solvers. (b) Computational time for each iteration and time window.

higher variations in the current signal within each time window, requiring higher number of iterations before the waveform relaxes to the actual solution.

The maximum time step enforced for the field and circuit solvers at each time window is shown in Figure 4.33a. Concerning the field solver, the smallest time step is imposed in the model for the first three time windows, such that the dynamics of the quench heaters is accurately resolved. This is crucial for accurately resolving the quench induced in the coil, and the consequent transient effects. Subsequently, the step is relaxed by a factor 2.5 for the central time windows, and further increased by a factor 2 for the resolution of the final part of the current decay, where the coil is almost completely discharged. Concerning the circuit solver, the first two time windows require a fine time stepping to resolve the state transition of the switches in the primary and secondary circuits. Later, the time stepping is progressively relaxed, following a relaxation strategy which is qualitatively the same as for the field solver. Convergence in the solution is acquired where the field and circuit maximum time stepping differ by up to an order of magnitude, showing the effectiveness of the WR method in tackling problems involving multirate phenomena. The computational time required for the monolithic and cosimulation solutions is about 15 and 60 minutes; the computational cost per each iteration of the WR method is shown in Figure 4.33. The windows $\mathcal{I}_3$ and $\mathcal{I}_4$ resolve the quench in the coil induced by heaters, and are the most expensive.

4.6 Summary

This chapter provides a rigorous verification of the implementation of the coupled $\vec{A} - \vec{H}$ field formulation with the finite element method. A set of models with increasing complexity allows verifying the numerical features which are required for field-circuit coupled simulations of applications based on HTS materials, in an incremental way. For all the verification cases, good agreement is obtained for the quantities of interest.

Starting from the simple model of a normal conducting tape, the coupled $\vec{A} - \vec{H}$ field formulation is verified against the results obtained with the monolithic $\vec{A}$ formulation for bulk and shell tape geometries, both in the 3D and 2D settings. For the thin-shell approximation, the consistency of results is investigated with respect to the skin depth of the tape. Subsequently, the non-linear electrical behavior associated to HTS materials is introduced by means of the power law in a model where a superconducting block is exposed to an external field. The block is modeled both as a bulk and a stack of shells, and results are compared with the monolithic $\vec{H}$ formulation.

The modeling of superconducting tapes and coils with the thin-shell approximation in a 2D setting is of great relevance for this work, as it allows simulating the dynamic field quality in both superconducting magnets and experimental devices, see Chapters 5 and 6. For this reason, a dedicated model of an individual HTS tape is discussed, and its results are compared to analytical solutions available in literature. The influence of the normal conducting coating and the impact of the thin-shell approximation on the computational performance is also discussed. Subsequently, tapes are arranged in coils implementing different connection schemes, and results are compared with the monolithic $\vec{H}$ formulation.

The last step consists in the verification of the field-circuit coupling interface, derived as an optimized Schwarz transmission condition. After the STEAM cosimulation framework is expanded to field models implementing the $\vec{A} - \vec{H}$ field formulation, a quench event occurring in an HTS solenoid protected by quench heaters is investigated. The cosimulation results obtained by means of the WR method are verified with the monolithic solution.

5 Validation: Feather-M2.1-2 Magnet

Screening currents are field-induced dynamic phenomena which occur in superconducting materials, leading to persistent magnetization. Such currents are of importance in ReBCO tapes, where the large size of the superconducting filaments and the high critical current density lead to strong magnetization phenomena. In consequence, superconducting accelerator magnets based on ReBCO tapes might experience a relevant degradation of the magnetic field quality in the magnet aperture, eventually leading to particle beam instabilities. Thus, persistent magnetization phenomena need to be accurately evaluated.

In this Chapter, the 2D finite element model of the Feather-M2.1-2 magnet is presented. The model is used to analyze the influence of the screening current-induced magnetic field on the field quality in the magnet aperture. The model relies on the coupled $\vec{A} - \vec{H}$ field formulation for eddy-current problems in the time domain introduced in Chapter 2. The numerical model of the Feather-M2.1-2 magnet is detailed, highlighting the key assumptions and simplifications. The numerical results for both the overall field quality in the magnet, and the contribution from persistent magnetization phenomena are compared with available magnetic measurements.

5.1 Magnetic Field Quality

This section closely follows [59, Chapter 6]. The magnetic field quality is commonly defined for accelerator magnets by means of a set of Fourier coefficients, known also as field harmonics or multipole coefficients. These coefficients are calculated from the general solution of the Laplace equation in a suitable coordinate system. The general solution is obtained with the method of separation of variables, and the integration constants are determined by comparison with the field values at the boundary. These values are given, for a circular coordinate system, by the radial or azimuthal components of the magnetic field at the prescribed boundary radius.

The magnetic field problem is given by means of the $\vec{A}$ formulation discussed in Section 2.8.4, as

$$\nabla \times \mu^{-1} \nabla \times \vec{A} + \sigma \partial_t \vec{A} = \vec{J}_{\mathrm{s}}, \tag{5.1}$$

with appropriate boundary and initial conditions. The magnetic field quality evaluation is typically restricted to the magnet aperture, where the particle beams traveling through the accelerator interact with the field produced by magnets. The magnet aperture is free of currents and magnetized materials, therefore $\vec{J}_{\mathrm{s}} = 0$, $\sigma = 0$, and $\mu = \mu_0$. The field problem is therefore reduced to the boundary problem given by the Laplace equation

$$\Delta \vec{A} = 0. \tag{5.2}$$

In the two-dimensional approximation of accelerator magnets, the axial field variations are neglected along the z-direction (the longitudinal axis of the magnet). This yields a scalar Laplace equation, whose general solution can be expressed as

$$A_z(r, \varphi) = \sum_{k=1}^{\infty} r^k (\mathcal{A}_k \sin k\varphi + \mathcal{B}_k \cos k\varphi), \tag{5.3}$$

where A_z gives the longitudinal component of the magnetic vector potential, $\mathcal{A}_k$ and $\mathcal{B}_k$ are the integration constants associated to the multipole coefficients, and (r, φ, z) represent the spatial coordinates of a cylindrical reference frame which is consistent with the magnet aperture. The magnetic field components are derived from (5.3) as

$$B_r(r, \varphi) = \frac{1}{r} \frac{dA_z}{d\varphi} = + \sum_{k=1}^{\infty} k r^{k-1} (\mathcal{A}_k \cos k\varphi - \mathcal{B}_k \sin k\varphi), \tag{5.4}$$

$$B_\phi(r, \varphi) = -\frac{dA_z}{dr} = - \sum_{k=1}^{\infty} k r^{k-1} (\mathcal{A}_k \sin k\varphi + \mathcal{B}_k \cos k\varphi). \tag{5.5}$$

The index k represents solutions which can be interpreted as field distributions provided by ideal magnet geometries. As an example, the indexes $k = 1, 2,$ and 3 correspond to the dipole, quadrupole, and sextupole field distributions, respectively.

5.1.1 Calculation of the multipole coefficients

The radial field component (5.4) is assumed to be known along a circle, either by simulations or measurements. The Fourier series expansion of the field components is given for a reference radius $r = r_0$ usually chosen as 2/3 of the radius of the magnet aperture, as a function of the angular coordinate φ. The field components are given by

$$B_r(r_0, \varphi) = + \sum_{k=1}^{\infty} (B_k(r_0) \sin k\varphi + A_k(r_0) \cos k\varphi), \tag{5.6}$$

$$B_\phi(r_0, \varphi) = + \sum_{k=1}^{\infty} (B_k(r_0) \cos k\varphi - A_k(r_0) \sin k\varphi). \tag{5.7}$$

The skew and normal multipole coefficients $A_k(r_0)$ and $B_k(r_0)$ are obtained for $k = 1, 2, 3, \ldots,$ as

$$A_k(r_0) = \frac{1}{\pi} \int_0^{2\pi} B_r(r_0, \varphi) \cos k\varphi \, d\varphi, \tag{5.8}$$

$$B_k(r_0) = \frac{1}{\pi} \int_0^{2\pi} B_r(r_0, \varphi) \sin k\varphi \, d\varphi, \tag{5.9}$$

whereas the coefficients for $k = 0$ are zero since the magnetic flux density is divergence-free. Fig. 5.1 shows the flux lines in cylindrical coordinates associated to the first $k = 6$ multipoles, for both the normal B_k and skew A_k components.

The numerical calculation of the field multipoles occurs in practice for a discrete series of N_k points equally spaced in the interval $[0, 2\pi)$, such that $\varphi_k = 2\pi k / N_k$, with $k = 0, 1, 2, \ldots, N_k - 1$. By using the Discrete
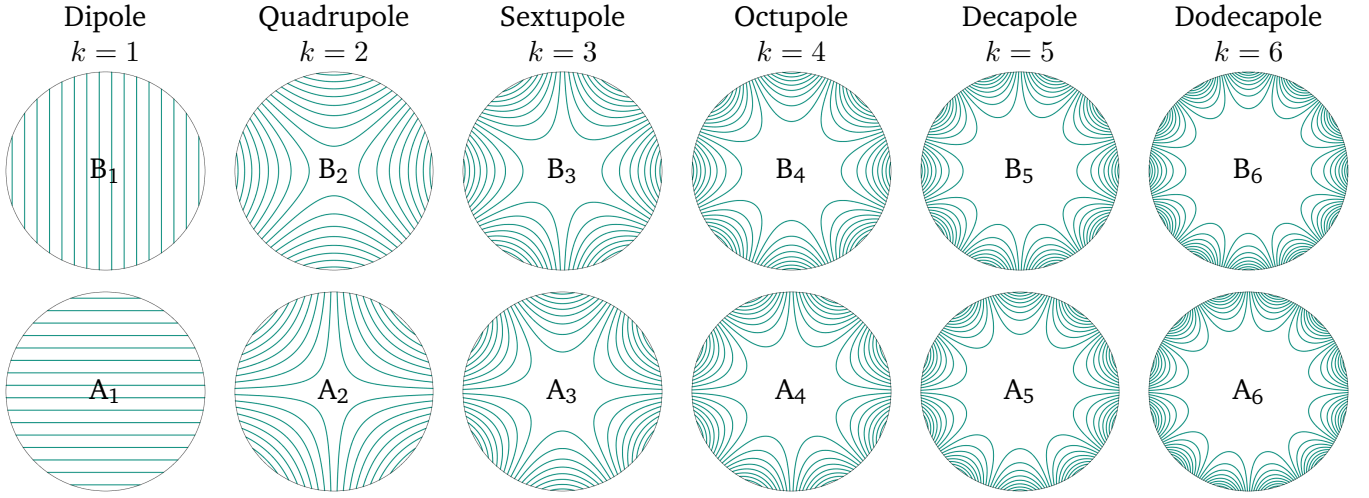
Figure 5.1. Magnetic field lines of the field multipoles in cylindrical coordinates, shown for $k = 1, 2.., 6$. The first and second row show the normal B_k and skew A_k multipole components.

Fourier Transform algorithm, N_k Fourier coefficients are calculated twice (due to the Hermitian symmetry of the transformation), as

$$A_k(r_0) = \frac{2}{N_k} \sum_{k=0}^{N_k-1} B_r(r_0, \varphi_k) \cos k\varphi_k, \tag{5.10}$$

$$B_k(r_0) = \frac{2}{N_k} \sum_{k=0}^{N_k-1} B_r(r_0, \varphi_k) \sin k\varphi_k, \tag{5.11}$$

which establishes a relation between the field components in (5.4) and (5.5), and the multipole coefficients $A_k(r_0)$ and $B_k(r_0)$ at a given reference radius r_0. For $r < r_0$, the field components are given by

$$B_r(r, \varphi) = + \sum_{k=1}^{\infty} \left(\frac{r}{r_0} \right)^{k-1} (B_k(r_0) \sin k\varphi + A_k(r_0) \cos k\varphi), \tag{5.12}$$

$$B_\phi(r, \varphi) = + \sum_{k=1}^{\infty} \left(\frac{r}{r_0} \right)^{k-1} (B_k(r_0) \cos k\varphi - A_k(r_0) \sin k\varphi). \tag{5.13}$$

The coefficients are often combined in the complex notation $C_k(r_0) = B_k(r_0) + iA_k(r_0)$ as the skew and normal pairs are orthogonal to each other. Moreover, the coefficients are typically normalized by the main field component $B_K(r_0)$ and denoted as b_k and a_k, with K being the index of the main field component. Thus, the field quality is quantified as a relative error c_k, for $k = 1, 2, 3, \ldots$, as

$$c_k(r_0) = b_k(r_0) + ia_k(r_0) = 10^4 \frac{C_k(r_0)}{B_K}, \tag{5.14}$$

and given in 1×10^{-4} units with respect to B_K at the reference radius r_0. It is worth mentioning that for reaching accelerator quality standards, the field multipoles shall be kept within a few units at nominal magnetic field, avoiding the need for strong corrector magnets [59].

1. Iron yoke
2. Iron pole
3. Aperture
4. Central deck
5. Wing deck
6. Coil ends

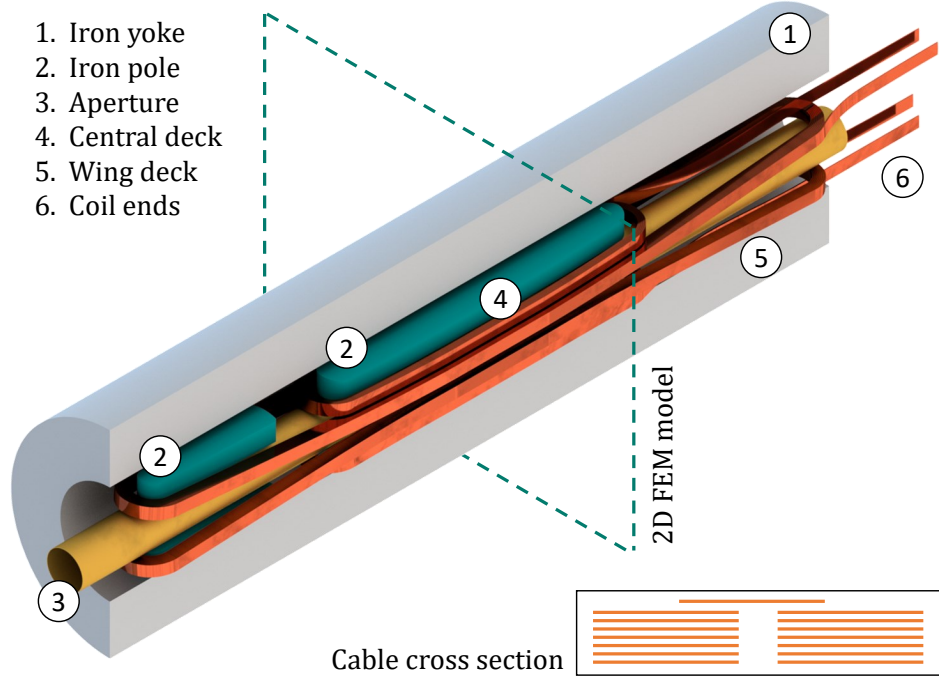2D FEM model

Cable cross section

Figure 5.2. Simplified rendering of the Feather-M2.1-2 magnet. The coil is composed of two pairs of central and wing decks. The cable is made of 15 tapes fully transposed with the Roebel technique. The cross section of the cable is shown in the lower-right corner. The magnetic circuit is composed of four iron poles and a cylindrical iron yoke (half-shown).

The magnetic field quality can also be conveniently given in terms of the total harmonic distortion (THD) factor $F_{\mathrm{d}}(r_0)$, which is a scalar quantity defined as

$$F_{\mathrm{d}}(r_0) = \sqrt{\sum_{k=1;\ k \neq K}^{\infty} b_k^2(r_0) + a_k^2(r_0)}. \tag{5.15}$$

The skew harmonics a_k are often omitted because they are usually zero due to the symmetric construction of accelerator magnets. Moreover, as the multipoles vanish according to r^{k-1}, only low-order coefficients are considered, typically up to the dodecapole component.

5.2 Numerical Model of the Feather-M2.1-2 Magnet

The Feather-M2.1-2 magnet is an HTS accelerator dipole insert-magnet [14, 21, 22] recently developed at CERN within the framework of the projects EuCARD-2 [19] and ARIES [20]. This demonstrator magnet is designed to produce a peak field of $5\,\mathrm{T}$ in its aperture at a nominal current of $10\,\mathrm{kA}$, in a background field of $13\,\mathrm{T}$. The Feather-M2.1-2 magnet is specifically designed for being operated as an insert inside the aperture of the FRESCA2 dipole magnet [23, 24, 271–273] which is used for cable testing purposes. The combination of the two magnets is referred to as a graded-coil configuration, since the FRESCA2 magnet is wound with a

Parameter	Unit	Value	Description
Sunam [277]			Producer
IBAD [278, 279]			Technology
Hastelloy C-276[265]			Substrate
Copper			Stabilizer
$\delta_{t,sub}$	μm	100	Substrate thickness
$\delta_{t,stab}$	μm	40	Stabilizer thickness
δ_t	μm	150	Tape thickness
δ_w	mm	5.5	Tape width
$I_{c,meas}$	A	300	@ 77 K, self-field
$J_c(\vec{B}, T)$	A mm^{-2}	fit	Fit in [280]
n	-	$4 \leq n \leq 30$	Power-law index

Table 5.1. Tape specifications.

Rutherford cable made of the LTS material Nb$_3$Sn. At the date of writing, the integration of the two magnets is in progress [274].

A simplified 3D graphical rendering of the Feather-M2.1-2 magnet is shown in Figure 5.2, where for the sake of clarity, only the components relevant for the numerical analysis are shown. The coil is composed of two poles, each of them made of two windings labeled as central and wing decks. Each deck implements the field-alignment concept, that is, decks are arranged such that the superconducting tapes are aligned with the magnetic field lines on the cross-sectional plane [68]. The magnetic field shape is controlled in the magnet aperture by means of iron poles. The functional role of the outer iron yoke is to intercept the stray field lines, such that the magnet can be operated in stand-alone mode. The central cross section of the magnet is used as input for the geometry of the 2D FEM model.

The magnetothermal behavior of the Feather-M2.1-2 magnet was recently tested in a stand-alone configuration [275], and the influence of the superconducting coil dynamics on the magnetic transfer function was measured by means of both Hall-probes [276] and rotating coil magnetometers. To better understand the dynamics of magnetization phenomena within the superconducting coil, the numerical model of the Feather-M2.1-2 magnet is verified against experimental data. The model refers to the magnet version M.1-2 [275], which is characterized by the use of a superconducting tape provided by the producer Sunam [277] which does not allow reaching the nominal performance of the magnet. This specific tape limits the magnet current to $5\,\mathrm{kA}$ and the peak field in the magnet to maximum value of about $3\,\mathrm{T}$.

5.2.1 Problem setting

The numerical model of the Feather-M2.1-2 magnet exploits the translational symmetry of the device, being implemented for a 2D setting. The model is composed of the superconducting coil, the iron yoke and the air region surrounding the magnet. The field problem is formulated using the coupled $\vec{A} - \vec{H}$ field formulation combined with the thin-shell approximation (see Section 2.14.2).

The computational domain Ω is decomposed into the conducting region $\Gamma_{c,H}$ representing the coil solved for the magnetic field strength $\vec{H}$, and the region Ω_A solved for the reduced magnetic vector potential $\vec{A}$, containing the conducting iron yoke $\Omega_{c,A}$ and the nonconducting air region $\Omega_{0,A}$. The computational domain is shown in Figure 5.3a, where the boundary Γ_{ref} shows the reference circumference where the magnetic field quality is evaluated in terms of a multipole series expansion. The dynamic effects occurring in the iron yoke
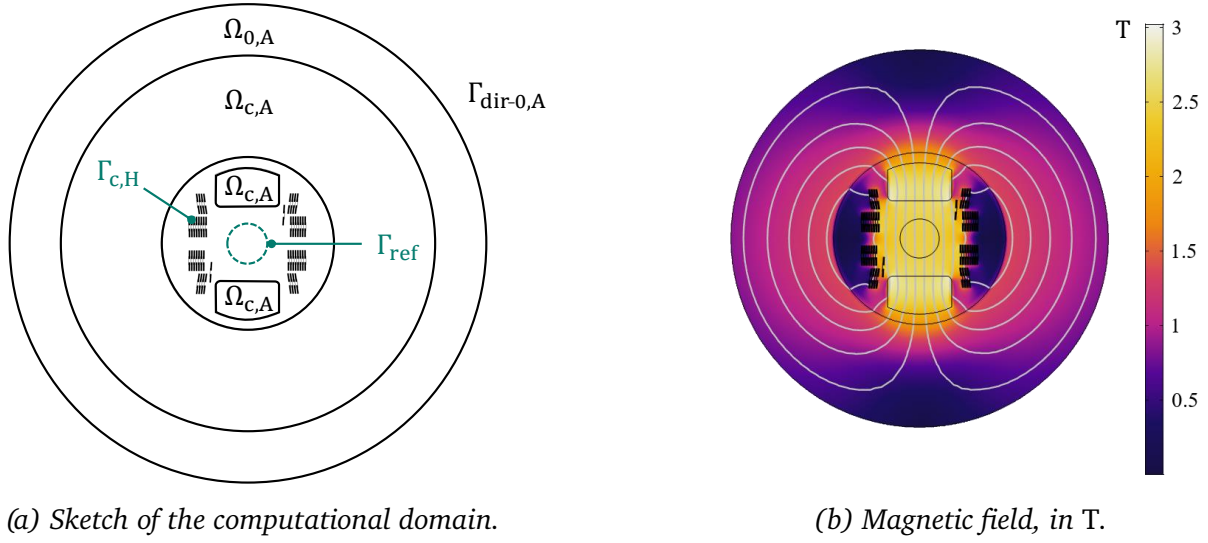
(a) Sketch of the computational domain.

(b) Magnetic field, in T.

Figure 5.3. Numerical model of the Feather-M2.1-2 magnet. (a) Decomposition of the computational domain. (b) Magnetic field in T, at $5\,\mathrm{kA}$ and $4.5\,\mathrm{K}$, shown for the cross section of the Feather-M2.1-2 magnet. The peak magnetic field reached in the aperture is about $2.5\,\mathrm{T}$.

and the structural elements of the magnet are neglected in the model because the magnetic field quality is always evaluated after these contributions are settled. According to the experimental conditions in [275], the temperature was kept constant during the data acquisition phases. For this reason, the thermal part of the field formulation is not implemented, and the heat balance equation is replaced with a constant temperature constraint $T = T_{\mathrm{op}}$, where T_{op} is the magnet operational temperature during experiments. The representation of the source domain $\Gamma_{\mathrm{c,H}}$ by means of thin shells is justified by the high aspect ratio of the superconducting tapes composing the coil. In this way, the geometric thickness of the tape is neglected, and the discretization of the thickness of the superconductor is avoided. As a consequence, the interface Γ_{HA} between the source and source-free regions corresponds to the coil domain $\Gamma_{\mathrm{c,H}}$.

The physical properties of the materials composing the tape are homogenized according to Section 3.7. The thin-shell approximation is adopted to ensure an acceptable computational time, as the 2D model accounts for 648 tapes over four quadrants. The geometric and superconducting properties of the tape are given in Table 5.1. In the 2D setting, homogeneous Dirichlet boundary conditions are imposed to $\vec{A}$ on the exterior boundary $\Gamma_{\mathrm{dir\text{-}0,A}}$. Homogeneous boundary conditions are justified by considering the exterior boundary sufficiently far from the tapes and the iron yoke (note that the exterior boundary in Figure 5.3a is not in scale). As an example, the magnetic field solution is shown in Figure 5.3b, in T, for a current of $5\,\mathrm{kA}$ at $4.5\,\mathrm{K}$. The model is implemented for a 2D transverse field configuration, thus neglecting the magnetic effects of the end-coils. This approximation is assumed since the aspect ratio between the coil width and length is greater than ten. Due to the presence of the layer jumps connecting the lower and the upper windings in the coil, the magnetic symmetry in the cross section of the magnet is not preserved. For this reason, the model accounts for a four-quadrants geometry, including the layer jumps in the first and third quadrant. The layer jump is visible in Figure 5.3, as a turn that is slightly misaligned with respect to the coil decks. The key features and the relevant simplifications of the model are discussed in the following.

(a) Photograph of a coiled Roebel cable (by Henry Barnard). Figure taken from [2], © CERN.
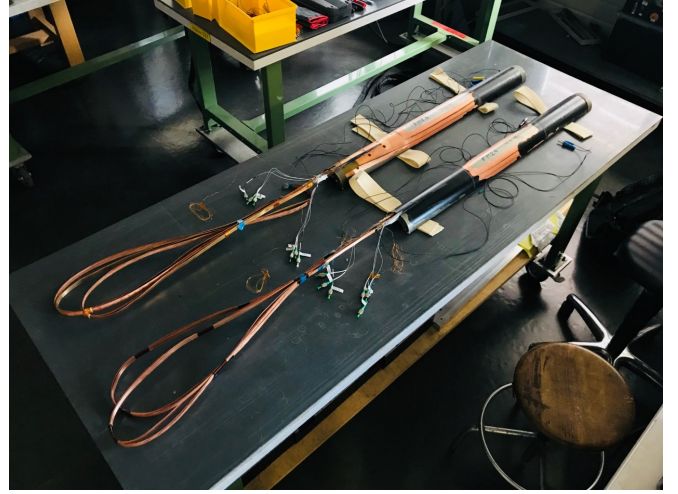
(b) Photograph of the upper and lower pole of the Feather-M2.1-2 magnet (by Jeroen Van Nugteren).

Figure 5.4. Roebel geometry, applied to (a) cables and (b) coils.

5.2.2 Current-sharing approximation

The cable adopted for the superconducting coil is composed of 15 tapes. The tapes are fully transposed by following the Roebel geometry [281, 282], a 100-years-old concept originally developed for reducing the AC losses in power-busbars made of copper [283]. Photographs of a Roebel cable and the superconducting coil of the Feather-M2.1-2 magnet are shown in Figures 5.4a and 5.4b. The cross section of the cable used in the 2D numerical model is shown in the box of Figure 5.2, where each line represents a tape. The tapes composing the Roebel cable are electrically connected at the ends in a parallel configuration. Moreover, the fully transposed geometry ensures that each superconducting path within the cable has the same electrical impedance, such that the source current is evenly distributed between the tapes. For this reason, it is assumed that each of the tapes carries the same fraction of source current, neglecting current redistribution phenomena between different tapes. Coupling currents possibly circulating between the tapes are also neglected, since they represent a second-order effect with respect to screening currents [14].

Current sharing phenomena are allowed between the superconducting and normal conducting fraction of the tapes. This is taken into account by means of the equivalent resistivity defined in Section 3.7 which homogenizes the conducting materials composing the multilayered structure of the tapes. This includes also the superconducting layer whose electrical properties are implemented by means of the power law (2.86). The power law is affected by the n-value given to the power-law index, which was experimentally quantified as $n = 5$ by dedicated measurements of the magnet [275]. Such a low value is outside the expected range of 20-30 [174], and it may be caused by unbalanced tape joints at the coil terminals [275]. However, the joint resistance does not have a relevant role in the determination of screening current phenomena and the related persistent magnetization, since the screening currents form loops which close within the tape, without being affecting by the tape joints. Unfortunately, the tape was not characterized individually and so the uncertainty of the superconducting properties of the tapes is significant and the n-value is not known. To overcome this issue, a parametric sweep is performed for $4 \leq n \leq 30$, quantifying the sensitivity of the model. The results are compared with measurements in Section 5.3.

symbol	g_0	g_1	g_2	g_3	T_{c0}	p_c	q_c	$B_{i0,c}$	γ_c	α_c
unit	–	–	–	–	K	–	–	T	–	$\mathrm{MA\,T\,mm^{-2}}$
value	0.03	0.25	0.06	0.06	93	0.5	2.5	140	2.44	1.86
symbol	ν_g	a	n_0	n_1	n_2	p_{ab}	q_{ab}	$B_{i0,ab}$	γ_{ab}	α_{ab}
unit	–	–	–	–	K	–	–	T	–	$\mathrm{MA\,T\,mm^{-2}}$
value	1.85	0.1	1	1.4	4.45	1	5	250	1.63	68.3

*Table 5.2. Parameters used for the function $J_{c,fit}$ [280].*

5.2.3 Critical current density fit

The critical current density J_c in (2.86) is a property of superconducting materials which is of crucial importance for the numerical model of the Feather-M2.1-2 magnet and, in general, for the numerical modeling of devices containing HTS materials. In accelerator magnets, J_c determines the resistivity of the tapes in the coil, affecting the dynamics of screening currents and, therefore, the field quality in the magnet aperture. For high-temperature superconducting tapes based on ReBCO compounds, J_c shows an anisotropic, field- and temperature-dependent behavior as $J_c(|\vec{B}|, T, \theta_B)$, where θ_B is the magnetic field angle with respect to the direction perpendicular to the wide surface of the tape. The anisotropy in the critical current density is shown in Figure 5.5a for a ReBCO tape from Fujikura [284], as a function of the magnetic field magnitude $|\vec{B}|$, temperature T and magnetic field angle θ_B.

The critical current density behavior is included in the model by means of the numerical fit $J_{c,fit}(|\vec{B}|, T, \theta_B)$ provided in [280], see also Appendix A. Since no characterization data was available for the Sunam tape used for the coil, the fit parameters are taken from [14] and given in Table 5.2. As a consequence, the fit is scaled to be consistent with the critical current measured in the magnet [275], by means of the fitting factor $f_c : \mathbb{R} \to \mathbb{R}$ determined as follows. First, the magnetic characteristic of the magnet, known also as the load line, is calculated by means of magnetostatic simulations. Due to the static regime, no dynamic effects can occur, and the current density is assumed homogeneous in the coil cross-section. The load line is shown in Figure 5.5b, given by the peak magnetic field $B_{p,coil}$ in the coil, as a function of the source current. Figure 5.5b shows also the critical current $I_{c,fit}$ as a function of the magnetic field and parametrized by the temperature, calculated from $J_{c,fit}$ by assuming the magnetic field angle $\theta_B = 0°$, thus for a magnetic field which is perpendicular to the wide face of the tapes in the cable. Second, the intersection points between the magnet load line and $I_{c,fit}$ are used for constructing the curves in Figure 5.5c which show $I_{c,fit}$ as a function of temperature and parametrized by the field angle. The same figure includes also the measured data points concerning the critical current of the coil $I_{c,meas}$. It is observed that the assumption of field perpendicularity gives the best agreement with the measured data. Finally, the fitting factor is obtained as

$$f_c(T) = \left. \frac{I_{c,meas}(T)}{J_{c,fit}(B_{p,coil}(T), T, \theta_B) S_{HTS}} \right|_{\theta_B = 0°}, \tag{5.16}$$

where S_{HTS} is the cross section of the superconducting fraction in the cable. The fitting factor is calculated as a function of temperature and shown in Figure 5.5d, parametrized by the field angle. The fitting factor f_c obtained for $\theta_B = 0°$ is used in the model for scaling the critical current density fit.
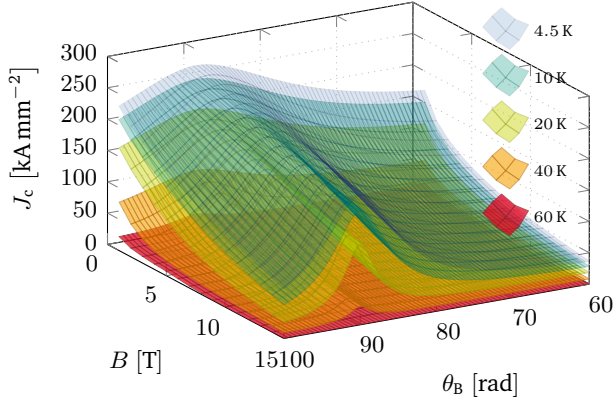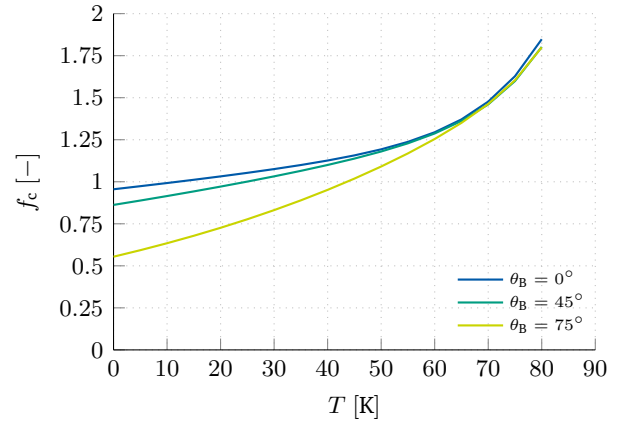
(a) Critical current density fit $J_{c,fit}(|\vec{B}|, T, \theta_B)$.
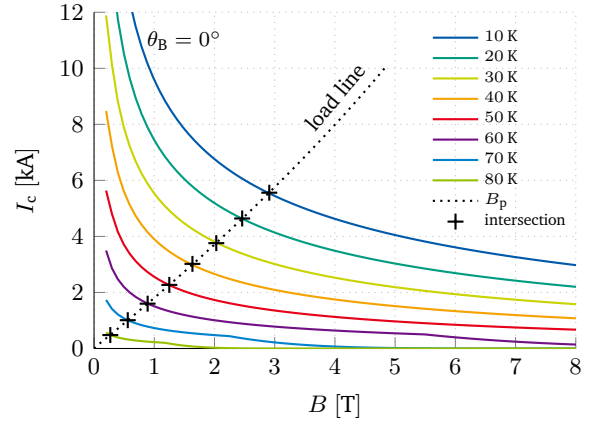
(b) Calculated critical current I_c, with $\theta_B = 0°$.
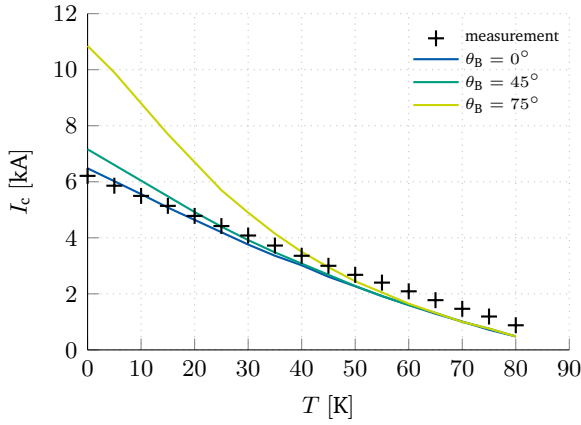
*(c) Calculated and measured critical current I_c.*

(d) Lifting factor f_c, for different field angles.

Figure 5.5. Lifting factor for the critical current density of the Feather-M2.1-2 coil. (a) Critical current density fit $J_{c,fit}(|\vec{B}|, T, \theta_B)$. (b) Calculated critical current by means of the magnet load line, for $\theta_B = 0°$. (c) Comparison of the calculated and measured critical current, for different field angles. (d) Lifting factor f_c, for different field angles.

5.2.4 Mesh sensitivity

The model uses a mesh of first-order elements in $\Gamma_{c,H}$, and second-order elements in $\Omega_{0,A}$. The magnetic field quality in the aperture of the Feather-M2.1-2 magnet is expressed by means of multipole coefficients, as discussed in Section 5.1. The multipole coefficients are calculated by applying the Fast Fourier Transform algorithm to the radial component of the magnetic field which is evaluated along the reference circumference in the magnet aperture. However, the finite resolution of the mesh in the spatial discretization (i.e. the finite number of mesh elements) introduces a numerical error perturbing the calculation of the multipole coefficients, as discussed in [285]. Therefore, a mesh sensitivity analysis is carried out to quantify the error in the multipoles.

The model used in the analysis is given by a circular non-conducting and source-free computational domain $\Omega_{0,A}$, solved for the magnetic vector potential $\vec{A}$. The model is shown in Figure 5.6a. A known magnetic field
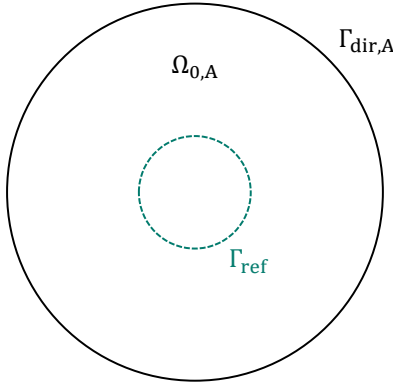
(a) Computational domain.
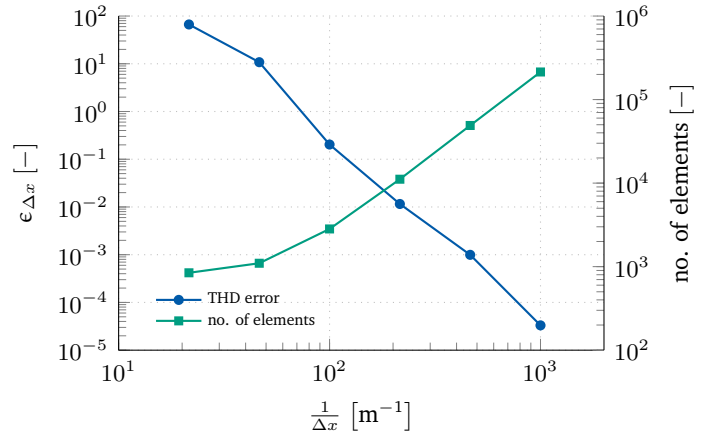
(b) relative error and number of elements in the mesh.

Figure 5.6. Mesh sensitivity analysis. (a) Sketch of the computational domain. (b) Relative error in the calculation of the total harmonic distortion index and number of elements in the mesh, as function of the reciprocal of the maximum mesh size.

configuration is used as an external field source, and it is applied by imposing a non-homogeneous Dirichlet boundary condition for $\vec{A}$ on the exterior boundary $\Gamma_{\text{dir,A}}$. In practice, by expressing a field in terms of its multipole decomposition, every multipole can be associated to a boundary condition, which can be applied independently on the exterior boundary such that the desired field configuration is obtained in $\Omega_{0,A}$. The multipoles are then calculated from the model along the reference circumference Γ_{ref}, and compared with the multipoles calculated analytically by knowing the solution field at the boundary. The relative error $\epsilon_{\Delta x}$ is defined as

$$\epsilon_{\Delta x}(\vec{B}) = \frac{|F_{\text{d}}(\vec{B}) - F_{\text{d}}^{\Delta x}(\vec{B})|}{F_{\text{d}}(\vec{B})}, \tag{5.17}$$

where F_{d} and $F_{\text{d}}^{\Delta x}$ are the THD factors in (5.15) for the field solutions obtained analytically and numerically. The error is shown in Figure 5.6b as a function of the reciprocal of the maximum element size Δx_{max}. The analysis shows that by adopting triangular elements with $\Delta x_{\text{max}} = 1\,\text{mm}$ for the mesh discretization, the estimated error in the calculation of the field multipoles is bounded below 3×10^{-5} units of THD. This threshold is assumed in the following as a sufficient accuracy.

5.2.5 Iron hysteresis

The choice for the magnetic material used in the iron yoke of the Feather-M2.1-2 magnet is optimized for minimizing the detrimental influence of the iron hysteresis on the magnetic field quality. Unfortunately, no material characterization data was available, however the magnetic material in use is similar to the one in use for the LHC main dipole magnets. Therefore, the nonlinear magnetic permeability curve $\mu(\vec{B})$ traditionally used for the simulation of the LHC magnets [286] is adopted in this magnet model. The $\mu(\vec{B})$ curve, also referred at as the first magnetization curve, is shown in Figure 5.7a by means of a dashed line.

From magnetostatic simulations, it is observed that in stand-alone operations, most of the outer iron yoke of the Feather-M2.1-2 magnet remains unsaturated up to the maximum current of $5\,\text{kA}$. As a consequence, it
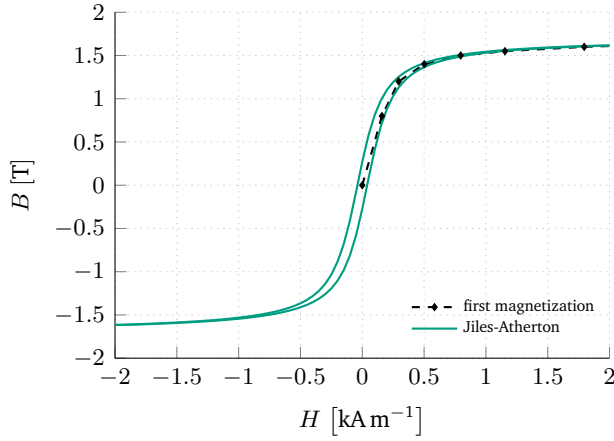
(a) Iron magnetic characteristics
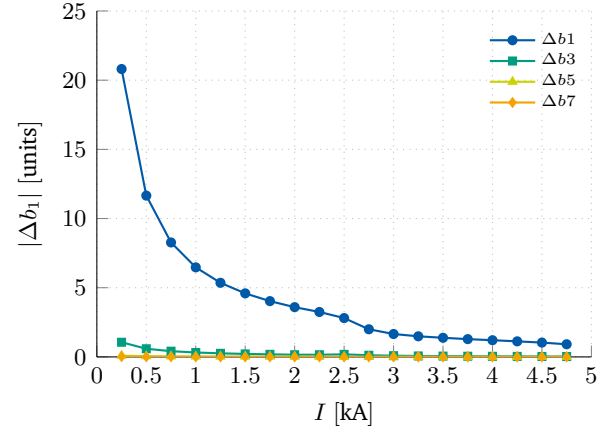
(b) Magnetization due to iron hysteresis

Figure 5.7. Magnetization contribution to the field quality due to iron hysteresis. (a) Nonlinear magnetic characteristics of the iron. (b) Amplitude of the magnetization loop of the field multipoles, as a function of current.

Name	Unit	Value	Description
M_s	$A\,m^{-1}$	1.35×10^6	Saturation magnetization
a	$A\,m^{-1}$	90	Domain wall density
k	$A\,m^{-1}$	40	Pinning loss
c	-	1×10^{-6}	Magnetization reversibility
α	-	50×10^{-6}	Inter-domain coupling

Table 5.3. Parameters for the Jiles-Atherton hysteresis model.

is not possible to neglect a-priori the contribution of the iron hysteresis on the field quality. A coercive field $H_c = 40\,A\,m^{-1}$ is considered for the material used in the iron yoke, in agreement with the LHC specifications ($H_c \leq 60\,A\,m^{-1}$ [59]). The hysteresis behavior of the iron is captured in the numerical simulations by using the Jiles-Atherton model [287]. The magnetization loop is determined from the first magnetization B(H) which is used as reference. The relevant parameters for the hysteresis model are obtained using the open-source algorithm from [288] and are given in Table 5.3.

The hysteresis contribution is quantified for a simplified version of the Feather-M2.1-2 numerical model. In detail, the simplified model assumes a homogeneous current density distribution in the coil cross section, and neglects dynamic and nonlinear effects with the exception of the hysteresis behavior of the iron. The field multipole coefficients are extracted as a function of the source current, for both the upper and the lower curve of the hysteresis loop from the Jiles-Atherton model. Then, the two obtained data sets $b_{up}(i_s)$ and $b_{dn}(i_s)$ are compared, and their difference $\Delta b(i_s) = b_{up}(i_s) - b_{dn}(i_s)$ provides the amplitude of the magnetization loop for each multipole coefficient and level of current source. In this way, the influence of the iron hysteresis on the magnetic field quality is estimated. The variation in the multipole coefficients $\Delta b(i_s)$ is shown in Figure 5.7b, in units, as a function of the source current. At low current, the hysteresis of the iron produces a minor influence on the main field component b_1, with a peak value of about 20 units rapidly decreasing once the current increases. Concerning the higher order multipoles b_3, b_5 and b_7, the hysteresis shows almost no influence since the magnetic contribution remains below one unit. Overall, the hysteresis contribution reduces once the current increases, since the width of the hysteresis loop narrows.

Scenario	T_{op} (K)	I_{p} (kA)	B_{p} (T)
1	4.5	5	2.5
2	9	4.75	2.4
3	25	3.75	2.0
4	68	1.75	1.0

Table 5.4. Main parameters for the simulated scenarios.

The analysis shows a limited influence from the iron hysteresis on the magnetic field quality, at the price of an increased computational cost. Moreover, the influence of the iron hysteresis on the screening currents in the coil can be reasonably assumed a second order effect, thus negligible. For this reason, the iron hysteresis is excluded from the numerical model of the Feather-M2.1-2 magnet.

5.3 Comparison of Simulations with Measurements

The numerical model of the Feather-M2.1-2 magnet is validated by comparing available experimental observations with the simulation results of the magnetic field quality in the magnet aperture. The comparison is carried out for four scenarios differing in the peak source current I_{p}, that is, in the peak magnetic field, and the operational temperature T_{op} of the magnet. The relevant parameters characterizing the scenarios are given in Table 5.4. In accordance with the measurements, T_{op} is assumed as homogeneous and constant in the numerical model, for each scenario. The scenarios at higher T_{op} feature the use of lower peak currents, keeping the ratio between the peak current and the critical current of the cable as constant. In the following, the measurement and simulation setups are discussed, and the comparison between experimental and numerical results is presented. All the simulations are carried out on a standard workstation (Intel® Core i7-3770 CPU @ 3.40 GHz, 32 GB of RAM, Windows-10® Enterprise 64-bit operating system), using the proprietary FEM software COMSOL.

5.3.1 Measurement setup

The magnetic field multipoles B_k and A_k introduced in Section 5.1 are measured by means of rotating-coil magnetometers, also known as harmonic or rotating coils, which work as electromagnetic transducers. Rotating coils are mounted on a shaft which is positioned parallel to the magnetic axis of the magnet, and rotated within the magnet aperture. The change of flux linkage Φ in the pick-up coil induces a voltage signal U_{m} according to the integral Faraday's law for MQS problems

$$U_{\mathrm{m}} = -\frac{d}{dt}\Phi \tag{5.18}$$

which is measured at the terminals of the coil. The voltage signal is integrated in time, and the obtained flux linkage is decomposed into a series expansion, as a function of the radial component of the magnetic field [59]. For rotating coils wound from wires of negligible thickness, and perfectly centered in the aperture of a magnet and rotating with angular velocity ω, the flux linkage is given at time t as

$$\Phi(t) = \sum_{k=1}^{\infty} f_{\mathrm{s}}(k) \left[A_k(r_{\mathrm{c0}}) \cos k\varphi - B_k(r_{\mathrm{c0}}) \sin k\varphi \right], \tag{5.19}$$

(a) First scenario.

(b) Second scenario.

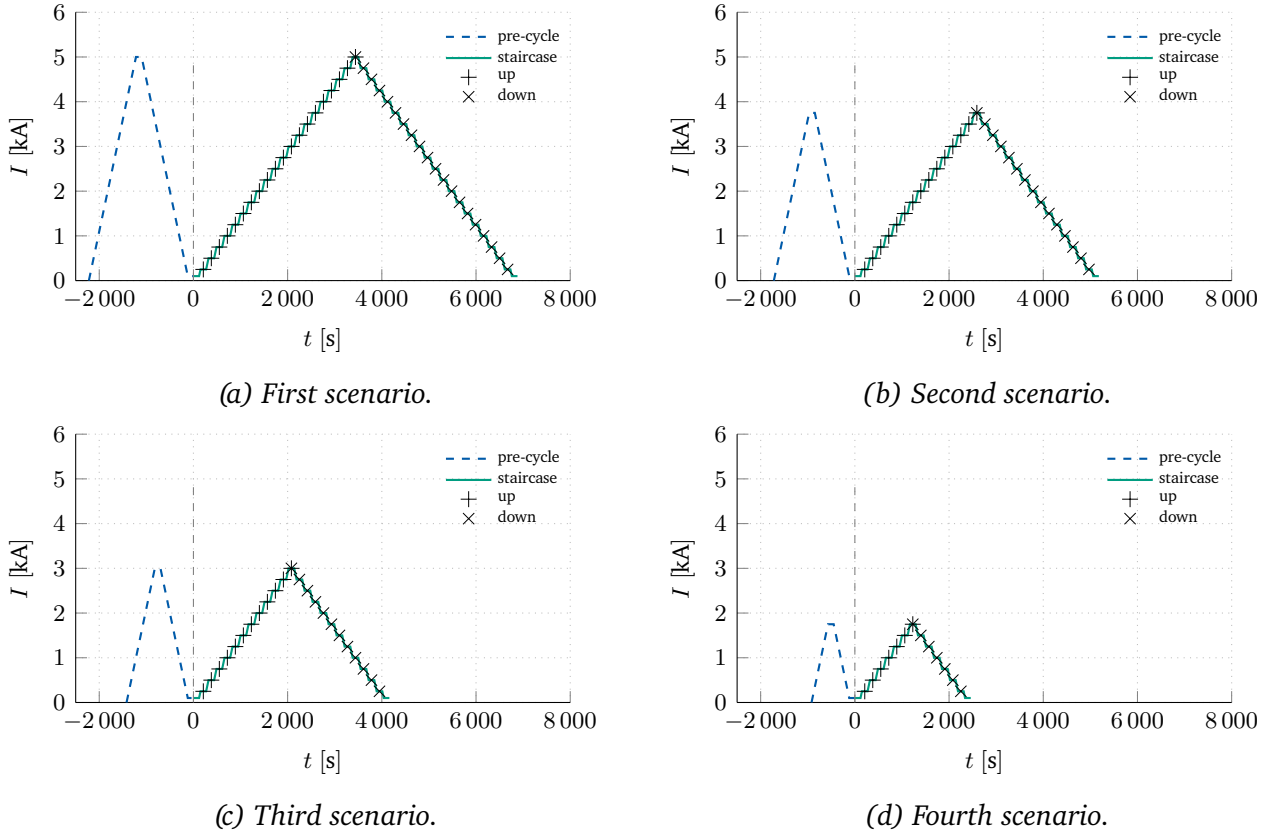(c) Third scenario.

(d) Fourth scenario.

Figure 5.8. *Current profiles used as source terms for the simulations of the four scenarios. The current follows a trapezoidal pre-cycle, then a staircase profile, up to the peak current and back. The markers at the current plateaus (up and down labels) represent the evaluation points for the magnetic field quality for both the ascending and descending part of the staircase.*

where $\varphi(t) = \omega t + \varphi_0$ is an arbitrary angle. The coil sensitivity factor $f_s : \mathbb{R} \to \mathbb{R}$ embeds the coil geometric parameters, namely the number of turns N_c, longitudinal length l_c and the mean radius r_{c0}, and it is given by

$$f_s(k) = \frac{2 N_c l_c r_{c0}}{k}. \tag{5.20}$$

The geometric parameters related to the coil sensitivity factor are known, being obtained either by calculation or by calibration of the rotating coil in reference dipole magnets [289], resulting in a constant coil sensitivity factor.

A dedicated rotating-coil magnetometer was developed and employed to test the Feather-M2.1-2 magnet in the variable temperature cryostat at CERN, after the encouraging results obtained from the flux sensors presented in [276]. The adopted coil shaft hosts a chain of five printed-circuit boards (PCBs), ($200\,\mathrm{mm}$ in length and $35\,\mathrm{mm}$ in width), that cover the entire magnet length including the fringe-field areas in the end-coil region. Every PCB board contains three coils which are mounted radially, providing an active surface of $1817\,\mathrm{cm}^2$. For measuring the magnetic-field harmonics, the sensitivity is improved by connecting two coils in anti series; in case of measurements in a dipole magnet, such as the Feather-M2.1-2, the signal from the central coil is subtracted to the one from the external coil. The rotating frequency of the coils is set to $2\,\mathrm{Hz}$, and the integration of the induced voltage signals is done by means of CERN proprietary digital cards [290].

The measurement results used for validating the numerical model of the magnet are taken from the longitudinal center of the magnet (the central element of the rotating shaft of 200 mm in length), delivering a measurement precision of a magnetic-field harmonic of ± 0.05 units.

5.3.2 Simulation setup

In the numerical model, the magnet is powered via a current source which matches the one used in the experimental procedure. As shown in the example in Figure 5.8, the current source profile can be separated in two phases consisting in a trapezoidal pre-cycle, and a staircase profile:

1. The pre-cycle waveform goes from $0\,\text{A}$ up to the peak current for the given scenario, and then back to $100\,\text{A}$. The pre-cycle is used for magnetizing the iron yoke, and for removing the dependency of the superconducting coil on the first magnetization cycle.
2. The staircase waveform spans from a minimum value of $0.25\,\text{kA}$ up to the peak current, and back. The steps in the signal are composed of ramps of $\Delta I = 250\,\text{A}$ at a rate of change of $10\,\text{A}\,\text{s}^{-1}$, and plateaus where the values are kept constant for $\Delta t_{\text{flat}} = 120\,\text{s}$. The purpose of the staircase is to bring the magnet into static conditions, at different current values.

The magnetic field is evaluated at the reference radius for each midpoint in the staircase plateaus, shown in Figure 5.8 with a marker, and the field quality is then calculated and compared with measurements. The shape of the steps in the staircase and the field evaluation point is kept consistent between the different scenarios given in Table 5.4, however the number of steps is adapted such that the prescribed peak current is not exceeded.

The staircase profile is chosen since it allows quantifying the influence of hysteresis phenomena occurring within both the superconducting coil and the iron yoke of the magnet (see [276]). With respect to Figure 5.8, each discrete current level in the staircase profile is reached twice, first during the current ramp-up and then again during the ramp-down. Therefore, it is possible to group the measured and simulated field quality dataset into pairs sharing the same current level. The related datasets are highlighted by the *up* and *down* labels. Subsequently, the difference of the field multipoles is calculated for each pair. In this way, the contributions of the non-ideal geometry of the coil and the iron saturation are canceled out, being the same for both evaluations in each pair, and the residual can be fully attributed to the hysteresis phenomena. In other words, the procedure allows for a calibration of all the non-hysteresis phenomena occurring in the magnet. Moreover, since the iron hysteresis was previously found to produce only a second-order effect on the field quality (see Section 5.2.5), the hysteresis contribution is fully attributed to the persistent magnetization of the superconducting coil.

5.3.3 Results: field quality

The measured and simulated field multipole coefficients are shown in Figure 5.9. In detail, the markers are assigned to the measurements which are grouped in the *up* and *down* datasets, according to the upward and downward part of the current staircase (see Figure 5.8), as discussed in the previous section. The area provided by the shaded region shows the upper and lower envelope of the numerical solutions obtained by means of parametric sweep of the n-value in the power law, for values between 4 and 30. As an example, solid lines present the simulation results for the value $n = 20$.
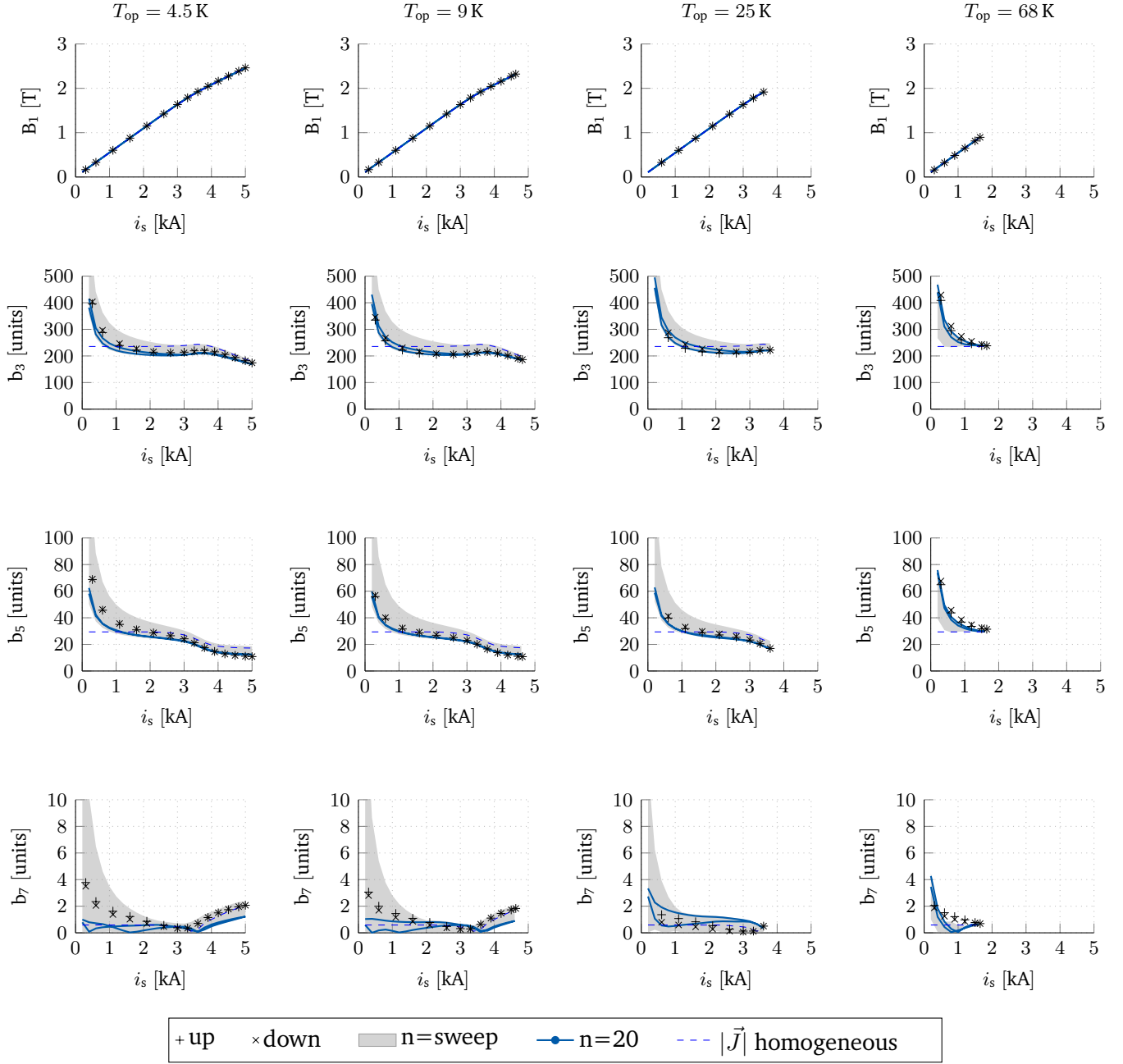
Figure 5.9. Magnetic field quality in the magnet aperture as a function of the current, using a current staircase profile (see Figure 5.8). Measurements are given by markers, whereas the shaded area corresponds to the envelope of the numerical solutions, obtained with the parametric sweep of the n-value as $4 \leq n \leq 30$. The solution for $n = 20$ is marked with a solid line. The dashed line is obtained by assuming a homogeneous current density distribution in the superconducting tapes. From left to right: results at 4.5, 9, 25, and 68 K. From top to bottom: results for the B_1, b_3, b_5, b_7 multipole coefficients.
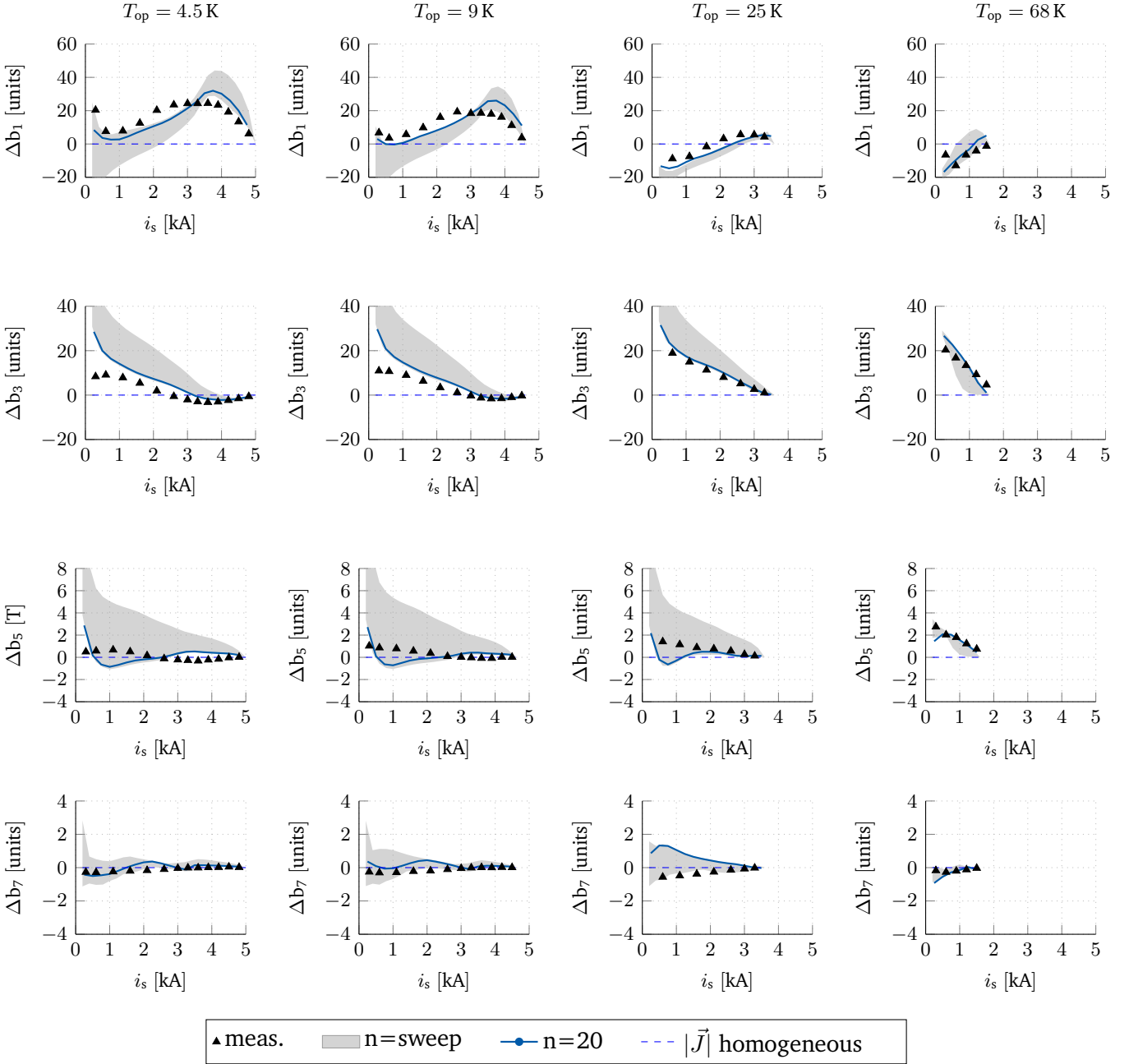
Figure 5.10. Screening currents-induced magnetic field contribution to the magnetic field quality, in units, as a function of the current in the magnet. Measurements are given by markers, whereas the shaded area corresponds to the envelope of the numerical solutions, obtained with the parametric sweep of the n-value as $4 \leq n \leq 30$. The solution for $n = 20$ is marked with a solid line. The dashed line is obtained by assuming a homogeneous current density distribution in the superconducting tapes. From left to right: results at 4.5, 9, 25, and 68 K. From top to bottom: results for the b_1, b_3, b_5, b_7 multipole coefficients.

The dashed lines show a limit case where the screening currents are disabled, thus not having any influence on the field quality. For instance, this is done for the $\vec{A} - \vec{H}$ coupled field formulation by artificially increasing the resistivity of the superconducting coil, such that a homogeneous current density distribution is achieved. The rows show, from top to bottom, the normal dipole field B_1 and the multipoles b_3, b_5 and b_7, as a function of the source current applied to the magnet. The columns discriminate the results according to the operational temperature of the magnet, namely 4.5, 9, 25, and $68\,\mathrm{K}$ which define the simulated scenario.

It is observed that the field multipoles show the same qualitative behavior through the different scenarios (see Figure 5.9, row by row). Moreover, the b_3 and b_5 multipoles decrease for increasing current. The b_7 coefficient is negligible with respect to the other multipoles. The scenario at $4.5\,\mathrm{K}$ shows the highest variation in the magnitude of the multipoles. At low current, the b_3 contribution increases of about a factor 2, from 200 to 400 units, and the b_5 multipole shows an increase of a factor 8, from 10 to 80 units. This is explained by higher screening currents at low temperature, due to the higher critical current density of the tape.

In Figure 5.9, the curves associated to the field multipoles create loops. Therefore, the magnetic configuration of the magnet is different for the ramp-up and ramp-down phases. As the measurements and simulations are done for static conditions, this difference is associated to hysteresis phenomena due to magnetization currents occurring in the superconducting coil. The loops are found to be at least one order of magnitude smaller than the absolute value of the multipole coefficients. For this reason, the width of the loops is presented separately in Figure 5.10. The layout of the figure and the meaning of symbols is consistent with Figure 5.9. The rows show, from top to bottom, the variation in units for the multipoles defined as Δb_1, Δb_3, Δb_5 and Δb_7, as a function of the source current. The columns separate the results by the operational temperature of the magnet, namely 4.5, 9, 25, and $68\,\mathrm{K}$.

The width of the magnetization loops associated to screening currents does not exceed twenty units for b_1 and b_3, two units for b_5 and one unit for b_7. A generally monotone trend is observed, showing that the field multipoles decrease in magnitude as the current increases, and tend to disappear as the current reaches its peak value. The b_1 coefficient is an exception, as it has a peak around $3.5\,\mathrm{kA}$, when the pole of the iron yoke saturates. In the limit case where the screening currents are neglected, the magnetization loops degenerate into a line or, in other words, the width of the magnetization loops is always zero.

5.3.4 Results: parametric sweep

Numerical simulations are carried out for a parametric sweep on the n-value of the power-law index for the range $4 \leq n \leq 30$, see Section 5.2.2. To compare simulations and field quality measurements, two quantities are introduced as a function of the n-value. The first is the field quality error $\varepsilon_b(n)$ which gives the relative difference of the measured and simulated field multipoles. The second is the persistent magnetization error $\varepsilon_{\Delta b}(n)$ which provides the relative difference between the measured and simulated magnetic loops associated to screening current phenomena. The two quantities combine the datasets from all the measured and simulated scenarios (subscripts m and s), reading

$$\varepsilon_b(n) = \frac{b_{\mathrm{m,tot}} - b_{\mathrm{s,tot}}}{b_{\mathrm{m,tot}}}, \tag{5.21}$$

$$\varepsilon_{\Delta b}(n) = \frac{\Delta b_{\mathrm{m,tot}} - \Delta b_{\mathrm{s,tot}}}{\Delta b_{\mathrm{m,tot}}}, \tag{5.22}$$
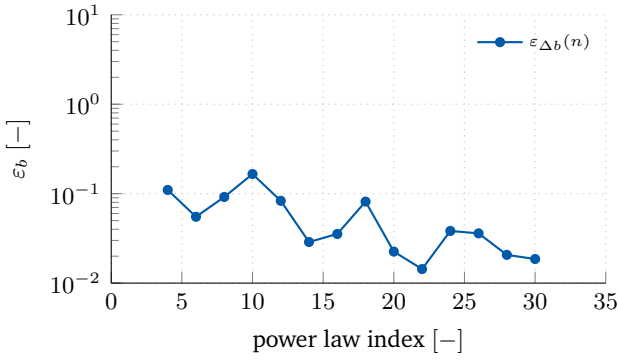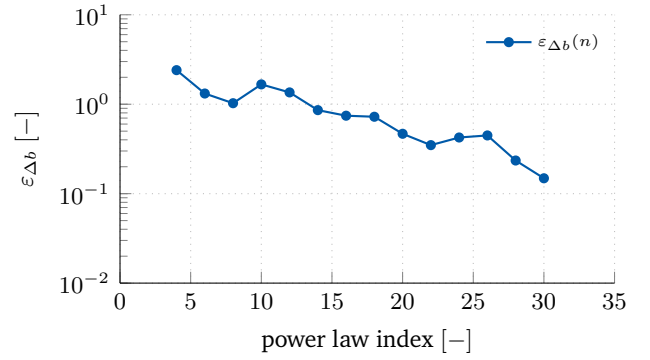
(a) Field quality.   (b) Persistent magnetization.

Figure 5.11. Difference between field quality measurements and simulations. Results are shown for (a) the field quality and (b) persistent magnetization contribution.

with

$$
b_{\mathrm{m,tot}} = \sum_{t_k}^{T_{\mathrm{op}}} \sum_{b_k=b_3}^{b_7} \sum_{i_k} |b_{k,\mathrm{m}}(n, t_k, i_k)|, \qquad \Delta b_{\mathrm{m,tot}} = \sum_{t_k}^{T_{\mathrm{op}}} \sum_{b_k=b_1}^{b_7} \sum_{i_k} |\Delta b_{k,\mathrm{m}}(n, t_k, i_k)|,
$$

$$
b_{\mathrm{s,tot}} = \sum_{t_k}^{T_{\mathrm{op}}} \sum_{b_k=b_3}^{b_7} \sum_{i_k} |b_{k,\mathrm{s}}(n, t_k, i_k)|, \qquad \Delta b_{\mathrm{s,tot}} = \sum_{t_k}^{T_{\mathrm{op}}} \sum_{b_k=b_1}^{b_7} \sum_{i_k} |\Delta b_{k,\mathrm{s}}(n, t_k, i_k)|,
$$

where t_k, b_k and i_k refer to the k-th temperature scenario, multipole component and current level in the staircase profile. The calculation of $\varepsilon_b(n)$ excludes the fundamental components b_1 which are trivial, whereas $\varepsilon_{\Delta b}(n)$ accounts also for the magnetization loops in the fundamental component of the magnetic field. The differences between measurements and simulations are quantified for each scenario as a function of n. The results are shown in Figure 5.11a and 5.11b for the differences in the field quality and persistent magnetization contributions. The errors tend to decrease as the index in the power law is increase.

5.4 Discussion

The analysis of the field quality in the Feather-M2.1-2 magnet provides b_3 and b_5 coefficients up to hundreds of units. This magnitude is much higher than the few units typically required by accelerator quality standards [59] (see Figure 5.9). The overall field error is dominated by the b_3 coefficient, whereas b$_5$ is about one order of magnitude smaller, and b$_7$ is negligible. These high multipoles are justified by the influence of the outer iron yoke. The yoke is designed for allowing the magnet to be operated in stand-alone mode, but it is not optimized for field quality purposes. At the same time, the measured field error is not an issue since the Feather-M2.1-2 magnet is designed to work as an insert in the FRESCA2 magnet where accelerator quality standards are not required.

The trend observed in the multipoles from Figure 5.9 can be justified as follows. The magnet design is optimized to deliver the best field quality when operating in nominal conditions [14]. For this reason, for increasingly higher source currents (i.e. by increasing main dipole field), the multipole coefficients are decreasing reaching their minimum for the nominal current of $5\,\mathrm{kA}$. However, if the operational temperature is
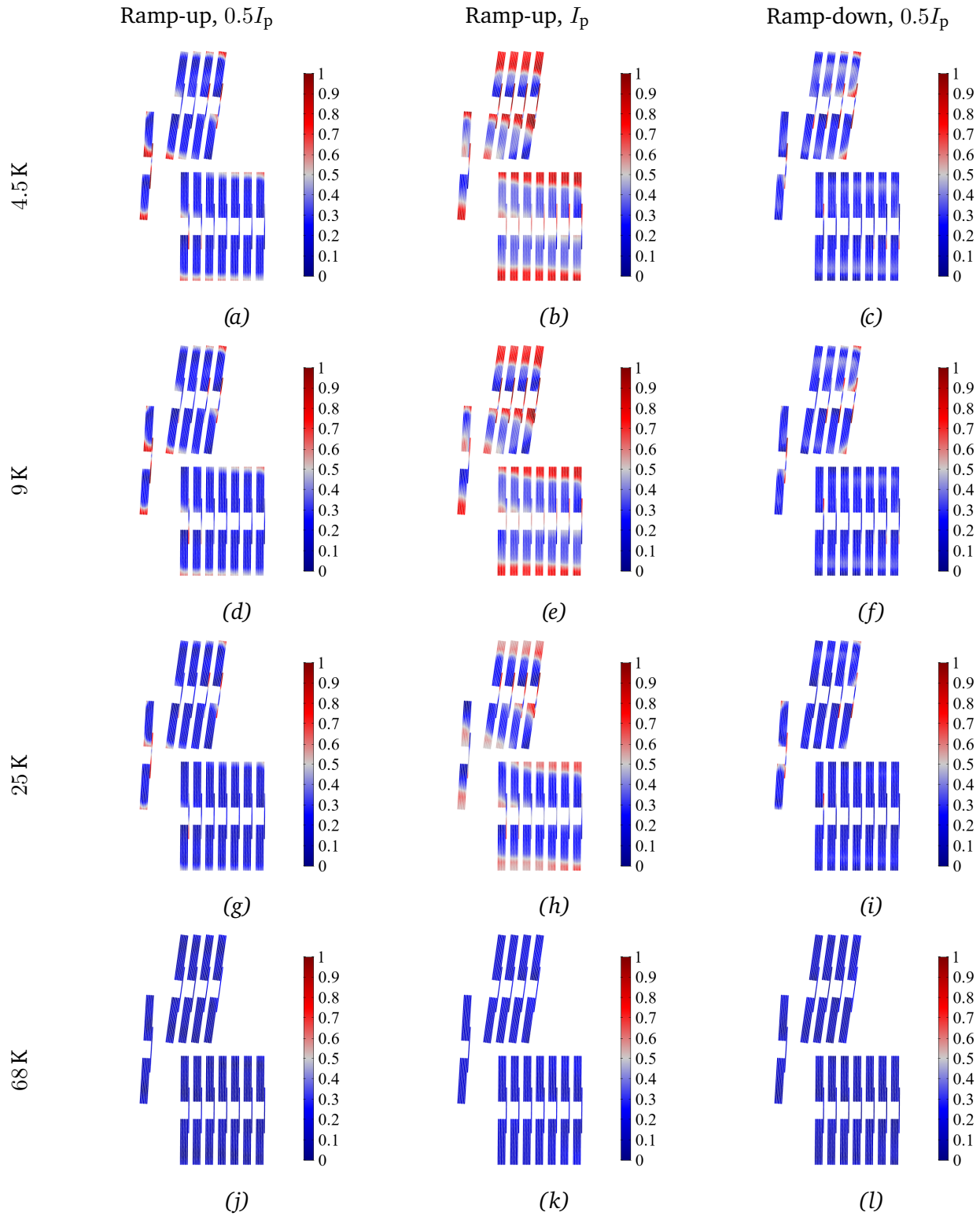
Figure 5.12. Current density distribution in the superconducting coil, normalized by the critical current density at zero field and $4.5\,\mathrm{K}$ $J_{\mathrm{crit},0} = 138\,\mathrm{kA}\,\mathrm{mm}^{-2}$. The distribution is given for different current levels and operational temperatures.

Figure 5.13. Net magnetic field contribution from screening currents in the superconducting coil, in T. The field map is given for different current levels and operational temperatures.

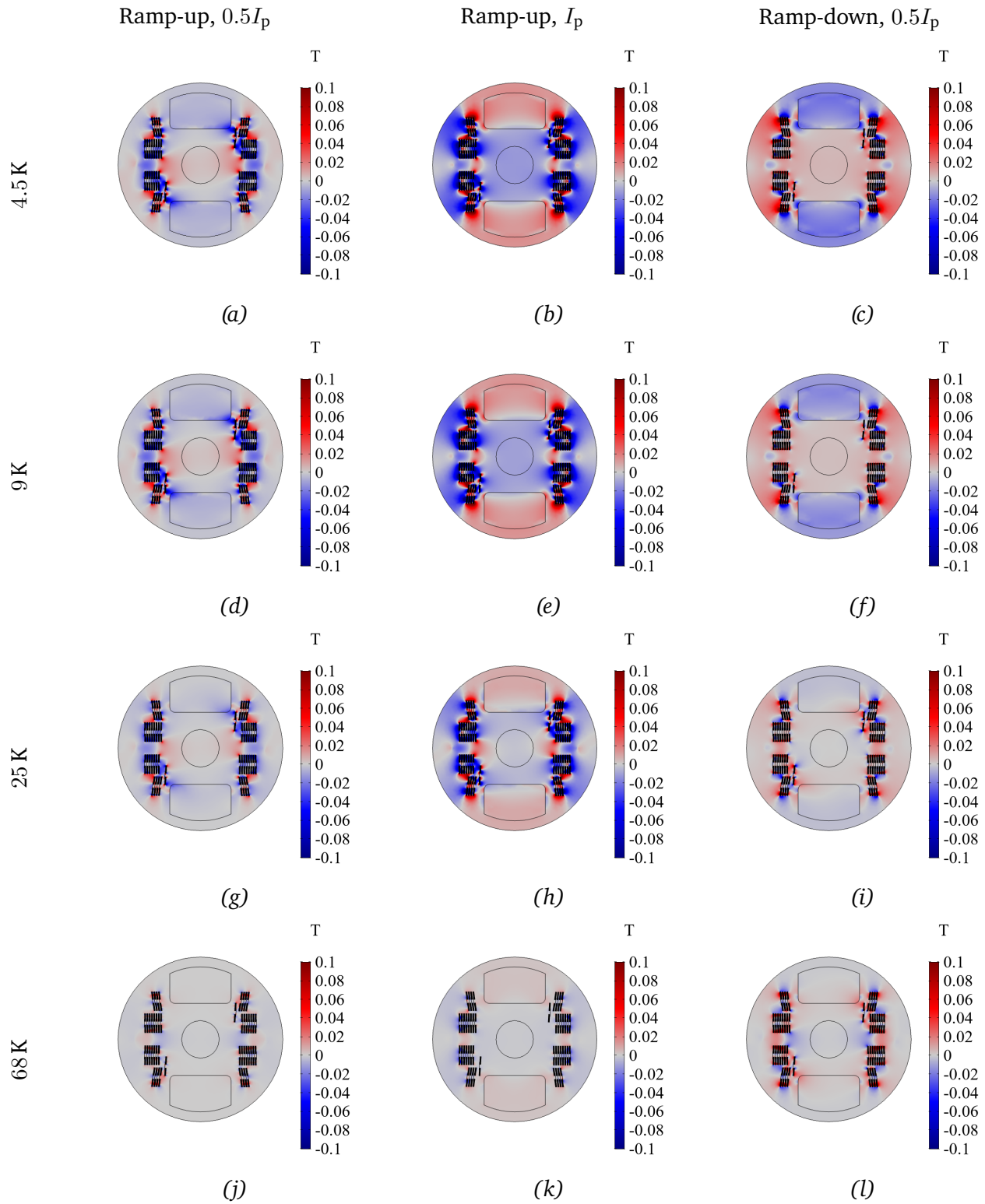increased, the source current needs to be reduced accordingly, to not exceed the cable critical current which is temperature-dependent. In consequence, the b_3 and b_5 multipole coefficients increase since the working point of the magnet then shifts from nominal conditions.

Concerning the behavior of the screening currents in the superconducting coil, their contribution to the field quality never exceeds 20 units, see Figure 5.10. Therefore, the influence of screening currents is about one order of magnitude smaller than the total field error (see Figure 5.9). The numerical analysis shows better agreement with measurements for high n-values ($\geq$20), whereas for small n-values ($\leq$10), the contribution of the screening currents tends to be overestimated, as shown in Figure 5.11. Numerical results seem to support the conclusion in [275] where the low n-value of 5 measured in the coil was attributed to the tape joints which do not play a role in the dynamics of the screening currents. Overall, the limited influence of the persistent magnetization on the field quality might be justified by the design of the coil. The alignment of the tapes is optimized to limit the interaction of the wide surface of the tapes with the magnetic field lines [68], limiting the flux linked to the surface of the tapes, and thus magnetization phenomena.

Once the operational temperature of the magnet is increased, the critical current density of the tape is reduced and, for the same magnitude of the source current, the resistivity of the superconducting material is increased. As a consequence, field diffusion phenomena in the tape occur at shorter time scale, consequently leading to a more homogeneous current density distribution in the tape and, ultimately, in the cable. This is shown by the current density distribution in the first quadrant of the coil in Figure 5.12. The current density distribution is normalized by $J_c(4.5\,\mathrm{K}, 0\,\mathrm{T}, 0°) = 138\,\mathrm{kA}\,\mathrm{mm}^{-2}$. The net magnetic field contribution given by the screening currents in the superconducting coil is shown in Figure 5.13. Once the source current is increased, the screening currents tend to vanish independently from the operational temperature. This might be explained by the saturation of the tape due to the external source current.

The numerical simulations are overall in good agreement with measurements, consistently reproducing both the global magnetic field quality and the contribution from persistent magnetization phenomena. However, simulation results are still affected by the uncertainty regarding the properties of the superconducting tapes used for the coil. Still, the analysis captures the most relevant dynamic phenomena characterizing the field-quality-behavior of HTS accelerator magnets. An extensive tape characterization is always recommended for future magnets, such that uncertainties can be minimized, and the confidence and accuracy in dynamic field quality simulations can be enhanced.

5.5 Summary

This chapter presents the analysis in the time domain of the demonstrator magnet Feather-M2.1-2, an HTS insert dipole developed for providing an additional $5\,\mathrm{T}$ to the background field produced by the $\mathrm{Nb_3Sn}$ FRESCA2 magnet, such that a peak field of $18\,\mathrm{T}$ is reached in the magnet aperture. The 2D finite element model of the Feather-M2.1-2 magnet relies on the coupled $\vec{A} - \vec{H}$ field formulation introduced in Chapter 2. Furthermore, the thin-shell approximation is applied for modeling the ReBCO tapes composing the Roebel cable which is used for the coil. Although uncertainty affects the critical current density of the tapes, the model requires only one scalar correction parameter which is applied to the power law. A parametric sweep is used to cope with uncertainty in the power-law index. Subsequently, a mesh sensitivity analysis is carried out to determine the maximum size for the mesh elements in the model. The hysteresis contribution of the ferromagnetic materials to the field quality is quantified by means of the Jiles-Atherton model for the iron yoke of the magnet.

The numerical analysis quantifies the impact of the screening current-induced magnetic field on the magnetic field quality in the magnet aperture. Simulations follow the same staircase-shaped powering cycle used for the magnet measurements at different temperatures. Numerical results are compared with available measurements for the magnet in a stand-alone configuration. The model provides an accurate quantification of the dynamic distribution of the screening currents, resolving the individual tapes. Simulations achieve satisfactory agreement with measurements, with a computational time less than one hour for each simulation, on a standard workstation. For the investigated case study, results show that the field quality error due to persistent magnetization phenomena affects mostly the main field component, and it is limited to 20 units. Furthermore, the error is significantly dampened once the source current is increased up to the operational value, as a consequence of the saturation of the current transport capacity of the tape. The iron hysteresis is estimated as a second-order effect, and the coupling between the screening currents and the hysteresis of the iron is found to be negligible.

6 Case Study: HALO

This chapter closely follows the work in [291], presenting a proof of concept for HTS screens leading to a passive cancellation of the magnetic field error in accelerator magnets. The device presented here is called HALO (harmonics-absorbing layered object) and relies on the persistent magnetization produced by stacks of ReBCO tapes.

The working principle of HTS screens is discussed with respect to the behavior of perfect electric conductors. Then, the experimental setup used for the proof of concept is described, with focus on the design of the HTS screens. A dedicated 2D numerical model is developed using the finite element method, implementing the coupled $\vec{A} - \vec{H}$ field formulation. Simulations are used for evaluating the performance limits of the HTS screens, and tracing the residual error measured in the magnetic field due to geometric defects. Afterwards, numerical and experimental results are compared. The performance of the screen is then explored for different design parameters, both with respect to experimental conditions and in accelerator-like working conditions, that is, in a $10\,\mathrm{T}$ background dipole field. Results are discussed, and conclusions and recommendations for the design of future HTS screens are given.

6.1 Working Principle

The working principle for superconducting screens is discussed with respect to a non-magnetized shell with finite thickness δ_s and constant resistivity ρ. The shell is surrounded by air, and all the magnetic properties are considered as constant. The shell is assumed to have translational symmetry, therefore the working principle is discussed with respect to a 2D setting. The cross section of the shell is shown in Figure 6.1a, together with a local coordinate system $(\vec{t}, \vec{n})$ oriented according to the shell wide surface. The shell is exposed to a time-dependent magnetic flux density $\vec{B}_\mathrm{s}$ with initial condition $\vec{B}_\mathrm{s}(0) = 0$, applied as an external source. Starting from Faraday's law, the current density $\vec{J}_\mathrm{i}$ induced in the shell is described by means of the relation

$$\nabla \times \rho \vec{J}_\mathrm{i} + \partial_t (\vec{B}_\mathrm{s} + \vec{B}_\mathrm{i}) = 0, \tag{6.1}$$

where $\vec{E} = \rho \vec{J}_\mathrm{i}$ represents the electric field strength driving the induced currents, and $\vec{B}_\mathrm{i}$ is the magnetic contribution from the shell to the total magnetic flux density $\vec{B}$. Due to the linearity of the field problem, $\vec{B}$ is given by the superposition of the source and induced magnetic fields, that is, $\vec{B} = \vec{B}_\mathrm{s} + \vec{B}_\mathrm{i}$. The distribution of the field lines is shown in Figure 6.1b, for an arbitrary orientation of the source field with respect to the shell.

The magnetic behavior for ideal screens is obtained in two steps. First, the thickness of the shell is assumed to be negligible, that is, $\delta_\mathrm{s} \to 0$ (see Figure 6.1c). In this way, the magnetic coupling occurs only for the normal component of the external field source, leaving the parallel component unaffected. At the same time, the induced current density flows only in the plane of the shell. Then, the differential operators and vectors
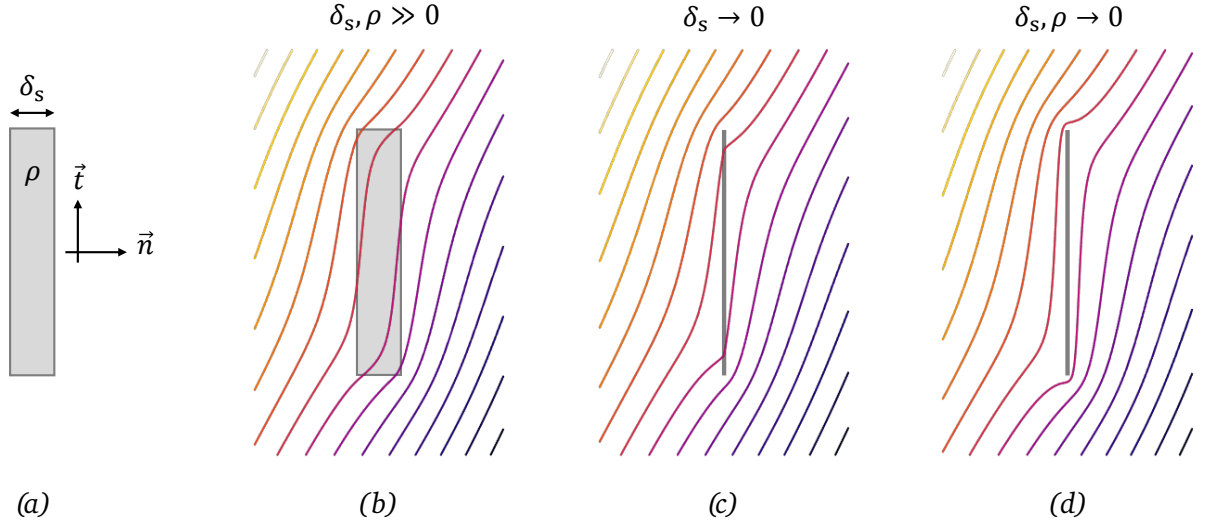
Figure 6.1. (a) Cross section of a non-magnetized, conducting shell of thickness δ_s and resistivity ρ. The magnetic flux lines distribution is shown for the cases of (b) finite δ_s and ρ, (c) negligible δ_s but finite ρ, and (d) negligible δ_s and ρ.

$\vec{v}$ are decomposed into their tangential and normal components (subscripts t and n) as $\nabla = \nabla_t + \nabla_n$ and $\vec{v} = \vec{v}_t + \vec{v}_n$, according to the local coordinate system in Figure 6.1a. The assumption of $\delta_s \to 0$ is incorporated by following Section 2.14, that is, by assuming no field variation can occur along the perpendicular direction of the tape. The relation (6.1) is therefore reduced to

$$\nabla_t \times \rho \vec{J}_{i,t} + \partial_t(\vec{B}_{s,n} + \vec{B}_{i,n}) = 0. \tag{6.2}$$

Second, the resistivity of the shell is assumed to be negligible, that is, $\rho \to 0$ (see Figure 6.1d). In this way, the material composing the shell becomes a perfect electric conductor (PEC). As a consequence, (6.2) is reduced to

$$\partial_t(\vec{B}_{s,n} + \vec{B}_{i,n}) = 0, \tag{6.3}$$

showing that the magnetic field has a constant value within the shell. By recalling that the external field was initially assumed to be zero, it is concluded that $\vec{B}_{i,n}$ is always equal and opposite to $\vec{B}_{s,n}$. Consequently, the induced currents screen out the magnetic field and are persistent, showing no decay over time. The magnitude of these screening currents is fixed by the magnetization which is required for canceling out the source field contribution from within the shell. Therefore, PECs can be considered as ideal magnetic screens.

Although PECs provide a perfect magnetic screening, they are a mathematical abstraction. However, the superconducting properties of HTS tapes can be exploited for achieving a reasonable approximation of $\rho \to 0$, producing persistent magnetization by means of screening currents. The persistent magnetization, combined with the negligible thickness of the tapes and their strong geometric anisotropy, produces a selective magnetic coupling with respect to the spatial components of the applied field. The tapes can be used for guiding the magnetic field lines by choosing a suitable orientation, thus achieving a field compensation only for specific field components. This is obtained by aligning the tapes with the main field direction, such that the cancellation effect occurs only for the undesired field components. In this way, the screens do not require any active control, and store a negligible fraction of the total magnetic energy in the main field. The working
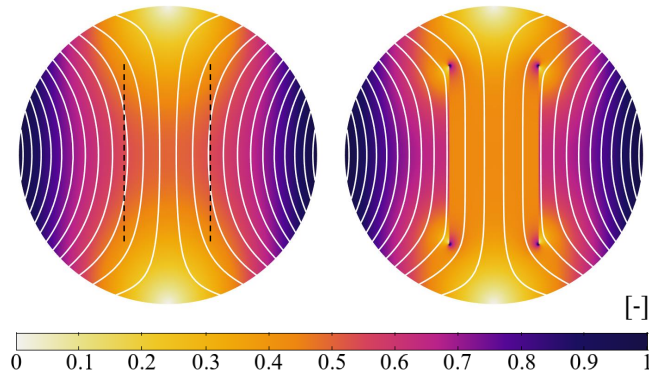
Figure 6.2. Example showing a normalized, non-ideal dipole magnetic field, before (left) and after (right) the introduction of the HTS screens. The expected and actual position of the screens is marked by dashed and solid lines.

principle is illustrated by the example provided in Figure 6.2, where a non-ideal dipole magnetic field is shown before (left) and after (right) the introduction of the HTS screens. Since the width of commercially available tapes is typically limited to $12\,\mathrm{mm}$, the equivalent screening surface can be increased by arranging the tapes side by side into layers. Layers can be stacked on top of each other, increasing the equivalent magnetic screening properties. The discussion of the working principle is carried out for straight screens and dipole magnetic field configurations, however the field-error cancellation is applicable also to 2D magnetic field configurations with higher number of magnetic poles (e.g. quadrupole fields) as long as the superconducting screens are shaped following the main field component.

6.2 Experimental Setup

The proof of concept for HTS screens is shown by improving the magnetic field quality in a given region of space by means of screening currents. The proof is achieved by quantifying the magnetic field quality with and without the presence of the HTS screens, using differential measurements. The experimental setup is composed of four key-elements:

1. a dipole field of known magnetic properties, provided by the reference dipole magnet MCB24 from the magnetic measurement laboratory at CERN;
2. a source of field perturbation, that is, two iron bars introduced in the magnet aperture such that the reference field is distorted;
3. the field-error cancellation, provided by two HTS screens;
4. a magnetic measurement system for characterizing the field quality, composed of a rotating coil [292, 293], a motor drive, and the data acquisition system for processing the probe signal.

6.2.1 Prototypes

The mechanical assembly ensures that the HTS screens and the iron bars are kept in the desired position, and provides the cryogenic environment needed for cooling the screens such that they enter the superconducting
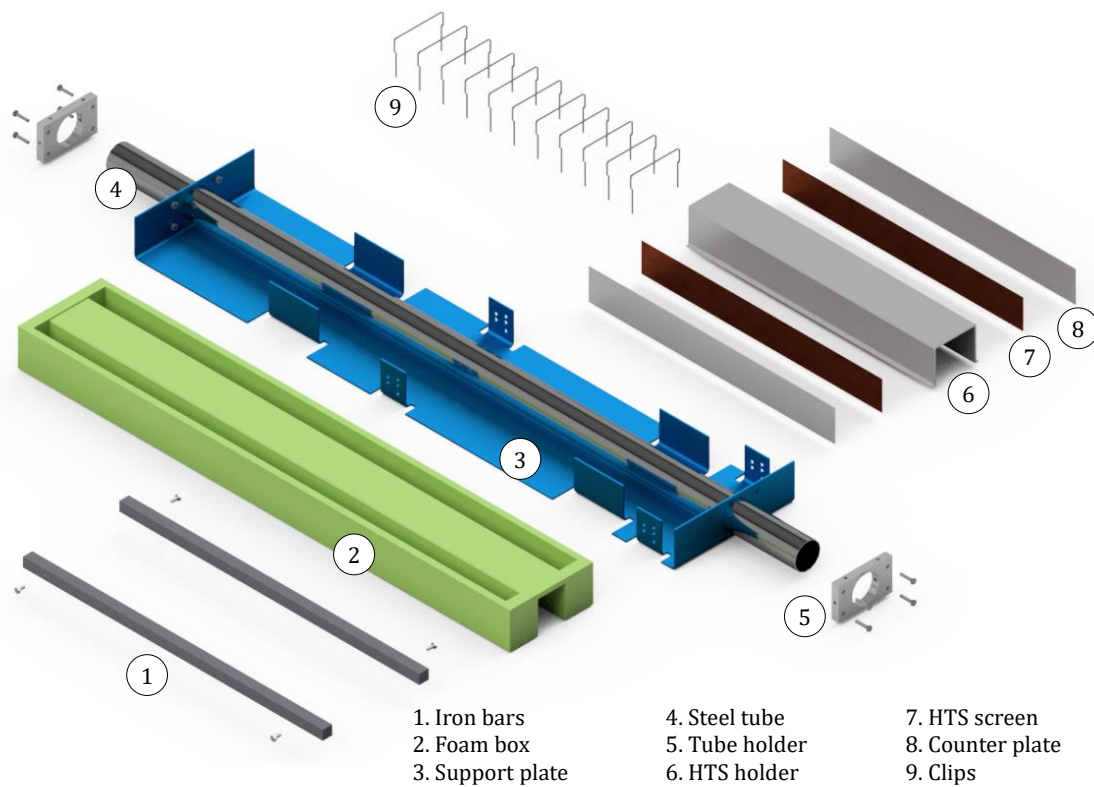
Figure 6.3. Exploded view of the experimental assembly. 1. iron bars, 2. polymide foam box, 3. aluminum support plate, 4. stainless steel tube, 5. aluminum collars, 6. aluminum HTS holder, 7. HTS screens, 8. aluminum counter plates, 9. stainless steel clips.

1. Iron bars
2. Foam box
3. Support plate
4. Steel tube
5. Tube holder
6. HTS holder
7. HTS screen
8. Counter plate
9. Clips
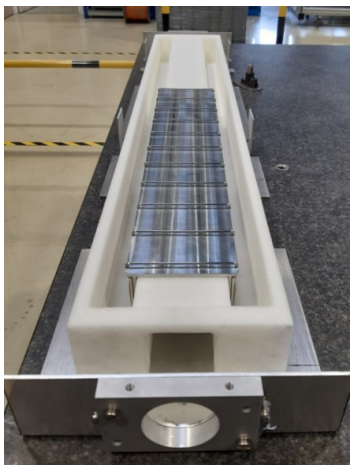
(a) Experimental assembly.
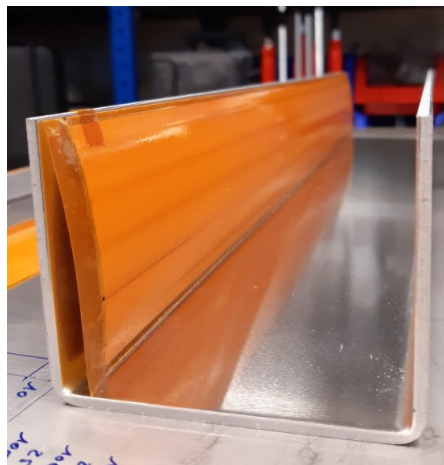
(b) First and second HTS holder prototype.

Figure 6.4. Photographs of (a) the experimental assembly and (b) the first and second prototype.

(a) Structure of one HTS screen.

(b) Photograph of one HTS screen.

1. Polymide tape
2. Epoxy adhesive
3. HTS tape

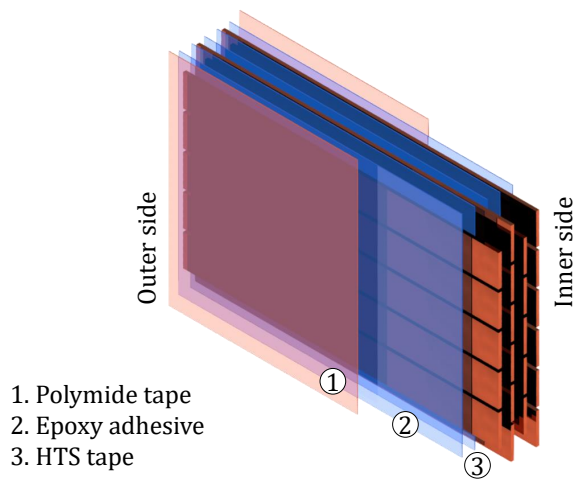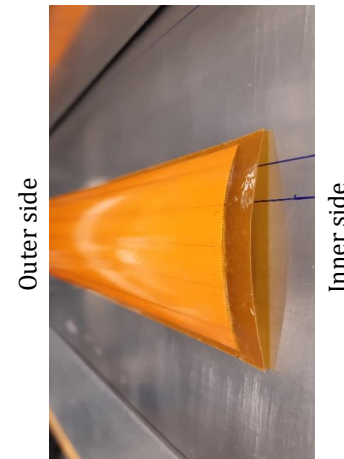*Figure 6.5. Multilayered composite structure characterizing the HTS screens. The figure shows one of the HTS screens, as (a) designed and (b) manufactured.*

state. The assembly is composed of an aluminum base plate, a stainless steel tube, two iron bars and a box made of polymide foam, hosting the HTS holder with the superconducting screens. The assembly is shown in Figure 6.3 as an exploded view highlighting the sub-components.

The plate provides both the mechanical reference for the alignment in the magnet aperture and the mechanical support for the remaining parts. The tube is bolted by means of collars to the front and back folded tabs of the plate, hosting the field measurement system. The iron bars are bolted on perforated folded tabs located on the left and right sides of the plate. A set of holes allows the iron bars to be vertically displaced, such that the field-error cancellation can be investigated for different iron configurations and, therefore, field-error scenarios. The box is made of a plastic foam (Solymide$^{\circledR}$) which is leak-tight and acts as a cryostat for cooling down the HTS screens to $77\,\mathrm{K}$ in liquid nitrogen. Three grooves are machined in the box, see Figure 6.4a: the central groove ensures the clearance for the tube containing the rotating coil, and two lateral grooves create two slots such that the HTS holder can slide into the box. The HTS holder provides the mechanical support and keeps the screens in parallel position. For this experimental setup, two prototype iterations for the HTS holder were developed and tested.

The HTS screens are manufactured with commercially available, second-generation HTS tapes; their relevant parameters are given in Table 6.1. The HTS spool is cut in $500\,\mathrm{mm}$ long tapes which are arranged in a multilayered composite structure, as shown in Figure 6.5a. Each layer composing the screen is obtained by aligning the tapes along their narrow edge, and then gluing them together with a $25\,\mathrm{\mu m}$ thick layer of epoxy adhesive. The process is iterated, stacking the layers on top of each other, until the prescribed number of layers is obtained. An offset equal to half of the tape width is introduced between each layer, obtaining a brick wall structure. The offset enhances the screening properties of the structure by preventing the magnetic flux lines to escape through the gaps between the tapes belonging to the same layer. All the even-order layers are one tape-width less wide than the odd-order layers, for symmetry reasons. The screens are finalized by applying a $75\,\mathrm{\mu m}$ thick polymide foil on both sides. The main advantages of this multilayered structure are the electrical insulation between each HTS layer and for the overall screen, the mechanical flexibility, and the scalability in terms of both width and thickness. The two $60\,\mathrm{mm}$ wide screens used for the proof of concept are composed of four layers, containing 5 and 4 tapes. The width of the screens is limited by the

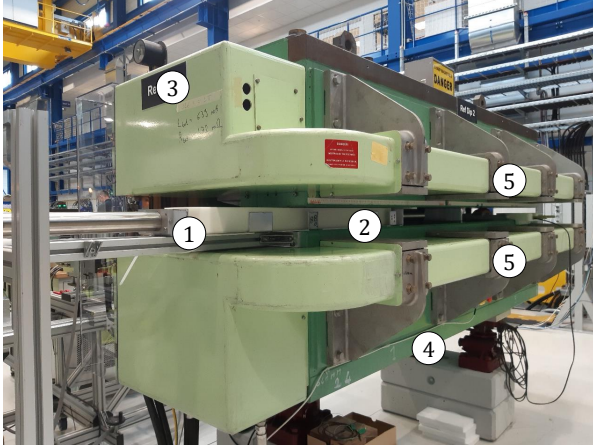| Parameter	Unit	Value	Description
Superpower Inc [294]			Producer
SCS12050-AP			Tape label
Hastelloy C-276			Substrate
δ_{w}	mm	12	Tape width
δ_{t}	μm	100	Tape thickness
$\delta_{\mathrm{t,Sc}}$	μm	1	ReBCO thickness
$\delta_{\mathrm{t,Ag}}$	μm	2	Silver thickness
$\delta_{\mathrm{t,Cu}}$	μm	20	Copper thickness
$\delta_{\mathrm{t,Hs}}$	μm	50	Hastelloy thickness
n-value	-	28	Power-law index
$I_{\mathrm{c,min}}(77\,\mathrm{K})$	A	304	Minimum critical current (self field)
$I_{\mathrm{c,avg}}(77\,\mathrm{K})$	A	320	Average critical current (self field)
$\sigma_{\mathrm{I_c}}$	-	0.042	Standard deviation

Table 6.1. Tape specifications.

available space within the aperture of the reference magnet, and the depth of the cryogenic box. One of the manufactured screens is shown in Figure 6.5b. The curvature in the screen is a result of stacking all the tapes on the same side which caused an amplification of the typical tape curvature. This mechanical behavior does not represent an issue, since the screens are flexible enough to be straightened by the HTS holder. For higher number of layers, therefore for stiffer screens, the curvature effect may be mitigated by turning the tapes in every second layer of each screen.

The first HTS holder prototype aimed for the simplicity of construction (see Figure 6.4b, left). The holder was obtained by bending an aluminum plate, and keeping the screens in place by means of a compression force between the holder and the foam box. The holder was used mainly as an exercise to better understand the behavior of the experimental assembly. However, it was found that the mechanical alignment of the first prototype was not sufficiently accurate for the proof of concept. In fact, the bending of the aluminum slab introduced stresses in the material which were released during the thermal cycles of the holder, degrading the mechanical alignment of the screens. Thanks to the experience gained with the first holder, an improved design was defined for the second prototype, see Figure 6.4b, right. Starting from an aluminum block, the holder was obtained by machining. The screens are kept straightened by means of two aluminum counter-plates pushed by clips positioned at every 50 mm along the holder. The clips are made of non-magnetic stainless steel, and are locked into holes drilled in the two fins at each side of the holder (Figure 6.4b, right). The second prototype is characterized by an improved mechanical tolerance and higher stiffness, producing a better cancellation of the field error. For this reason, experimental activity focused mainly on the second prototype.

6.2.2 Reference dipole and measurement system

The reference dipole magnet used for the experiment is shown in Figure 6.6. The magnet is normal-conducting and has a linear transfer function of $316\,\mathrm{A\,T^{-1}}$ for the 0-1 T field range. The magnet operations are always preceded by an initial de-gaussing cycle. Before each experiment, the magnet goes through a pre-cycle, such that the magnetization of the iron yoke is kept consistent through all the measurements. The profile used for the source current $i_{\mathrm{m}}(t)$ is shown in Figure 6.7. The pre-cycle consists in a trapezoidal profile, going from zero up to the nominal current $I_{\mathrm{n}} = 316\,\mathrm{A}$, and back.

(a) Magnet side view.

1. Experiment
2. HTS screens
3. Dipole magnet
4. Iron yoke
5. Magnet coils
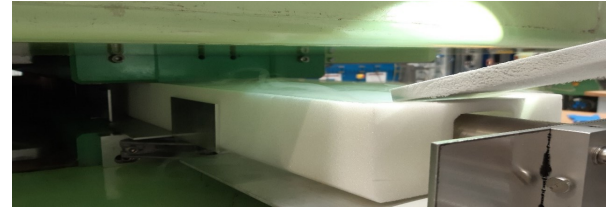6. Steel pipe
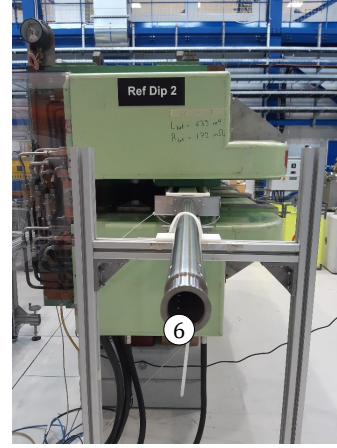
(b) Magnet front view.

(c) Magnet aperture.

(d) Magnet aperture, after cool-down.

Figure 6.6. Photographs of the reference dipole magnet MCB24. (a) Side and (b) front view. The magnet aperture is detailed in (c) and (d).

After the pre-cyle, the setup is fixed into the magnet aperture, see Figure 6.6c. The foam box is 500 mm longer than the HTS screens and sticks out from the magnet aperture, allowing for refilling with liquid nitrogen, see Figure 6.6d. Each test cycle is made of two trapezoidal curves, up to the peak source current $I_s = 31.6$ A producing 100 mT of magnetic field in the magnet aperture. The peak value of the magnetic field is kept well below the nominal value of the magnet, being limited by the critical current density of the tapes at 77 K; the experimental HALO screen is expected to withstand higher magnetic fields when cooled to 4 K due to the higher critical current density, but this test was not possible due to practical considerations. In addition, the relatively low operating current of the magnet limited the forces on the iron bars. The current is kept constant for about 120 s, to settle possible dynamic effects in the normal conducting parts of the experimental setup. For each test cycle, measurements are acquired for both the current plateaus (see Figure 6.7), showing negligible difference. The data presented in this work are taken from the second curve, such that the HTS tapes are always exposed to at least one magnetization cycle.

The magnetic field quality is measured in the magnet aperture by means of rotating coils whose working principle is discussed in Section 5.3.1. The coil used for the HALO characterization is composed of a printed-circuit board (PCB), (36.5 mm long and 47 mm wide), aligned with the longitudinal center of the HTS screens. The PCB contains five coils mounted radially, with a total active surface of 312 cm^2. CERN proprietary digital cards [290] integrate the induced voltages in the coils rotating at a frequency of 1 Hz. Each measurement is given by the average of sixty rotations of the coils. The measurements have a typical precision of a magnetic-field harmonic of ± 0.05 units.
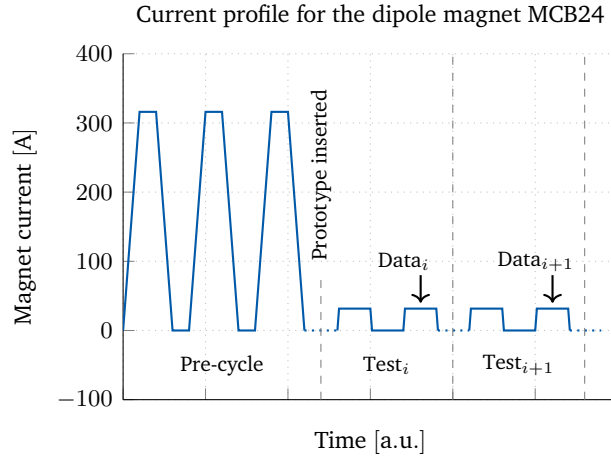
Figure 6.7. Current cycle used in the reference dipole magnet.

6.3 Numerical Model

The HALO experimental setup features translational symmetry, therefore the related numerical model is implemented in the 2D setting. The model contains the reference dipole magnet comprising the normal-conducting coils and iron yoke, the superconducting screens, and the iron bars in the magnet aperture.

The computational domain Ω corresponds to the regions Ω_H and Ω_A, such that $\Omega_H \cup \Omega_A = \Omega$. The region Ω_H corresponds to the superconducting tapes composing the HTS screens. The region Ω_A is further separated into the source region $\Omega_{s,A}$ containing the coils of the magnet, the conducting region $\Omega_{c,A}$ containing the iron yoke and the iron bars, and the nonconducting region $\Omega_{0,A}$ containing the air region and the experimental setup except for the superconducting tapes. A constant magnetic permeability μ_0 is assumed in $\Omega_{c,H}$, whereas a nonlinear dependency $\mu(\vec{B})$ is considered for the iron yoke and the iron bars in $\Omega_{c,A}$. Due to the high aspect ratio of the tapes, and their negligible thickness δ_t, the thin-shell approximation discussed in Section 2.14 is applied to Ω_H. The region is reduced to r conducting shells $\Gamma_{c,H}^r$, one per tape, such that

$$\Gamma_{c,H} = \sum_{r=1}^{N_t} \Gamma_{c,H}^r,$$ (6.4)

where N_t is the number of tapes. The domain decomposition is shown in Figure 6.8. The equivalent resistivity of the superconducting tapes in the thin-shell approximation is obtained as discussed in Section 3.7. The dynamic effects occurring in the iron yoke, the iron bars, the normal conducting coils, and the normal conducting part of the experimental setup are neglected in the model because the magnetic field quality is always evaluated after these contributions are settled.

The domain $\Omega_{s,A}$ is equipped with a distribution function for stranded conductors $\vec{\chi}_{str}$ (see Section 2.9.1), whereas each of the domains $\Gamma_{c,H}^r$ is equipped with a distribution function for solid conductors $\vec{\chi}_{sol}^r$ (see Section 2.9.2), for $r = 1, .., N_t$. The function $\vec{\chi}_{str}$ is used for assigning the source current i_s to the magnet coil, whereas the function $\vec{\chi}_{sol}^r$ is used to enforce a zero net current through each of the tapes in the 2D setting. With

(a) Computational domain.
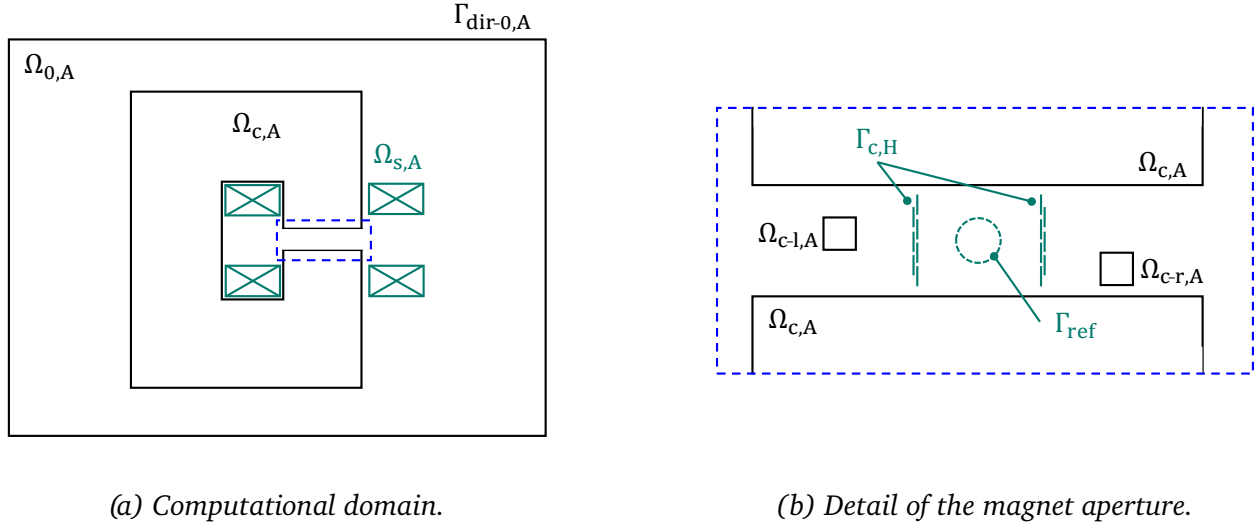
(b) Detail of the magnet aperture.

Figure 6.8. Sketch of the computational domain. (a) The domain is decomposed into the nonconducting air $\Omega_{0,A}$, the conducting iron yoke $\Omega_{c,A}$, and the coil $\Omega_{s,A}$ providing the field source. (b) Detail of the magnet aperture showing left and right iron bars $\Omega_{c\text{-}l,A}$ and $\Omega_{c\text{-}r,A}$, and the HTS screens $\Gamma_{c,H}$. The reference radius is indicated by Γ_{ref}.

the previous definitions, the obtained field problem is given for $r = 1, .., N_t$ as

$$\nabla \times \mu^{-1}\nabla \times \vec{A} + \sigma \partial_t \vec{A} - \vec{\chi}_{str} i_s = 0 \qquad \text{in } \Omega_A, \tag{6.5}$$

$$\nabla \times \rho \nabla \times \vec{H}_n^r + \partial_t \mu \vec{H}_n^r - \nabla \times \vec{\chi}_{sol}^r u_s^r = 0 \qquad \text{in } \Gamma_{c,H}^r, \tag{6.6}$$

$$\delta_t \int_{\Gamma_{c,H}^r} \vec{\chi}_{sol}^r \cdot (\nabla \times \vec{H}_n^r) \, d\Gamma = 0, \tag{6.7}$$

where u_s^r is source voltage for the r-th tape treated as an algebraic unknown. For the purpose of this analysis, the algebraic constraint in (6.7) prescribes a total current equal to zero since the tapes are passive and do not form closed loops. Homogeneous Dirichlet boundary conditions are imposed to $\vec{A}$ on the exterior boundary $\Gamma_{dir\text{-}0,A}$ which is set sufficiently far from the magnetic field sources in the model. The model uses a mesh of first-order elements in $\Gamma_{c,H}$, and second-order elements in $\Omega_{0,A}$.

As an example, the field solution is shown in Figure 6.9a for a dipole magnetic field of $100 \, \text{mT}$ in the magnet aperture. The field source is provided by means of a normal conducting coil, marked with crossed boxes. The c-shaped iron yoke guides the field lines in the magnet aperture, where the experimental setup is positioned. A detailed view of the magnet aperture is given in Figure 6.9b, where the top and bottom plots refer to the cases without and with the experimental setup. For the second case, the field perturbation introduced by the iron bars is clearly visible. The position of the HTS screens is highlighted by dashed lines.

6.3.1 Constitutive relations

The ferromagnetic material used in the model for both the iron yoke and the iron bars consists of pure iron (Fe $> 99.8\%$). The ferromagnetic curve was measured with a split-coil permeameter for a sample of the

(a) Experimental setup.   *(b) Detail of the magnet aperture.*
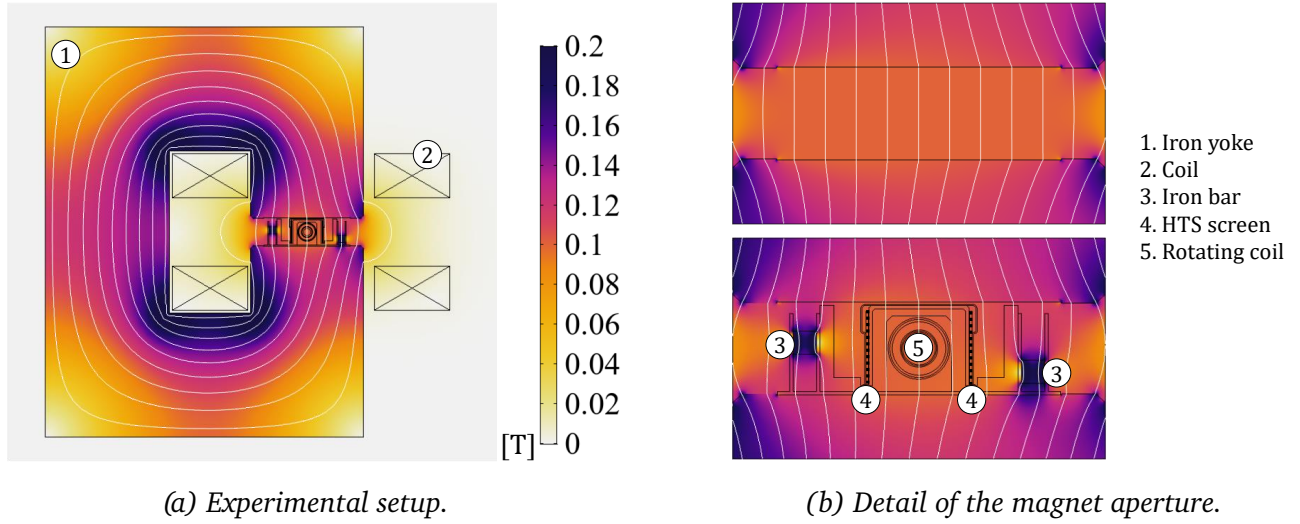
Figure 6.9. Numerical simulations of the experimental setup. (a) Magnetic field, in T, in the cross section of the reference dipole magnet. (b) Detailed view of the magnet aperture, without (top) and with (bottom) the experimental setup.

material used for the bars [267], and implemented in the numerical model as a lookup table. The B-H curve and the relative permeability μ_r are shown in Figures 6.10a and 6.10b.

The highly nonlinear electric field-current density relation characterizing HTS materials is modeled by means of the power law in (2.86). The anisotropic and field-dependent behavior of the critical current density J_c is modeled by means of the lifting function $f_l(\vec{B}, T)$. The function is shown in Figure 6.10b, as a function of the field angle with respect of the normal direction of the wide surface of the tape (see the box in Figure 6.10b), for a background field of $100\,\mathrm{mT}$. The lifting function is taken from data in [295], where tapes manufactured with the same technology and by the same producer are considered. The critical current density is implemented in the model as

$$J_c(\vec{B}, T) = f_l(\vec{B}, T)\frac{I_{c,\min}}{\delta_w \delta_{t,Sc}},\tag{6.8}$$

where the minimum critical current $I_{c,\min}$, the width δ_w and the thickness $\delta_{t,Sc}$ of the superconducting layer are given in Table 6.1.

6.3.2 Geometric defects and field quality

After the first cool-down and the leak-tight test for the experimental assembly, a visual inspection was carried out for the first prototype. The inspection highlighted the presence of gaps between the HTS holder and the foam box, as well as displacements and corrugations for both the left and right screens, see Figure 6.11a. Such undesired geometric deformations arise from intrinsic stresses in the materials which were released during the cool-down, and were found to detrimentally affect the field quality. As a consequence of the separation of the holder from the box and the loss of compression force, both HTS screens suffered from displacement and deformation.

The numerical model accounts for the observed geometric deformations as follows. The HTS screens are implemented as two joint arcs of a parabola, whose shape is determined by the parameters d_{up} and d_{dn}.
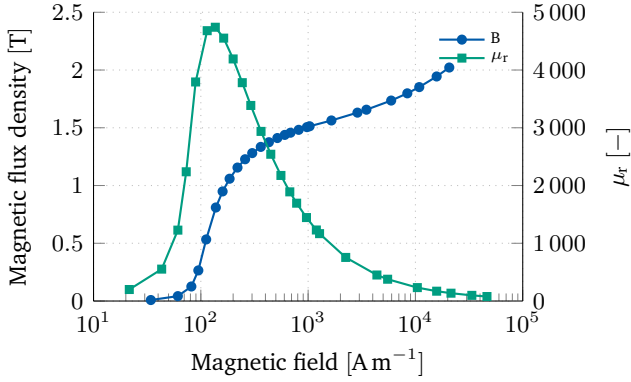
(a) Ferromagnetic curve.
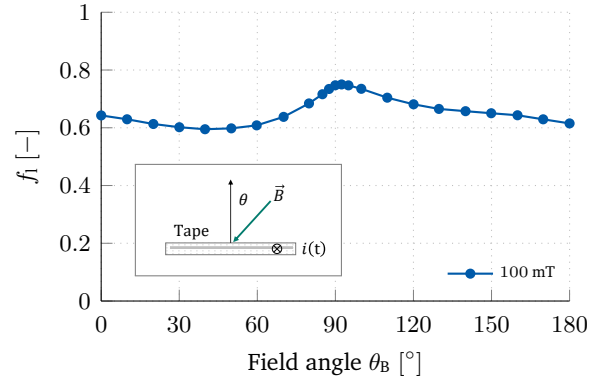
(b) Lifting function at $77\,\mathrm{K}$.

Figure 6.10. Constitutive relations. (a) Measured ferromagnetic curve for the nonlinear $\mu(\vec{B})$ relation. (b) Lifting function as a function of the field angle, for tapes at $77\,\mathrm{K}$, parametrized with the magnetic field magnitude.

Also, screens are allowed to rotate around their central point, with an angle d_θ. Therefore, three degrees of freedom are introduced in the geometry of each screen, and the overall geometric defect of the HTS screens $\mathbf{d}_\mathrm{g}$ is defined by the vector

$$\mathbf{d}_\mathrm{g} = \left[d_{\mathrm{up},\mathrm{l}}, d_{\mathrm{dn},\mathrm{r}}, d_{\mathrm{dn},\mathrm{l}}, d_{\mathrm{dn},\mathrm{r}}, d_{\theta,\mathrm{l}}, d_{\theta,\mathrm{r}}\right]^\top, \tag{6.9}$$

where the subscripts l and r denote the left and right screens. The geometric defects introduced in the model are shown in Figure 6.11b. It is worth noting that the case with flat screens corresponds to $d_\mathrm{up}, d_\mathrm{dn} \to 0$, whereas for perfectly parallel screens the further constraint $d_\theta \to 0$ needs to be fulfilled. The parameters composing the vector $\mathbf{d}_\mathrm{g}$ are quantified by solving a minimization problem. The minimum is sought by means of the MATLAB® [296] implementation of the particle swarm optimization (PSO) algorithm [297]. The penalty function $f_\mathrm{p}(\mathbf{d}_\mathrm{g})$ adopted for the PSO minimizes the difference between field quality measurements and simulations. The optimization problem reads

$$\begin{cases} \min_{\mathbf{d}_\mathrm{g}} \quad f_\mathrm{p}(\mathbf{d}_\mathrm{g}) \\[2mm] \quad \text{with } f_\mathrm{p}(\mathbf{d}_\mathrm{g}) = \sum_{k=2}^{6} \left(|a_{k,\mathrm{m}} - a_{k,\mathrm{s}}(\mathbf{d}_\mathrm{g})| + |b_{k,\mathrm{m}} - b_{k,\mathrm{s}}(\mathbf{d}_\mathrm{g})|\right) \\[2mm] \quad \text{s.t.} \begin{cases} |d_{\mathrm{up},j}|, |d_{\mathrm{dn},j}| - x_\mathrm{c} \le 0 \\ |d_{\theta,j}| - \theta_\mathrm{c} \le 0 \end{cases} \text{with } j = \mathrm{l}, \mathrm{r} \end{cases} \tag{6.10}$$

where the multipole coefficients $a_{k,\mathrm{m}}$ and $b_{k,\mathrm{m}}$ are obtained from measurements, whereas the coefficients $a_{k,\mathrm{s}}(\mathbf{d}_\mathrm{g})$ and $b_{k,\mathrm{s}}(\mathbf{d}_\mathrm{g})$ are calculated numerically. The maximum geometric defects in displacement and angle are set to $x_\mathrm{c} = 2.5\,\mathrm{mm}$ and $\theta_\mathrm{c} = 50\,\mathrm{mrad}$. The index k is limited to the dodecapole component, given that high order field components are found to be of much lower magnitude. The results of the optimization problem are discussed in Section 6.4, where the simulated field error arising from geometric defects is matched with the experimental observations.
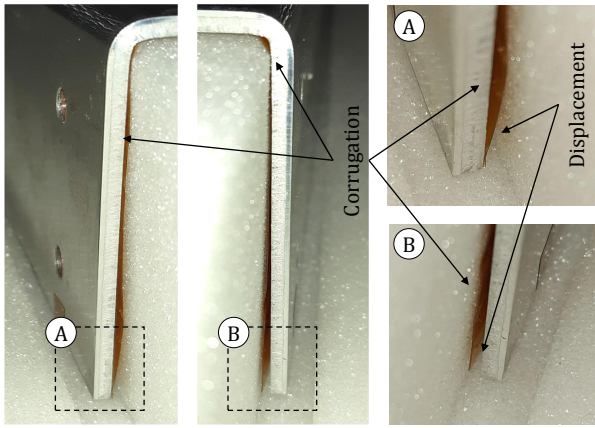
(a) Visual inspection.
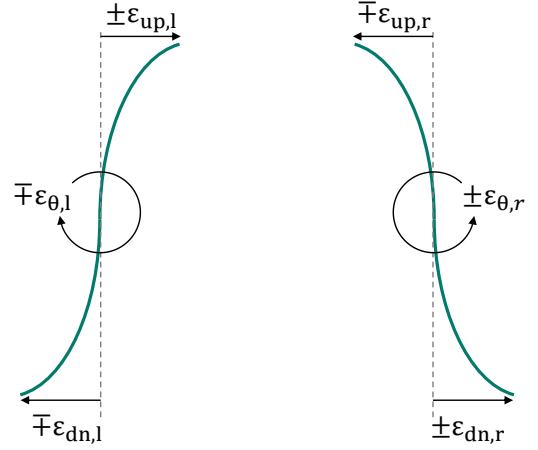
(b) Geometric error parameters.

Figure 6.11. (a) Visual inspection of the first HTS holder prototype, highlighting gaps between the holder and the foam box, as well as displacements and corrugations for both the left and right HTS screens. (b) Geometric error parameters, used to implement a realistic geometry for the HTS screen.

6.3.3 Forces on iron bars

The magnetic force $\vec{F}_m$ acting on the iron bars during the tests may cause deformation of the support plate, causing an undesired displacement of the HTS screens. If uncontrolled, the force may compromise the integrity of the experimental assembly, causing a spill of the liquid nitrogen over the normal conducting coils of the magnet and their powering system, possibly leading to irreversible damage. For this reason, the absolute value of the horizontal and vertical components $F_{m,x}$ and $F_{m,y}$ of the magnetic force are required to remain below $5\,\mathrm{kg}$, thus limiting the peak magnetic field during the tests. The magnetic force is calculated in magnetostatic regime by means of the Maxwell's magnetic stress tensor $\boldsymbol{\sigma}_m$ [255]. The force acting on a body Ω is given by

$$\vec{F}_m = \int_\Omega \nabla \cdot \boldsymbol{\sigma}_m \, \mathrm{d}\Omega = \int_{\partial\Omega} \boldsymbol{\sigma}_m \cdot \vec{n} \, \mathrm{d}\Gamma, \tag{6.11}$$

where $\Gamma = \partial\Omega$ and $\vec{n}$ is the normal unit vector. The tensor $\boldsymbol{\sigma}_m$ is formulated component-wise as

$$\sigma_m^{k,j} = \mu \left[H_k H_j - \frac{1}{2} H^2 \delta_{k,j}, \right] \qquad \text{with } k,j = x,y,z \qquad \text{and } \delta_{k,j} = \begin{cases} 0 & \text{if } k \neq j \\ 1 & \text{if } k = j \end{cases} \tag{6.12}$$

where $\delta_{k,j}$ is the Kronecker delta. The x and y components of the peak magnetic force acting on the iron bars are shown in Figure 6.12, as a function of the dipole magnetic field. The different cases refer to all possible geometric configurations for the iron bars, given in terms of left and right vertical offset with respect to the mid-plane of the rotating coil. The results for y-symmetric configurations, that is, for iron bars with the same y-coordinate, are shown in Figure 6.12a and 6.12b. The other configurations are shown in Figure 6.12c and 6.12d. By limiting the magnetic flux density to $100\,\mathrm{mT}$, the components of $\vec{F}_m$ never exceed the limit $F_{m,\max} = 5\,\mathrm{kg}$.

(a) Horizontal force, y-symmetric bars.

(b) Vertical force.

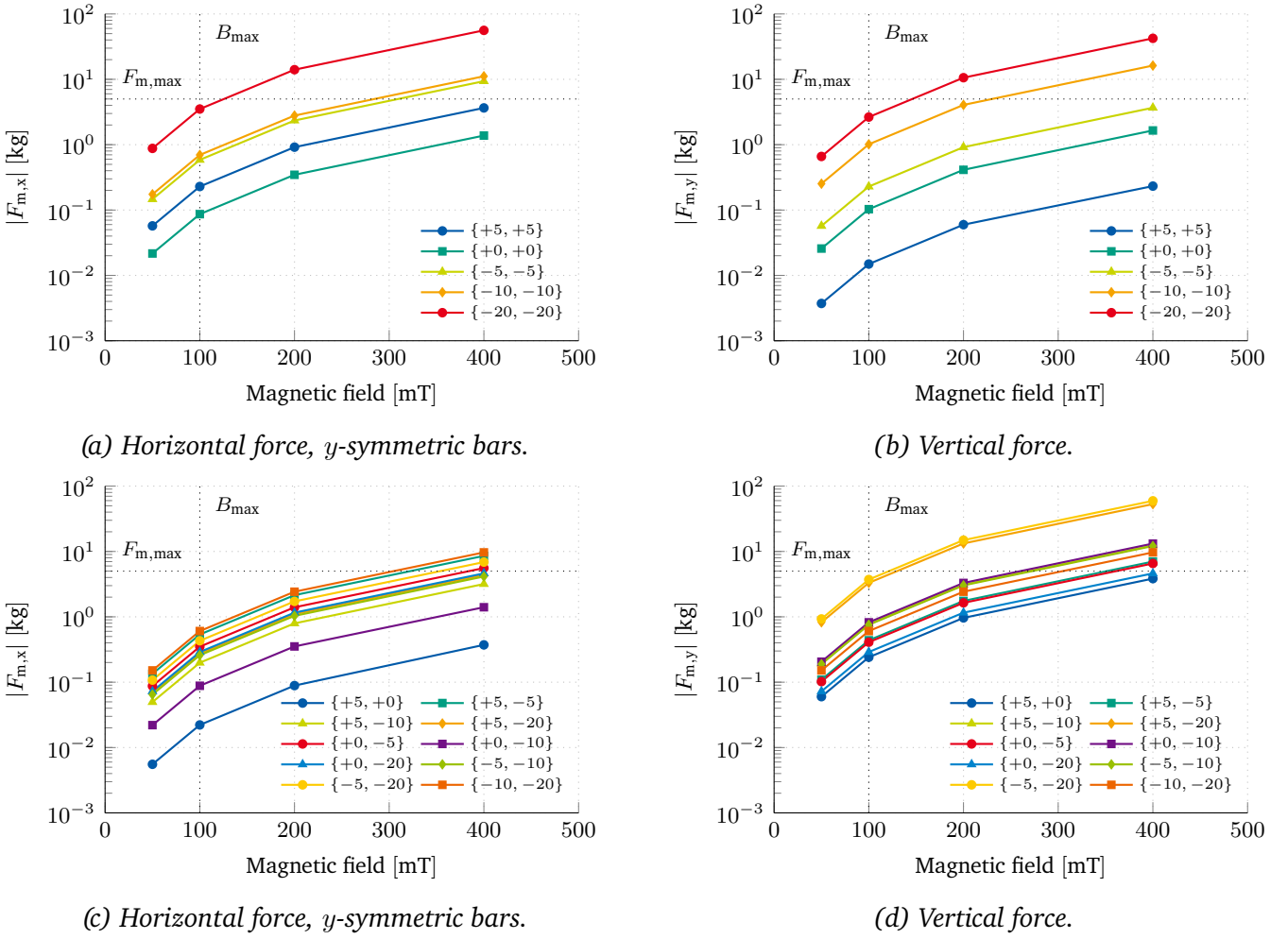*(c) Horizontal force, y-symmetric bars.*

(d) Vertical force.

Figure 6.12. Peak magnetic force acting on the iron bars. Results are presented for the x and y force components, and grouped in symmetric and non-symmetric iron bar configurations. The vertical offset of the left and right iron bars is given in mm in the legends.

6.4 Experimental and Numerical Results

The test campaign for the two HALO prototypes is organized in two main parts, assessing the behavior of the HALO device without and with the iron bars. In this way, the net contribution of the HTS screens is assessed by differential measurements.

In the first part, the HTS screens are characterized both at room temperature ($300\,\mathrm{K}$) and in liquid nitrogen ($77\,\mathrm{K}$), in a dipole background field. The first measurement quantifies the magnetic contribution from the normal conducting materials in the assembly, for example the aluminum support plate. The second measurement quantifies the magnetic coupling of the HTS screens with the background field, which is strongly influenced by the precise alignment of the tapes with respect to the magnetic field lines. The tests at room temperature and at cold are made for both prototypes of the HTS holder. The field quality measured in the tests at cold is used for calibrating the numerical model. In the second part, a field-error contribution is added to the dipole magnetic field of the reference magnet by introducing two iron bars in the magnet aperture.

| No.	T_{op} K	B_{op} mT	r_0 mm	Iron bars	Δy_l mm	Δy_r mm	Scenario label
				1st HTS holder prototype			
1.	300	100	15	No	n.a.		n.a.
2.	77	100	15	No	n.a.		
3.	300	100	15	Yes	+5	−20	medium
4.	77	100	15	Yes	+5	−20	
				2nd HTS holder prototype			
5.	300	100	15	No	n.a.		n.a.
6.	77	100	15	No	n.a.		
7.	300	100	15	Yes	+5	+0	low
8.	77	100	15	Yes	+5	+0	
9.	300	100	15	Yes	+5	−20	medium
10.	77	100	15	Yes	+5	−20	
11.	300	100	15	Yes	−20	−10	high
12.	77	100	15	Yes	−20	−10	
13.	300	100	15	Yes	−20	+5	check
14.	77	100	15	Yes	−20	+5	

Table 6.2. Test campaign.

The magnitude of the field-error contribution is modulated by applying the vertical offsets Δy_l and Δy_r to the left and right iron bars, ranging between $+5$ and -20 mm with respect to the horizontal mid-plane of the rotating coil. The field quality is measured first at $300\,K$ where it is influenced only by the iron bars, and then at $77\,K$, where the HTS screens are superconducting and also affect the magnetic field. In this way, a comparison of the two measurements gives the net contribution of the HTS screens to the field-error cancellation.

Four different scenarios are proposed. In the first three scenarios the magnitude for the field error is progressively increased by acting on the position of the iron bars, therefore they are labeled as *low*, *medium* and *high*. The fourth scenario features an anti-symmetric geometric configuration for the iron with respect to the second scenario, providing field errors of the same magnitude. This last scenario was used for checking the analysis method, therefore it is labeled as *check*. The most relevant parameters and features are given in Table 6.2. All the test are performed in a $100\,mT$ background dipole field determined by evaluating the Lorentz forces acting on the iron bars, as discussed in Section 6.3.3. All the multipoles are evaluated at a reference radius of $r_0 = 15\,mm$. The first HTS holder prototype was characterized only for the *medium* error scenario, as it was found that the field contribution from the HALO itself was significant due to geometric deformation in the tapes. The second prototype was characterized for all the four scenarios.

Measurements are compared with simulations. With respect to the tests at $77\,K$, two geometric models for each HTS screen prototype are considered. The first assumes perfectly parallel and flat HTS tapes, whereas the second includes the geometric defects introduced in the optimization problem (6.9). All the simulations are carried out on a standard workstation (Intel® Core i7-3770 CPU @ $3.40\,GHz$, $32\,GB$ of RAM, Windows-10® Enterprise 64-bit operating system), using the proprietary FEM software COMSOL.
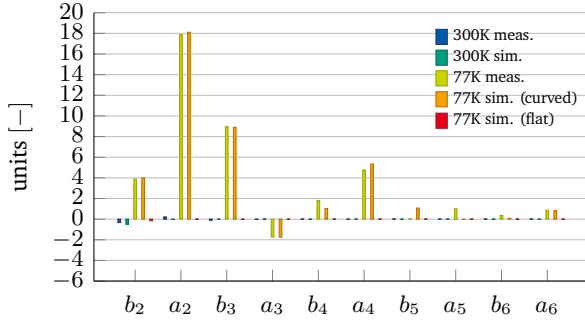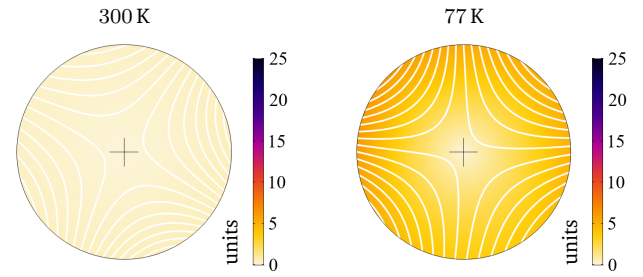
(a) First prototype in dipole field.
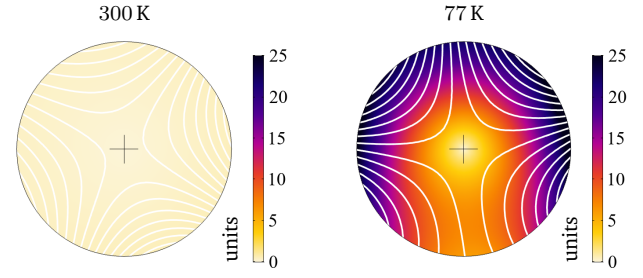
(b) First prototype in dipole field.
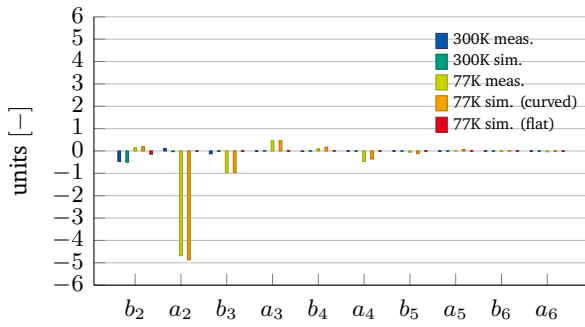
(c) Second prototype in dipole field.

(d) Second prototype in dipole field.

Figure 6.13. Measured and simulated magnetic field quality for both the prototypes, without iron bars. Left: multipole series expansion at both 300 K and 77 K, in a dipole background field. Right: Magnetic field error seen by the rotating coil, reconstructed from measurements.

6.4.1 Prototypes without iron bars

The magnetic field quality is evaluated for the experimental setup mounted without iron bars in the magnet aperture in a dipole background field. Measurement and simulation results are shown for the first prototype in Figures 6.13a and 6.13b. Measurements performed at 300 K quantify the influence of undesired magnetization and dynamic phenomena possibly occurring in the normal conducting parts of the experimental setup. Their influence is found to be within 0.5 units of field error. Subsequently, measurements with the HTS screen at 77 K show an undesired self-field error characterized by the a_2 and b_3 components, with contributions from b_2 and a_4. The measured and simulated THD factor for the first prototype is equal to 21. If flat screen geometries are considered in simulations, the absence of geometric defects ensures a negligible THD factor, highlighting the importance of minimal geometric tolerances for practical HALO devices.

The same measurement and simulation results are shown for the second prototype in Figures 6.13c and 6.13d. The field error obtained at room temperature remains unchanged, whereas measurements at cold show five units of a_2 with minor contributions below one unit, thus giving a THD factor of five. With respect to the first prototype, the overall self-field error is reduced by about a factor of four. Simulation results accounting for geometric defects reproduce measurements well, showing that the origin of the remaining field error

is quite well understood. Results suggest that further reductions of the THD factor require to improve the manufacturing techniques of the HTS assembly.

The net magnetic contribution provided by the HTS screens is shown for the rotating coil region in Figure 6.13b and 6.13d. The field solution is numerically reconstructed from the measured multipoles for both the versions of the HTS holder, at 77 K. The field distribution shows a quadrupole field component dominating in both cases, with a field gradient qualitatively higher for the first prototype.

6.4.2 Geometric quality analysis

The minimization problem in (6.10) is solved by using as a reference the field quality measured for both the prototypes at 77 K, without iron bars. The performance of the PSO is shown in Figure 6.14, where the left and right columns refer to the first and second prototype. From top to bottom, the first three rows show the behavior of the penalty function $f_p(\mathbf{d}_g)$ within the parametric space, by means of 2D projections where each dot corresponds to a function evaluation. The fourth row represents the minimum value of $f_p(\mathbf{d}_g)$ for each iteration of the PSO. Residuals below 1.5 and and 0.5 units were obtained for the first and second prototypes, respectively.

The calculated parameters are given in Table 6.3. Although the first prototype suffered from relevant geometric defects, with magnitudes up to a few millimeters, the improved design of the second prototype reduced the imperfections affecting both curvature and rotation by more than two orders of magnitude. The geometric parameters are used for reconstructing the shape of the two HTS screen prototypes, as shown in Figure 6.15a. For the sake of clarity, imperfections are graphically magnified by a factor ten. The position of the rotating coil and the horizontal mid-plane are also included. Note that from Figure 6.11, the distortion shown in Figure 6.15a is already apparent. The first prototype is affected by substantial geometric deformation, whereas the second prototype is much closer to the reference geometry. A residual deformation of the left screen still persists in the second prototype, causing a non-perfect parallelism between the tapes.

The self-field contribution from the HTS screens is affected by mechanical tolerances. The worst-case screens are determined numerically using the model of the experimental setup. In detail, the PSO algorithm is used for finding the worst-case screen deformation in terms of maximum THD factor. The PSO constraints are provided by prescribing the mechanical tolerances as maximum geometric defects in (6.10). Results in Figure 6.15b show that the THD factor can be kept below 1 unit by applying tolerances of 25 μm. As an example, the same tolerances were used for the manufacturing of the austenitic steel collars of the superconducting coils in the LHC main dipole magnets [298]. For perfectly parallel screens in the thin-shell approximation, the self-field error disappears. In practice, the residual error is expected to be nonzero due to the finite thickness of the superconducting tapes, however it is considered as a second-order effect since the approximation introduced by the thin-shell model is negligible (see Section 4.3.5).

6.4.3 HTS screens with iron bars

After the iron bars are mounted in the magnet aperture, the resulting magnetic field quality is determined. Measurements at 300 K are influenced only by the iron bars, whereas at 77 K, the HALO contribution is also included.

First Prototype   Second Prototype

(a) Left screen curvature.   *(b) Left screen curvature.*

(c) Right screen curvature.   *(d) Right screen curvature.*

(e) Left screen rotation.   *(f) Right screen rotation.*
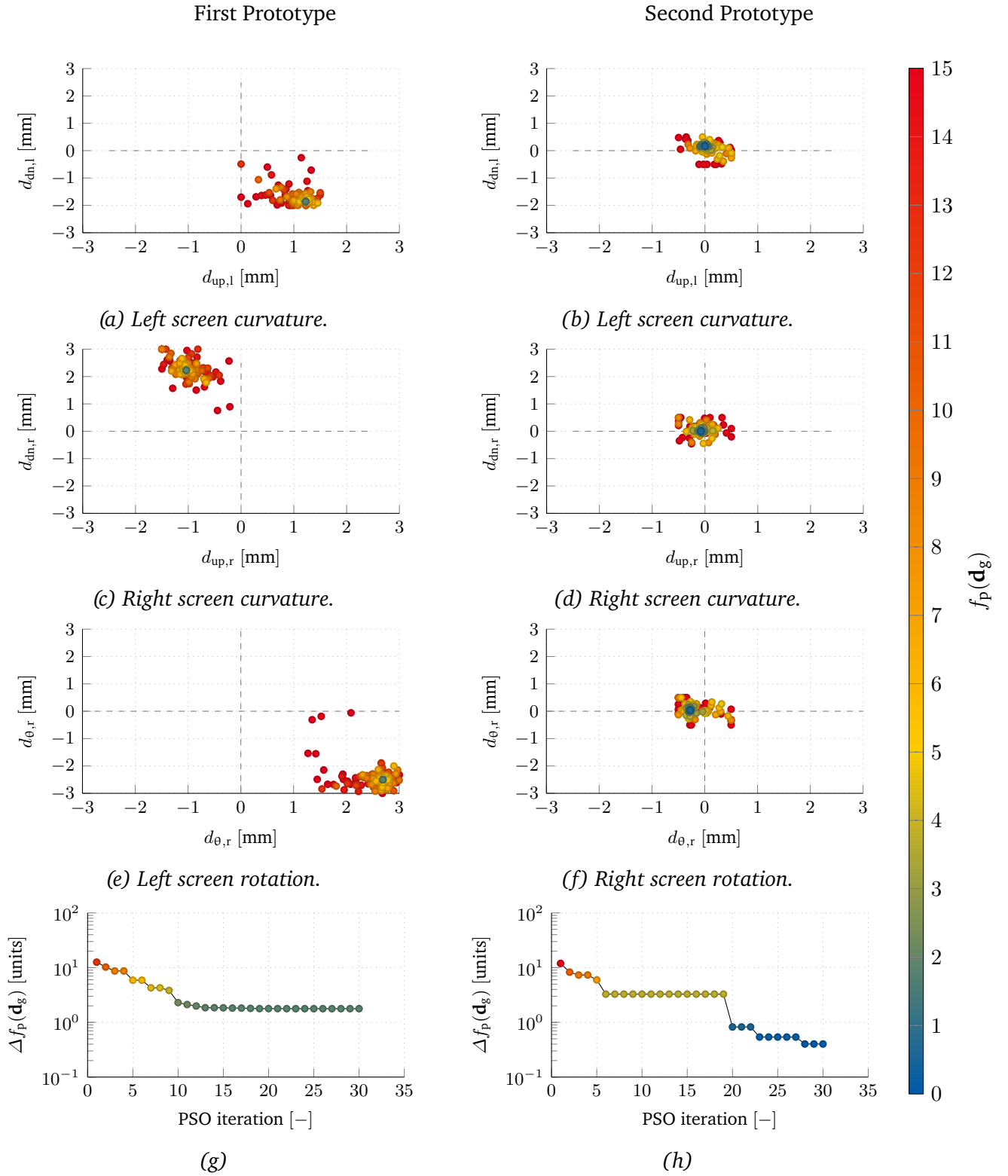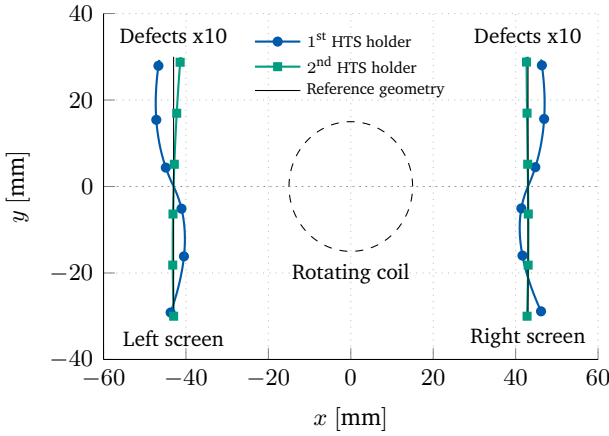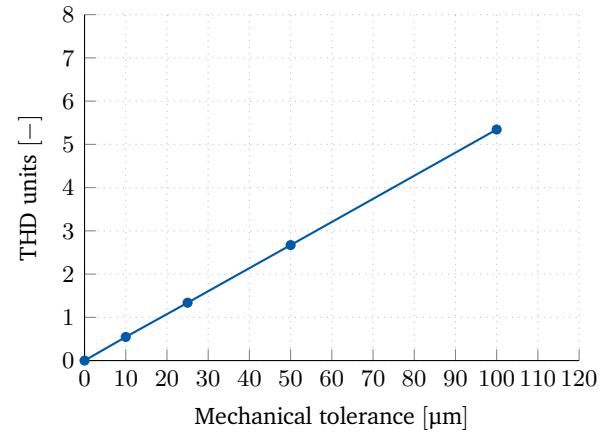
(g)   *(h)*

Figure 6.14. Geometric imperfections in the screens, calculated with the PSO algorithm. The two columns refer to the first and the second prototype. Results show the curvature of the left (a,b) and right (c,d) screens, their rotation (e,f), and the residual of the PSO algorithm in fitting the measured field error.

Screen	Error	Unit	1st holder	2nd holder
	d_{up}	µm	1200	-1
Left	d_{dn}	µm	-1900	170
	d_{θ}	mrad	47	-5
	d_{up}	µm	-1000	-75
Right	d_{dn}	µm	2100	5
	d_{θ}	mrad	-42	1

Table 6.3. Geometric error parameters.


*(a) Geometric error.*

(b) Self-field error.

Figure 6.15. Geometric and self-field error of the HTS screens. Left: deformation of the two prototypes, rendered with a factor ten amplification, compared with the reference geometry of perfectly parallel HTS screens. Right: simulated self-field error, in THD units, as a function of the mechanical tolerance prescribed for the screens. The results are given for the worst-case design within prescribed tolerances.

For the first prototype, the iron bars are mounted according to the *medium* error scenario (see Table 6.2), introducing 30 units of a_2 and 15 units of a_3, with a minor contribution from the b_2 component. The magnetic field quality is shown in Figure 6.16. The plot on the left provides measurement and simulation results as a multipole series expansion, whereas the plot on the right shows the field distribution in the region defined by the rotating coil, within the magnet aperture. For this magnetic configuration, the HALO reduces the a_2 and a_3 contributions, whereas the b_2, b_3 and b_4 errors are increased. This increase is due to the self-field generated by the HTS screen, and it is caused by the geometric deformation in the first HALO prototype (see Section 6.4.1).

For the second prototype, the iron bars are mounted according to all the four scenarios given in Table 6.2. The magnetic field quality is shown in units in Figure 6.17. Again, the left column provides measurements and simulation results as a multipole series expansion, whereas the right column shows the field distribution within the magnet aperture. The field error introduced by the iron bars at $300\,\text{K}$ is given for the *low* error scenario by 10 units of a_2, with minor contributions of b_3 and a_3 (Figure 6.17a); for the *medium* error scenario by 30 units of a_2 and 15 units of a_3, with minor contribution of b_2 (Figure 6.17c); for the *high* error scenario by 70 units of a_2 and 10 units of a_3 with minor contribution from b_2 and a_4 (Figure 6.17e). The *check* error scenario provides an error equal in magnitude to the *medium* error scenario, but with inverted sign for the
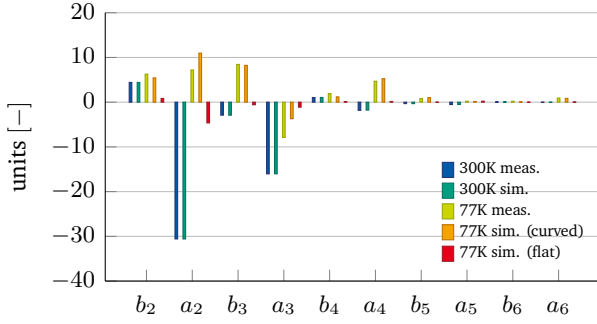
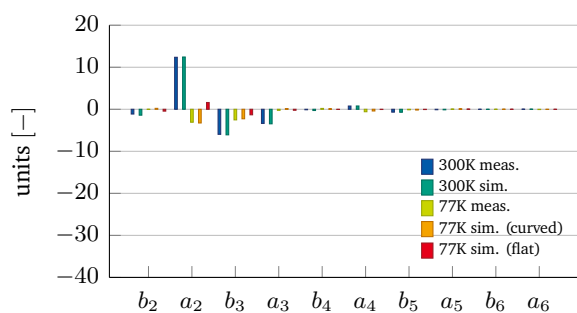(a) First prototype, $medium$ field error.
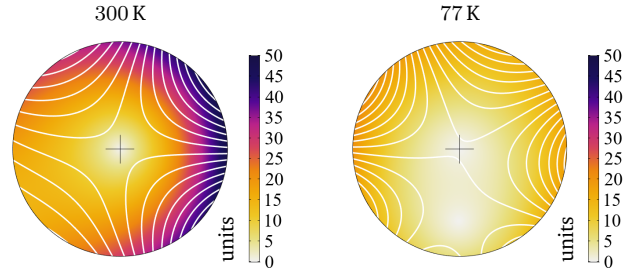
(b) Magnetic field error.

Figure 6.16. *Measured and simulated magnetic field quality for the first prototype, with iron bars. Left: multipole series expansion at both* 300 K *and* 77 K, *in a dipole background field. Right: Magnetic field error seen by the rotating coil, reconstructed from measurements.*

normal even-order and the skew odd-order multipoles (Figure 6.17g). By cooling the HTS screens to 77 K, the HALO is turned into the superconducting state, and a reduction of the field error is measured. The reduction occurs for each scenario, and for every multipole component introduced by the iron bars (see Figure 6.17 and 6.16). The reduction factor for the principal error multipoles is found to be between three and four, higher for components with higher magnitude. Concerning the higher order multipoles with order > 4, no field perturbation is observed with respect to 300 K. These components remain within the noise floor of the background field. The net magnetic contribution provided by the HTS screens in the rotating coil region is shown in the right column of Figure 6.17, from top to bottom for the low, $medium$, $high$, and $check$ error scenarios. Results are shown for both the setup at 300 K and 77 K. For all the scenarios, from the left to the right column, a reduction in the field error and an improvement in the homogeneity of the magnetic field distribution is achieved.

Simulation results accounting for geometric defects reproduce measurements quite well showing that curved and flat geometries are in qualitative agreement, with the screens working closer to ideal conditions with respect to the first prototype. The geometric defects of the HTS layers in the two prototypes are determined only once and in the absence of iron. With the subsequent addition of iron, the measured and simulated results (Figure 6.16 and 6.17) show a high degree of consistency, without the need of 're-fitting' for geometric deformation, suggesting excellent predictive properties of the simulation model.

6.4.4 Field-error cancellation

The THD factor previously defined in (5.15), is calculated for the magnetic field quality obtained for the first and second prototype (Figures 6.16 and 6.17) in the different iron configurations, at 300 K and 77 K. Results are shown in Figure 6.18, for both measurements and simulations. The magnetic contribution produced by the screening currents in the HTS screens produces a reduction of the THD factor for each scenario, and for both the first and the second prototype. The highest reduction is obtained in the scenario at high field error, because the self-field contribution due to geometric deformation in the HTS screens is less relevant.

(a) Second prototype, low field error.
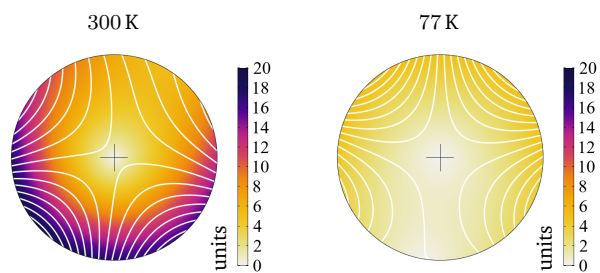
(b) Second prototype, low field error.
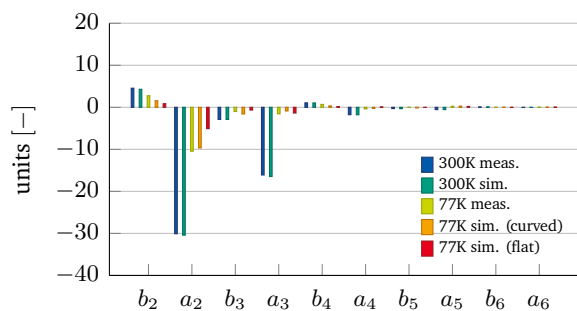
(c) Second prototype, medium field error.
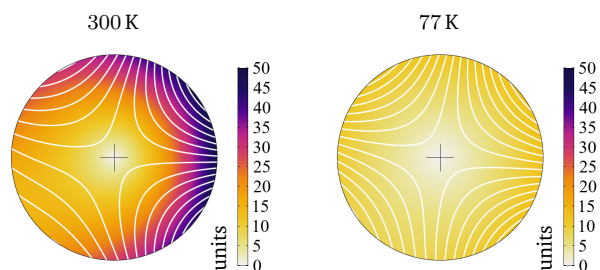
(d) Second prototype, medium field error.
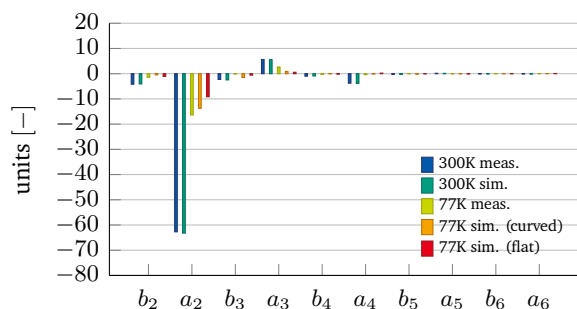
(e) Second prototype, high field error.
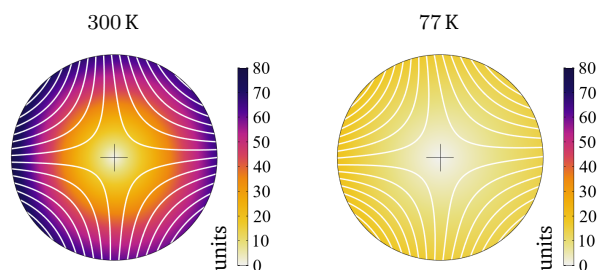
(f) Second prototype, high field error
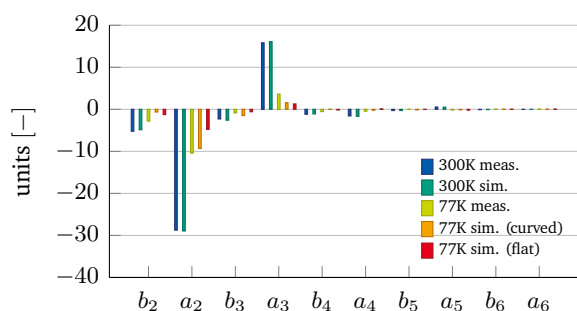
(g) Second prototype, check field error.
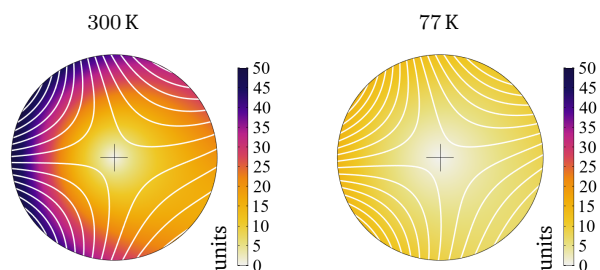
(h) Second prototype, check field error.

Figure 6.17. Measured and simulated magnetic field quality for the second prototype, with iron bars. Left: multipole series expansion at both 300 K and 77 K, in a dipole background field. Right: Magnetic field error seen by the rotating coil, reconstructed from measurements.
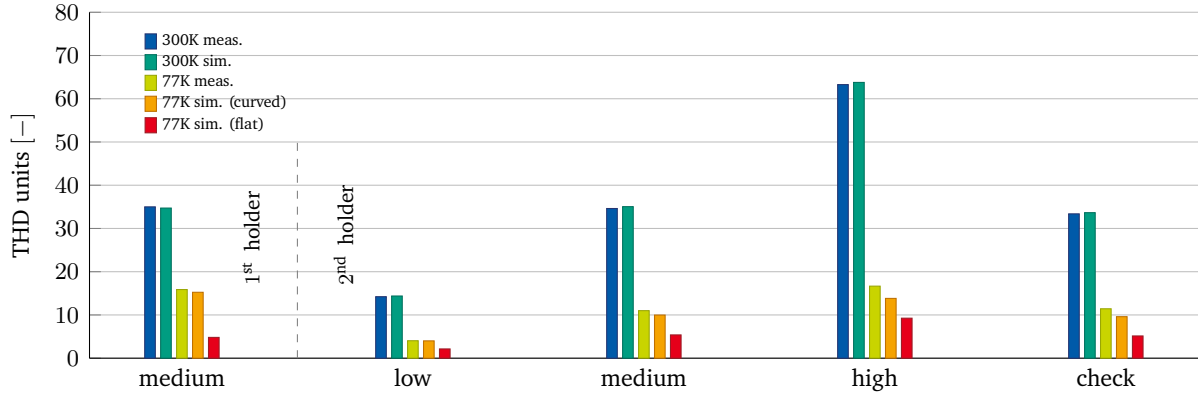
Figure 6.18. Measured and simulated magnetic field quality, given in units as a THD factor. Results are shown for four different positions of the iron bars. The field error is shown for the prototypes at both $300\,\mathrm{K}$ and $77\,\mathrm{K}$. Simulation results are also shown for HTS screens with flat geometry.

The overall field-cancellation performance of the HTS screens is quantified by means of two efficiency parameters. The first parameter is the geometric efficiency η_g which measures the performance degradation caused by non-ideal screen geometries. It is defined as

$$\eta_\mathrm{g}(\mathbf{d}_\mathrm{g}) = 1 - \frac{F_\mathrm{d}(\vec{B}_\mathrm{halo})}{F_\mathrm{d}(\vec{B}_\mathrm{iron})} = 1 - \frac{1}{Q_\mathrm{g}}, \tag{6.13}$$

where Q_g is the geometric quality factor, and $\vec{B}_\mathrm{halo}$ and $\vec{B}_\mathrm{iron}$ indicate the field in the dipole magnet affected by the geometric defects $\mathbf{d}_\mathrm{g}$ in the HTS screens and by the iron bars, respectively. For ensuring a high efficiency, therefore a high geometric quality factor, the field error from the screens must be negligible with respect to the overall field error. For perfectly parallel and infinitely thin screens, that is, $|\mathbf{d}_\mathrm{g}| \to 0$ and $\eta_\mathrm{g}(\mathbf{d}_\mathrm{g}) \to 1$, the screens reach the theoretical performance predicted by simulations with flat screens. The second parameter is the magnetic efficiency η_m which measures the overall field quality improvement after the field-error cancellation. It is defined as

$$\eta_\mathrm{m} = 1 - \frac{F_\mathrm{d}(\vec{B}_\mathrm{both})}{F_\mathrm{d}(\vec{B}_\mathrm{iron})} = 1 - \frac{1}{Q_\mathrm{m}}, \tag{6.14}$$

where Q_m is the magnetic quality factor, $\vec{B}_\mathrm{both}$ is the magnetic field in the dipole magnet with both HALO and the iron bars. The magnetic efficiency is affected not only by the geometric defects, but also by the width, thickness, and position of the screens, therefore their design. In case of a complete cancellation of the magnetic field error, that is, $F_\mathrm{d}(\vec{B}_\mathrm{both}) \to 0$, then $\eta_\mathrm{m} = 1$.

The geometric and magnetic efficiency and their quality factors are given in Table 6.4 for both prototypes, and all iron configurations. The first prototype features $\eta_\mathrm{g} = 0.4$, $\eta_\mathrm{m} = 0.6$ and $Q_\mathrm{m} = 2.4$. A performance increase is observed with the second prototype, achieving a η_g of up to 90% and η_m of up to 75%, producing a Q_m between 2.9 and 3.8. It is found that the field quality is improved by a factor of almost four for the high field-error scenario. For the scenarios where $Q_\mathrm{g} < Q_\mathrm{m}$, a partial compensation of the field error due to the iron bars was accidentally obtained by the HALO self-field contribution.

No.	Holder	Field error	η_g	η_m	Q_g	Q_m
1	1st	medium	0.40	0.58	1.7	2.4
2	2nd	low	0.65	0.72	2.8	3.5
3	2nd	medium	0.86	0.68	6.9	3.1
4	2nd	high	0.92	0.74	12.6	3.8
5	2nd	check	0.85	0.66	6.7	2.9

Table 6.4. HALO performance.

6.5 Numerical Extrapolation at $100\,\mathrm{mT}$

Numerical simulations of the experimental setup at $100\,\mathrm{mT}$ and $77\,\mathrm{K}$ show that in case the geometric defects are fully compensated, flat screens would further improve the prototype performance in each of the iron scenarios. However, this is not sufficient for ensuring a cancellation of the field error below 1 unit of THD. At the same time, measurements do not allow to draw conclusions regarding the persistency of the currents over time. Therefore, the prototype performance is extrapolated by means of simulations beyond the reference design parameters. Perfectly flat and parallel screens are assumed, and the extrapolation is carried out with regards to the width of the screens, the number of layers per screen, and the critical current of the tapes. The magnetic field quality is evaluated $100\,\mathrm{s}$ after steady state operations. Also, simulations are carried out for time intervals up to $100\,\mathrm{h}$ of steady state operations, and the drift of the screening currents is assessed.

6.5.1 HTS screens geometry

The number of tapes per layer is increased from 5 to 6 (4 to 5 for the odd-order layers) to obtain up to $70\,\mathrm{mm}$-wide screens. The maximum width of the screens, that is, the maximum number of tapes per layer, is fixed by the magnet aperture. At the same time, the number of layers per screen is increased, from 4 to 16. Although the magnet coil design and the clearance of the magnet aperture may pose geometric limits to the design of the screen, the number of layers shall pose less challenges due to the negligible thickness of the tapes. The number of tapes per layer is combined with the number of layers, and the possible design combinations are investigated. Results are given in the left column of Figure 6.19, for all four iron scenarios, where the dashed lines show the field error without the screens. The calculated THD factor is shown as a function of the number of tapes per layer, and it is parametrized with the number of layers in the HTS screens. The experimental conditions correspond to 5 tapes per layer, and 4 layers. By increasing both the width of the screens and the number of layers, it is possible to obtain a residual in the THD factor below one unit, in each of the iron scenarios.

6.5.2 Critical current

The experimental setup is simulated for all four iron scenarios, applying a scaling factor $0.5 \leq k_{I_c} \leq 1.5$ to the critical current I_c of the superconducting tapes. Results are shown in Figure 6.20a, in THD units, as a function of the scaling factor applied to the tape critical current, for the four iron scenarios. The experimental conditions correspond to a unitary scaling factor. A reduction of the critical current ($k_{I_c} < 1$) has a detrimental effect on the HALO performance as it increases the residual THD factor after the field-error cancellation, with an exception for the *low* iron scenario where the I_c is still sufficient since no degradation is observed.
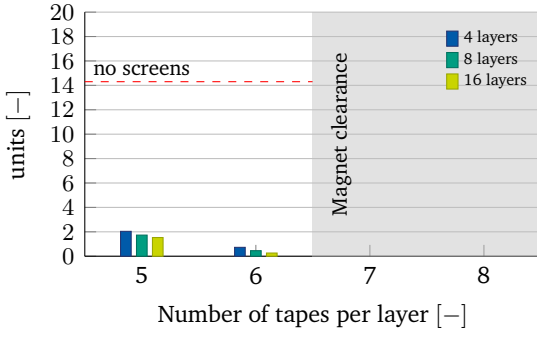
(a) THD, low-error scenario.
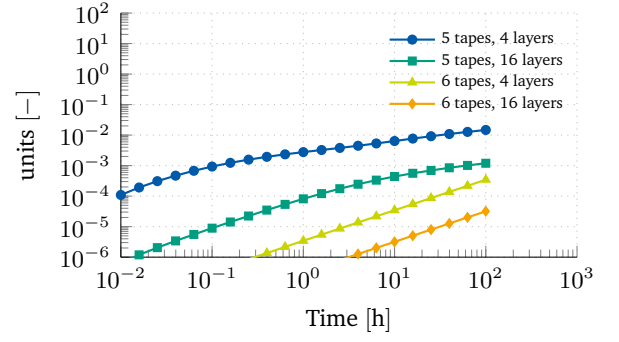
(b) THD drift, low-error scenario.
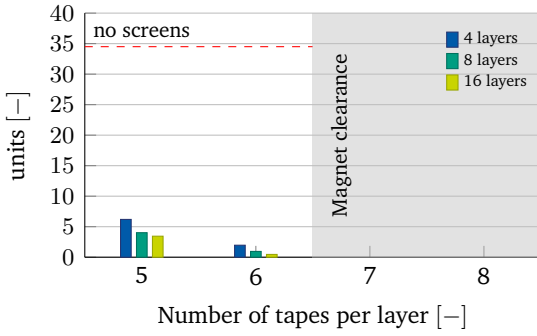
(c) THD, medium-error scenario.
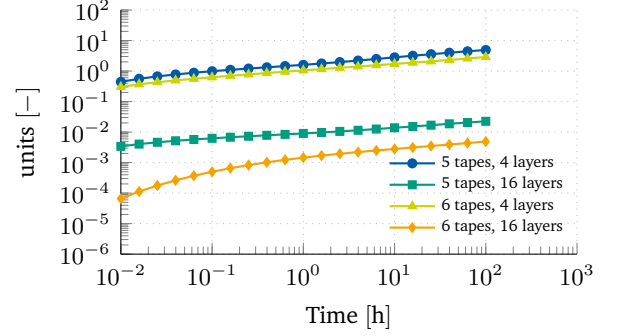
(d) THD drift, medium-error scenario.
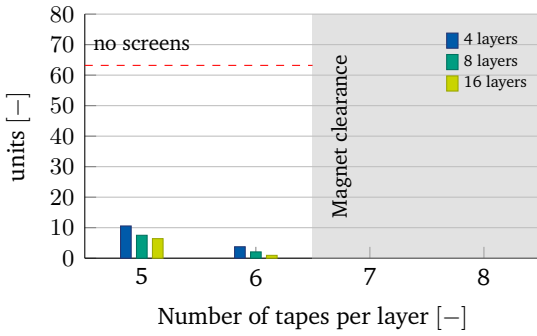
(e) THD, high-error scenario.
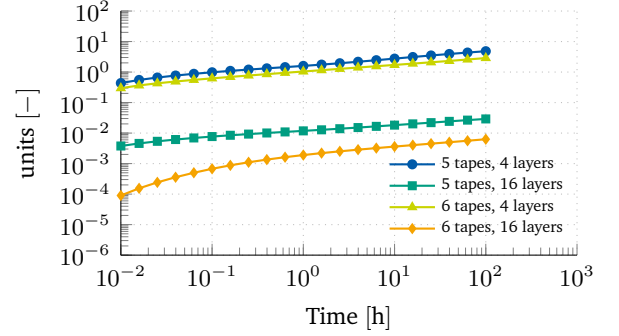
(f) THD drift, high-error scenario.
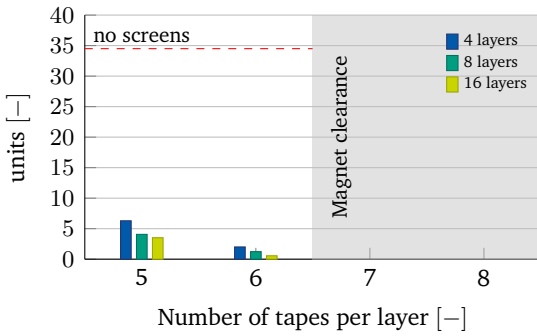
(g) THD, check-error scenario.
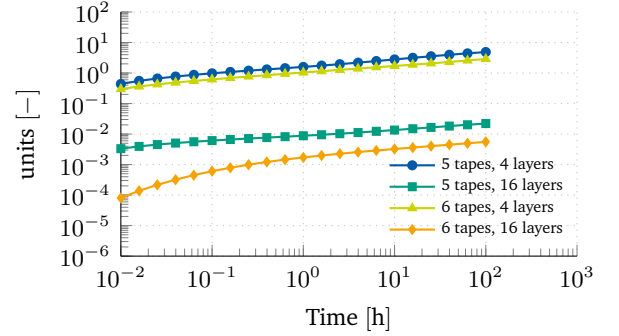
(h) THD drift, check-error scenario.

Figure 6.19. Left column: simulated THD factor, in units, as a function of the number of tapes per layer. Right column: simulated drift of the THD factor, in units, as a function of time.
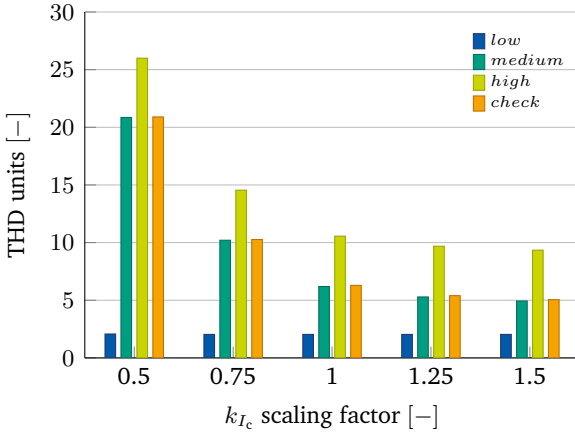
(a) THD.
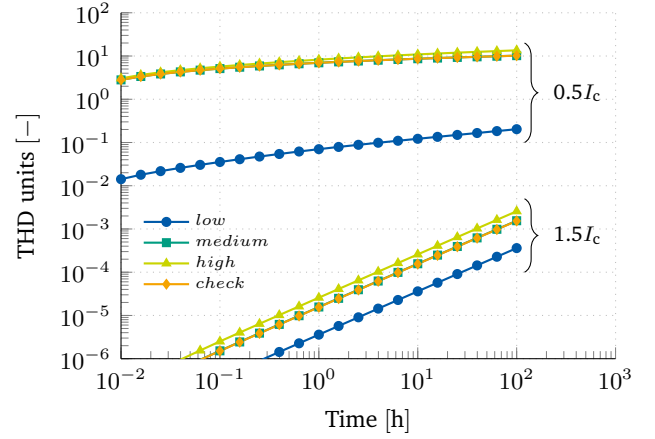
(b) THD drift.

Figure 6.20. (a) THD factor, as a function of the scaling factor applied to the tape critical current. (b) Simulated drift of the THD factor, in units, as a function of time.

Conversely, an increase of the critical current ($k_{I_c} > 1$) is beneficial, as the residual THD factor is decreased, again with the exception of the *low* iron scenario. However, the reduction of the field error is marginal and tends to disappear for higher critical currents.

6.5.3 Screening currents drift

The magnetic behavior of the HTS screens is simulated by means of the numerical model detailed in Section 6.3. By using a linear ramp for the source current, the magnetic field in the dipole magnet is increased from zero up to the reference value of $100\,\text{mT}$. Then, the magnetic contribution of the screening currents is evaluated for up to $100\,\text{h}$ of stable operations. The field drift is calculated as the evolution in time of the THD factor with respect to the value at the end of the field ramp.

The influence of the number of tapes and layers on the field drift is shown in the right column of Figure 6.19. Numerical results show a drift of the THD factor for the *high* iron scenario exceeding 1 unit within $100\,\text{h}$ in the 4-layers configuration, whereas in the 16-layers configuration the increase remains below 0.01 units. The same qualitative behavior is found for the remaining scenarios. Concerning the influence of the tape critical current, a general trend is observed in Figure 6.20b where, with an insufficient critical current, the THD factor exceeds 10 units over a duration of 100 h, whereas with a sufficiently high critical current, the increase in THD with time is negligible in all scenarios.

Higher critical currents are beneficial for the stability of the screening currents, and are therefore preferable for the screens also in case there is no performance increase in the residual of the THD factor. The increase can be achieved by using high-I_C tapes and increasing the number of layers.
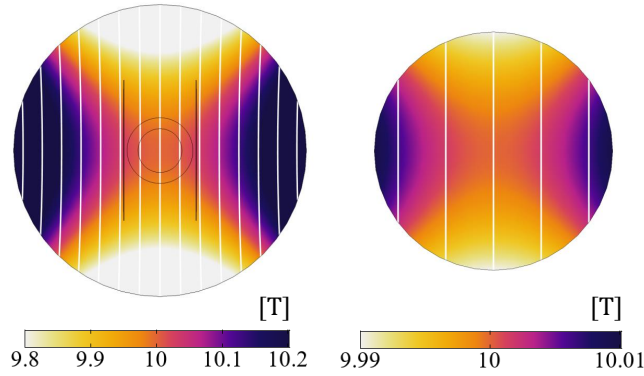
Figure 6.21. Case study for numerical extrapolation. Left: dipole magnetic field of $10\,\mathrm{T}$*, affected by 10 units of* b_3*. The two circles represent the reference circumference and the magnet aperture. The HALO position is also shown. Right: magnetic field inside the reference circumference.*

6.6 Numerical Extrapolation at $10\,\mathrm{T}$

Although the prototype is operated at $77\,\mathrm{K}$ and $100\,\mathrm{mT}$, within accelerator magnets the expected conditions for HTS screens are characterized by lower temperatures and higher fields. An increase in the magnetic field leads to a reduction of the critical current in the tapes, whereas a decrease in the temperature has the opposite effect (see e.g [30]). The behavior of the HALO technology is extrapolated to accelerator-like operational conditions by means of numerical simulations. Perfectly flat and parallel screens are assumed. Simulations are parametrized by the width of the screen, the number of layers per screen, and the horizontal distance of the screens from the magnet aperture. Following the same method described in Section 6.5, the magnetic field quality is evaluated $100\,\mathrm{s}$ after steady state operations, and the drift of the screening currents is assessed for $100\,\mathrm{h}$ of steady state operations.

The screens are assumed to be operated at $4.5\,\mathrm{K}$, in a background dipole field of $10\,\mathrm{T}$ with an error of 10 units of b_3. The model used for the extrapolation is shown in Figure 6.21, where the magnetic field is imposed by a boundary source. The magnetic field and the field error are chosen to qualitatively reproduce a field-scenario within the LHC [3]. The geometric setup of the screens and the reference radius is retained from the experiment. The screens are positioned with an horizontal gap of $2\,\mathrm{mm}$ with respect to the magnet aperture. The magnet aperture radius is $3/2$ bigger than the reference radius. The gap accounts for the structural elements such as the beam screen and the surrounding steel pipe [3].

The magnetic field error is negligible if compared to the dipole field. As a consequence, the magnetic field lines are assumed to be aligned with the HTS screens. The anisotropic behavior of the HTS tapes allows achieving a higher critical current in the screens. In the following, a critical current per unit of length $I_\mathrm{c} = 250\,\mathrm{A\,mm^{-1}}$ is assumed, conform with the measurements on commercially available tapes from [30] and [31].

6.6.1 HTS screens geometry

The number of tapes per layer is increased from 5 to 8 (4 to 7 for the odd-order layers), obtaining up to $100\,\mathrm{mm}$-wide screens. The number of layers per screen is also increased, from 4 to 16. The number of
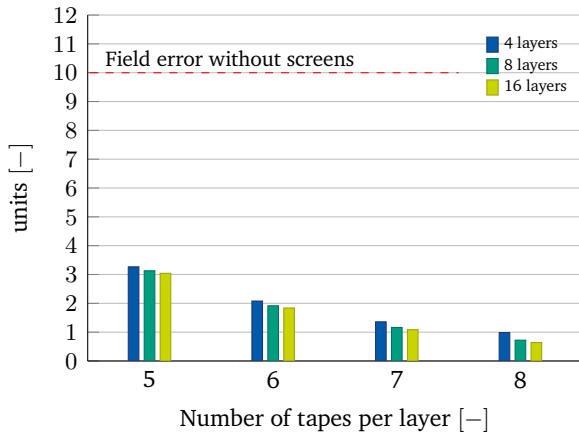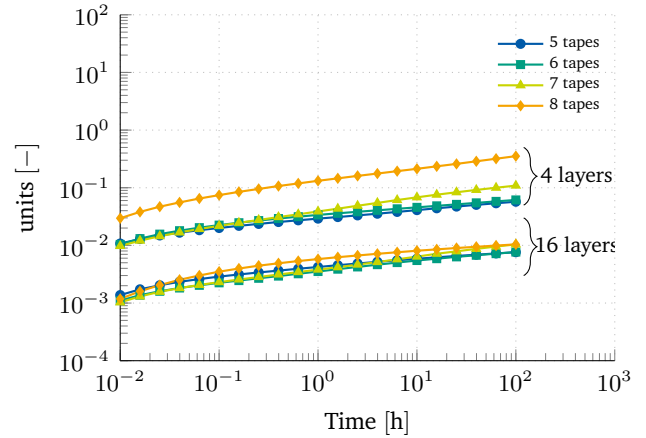
*(a) THD.* *(b) THD drift.*

Figure 6.22. (a) Simulated THD factor, in units, as a function of the number of tapes per layer. (b) Simulated drift of the THD factor, in units, as a function of time.

tapes per layer is combined with the number of layers, and the possible design combinations are investigated.

The magnetic field is linearly increased from zero up to $10\,$T within $10\,$s, then it is kept constant. The results are shown in Figure 6.22a, in terms of the THD factor as a function of the number of tapes per layer, and parametrized with the number of layers in the HTS screens. For the given magnetic configuration, the magnetic field error is reduced below one unit. If a field quality constraint is prescribed, for example in terms of maximum THD value, the screen design can be adapted to match the requirements.

The field-error cancellation is more effective for superconducting screens closer to the magnet aperture. This is shown in Fig. 6.23a, where the THD factor is calculated as a function of the number of tapes per layer, and parametrized with the distance between the screens and the magnet aperture. For the shortest screen made of 5 tapes, an increase of about $0.3\,$units/mm is found, whereas for the longest screen made of 8 tapes an increase of about $0.1\,$units/mm is obtained. Therefore, for this case, the sensitivity of the screen to the horizontal offset with respect to the magnet aperture is weaker for longer screens.

6.6.2 Screening currents drift

The drift of the THD factor is calculated as discussed in Section 6.5.3. The influence of the number of tapes and layers on the field drift is shown in Figure 6.22b. Numerical results show an increase for the THD factor below 0.1 units within $100\,$h, for HTS screens with 4 layers. For the case of a 16-layers design, the drift is reduced by about one order of magnitude, remaining below 0.01 units. If a maximum drift constraint is prescribed, it is possible to scale the screen design such that requirements are met.

The influence of the horizontal distance of the screens from the magnet aperture is shown in Figure 6.23b, considering 16-layers screens. For all the considered cases, the drift shows the same qualitative behavior, remaining below 0.1 units within $100\,$h of stable operations. Results confirm that higher critical currents are beneficial for the stability of the screening currents, and that the distance from the magnet aperture
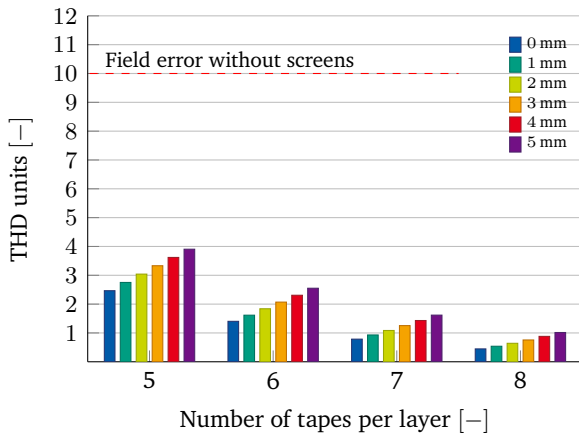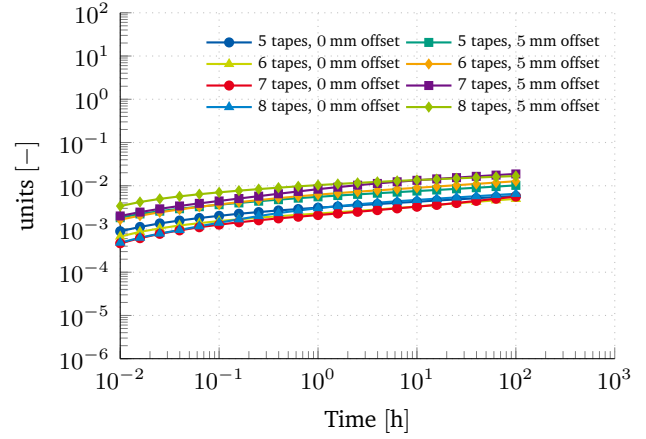
(a) THD.   *(b) THD drift.*

Figure 6.23. (a) Simulated magnetic field quality for 16-layers screens, in units as a THD factor. Results are given as a function of the number of tapes per layer, and parametrized with the horizontal displacement of the HTS screens with respect to the magnet aperture. (b) Simulated drift of the THD factor, in units, as a function of time.

influences the screen performance in terms of field-error cancellation, but is not crucial for the drift of the screening currents.

6.7 Discussion

The field quality measurements obtained for both the first and the second prototype (see Figures 6.16 and 6.17) highlight a relevant reduction of the field error in all the presented scenarios. The field quality improvement appears after the HALO has transitioned to the superconducting state, and it is obtained thanks to the magnetic contribution of screening currents induced in the HTS tapes.

The cancellation of the undesired field error occurs for all multipole components, contributing to the homogenization of the magnetic field in the magnet aperture, as shown by the magnetic field distribution in the right column of Figures 6.16 and 6.17. Considering the second prototype, the THD factor is reduced by a factor of three to four depending on the field-error scenario (see Figure 6.18). Overall, the field-error cancellation provided by means of HTS screens constitutes a net improvement for the magnetic field quality. Therefore, the proof of concept for the HALO technology can be considered successful.

The measured field-error cancellation for the two prototypes was about 70% and 90% of the value predicted by simulations, assuming perfectly positioned and straight screens. The discrepancy is due to geometric deformation of the HTS screens, caused by mechanical tolerances which affected the manufacturing of the prototypes. Such deformation introduces a self-field error which has a detrimental influence, posing an upper limit to the HALO performance. It is found that the self-field error delivers a constant field contribution whose relevance decreases as the overall field error increases.

With the second prototype, the THD factor due to the self-field error went down from twenty-one to five units. This error can be further reduced by suitable design choices, sufficiently tight mechanical tolerances, and a precise manufacturing process. Stiff HTS holders are recommended for mechanically sup-

porting the tapes. As an example, rectangular blocks with precisely machined outer surfaces may be used as both beam pipes and HTS holders, providing a natural integration of the screen within accelerator magnets.

Simulations considering flat-screen geometries are in qualitative agreement with measurements, although they systematically overestimate the HALO performance. A visual inspection of the first HTS holder prototype identified geometric defects. These imperfections were integrated in the model by means of curved screens, and quantified via an optimization algorithm, leading to simulations that are in full quantitative agreement with measurements. Optimization results shall be used carefully, since over-fitting is a risk, for example of the superconducting properties of the tapes. However, the geometric defects for the two prototypes are determined only once and in the absence of iron. With the subsequent addition of iron, and in spite of the absence of 're-fitting' for geometric deformation, the measured and simulated results in Figures 6.16 and 6.17 show a high degree of consistency, which is a strong indication of the good predictive value of the numerical model. At the same time, simulations supported the interpretation of the self-field error in the first prototype, providing valuable insights for the design of the second iteration.

The HTS screens are simulated at $4.5\,\mathrm{K}$ and in $10\,\mathrm{T}$ dipole background field which are working conditions typical of accelerator magnets. The field-error cancellation is still effective as long as the equivalent critical current density of the screens is increased accordingly, that is, by increasing the number of layers and decreasing the operational temperature. Numerical results show also that the field-error cancellation can be improved by increasing the width and the number of layers of the HTS screens. The THD factor is reduced below one unit, leading to a nearly perfect cancellation of the field error. The decay of the screening currents over time, and the consequent degradation of the field quality, is expected to remain within 0.1 units over 10 hours, being negligible in comparison with the operating time of accelerator circuits [3].

The persistency of the screening currents is the cornerstone of the overall HALO technology. For this reason, the screening currents decay rate must cope with the field quality requirements in the target application. The field drift can be kept within specifications by choosing appropriate design features for HALO, such as the critical current of the tapes and number of layers in the screens. In an accelerator magnet, the HTS screens must be centered as close as possible around the beam vacuum chamber. The HALO technology is expected to provide the maximal benefit to magnets made of ReBCO tapes, as at low current the field quality in those magnets is expected to be heavily degraded by persistent magnetization phenomena.

The maximum field error which can be possibly canceled is determined by the equivalent critical current of the HTS screens. This parameter can be increased either by increasing the number of layers of tapes, or decreasing the operational temperature. In order to integrate HALO in accelerator magnets, the combination of both strategies is envisioned, as the magnetic fields are expected to be up to two orders of magnitude higher than in the experimental setup used for the proof of concept. For this reason, an operational temperature below $20\,\mathrm{K}$ is recommended.

6.8 Proposed Next Steps

The experimental and simulation studies of HALO show that the experimentally observed behavior is well understood and that HALO may have a significant positive impact on the field quality of accelerator magnets. An interesting candidate for a future practical application of HALO is the common coil design [299]. The common coil design features large race-tracks that give most of the field magnitude over the bore, in

(a) Cross section of the magnet.   *(b) Detail of the magnet aperture.*
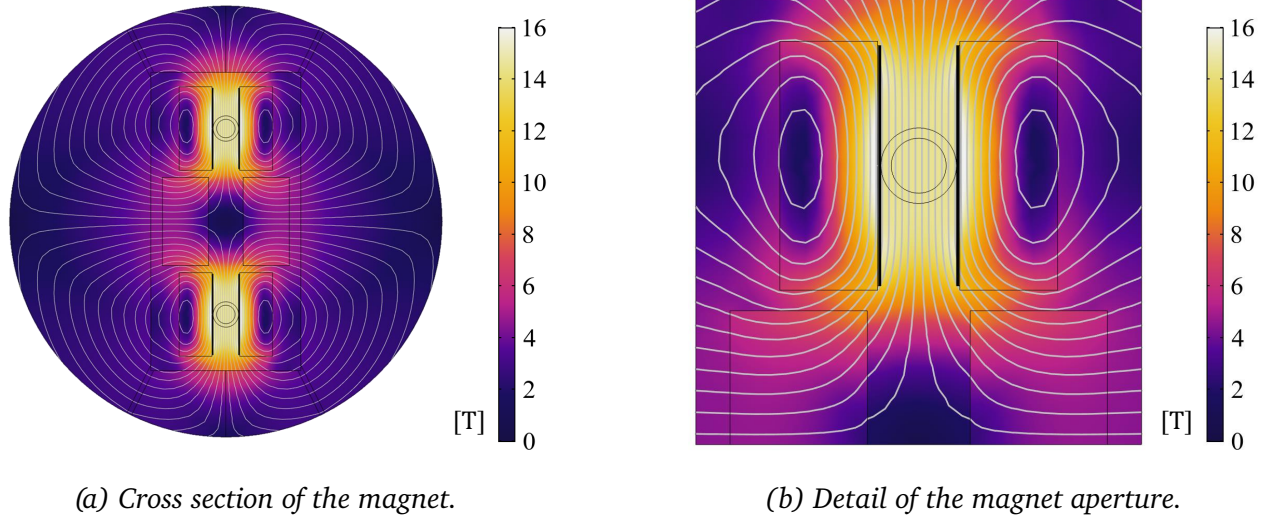
Figure 6.24. Magnetic field in the simplified model of the FCC common coil. (a) Magnetic field, in T*, in the cross section of the magnet. (b) Detail of the magnet aperture.*

combination with smaller correction coils that are needed for improving the field quality. This design is of relevance, as race-track coils can be combined in a common-coil design which is one of the candidates for the superconducting magnets to be used in the Future Circular Collider [9]. However, despite the simplicity in the design of race-track coils, correction coils must be added to the magnet design. The correction coils are unfortunately necessary, as the race-track coils by themselves cannot match the accelerator standards in the field quality [300, 301].

The common coil is a very interesting candidate for use with HALO, as HTS screens could replace the correction coils. Consequently, the magnet design could focus on easy-to-produce race-track coils in combination with HALO. To motivate this subsequent study, we present a preliminary investigation for a simplified model in the 2D setting of the common coil proposed in [300]. The magnet geometry and the magnetic field map are shown in Figure 6.24a. Here, two HTS screens are added between each of the aperture and the race-track coil, as highlighted by the detail view in Figure 6.24b. The screens are 140 mm wide and are composed of 12 layers, each with a critical current per unit of length $I_c = 200\,\mathrm{A\,mm^{-1}}$. The simulated magnetic field quality is reported in Figure 6.25a as a multipole series expansion, for the cases without and with HALO. The magnetic field error in the magnet aperture is shown in Figure 6.25b. The THD factor of the common coil design without correction coils is reduced from 147 to 6 units in the cross-sectional plane. Unfortunately, a detailed study of the common coil design in combination with HALO (including a detailed study of the ends) is outside the scope of this thesis work, but the preliminary results presented here give motivation to proceed with HALO for high-field accelerator magnets, in particular for fully-racetrack-based common coil magnets.

6.9 Summary

This chapter discusses the proof of concept of HALO, a device composed of HTS screens for the magnetic field-error cancellation in accelerator magnets. The working principle is based on the persistent magnetization phenomena produced by screening currents in ReBCO tapes. The magnetization is used for shap-
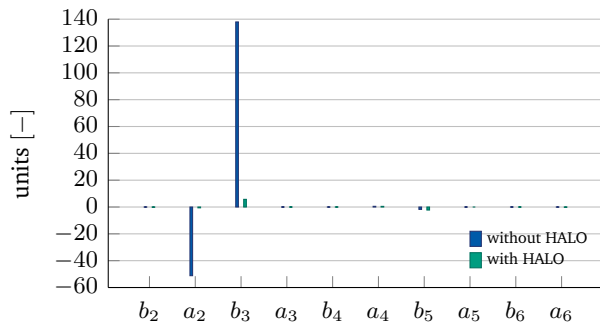
(a) Magnetic field error.
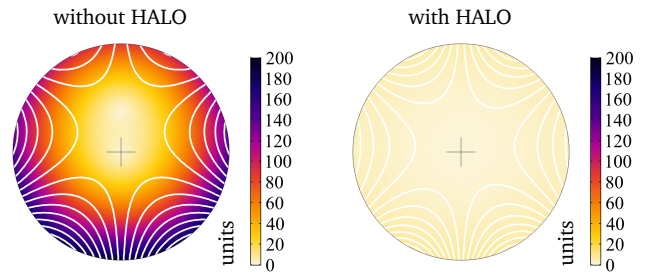
(b) Magnetic field error.

Figure 6.25. *Simulated magnetic field quality for the FCC common coil design, before and after the introduction of HTS screens. (a) Multipole series expansion. (b) Magnetic field error in the magnet aperture.*

ing the magnetic field in the aperture of accelerator magnets. The screens are aligned with the main field component, providing a selective field-error cancellation for both dynamic and static field-error contributions.

Two prototypes were built and tested, differing in the design of the HTS holder. It was found in the first prototype that undesired geometric defects add a detrimental effect on the measured field quality, limiting the sensitivity of the experimental assembly. The lessons learned were applied to the second prototype whose geometric defects were substantially smaller. The prototypes were tested in the aperture of a reference dipole magnet whose field was perturbed by means of iron bars. The magnetic field quality was measured for four field-error configurations, obtained by varying the position of the iron bars in the magnet aperture. Measurements show that the second HALO prototype provides a significant reduction of the THD factor associated to the field error, up to a factor of four, reaching up to 90% of the performance predicted by numerical simulations.

The numerical analysis is carried out under magnetoquasistatic assumptions, using a model in the 2D setting implementing the coupled $\vec{A} - \vec{H}$ formulation from Chapter 2, and the thin-shell approximation for the tapes composing the HTS screens. Simulations provide the theoretical performance of HALO in case of perfectly parallel HTS screens, and quantify the influence of geometric defects in the screens, achieving quantitative agreement with measurements. Numerical extrapolation on the prototype shows that a complete error cancellation may be achieved by increasing the width and the thickness of the screens. At the same time, the field-quality drift due to the decay of screening currents can be reduced by increasing the equivalent critical current of the screens. The screens are also simulated for operational conditions compatible with accelerator magnets, showing that the decay of screening currents is not an issue, and that the typical field quality requirements for accelerator magnets are at reach.

7 Conclusions and Outlook

This work is motivated by the recent advancements in the application of high-temperature superconducting technology to accelerator magnets for particle physics. It focuses on the development of a coupled $\vec{A} - \vec{H}$ field formulation for transient magnetothermal simulations of systems comprising high-temperature superconductors, especially ReBCO tapes, and on the development of proof-of-concept superconducting screens for magnetic field-error cancellation in accelerator magnets.

The electromagnetic behavior of HTS materials is simulated as an eddy-current problem in the time domain by means of the finite element method. This allows resolving the current density distribution within the superconductor, in particular screening current phenomena and their influence on the magnetic field quality. As screening currents are the principal contribution to Joule losses, the field problem is extended by the heat balance equation, such that quench phenomena are also included. In this way, it is possible investigating the magnetothermal behavior in systems made of high-temperature superconductors. The main challenge is identified in the nonlinear electrical behavior of superconducting materials, traditionally represented by means of an empirical power law. It has been shown that finite material properties are ensured in both (super)conducting and nonconducting materials by means of a coupled $\vec{A} - \vec{H}$ field formulation combined with a domain decomposition strategy. On the one hand, magnetic-field conforming formulations are resistivity-based, and can be easily extended to superconducting materials. On the other hand, the magnetic vector potential is preferred to scalar-potential formulations in the remaining computational domain for ensuring higher precision in ferromagnetic regions, avoiding cut-sets in case of domains with non-trivial topology. Such advantages come at a price of a higher number of degrees of freedom in the 3D setting. The formulation is complemented with solid conductor models for the coupling with voltages and/or currents belonging to external circuits. The implementation of the formulation is verified against reference solutions for individual tapes in the 3D setting, and coils in the 2D setting. To cope with field-circuit coupled simulations of circuits containing accelerator magnets, a coupling interface is derived as an optimized Schwarz transmission condition which is approximated for small frequencies by a Taylor series expansion, truncated to the first order. The transmission condition is physically interpreted as connecting the magnetothermal field model to the circuit as the series of an inductance, a resistance, and a voltage correction term. The coupling interface is successfully used for the cosimulation of a quench event in an HTS solenoid, using the waveform relaxation method.

It is found that superconducting tapes exhibiting a high aspect ratio can be approximated as thin shells by solving for the normal component of $\vec{H}$ within the superconductor. The formulation is understood as formally identical to a $\vec{T}$ formulation with a single-vector component. For stranded multifilamentary conductors, the field problem is reduced to a monolithic $\vec{A}$ field formulation which implements an equivalent magnetization model. The thin-shell approximation is verified by comparison with analytical solutions available in literature. It is also verified that accurate results are obtained as long as the thickness of the tape is below the skin depth. Consequently, it is shown that a block of superconducting material can be modeled by means of a stack of shells, obtaining consistent results for magnetic fields applied perpendicularly to the wide surface of the block. The thin-shell approximation plays a crucial role in reducing the computational time: in case of

superconducting tapes in the 2D setting, a speed-up of about two orders of magnitude is observed with respect to models of fully-resolved tapes implementing the $\vec{H}$ formulation. The approximation is recommended for simulating coils with a high number of individually-insulated turns. However, in case of no-insulation (or partial-insulation) coils, the thin-shell approximation cannot capture the local current redistribution phenomena occurring between different tapes in case of a quench, therefore models with fully-resolved tapes are necessary.

The coupled $\vec{A} - \vec{H}$ field formulation is validated against field quality measurements in the HTS insert dipole magnet Feather-M2.1-2. It is shown that the 2D numerical model provides an accurate quantification of the dynamic distribution of the screening currents. The model requires a free parameter for the power law obtained from the critical current of the coil, compensating for the uncertainty in the critical current density of the tape. At the same time, a parametric sweep is used to cope with the uncertainty in the power-law index. The influence of the iron hysteresis on the field quality is found to be negligible with respect to screening currents. Although simulations and measurements are in satisfactory agreement, the model can be improved by a better knowledge of both the critical surface of the tape used in the coil, thus eliminating the free parameter used for describing the critical current, and the magnetization curve of the iron used for the yoke. These numerical results can be used not only for the magnetic field quality analysis, but also for the calculation of the Joule losses and the dynamic forces in the coil. Therefore, such modeling approach can be integrated in the future design of HTS magnets, for example within a numerical optimization workflow for quench protection studies.

The need for high magnetic field quality in accelerator magnets has resulted in the proposal of superconducting screens for magnetic field-error cancellation, and the subsequent development of HALO. Experiments have confirmed the effectiveness of brick-layer structures composed of HTS tapes in improving the magnetic field quality by means of persistent magnetization. Tight mechanical tolerances are necessary for the manufacturing of the mechanical support for the screens, this to minimize geometric deformations and to ensure the geometric alignment with the main field component. The performance of the screens depends also on their geometric properties and equivalent critical current. It is found that the error cancellation is improved by increasing the width of the screens, their number of layers, and by positioning the screens as close as possible to the magnet aperture. In particular, the number of layers can be adjusted such that the associated time constant for decay of the screening currents is well above the cycle time in circuits of accelerator magnets.

The HTS screens are applicable regardless of the technology used for the magnet, and might be applied to simple and inexpensive coils with large field errors. Promising candidates for the HALO technology are race-track coils (such as common coils), as they are simple to construct and might rely on superconducting screens instead of auxiliary coils for field quality improvement. Moreover, HTS screens might be of use for applications beside accelerator magnets where stringent field quality requirements need to be satisfied.

7.1 Outlook

The theoretical, numerical and experimental results presented in this work have led to new questions to be investigated in future work.

The $\vec{A} - \vec{H}$ coupled field formulation could be further extended to include a scalar potential ϕ for the nonconducting domains, limiting the use of the magnetic vector potential to ferromagnetic materials. This would

(a) HALO applied to a racetrack coil.

(b) Simple no-insulation coil.
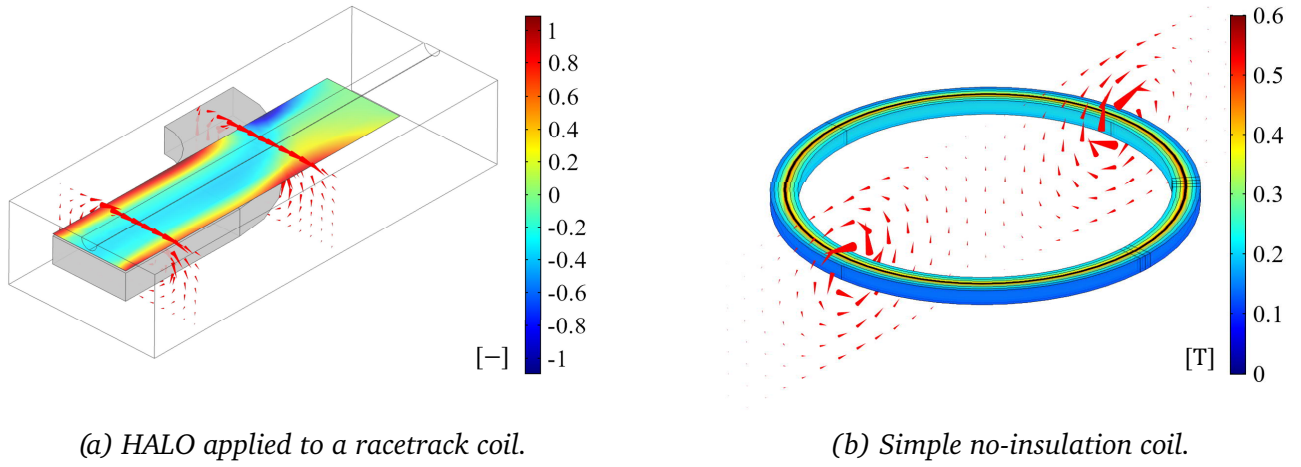
Figure 7.1. Examples of 3D models. (a) Current density distribution in a HTS screen for the end-coil region of a racetrack coil (only 1/8 of the model is shown). The half-cylinder shows the position of the magnet aperture. (b) Magnetic field produced by a simple no-insulation coil made of five turns, once stationary conditions are reached.

lead to an $\vec{A}, \vec{H} - \varphi$ formulation, reducing the number of degrees of freedom in 3D models which could reduce the computational cost. A further step would be extending the scalar potential to the conducting regions, thus obtaining a coupled $\vec{A}, \vec{T} - \psi$, formulation which would be suitable also in the magnetostatic approximation. Another point consists in improving the optimized transmission condition in the waveform relaxation algorithm for accelerator magnets in circuits, which has been approximated by means of a Taylor series expansion. This leaves the possibility of adding more terms of the series to potentially further speed up the iteration convergence.

Field quality in HTS accelerator magnets is an open topic. The HTS screens are a promising technology for reducing the impact of screening currents. They should be tested in accelerator-like conditions, and possibly integrated into the design of a full-size accelerator magnet. The end coil region is of particular interest, and for this detailed 3D modeling is required. As an example, Figure 7.1a shows the current density in an HTS screen for the end-coil region of a racetrack coil.

Another open topic is the protection of HTS cables from the consequences of a quench. A potential solution is offered by the no-insulation (NI) coil concept, which must be carefully studied due to potentially unbalanced Lorentz forces once the current redistributes in the coil. Moreover, NI coils could be combined with HTS screens for compensating the field error introduced by eddy currents. Figure 7.1b shows an example of a five-turns, no-insulation coil simulated with $\vec{A} - \vec{H}$ coupled field formulation.

As shown in Figures 7.1a and 7.1b, it is already demonstrated that the formulation described in this thesis is sufficiently advanced to model three-dimensional transient effects in accelerator magnets and non-insulated coil transient behavior, however further studies are needed to fully work out the implications of this type of modeling. The formulation might support the design of future accelerator magnets based on HTS tapes, investigating the impact of persistent magnetization phenomena on screening currents, and the effectiveness of quench detection and protection methods.

A ReBCO Critical Current Density

Numerical Fit

In ReBCO conductors, the critical current density $J_c(\vec{B}, T)$ shows an anisotropic, field- and temperature-dependent behavior. This can be modeled, for example, by means of the angular-dependent scaling relation in [280]. The fit is formalized with respect to the tangential and normal directions of the tape associated to the subscripts ab and c, consistently with [280]. The fit requires the input quantities $|\vec{B}|$, T, θ_B. The field angle θ_B is defined as the angle between $\vec{B}$ and the normal unit vector $\vec{n}$ perpendicular to the tape wide surface, reading

$$\theta_B = \arccos\left(\frac{\vec{B} \cdot \vec{n}}{|\vec{B}|}\right). \tag{A.1}$$

The temperature and magnetic flux density are normalized by the critical temperature T_{c0}, and the tangential and normal irreversibility fields $B_{i,ab}$ and $B_{i,c}$, as

$$t = \frac{T}{T_{c0}}, \qquad b_{ab} = \frac{|\vec{B}|}{B_{i,ab}}, \qquad b_n = \frac{|\vec{B}|}{B_{i,c}}. \tag{A.2}$$
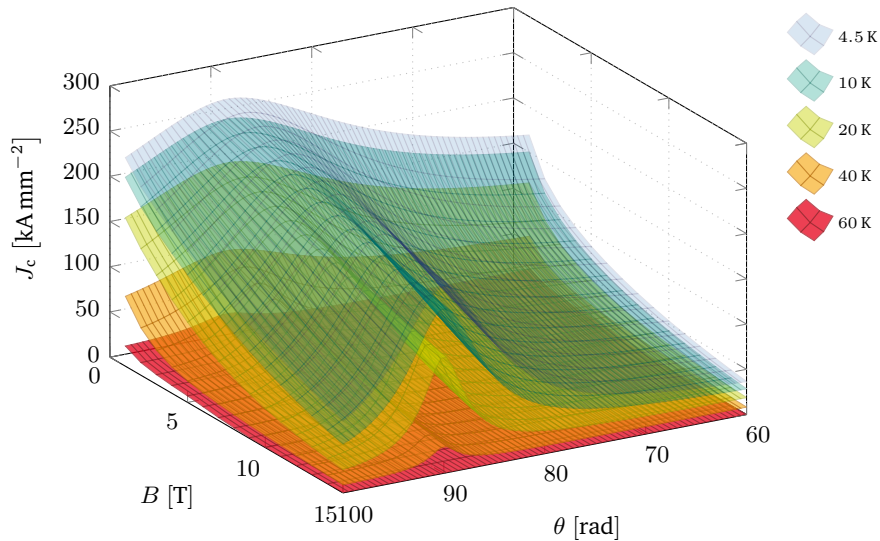

Figure A.1. Critical current density, in $kA\,mm^{-2}$, as a function of the magnetic flux density and field angle, parametrized by the temperature.

symbol	g_0	g_1	g_2	g_3	T_{c0}	p_c	q_c	$B_{i0,c}$	γ_c	α_c
unit	–	–	–	–	K	–	–	T	–	$\mathrm{MA\,T\,mm^{-2}}$
value	0.03	0.25	0.06	0.06	93	0.5	2.5	140	2.44	1.86

symbol	ν_g	a	n_0	n_1	n_2	p_{ab}	q_{ab}	$B_{i0,ab}$	γ_{ab}	α_{ab}
unit	–	–	–	–	K	–	–	T	–	$\mathrm{MA\,T\,mm^{-2}}$
value	1.85	0.1	1	1.4	4.45	1	5	250	1.63	68.3

Table A.1. Parameters used for the J_c fit

The irreversibility fields are given by

$$B_{i,ab} = B_{i0,ab} \left((1 - t^{n_1})^{n_2} + a\left(1 - t^n\right) \right), \tag{A.3}$$
$$B_{i,c} = B_{i0,c} \left(1 - t^n\right), \tag{A.4}$$

where $B_{i0,ab}$ and $B_{i0,c}$ are the maximum irreversibility fields for the two tape directions, and n, n_1, and n_2 are fitting parameters. The critical current density is obtained separately for the tangential and perpendicular directions, reading

$$J_{c,ab}(|\vec{B}|, T) = \begin{cases} \dfrac{\alpha_{ab}}{|\vec{B}|} (b_{ab})^{p_{ab}} (1 - b_{ab})^{q_{ab}} \left((1 - t^{n_1})^{n_2} + a((1 - t^n))^{\gamma_{ab}}\right) & \text{if } t \text{ and } b_{ab} < 1, \\ 0 & \text{otherwise}, \end{cases} \tag{A.5}$$

$$J_{c,c}(|\vec{B}|, T) = \begin{cases} \dfrac{\alpha_c}{|\vec{B}|} (b_c)^{p_c} (1 - b_c)^{q_c} (1 - t^n)^{\gamma_c} & \text{if } t \text{ and } b_c < 1, \\ 0 & \text{otherwise}, \end{cases} \tag{A.6}$$

where α_{ab} and α_c are normalization constants, and p_{ab}, p_c, q_{ab}, q_c, γ_{ab}, and γ_c are fitting parameters related to the field and temperature dependency for the two tape directions. The angular dependency on the critical current density is included by means of the anisotropy factor $g(|\vec{B}|, T)$, defined by

$$g(|\vec{B}|, T) = g_0 + g_1 e^{g_2 |\vec{B}| e^{-g_3 T}} \tag{A.7}$$

where g_0, g_1 and g_2 are fitting parameters. The previous definitions are combined into the critical current density fit which reads

$$J_c(|\vec{B}|, T, \theta_B) = \min(J_{c,c}(|\vec{B}|, T), J_{c,ab}(|\vec{B}|, T)) + \frac{\max((J_{c,ab}(|\vec{B}|, T) - J_{c,ab}(|\vec{B}|, T)), 0)}{1 + \left(\dfrac{\theta_{\pi/2-B}}{g(|\vec{B}|, T)}\right)^{\nu_g}}, \tag{A.8}$$

where ν_g is a fitting parameter. The purpose of the min and max functions is to ensure a consistent fit behavior for $J_{c,c} > J_{c,ab}$ which may occur at temperatures close to T_{c0}. The fit is unstable for $|\vec{B}| \to 0$, therefore a lower limit of $B_{\min} = 10\,\mathrm{mT}$ is prescribed, that is, $|\vec{B}| = B_{\min}$ if $|\vec{B}| < B_{\min}$. As an example, the fit (A.8) is shown in Figure A.1 for a tape produced by Fujikura [284], using the parameters given in Table A.1.

B Material Law for Resistivity

The comparison proposed in this section follows closely the work in [172]. The nonlinear resistivity ρ in HTS materials can be modeled by means of the phenomenological percolation-depinning law proposed in [170]. The relation introduces a lower limit $J_{\mathrm{c,min}}(\vec{B},T)$ for the current density. For $|\vec{J}| \le J_{\mathrm{c,min}}$, the magnetic field is frozen in the superconductor, therefore no flux creep can occur and the current density flow is perfectly lossless [1]. The percolation-depinning law reads

$$\rho(|\vec{J}|, \vec{B}, T) = \begin{cases} 0, & \text{if } |\vec{J}| < J_{\mathrm{c,min}}(\vec{B},T) \\ \dfrac{E_{\mathrm{c}}}{J_{\mathrm{c}}(\vec{B},T)} \left(\dfrac{|\vec{J}| - J_{\mathrm{c,min}}(\vec{B},T)}{J_{\mathrm{c}}(\vec{B},T) - J_{\mathrm{c,min}}(\vec{B},T)} \right)^{n(\vec{B},T)-1}, & \text{if } |\vec{J}| > J_{\mathrm{c,min}}(\vec{B},T) \end{cases} \tag{B.1}$$

where $\vec{J}$ is the current density, E_{c} is the critical electric field, and $J_{\mathrm{c}}(\vec{B},T)$ and $n(\vec{B},T)$ are the anisotropic field- and temperature-dependent critical current density and power-law index.

In practice, $J_{\mathrm{c,min}}(\vec{B},T)$ decreases to zero as $\vec{B}$ or T are increased (see [170] and the references therein). Therefore, the percolation-depinning law can be simplified into the widely used power law [171], obtained by applying the asymptotic approximation $J_{\mathrm{c,min}} \to 0$ to (B.1), thus neglecting frozen-field phenomena. The power law reads

$$\rho(|\vec{J}|, \vec{B}, T) = \frac{E_{\mathrm{c}}}{J_{\mathrm{c}}(\vec{B},T)} \left(\frac{|\vec{J}|}{J_{\mathrm{c}}(\vec{B},T)} \right)^{n(\vec{B},T)-1}, \tag{B.2}$$

where the value of E_{c} is arbitrary, and it is typically set to $1 \times 10^{-4}\,\mathrm{V\,m^{-1}}$ [173]. Subsequently, J_{c} is determined as the value for which E_{c} is reached in the material. The n-value typically ranges from 40 to 50 for LTS materials [174], and from 20 to 30 in HTS materials [175]. An example of the J_{c} behavior is given in Appendix A.

For increasing n-values, (B.2) gets steeper for $|\vec{J}| > J_{\mathrm{c}}$. Therefore, the power law can be simplified into the critical-state model [176, 177], obtained from (B.2) by the asymptotic approximation $n \to \infty$. The critical-state model reads

$$\rho(|\vec{J}|, \vec{B}, T) = \begin{cases} 0, & \text{if } |\vec{J}| \le J_{\mathrm{c}}(\vec{B},T), \\ [0,+\infty), & \text{if } |\vec{J}| = J_{\mathrm{c}}(\vec{B},T), \\ \varnothing, & \text{if } |\vec{J}| > J_{\mathrm{c}}(\vec{B},T), \end{cases} \tag{B.3}$$

and corresponds to a nonsmooth, multivalued relation where the current density is either equal to zero or $J_{\mathrm{c}}(\vec{B},T)$. Numerical methods for implementing (B.3) are provided for example in [302, 303].
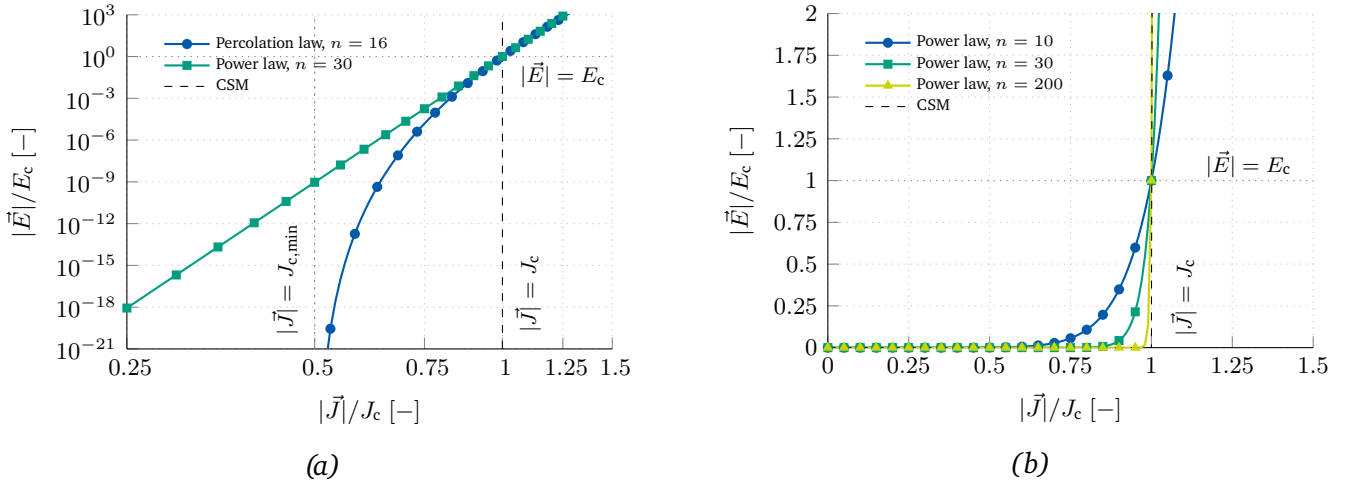
Figure B.1. Quantitative behavior of ρ in HTS materials, normalized by J_c and E_c, assuming constant parameters. (a) Comparison of the percolation law, power law and critical state model. (b) Comparison of the power law, parametrized by n, and the critical state model.

Comparison

The quantitative behavior of (B.1)-(B.3) is shown in Figure B.1a, assuming constant n and J_c. The percolation-depinning law converges to the power law as the current density is increased above $J_{c,min}$. The power-law behavior is parametrized by the n value and shown in Figure B.1b. For $n \to \infty$ the power law approximates the behavior of the critical state model.

The percolation-depinning law provides the most general relation, whereas the power law and the critical state model are particular cases obtained by successive simplifications. On the one hand, the magnetic field and temperature values adopted in practical applications ensure that the current density is typically much higher than the lower limit considered in the percolation-depinning relation. On the other hand, the critical state model does not allow for field relaxation phenomena occurring in HTS materials. A comparison of numerical examples implementing (B.1)-(B.3) is available in [172].

List of acronyms

BC	Boundary condition
CF	Current flow
BDF	Backward differentiation formula
BSCCO	Bismuth strontium calcium copper oxide
BVP	Boundary value problem
CERN	European Organization for Nuclear Research
CLIQ	Coupling-loss induced quench
DAE	Differential algebraic equation
DW	Darwin
EM	Electromagnetic
EQS	Electroquasistatic
ES	Electrostatic
FCC	Future Circular Collider
FEM	Finite element method
FM	Full Maxwell
HALO	Harmonics-absorbing layered-object
HTS	High-temperature superconductor
IC	Initial condition
IFCC	Inter-filament coupling current
ISCC	Inter-strand coupling current
IVP	Initial value problem
KCL	Kirchhoff's current law
KVL	Kirchhoff's voltage law
LHC	Large Hadron Collider
LTE	Local truncation error
LTS	Low-temperature superconductor
MNA	Modified nodal analysis
MQS	Magnetoquasistatic
MS	Magnetostatic
NI	No-insulation
ODE	Ordinary differential equation
PDE	Partial differential equation
PEC	Perfect electric conductor
PMC	Perfect magnetic conductor
PSO	Particle swarm optimization
ReBCO	Rare-earth copper barium oxide
SPICE	Simulation program with integrated circuit emphasis
STEAM	Simulation of transient effects in accelerator magnets
THD	Total harmonic distortion
WR	Waveform relaxation

Bibliography

[1]   M. N. Wilson, *Superconducting magnets*. Clarendon Press Oxford, 1983.

[2]   CERN Document Server, https://cds.cern.ch/. Terms of use: https://copyright.web.cern.ch/.

[3]   O. Brüning *et al.*, *LHC design report*. European Organization for Nuclear Research, 2004.

[4]   ALICE Collaboration, "The ALICE experiment at the CERN LHC", *Journal of Instrumentation*, vol. 3, no. 08, S08002, 2008.

[5]   ATLAS Collaboration, "The ATLAS experiment at the CERN large hadron collider", *Journal of instrumentation*, vol. 3, S08003, 2008.

[6]   CMS Collaboration, "The CMS experiment at the CERN LHC", *Journal of instrumentation*, vol. 3, no. 08, S08005, 2008.

[7]   LHCb Collaboration, "The LHCb detector at the LHC", *Journal of instrumentation*, vol. 3, no. 08, S08005, 2008.

[8]   P. Kapitza, "Viscosity of liquid helium below the λ-point", *Nature*, vol. 141, no. 3558, pp. 74–74, 1938.

[9]   FCC collaboration, "FCC-hh: The Hadron Collider: Future Circular Collider Conceptual Design Report Volume 3", *European Physical Journal: Special Topics*, vol. 228, no. 4, pp. 755–1107, 2019.

[10] M. Tinkham, *Introduction to superconductivity*. Courier Corporation, 2004.

[11] H. K. Onnes, *Sur les résistances électriques*. Gauthier Villars, 1912.

[12] W. Meissner and R. Ochsenfeld, "Ein neuer effekt bei eintritt der supraleitfähigkeit", *Naturwissenschaften*, vol. 21, no. 44, pp. 787–788, 1933.

[13] A. A. Abrikosov, "The magnetic properties of superconducting alloys", *Journal of Physics and Chemistry of Solids*, vol. 2, no. 3, pp. 199–208, 1957.

[14] J. Van Nugteren, "High temperature superconductor accelerator magnets", Ph.D. dissertation, Twente U., Enschede, Enschede, 2016.

[15] H. Müller and T. Schneider, "Heat treatment of Nb_3Sn conductors", *Cryogenics*, vol. 48, no. 7-8, pp. 323–330, 2008.

[16] A. Golovashkin *et al.*, "Low temperature direct measurements of Hc2 in HTSC using megagauss magnetic fields", *Physica C: Superconductivity*, vol. 185, pp. 1859–1860, 1991.

[17] J. Van Nugteren *et al.*, "Toward ReBCO 20 T+ Dipoles for Accelerators", *IEEE Transactions on Applied Superconductivity*, vol. 28, no. 4, pp. 1–9, 2018.

[18] L. Rossi and C. Senatore, "HTS Accelerator Magnet and Conductor Development in Europe", *Instruments*, vol. 5, no. 1, p. 8, 2021.

[19] L. Rossi *et al.*, "The EuCARD-2 future magnets European collaboration for accelerator-quality HTS magnets", *IEEE transactions on applied superconductivity*, vol. 25, no. 3, pp. 1–7, 2015.

[20]   The ARIES project, Available online: https://aries.web.cern.ch, accessed on 01 March 2022.

[21]   G. Kirby *et al.*, "Accelerator-quality HTS dipole magnet demonstrator designs for the EuCARD-2 5T 40-mm clear aperture magnet", *IEEE Transactions on Applied Superconductivity*, vol. 25, no. 3, pp. 1–5, 2014.

[22]   J. Van Nugteren *et al.*, "Study of a 5 T research dipole insert-magnet using an anisotropic ReBCO Roebel cable", *IEEE transactions on applied superconductivity*, vol. 25, no. 3, pp. 1–5, 2014.

[23]   A. Milanese *et al.*, "Design of the EuCARD high field model dipole magnet FRESCA2", *IEEE transactions on applied superconductivity*, vol. 22, no. 3, pp. 4 002 604–4 002 604, 2011.

[24]   G. Willering *et al.*, "Tests of the FRESCA2 100 mm bore Nb_3Sn block-coil magnet to a record field of 14.6 T", *IEEE Transactions on Applied Superconductivity*, vol. 29, no. 5, 2019.

[25]   H. Maeda, Y. Tanaka, M. Fukutomi, and T. Asano, "A new high-T_c oxide superconductor without a rare earth element", *Japanese Journal of Applied Physics*, vol. 27, no. 2A, p. L209, 1988.

[26]   T. Sekitani, Y. H. Matsuda, and N. Miura, "Measurement of the upper critical field of optimally-doped YBa2Cu3O7-δ in megagauss magnetic fields", *New Journal of Physics*, vol. 9, no. 3, p. 47, 2007.

[27]   M.-K. Wu *et al.*, "Superconductivity at 93 K in a new mixed-phase Y-Ba-Cu-O compound system at ambient pressure", *Physical review letters*, vol. 58, no. 9, p. 908, 1987.

[28]   L. Bottura and L. Rossi, "Technical and Economical Comparison YBCO/Bi-2212 Magnets", No. EDMS 1325245 (CERN, Geneva, 2026), Tech. Rep., 2016, Available online: https://edms.cern.ch/ui/#!master/navigator/document?D:1779412637:1779412637:subDocs, accessed on 01 March 2022.

[29]   M. Cyrot and D. Pavuna, *Introduction to superconductivity and high-T_c materials*. World Scientific Publishing Company, 1992.

[30]   C. Senatore *et al.*, "Field and temperature scaling of the critical current density in commercial REBCO coated conductors", *Superconductor Science and Technology*, vol. 29, no. 1, p. 014 002, 2015.

[31]   T. Benkel *et al.*, "REBCO performance at high field with low incident angle and preliminary tests for a 10-T insert", *IEEE Transactions on Applied Superconductivity*, vol. 26, no. 3, pp. 1–5, 2016.

[32]   CERN Accelerating News, https://acceleratingnews.web.cern.ch/, Terms of use: CC BY-NC 3.0. Accessed on 01 March 2022.

[33]   S. Song *et al.*, "Quench detection method for HTS coils using electromagnetically coupled coils", *IEEE Transactions on Applied Superconductivity*, vol. 25, no. 3, pp. 1–4, 2014.

[34]   M. Marchevsky *et al.*, "Localization of quenches and mechanical disturbances in the Mu2e transport solenoid prototype using acoustic emission technique", *IEEE Transactions on Applied Superconductivity*, vol. 26, no. 4, pp. 1–5, 2016.

[35]   M. Marchevsky *et al.*, "Quench detection for high-temperature superconductor conductors using acoustic thermometry", *IEEE Transactions on Applied Superconductivity*, vol. 28, no. 4, pp. 1–5, 2018.

[36]   M. Marchevsky *et al.*, "Axial-field magnetic quench antenna for the superconducting accelerator magnets", *IEEE Transactions on Applied Superconductivity*, vol. 25, no. 3, pp. 1–5, 2015.

[37]   F. Scurti, S. Ishmael, G. Flanagan, and J. Schwartz, "Quench detection for high temperature superconductor magnets: a novel technique based on Rayleigh-backscattering interrogated optical fibers", *Superconductor Science and Technology*, vol. 29, no. 3, 03LT01, 2016.

[38]   A. Akbar *et al.*, "Fast Hotspot Detection in SFCLs by Exploiting Strain Response in Optical Fiber Sensing", *IEEE Transactions on Applied Superconductivity*, vol. 31, no. 5, pp. 1–5, 2021.

[39] A. Dudarev *et al.*, "Quench propagation and detection in the superconducting bus-bars of the atlas magnets", *IEEE transactions on applied superconductivity*, vol. 10, no. 1, pp. 381–384, 2000.

[40] S. Hasegawa, S. Ito, G. Nishijima, and H. Hashizume, "Quench detection performance of low-temperature superconducting quench detectors for rebco tape in magnetic fields", *IEEE Transactions on Applied Superconductivity*, vol. 31, no. 5, pp. 1–5, 2021.

[41] R. Kang, J. Wang, and Q. Xu, "Detecting quench in hts magnets with lts wires–a theoretical and numerical analysis", *arXiv preprint arXiv:2109.03982*, 2021.

[42] E. Ravaioli *et al.*, "A new quench detection method for HTS magnets: Stray-capacitance change monitoring", *Physica Scripta*, vol. 95, no. 1, p. 015 002, 2019.

[43] J. M. Pfotenhauer, F. Kessler, and M. A. Hilal, "Voltage detection and magnet protection", *IEEE transactions on applied superconductivity*, vol. 3, no. 1, pp. 273–276, 1993.

[44] R. Denz *et al.*, "Upgrade of the protection system for superconducting circuits in the lhc", *PAC09, Vancouver, CND*, 2009.

[45] R. Denz, E. de Matteis, A. Siemko, and J. Steckert, "Next generation of quench detection systems for the high-luminosity upgrade of the lhc", *IEEE Transactions on Applied Superconductivity*, vol. 27, no. 4, pp. 1–4, 2016.

[46] F. Rodriguez-Mateos and F. Sonnemann, "Quench heater studies for the LHC magnets", in *Particle Accelerator Conference, 2001. PAC 2001. Proceedings of the 2001*, IEEE, vol. 5, 2001, pp. 3451–3453.

[47] E. Ravaioli, "CLIQ. A new quench protection technology for superconducting magnets", 2015.

[48] J. van Nugteren *et al.*, "A fast quench protection system for high-temperature superconducting magnets", *IEEE Transactions on Applied Superconductivity*, vol. 29, no. 1, pp. 1–8, 2018.

[49] J. S. Murtomäki *et al.*, "ICED—Inductively Coupled Energy Dissipater for Future High-Field Accelerator Magnets", *IEEE Transactions on Applied Superconductivity*, vol. 28, no. 8, pp. 1–15, 2018.

[50] M. Mentink and T. Salmi, "Quench absorption coils: a quench protection concept for high-field superconducting accelerator magnets", *Superconductor Science and Technology*, vol. 30, no. 6, p. 064 002, 2017.

[51] M. Mentink and E. Ravaioli, "Secondary CLIQ, a robust, redundant, and cost-effective means of protecting high-field accelerator magnets", *Superconductor Science and Technology*, vol. 33, no. 8, p. 085 005, 2020.

[52] S. Hahn, D. K. Park, J. Bascuñán, and Y. Iwasa, "HTS pancake coils without turn-to-turn insulation", *IEEE transactions on applied superconductivity*, vol. 21, no. 3, pp. 1592–1595, 2010.

[53] S. Hahn *et al.*, "No-insulation multi-width winding technique for high temperature superconducting magnet", *Applied physics letters*, vol. 103, no. 17, p. 173 511, 2013.

[54] S. Hahn *et al.*, "Current status of and challenges for no-insulation HTS winding technique", *Journal of Cryogenics and Superconductivity Society of Japan*, vol. 53, no. 1, pp. 2–9, 2018.

[55] J. Van Nugteren *et al.*, "Measurement and analysis of normal zone propagation in a ReBCO coated conductor at temperatures below 50 K", *Physics procedia*, vol. 67, pp. 945–951, 2015.

[56] M. Bonura and C. Senatore, "An equation for the quench propagation velocity valid for high field magnet use of REBCO coated conductors", *Applied Physics Letters*, vol. 108, no. 24, p. 242 602, 2016.

[57] M. Marchevsky, "Quench detection and protection for high-temperature superconductor accelerator magnets", *Instruments*, vol. 5, no. 3, p. 27, 2021.

[58] J. Shi and D. Yao, "Collective beam-beam effects in hadron colliders", *Physical Review E,* vol. 62, no. 1, p. 1258, 2000.

[59] S. Russenschuck, *Field computation for accelerator magnets: analytical and numerical methods for electromagnetic design and optimization*. John Wiley & Sons, 2011.

[60] D. Uglietti, Y. Yanagisawa, H. Maeda, and T. Kiyoshi, "Measurements of magnetic field induced by screening currents in YBCO solenoid coils", *Superconductor Science and Technology*, vol. 23, no. 11, p. 115 002, 2010.

[61] Y. Yanagisawa *et al.*, "Magnitude of the screening field for YBCO coils", *IEEE transactions on applied superconductivity,* vol. 21, no. 3, pp. 1640–1643, 2010.

[62] N. Amemiya *et al.*, "Magnetisation and field quality of a cosine-theta dipole magnet wound with coated conductors for rotating gantry for hadron cancer therapy", *Superconductor Science and Technology*, vol. 29, no. 2, p. 024 006, 2015.

[63] G. Dilasser, P. Fazilleau, and P. Tixador, "Experimental measurement and numerical simulation of the screening current-induced field decay in a small ReBCO coil", *IEEE Transactions on Applied Superconductivity*, vol. 27, no. 4, pp. 1–4, 2016.

[64] L. Wang *et al.*, "Screening current-induced magnetic field in a noninsulated GdBCO HTS coil for a 24 T all-superconducting magnet", *IEEE Transactions on Applied Superconductivity*, vol. 27, no. 4, pp. 1–6, 2016.

[65] P. Fazilleau, F. Borgnolutti, G. Dilasser, and M. Durante, "Screening currents within the EuCARD HTS dipole", *IEEE Transactions on Applied Superconductivity*, vol. 28, no. 4, pp. 1–5, 2018.

[66] S. Noguchi *et al.*, "A simple screening current-induced magnetic field estimation method for REBCO pancake coils", *Superconductor Science and Technology*, 2019.

[67] R. Nast *et al.*, "Influence of laser striations on the properties of coated conductors", in *Journal of Physics: Conference Series*, IOP Publishing, vol. 507, 2014, p. 022 023.

[68] J. Van Nugteren *et al.*, "Measurement and numerical evaluation of AC losses in a ReBCO Roebel Cable at 4.5 K", *IEEE transactions on applied superconductivity*, vol. 26, no. 3, pp. 1–7, 2016.

[69] P. Dular *et al.*, "Magnetostatic and magnetodynamic mixed formulations compared with conventional formulations", *IEEE Transactions on Magnetics*, vol. 33, no. 2, pp. 1302–1305, 1997.

[70] O. Bíró, "Edge element formulations of eddy current problems", *Computer methods in applied mechanics and engineering*, vol. 169, no. 3-4, pp. 391–405, 1999.

[71] A. Bossavit, *Computational electromagnetism: variational formulations, complementarity, edge elements*. Academic Press, 1998.

[72] C. Carpenter, "Comparison of alternative formulations of 3-dimensional magnetic-field and eddy-current problems at power frequencies", *Proceedings of the Institution of Electrical Engineers*, vol. 124, no. 11, pp. 1026–1034, 1977.

[73] D. Rodger and N. Atkinson, "Finite element method for 3D eddy current flow in thin conducting sheets", *IEE Proceedings A-Physical Science, Measurement and Instrumentation, Management and Education-Reviews*, vol. 135, no. 6, pp. 369–374, 1988.

[74] O. Bíró *et al.*, "FEM calculation of eddy current losses and forces in thin conducting sheets of test facilities for fusion reactor components", *IEEE transactions on magnetics,* vol. 28, no. 2, pp. 1509–1512, 1992.

[75] L. Krähenbühl and D. Muller, "Thin layers in electrical engineering-example of shell models in analysing eddy-currents by boundary and finite element methods", *IEEE Transactions on Magnetics*, vol. 29, no. 2, pp. 1450–1455, 1993.

[76] A. Campbell, "A new method of determining the critical state in superconductors", *Superconductor Science and Technology*, vol. 20, no. 3, p. 292, 2007.

[77] S. Mykola and G. Fedor, "A–V formulation for numerical modelling of superconductor magnetization in true 3D geometry", *Superconductor Science and Technology*, vol. 32, no. 11, p. 115 001, 2019.

[78] K. Zhang *et al.*, "Magnetization Current Simulation of High-Temperature Bulk Superconductors Using the ANSYS Iterative Algorithm Method", *IEEE Transactions on Applied Superconductivity*, vol. 31, no. 2, pp. 1–6, 2020.

[79] R. Brambilla, F. Grilli, and L. Martini, "Development of an edge-element model for AC loss computation of high-temperature superconductors", *Superconductor Science and Technology*, vol. 20, no. 1, p. 16, 2006.

[80] M. Nii, N. Amemiya, and T. Nakamura, "Three-dimensional model for numerical electromagnetic field analyses of coated superconductors and its application to Roebel cables", *Superconductor Science and Technology*, vol. 25, no. 9, p. 095 011, 2012.

[81] A. Stenvall, V. Lahtinen, and M. Lyly, "An H-formulation-based three-dimensional hysteresis loss modelling tool in a simulation including time varying applied field and transport current: the fundamental problem and its solution", *Superconductor Science and Technology*, vol. 27, no. 10, p. 104 004, 2014.

[82] A. Arsenault, F. Sirois, and F. Grilli, "Implementation of the H-ϕ formulation in COMSOL Multiphysics for simulating the magnetization of bulk superconductors and comparison with the H-formulation", *IEEE Transactions on Applied Superconductivity*, vol. 31, no. 2, pp. 1–11, 2020.

[83] K. Qian, Y. Terao, and H. Ohsaki, "Three-Dimensional Electromagnetic and Thermal Field Coupled Analysis of Different Types of REBCO Coils Under Overcurrent Conditions", *IEEE Transactions on Applied Superconductivity*, vol. 31, no. 5, pp. 1–8, 2021.

[84] V. Zermeno *et al.*, "Towards faster FEM simulation of thin film superconductors: A multiscale approach", *IEEE Transactions on Applied Superconductivity*, vol. 21, no. 3, pp. 3273–3276, 2011.

[85] R. Mataira, M. Ainslie, R. Badcock, and C. Bumby, "Finite-element modelling of no-insulation HTS coils using rotated anisotropic resistivity", *Superconductor Science and Technology*, vol. 33, no. 8, 08LT01, 2020.

[86] E. Berrospe-Juarez, F. Trillaud, V. M. Zermeño, and F. Grilli, "Advanced electromagnetic modeling of large-scale high-temperature superconductor systems based on H and T–A formulations", *Superconductor Science and Technology*, vol. 34, no. 4, p. 044 002, 2021.

[87] B. Shen, F. Grilli, and T. Coombs, "Overview of H-formulation: A versatile tool for modeling electromagnetics in high-temperature superconductor applications", *IEEE access*, vol. 8, pp. 100 403–100 414, 2020.

[88] F. Grilli *et al.*, "Electromagnetic Modeling of Superconductors With Commercial Software: Possibilities With Two Vector Potential-Based Formulations", *IEEE Transactions on Applied Superconductivity*, vol. 31, no. 1, pp. 1–9, 2020.

[89] R. Brambilla *et al.*, "A finite-element method framework for modeling rotating machines with superconducting windings", *IEEE Transactions on Applied Superconductivity*, vol. 28, no. 5, pp. 1–11, 2018.

[90] Y. Yang, H. Yong, X. Zhang, and Y. Zhou, "Numerical Simulation of Superconducting Generator Based on the T–A Formulation", *IEEE Transactions on Applied Superconductivity*, vol. 30, no. 8, pp. 1–11, 2020.

[91] T. Benkel *et al.*, "T–A-formulation to model electrical machines with HTS coated conductor coils", *IEEE Transactions on Applied Superconductivity*, vol. 30, no. 6, pp. 1–7, 2020.

[92] H. Zhang, M. Zhang, and W. Yuan, "An efficient 3D finite element method model based on the T–A formulation for superconducting coated conductors", *Superconductor Science and Technology*, vol. 30, no. 2, p. 024 005, 2016.

[93] Y. Wang *et al.*, "Study of the magnetization loss of CORC® cables using a 3D T–A formulation", *Superconductor Science and Technology*, vol. 32, no. 2, p. 025 003, 2019.

[94] Y. Wang *et al.*, "Electromagnetic modelling using T–A formulation for high-temperature superconductor (RE) Ba2Cu3O x high field magnets", *High Voltage*, vol. 5, no. 2, pp. 218–226, 2020.

[95] J. Dular, C. Geuzaine, and B. Vanderheyden, "Finite Element Formulations for Systems with High-Temperature Superconductors", *IEEE Transactions on Applied Superconductivity*, pp. 1–1, 2019.

[96] B. Rozier, A. Badel, B. Ramdane, and G. Meunier, "Modeling of Dynamic Current Distribution in RE-BCO Insulated Coils Using a Volume Integral Formulation for Protection Purpose", *IEEE Transactions on Applied Superconductivity*, vol. 29, no. 5, pp. 1–5, 2019.

[97] R. Blandine, B. Arnaud, R. Brahim, and M. Gérard, "Calculation of the local current density in high-temperature superconducting insulated rare earth–barium–copper oxide coils using a volume integral formulation and its contribution to coil protection", *Superconductor Science and Technology*, vol. 32, no. 4, p. 044 008, 2019.

[98] Y. Statra, H. Menana, L. Belguerras, and B. Douine, "A volume integral approach for the modelling and design of HTS coils", *COMPEL-The international journal for computation and mathematics in electrical and electronic engineering*, 2019.

[99] A. Badel *et al.*, "Modeling of 'quench'or the occurrence and propagation of dissipative zones in RE-BCO high temperature superconducting coils", *Superconductor Science and Technology*, vol. 32, no. 9, p. 094 001, 2019.

[100] F. Grilli *et al.*, "Computation of Losses in HTS Under the Action of Varying Magnetic Fields and Currents", *IEEE Transactions on Applied Superconductivity*, vol. 24, no. 1, pp. 78–110, 2014.

[101] M. Maciejewski *et al.*, "Application of the waveform relaxation technique to the co-simulation of power converter controller and electrical circuit models", in *2017 22nd International Conference on Methods and Models in Automation and Robotics (MMAR)*, IEEE, 2017, pp. 837–842.

[102] M. Maciejewski *et al.*, "Coupling of Magneto-Thermal and Mechanical Superconducting Magnet Models by Means of Mesh-Based Interpolation", *IEEE Transactions on Applied Superconductivity*, vol. 28, no. 3, 2018.

[103] G. Bedrosian, "A New Method for Coupling Finite Element Field Solutions with External Circuits and Kinematics", *IEEE Transactions on Magnetics*, vol. 29, no. 2, pp. 1664–1668, 1993.

[104] P. Zhou *et al.*, "A general cosimulation approach for coupled field-circuit problems", *IEEE transactions on magnetics*, vol. 42, no. 4, pp. 1051–1054, 2006.

[105] E. Lelarasmee, A. E. Ruehli, and A. L. Sangiovanni-Vincentelli, "The waveform relaxation method for time-domain analysis of large scale integrated circuits", *IEEE transactions on computer-aided design of integrated circuits and systems*, vol. 1, no. 3, pp. 131–145, 1982.

[106] S. Schöps, H. De Gersem, and A. Bartel, "A cosimulation framework for multirate time integration of field/circuit coupled problems", *IEEE Transactions on Magnetics*, vol. 46, no. 8, pp. 3233–3236, 2010.

[107] S. Schops, H. De Gersem, and A. Bartel, "Higher-order cosimulation of field/circuit coupled problems", *IEEE transactions on magnetics*, vol. 48, no. 2, pp. 535–538, 2012.

[108] M. J. Gander, "Optimized schwarz methods", *SIAM Journal on Numerical Analysis*, vol. 44, no. 2, pp. 699–731, 2006.

[109] F. Nataf, "Recent Developments on Optimized Schwarz Methods", in *Domain Decomposition Methods in Science and Engineering XVI*, O. B. Widlund and D. E. Keyes, Eds., Berlin, Heidelberg: Springer, 2007, pp. 115–125.

[110] M. J. Gander and A. E. Ruehli, "Optimized waveform relaxation methods for RC type circuits", *IEEE Transactions on Circuits and Systems*, vol. 51, no. 4, pp. 755–768, 2004.

[111] M. Al-Khaleel, M. J. Gander, and A. E. Ruehli, "Optimization of Transmission Conditions in Waveform Relaxation Techniques for RC Circuits", *SIAM Journal on Numerical Analysis*, vol. 52, no. 2, pp. 1076–1101, 2014.

[112] J. de Dieu Nshimiyimana *et al.*, "Co-simulation of of finite element and circuit solvers using optimized waveform relaxation", in *2016 IEEE International Energy Conference (ENERGYCON)*, IEEE, 2016, pp. 1–6.

[113] I. Cortes Garcia *et al.*, "Optimized field/circuit coupling for the simulation of quenches in superconducting magnets", *IEEE Journal on Multiscale and Multiphysics Computational Techniques*, vol. 2, pp. 97–104, 2017.

[114] L. Bortot *et al.*, "A Consistent Simulation of Electrothermal Transients in Accelerator Circuits", *IEEE Transactions on Applied Superconductivity*, vol. 27, no. 4, pp. 1–5, 2017.

[115] A. M. Fernandez Navarro *et al.*, "Simulation of a Quench Event in the Reconfigured LHC Main Dipole Circuit Including the 11 T Magnets for the High-Luminosity Upgrade", *IEEE Transactions on Applied Superconductivity*, vol. 28, no. 4, 2018.

[116] L. Bortot *et al.*, "STEAM: A hierarchical cosimulation framework for superconducting accelerator magnet circuits", *IEEE Transactions on Applied Superconductivity*, vol. 28, no. 3, pp. 1–6, 2018.

[117] E. Ravaioli *et al.*, "Quench Protection of the First 4-m-Long Prototype of the HL-LHC Nb$_3$Sn Quadrupole Magnet", *IEEE Transactions on Applied Superconductivity*, vol. 29, no. 5, pp. 1–5, 2019.

[118] M. Prioli *et al.*, "The CLIQ quench protection system applied to the 16 T FCC-hh dipole magnets", *IEEE Transactions on Applied Superconductivity*, vol. 29, no. 8, pp. 1–9, 2019.

[119] M. Prioli *et al.*, "Conceptual design of the FCC-hh dipole circuits with integrated CLIQ protection system", *IEEE Transactions on Applied Superconductivity*, vol. 29, no. 8, pp. 1–9, 2019.

[120] M. Maciejewski, "Co-simulation of transient effects in superconducting accelerator magnets", Ph.D. dissertation, Lodz, Tech. U., 2019.

[121] F. Gömöry *et al.*, "Experimental realization of a magnetic cloak", *Science*, vol. 335, no. 6075, pp. 1466–1468, 2012.

[122] Ł. Tomków, M. Ciszek, and M. Chorowski, "Combined magnetic screen made of Bi-2223 bulk cylinder and YBCO tape rings—Modeling and experiments", *Journal of Applied Physics*, vol. 117, no. 4, p. 043 901, 2015.

[123] I. Frollo *et al.*, "Magnetic field homogeneity adjustment for magnetic resonance imaging equipment", *IEEE Transactions on Magnetics*, vol. 54, no. 5, pp. 1–9, 2018.

[124] T. Wang, S. Xiao, X. Liu, and Y. Li, "A 3.35 T Actively Shielded Superconducting Magnet for Dynamic Nuclear Polarization Device", *IEEE Transactions on Applied Superconductivity*, vol. 26, no. 4, pp. 1–4, 2016.

[125] D. Barna, "High field septum magnet using a superconducting shield for the future circular collider", *Physical Review Accelerators and Beams*, vol. 20, no. 4, p. 041 002, 2017.

[126] D. Barna *et al.*, "Nbti/nb/cu multilayer shield for the superconducting shield (sushi) septum", *IEEE Transactions on Applied Superconductivity*, vol. 29, no. 1, pp. 1–8, 2018.

[127] Ł. Tomków, E. Kulikov, K. Kozłowski, and V. Drobin, "Improvement of the homogeneity of magnetic field by the attenuation of a selected component with an open superconducting shield made of commercial tapes", *Journal of Applied Physics*, vol. 126, no. 8, p. 083 903, 2019.

[128] J. van Nugteren *et al.*, "Persistent Current Shim Coils for Future High Field Accelerator Magnets", No. EDMS 1574002 (CERN, Geneva, 2021), Tech. Rep., 2016, Available online: https://edms.cern.ch/ui/#!master/navigator/document?D:1255633525:1255633525:subDocs, accessed on 01 March 2022.

[129] PHD Thesis Repository on CERNBox, Available online: https://cernbox.cern.ch/index.php/s/dlBnV6uj5BHDZUh, accessed on 01 March 2022.

[130] J. C. Maxwell, "A Dynamical Theory of the Electromagnetic Field", *Royal Society Transactions*, vol. CLV, pp. 459–512, 1864.

[131] J. D. Jackson, *Classical Electrodynamics*, 3rd. New York, NY, USA: Wiley & Sons, 1998.

[132] F. Assous, P. Ciarlet, and S. Labrunie, *Mathematical foundations of computational electromagnetism*. Springer, 2018.

[133] D. F. Griffiths, *Introduction to Electrodynamics*. Upper Saddle River, NJ, USA: Prentice-Hall, 1999.

[134] G. Beer and J. Meek, "Infinite Domain Elements", *Int. J. Numer. Meth. Eng.*, vol. 17, no. 1, pp. 43–52, 1981.

[135] F. Henrotte *et al.*, "Finite element modelling with transformation techniques", *IEEE Transactions on Magnetics*, vol. 35, no. 3, pp. 1434–1437, 1999.

[136] T. L. Bergman, A. S. Lavine, F. P. Incropera, and D. P. DeWitt, *Introduction to Heat Transfer*, 6th ed. John Wiley & Sons, Ltd., 2011.

[137] J. H. Lienhard, *A Heat Transfer Textbook* (Dover Books on Engineering), 4th ed. Dover Publications, 2011.

[138] H. K. Dirks, "Quasi-Stationary Fields for Microelectronic Applications", *Electrical Engineering (Archiv für Elektrotechnik)*, vol. 79, no. 2, pp. 145–155, 1996.

[139] I. Cortes Garcia, S. Schöps, H. De Gersem, and S. Baumanns, "Systems of Differential Algebraic Equations in Computational Electromagnetics", in *Applications of Differential-Algebraic Equations: Examples and Benchmarks*, ser. Differential-Algebraic Equations Forum, A. Campbell Stephenand Ilchmann, V. Mehrmann, and T. Reis, Eds., Heidelberg: Springer, 2019.

[140] J. Larsson, "Electromagnetics from a quasistatic perspective", *American Journal of Physics*, vol. 75, no. 3, pp. 230–239, 2007.

[141] S. Koch and T. Weiland, "Different types of quasistationary formulations for time domain simulations", *Radio Science*, vol. 46, no. 5, 2011.

[142] H. A. Haus and J. R. Melcher, *Electromagnetic Fields and Energy*. Prentice-Hall, 1989. [Online]. Available: http://web.mit.edu/6.013_book/www/.

[143] K. Schmidt, O. Sterz, and R. Hiptmair, "Estimating the Eddy-Current Modeling Error", *IEEE Transactions on Magnetics*, vol. 44, no. 6, pp. 686–689, 2008.

[144] T. Steinmetz, S. Kurz, and M. Clemens, "Domains of validity of quasistatic and quasistationary field approximations", *COMPEL: The International Journal for Computation and Mathematics in Electrical and Electronic Engineering*, vol. 30, no. 4, pp. 1237–1247, 2011.

[145] O. Bíró and K. Preis, "On the use of the magnetic vector potential in the finite-element analysis of three-dimensional eddy currents", *IEEE Transactions on magnetics*, vol. 25, no. 4, pp. 3145–3159, 1989.

[146] K. J. Binns, C. Trowbridge, and P. Lawrenson, *The analytical and numerical solution of electric and magnetic fields*. Wiley, 1992.

[147] C. J. Carpenter, "Comparison of alternative formulations of 3-dimensional magnetic-field and eddy-current problems at power frequencies", *IEE Proceedings B - Electric Power Applications*, vol. 127, no. 5, p. 332, 1980.

[148] J. P. Webb and B. Forghani, "The Low-Frequency Performance of $H-\phi$ and $T-\Omega$ Methods using Edge Elements for 3D Eddy Current Problems", *IEEE Transactions on Magnetics*, vol. 29, no. 6, pp. 2461–2463, 1993.

[149] O. Bíró, K. Preis, and K. R. Richter, "Various FEM formulations for the calculation of transient 3D eddy currents in nonlinear media", *IEEE Transactions on Magnetics*, vol. 31, no. 3, pp. 1307–1312, 1995.

[150] O. Bíró *et al.*, "Computation of 3-D current driven skin effect problems using a current vector potential", *IEEE Transactions on Magnetics*, vol. 29, no. 2, pp. 1325–1328, 1993.

[151] A. Kameari, "Calculation of transient 3D eddy-current using edge elements", *IEEE Transactions on Magnetics*, vol. 26, no. 5, pp. 466–469, 1990.

[152] J. B. Manges and Z. J. Cendes, "Tree-Cotree Decompositions for First-Order Complete Tangential Vector Finite Elements", *International Journal for Numerical Methods in Engineering*, vol. 40, no. 9, pp. 1667–1685, 1997.

[153] M. Clemens and T. Weiland, "Regularization of eddy-current formulations using discrete grad-div operators", *IEEE Transactions on Magnetics*, vol. 38, no. 2, pp. 569–572, 2002.

[154] C. Emson and J. Simkin, "An optimal method for 3-D eddy currents", *IEEE Transactions on Magnetics*, vol. 19, no. 6, pp. 2450–2452, 1983.

[155] C. Emson and C. Trowbridge, "Transient 3D eddy currents using modified magnetic vector potentials and magnetic scalar potentials", *IEEE Transactions on Magnetics*, vol. 24, no. 1, pp. 86–89, 1988.

[156] S. Schöps, H. De Gersem, and T. Weiland, "Winding Functions in Transient Magnetoquasistatic Field-Circuit Coupled Simulations", *COMPEL: The International Journal for Computation and Mathematics in Electrical and Electronic Engineering*, vol. 32, no. 6, pp. 2063–2083, 2013.

[157] A. Bartel, S. Baumanns, and S. Schöps, "Structural Analysis of Electrical Circuits Including Magneto-quasistatic Devices", *Applied Numerical Mathematics*, vol. 61, pp. 1257–1270, 2011.

[158] H. De Gersem and K. Hameyer, "A Finite Element Model for Foil Winding Simulation", *IEEE Transactions on Magnetics*, vol. 37, no. 5, pp. 3472–3432, 2001.

[159] H. De Gersem, K. Hameyer, and T. Weiland, "Field-Circuit Coupled Models in Electromagnetic Simulation", *Journal of Computational and Applied Mathematics*, vol. 168, no. 1-2, pp. 125–133, 2004.

[160] D. N. Dyck and J. P. Webb, "Solenoidal current flows for filamentary conductors", *IEEE Transactions on Magnetics*, vol. 40, no. 2, pp. 810–813, 2004.

[161] A. Alonso Rodríguez and A. Valli, "Voltage and current excitation for time-harmonic eddy-current problems", *SIAM Journal on Applied Mathematics*, vol. 68, no. 5, pp. 1477–1494, 2008.

[162] I. Cortes Garcia, H. De Gersem, and S. Schöps, "A Structural Analysis of Field/Circuit Coupled Problems Based on a Generalised Circuit Element", *Numerical Algorithms*, vol. 83, no. 1, pp. 373–394, 2020. arXiv: 1801.07081.

[163] D. Shen, G. Meunier, J.-L. Coulomb, and J. C. Sabonnadière, "Solution of Magnetic Fields and Electrical Circuits Combined Problems", *IEEE Transactions on Magnetics*, vol. 21, no. 6, pp. 2288–2291, 1985.

[164] L. W. Nagel, "SPICE2: a Computer Program to Simulate Semiconductor Circuits", University of Berkeley, Technical Report, 1975.

[165] C.-W. Ho, A. E. Ruehli, and P. A. Brennan, "The Modified Nodal Approach to Network Analysis", *IEEE Transactions on Circuits and Systems*, vol. 22, no. 6, pp. 504–509, 1975.

[166] M. Günther, U. Feldmann, and E. J. W. ter Maten, "Modelling and Discretization of Circuit Problems", in *Numerical Methods in Electromagnetics*, ser. Handbook of Numerical Analysis, W. H. A. Schilders and E. J. W. ter Maten, Eds., vol. 13, Amsterdam, Netherlands: Elsevier, 2005, pp. 523–659.

[167] D. Estévez Schwarz and C. Tischendorf, "Structural analysis of electric circuits and consequences for MNA", *International Journal of Circuit Theory and Applications*, vol. 28, no. 2, pp. 131–162, 2000.

[168] A. Bossavit, "On the geometry of electromagnetism. (4): 'Maxwell's house'", *The Japan Society of Applied Electromagnetics and Mechanics*, vol. 6, no. 4, pp. 318–326, 1999.

[169] E. Tonti, "On the Geometrical Structure of Electromagnetism", in *Gravitation, Electromagnetism and Geometrical Structures*, G. Ferrarese, Ed. Bologna, Italy: Pitagora Editrice, 1995, pp. 281–308.

[170] K. Yamafuji and T. Kiss, "Current-voltage characteristics near the glass-liquid transition in high-T_c superconductors", *Physica C: Superconductivity*, vol. 290, no. 1-2, pp. 9–22, 1997.

[171] J. Rhyner, "Magnetic properties and AC-losses of superconductors with power law current—voltage characteristics", *Physica C: Superconductivity*, vol. 212, no. 3-4, pp. 292–300, 1993.

[172] F. Sirois, F. Grilli, and A. Morandi, "Comparison of constitutive laws for modeling high-temperature superconductors", *IEEE Transactions on Applied Superconductivity*, vol. 29, no. 1, pp. 1–10, 2018.

[173] D. Dew-Hughes, "Model for flux creep in high T_c superconductors", *Cryogenics*, vol. 28, no. 10, pp. 674–677, 1988.

[174] A. K. Ghosh, "V–I transition and n-value of multifilamentary LTS and HTS wires and cables", *Physica C: Superconductivity*, vol. 401, no. 1-4, pp. 15–21, 2004.

[175] X. Zhang *et al.*, "Study of critical current and n-values of 2G HTS tapes: Their magnetic field-angular dependence", *Journal of Superconductivity and Novel Magnetism*, vol. 31, no. 12, pp. 3847–3854, 2018.

[176] C. P. Bean, "Magnetization of hard superconductors", *Physical review letters*, vol. 8, no. 6, p. 250, 1962.

[177] C. P. Bean, "Magnetization of high-field superconductors", *Reviews of Modern Physics*, vol. 36, no. 1, p. 31, 1964.

[178] B. Heise, "Analysis of a fully discrete finite element method for a nonlinear magnetic field problem", *SIAM Journal on Numerical Analysis*, vol. 31, no. 3, pp. 745–759, 1994.

[179] A. Arsenault, F. Sirois, and F. Grilli, "Efficient Modeling of High-Temperature Superconductors Surrounded by Magnetic Components Using a Reduced H-phi Formulation", *IEEE Transactions on Applied Superconductivity*, vol. 31, no. 4, pp. 1–9, 2021.

[180] N. Riva *et al.*, "The eta-beta model model: an alternative to the power-law model for numerical simulations of REBCO tapes", *arXiv preprint arXiv:2106.11412*, 2021.

[181] D. Ruiz-Alonso, T. A. Coombs, and A. M. Campbell, "Numerical analysis of high-temperature superconductors with the critical-state model", *IEEE transactions on applied superconductivity*, vol. 14, no. 4, pp. 2053–2063, 2004.

[182] V. Lahtinen *et al.*, "A finite element simulation tool for predicting hysteresis losses in superconductors using an H-oriented formulation with cohomology basis functions", *Journal of Superconductivity and Novel Magnetism*, vol. 28, no. 8, pp. 2345–2354, 2015.

[183] Q. Li *et al.*, "Numerical modeling of dynamic loss in HTS-coated conductors under perpendicular magnetic fields", *IEEE Transactions on Applied Superconductivity*, vol. 28, no. 2, pp. 1–6, 2017.

[184] P. Dłotko, B. Kapidani, S. Pitassi, and R. Specogna, "Fake Conductivity or Cohomology: Which to Use When Solving Eddy Current Problems With h-Formulations?", *IEEE Transactions on Magnetics*, vol. 55, no. 6, pp. 1–4, 2019.

[185] L. Bortot *et al.*, "A Coupled A–H Formulation for Magneto-Thermal Transients in High-Temperature Superconducting Magnets", *IEEE Transactions on Applied Superconductivity*, vol. 30, no. 5, pp. 1–11, 2020.

[186] L. Bortot *et al.*, "Numerical analysis of the screening current-induced magnetic field in the HTS insert dipole magnet Feather-M2. 1-2", *Superconductor Science and Technology*, vol. 33, no. 12, p. 125 008, 2020.

[187] Y. Yan, T. Qu, and F. Grilli, "Numerical Modeling of AC Loss in HTS Coated Conductors and Roebel Cable Using T–A Formulation and Comparison With H Formulation", *IEEE Access*, vol. 9, pp. 49 649–49 659, 2021.

[188] G. dos Santos *et al.*, "Multi-objective optimization for the superconducting bias coil of a saturated iron core fault current limiter using the TA formulation", *Superconductor Science and Technology*, vol. 34, no. 2, p. 025 012, 2021.

[189] J. Dular *et al.*, "On the stability of mixed finite-element formulations for high-temperature superconductors", *IEEE Transactions on Applied Superconductivity*, vol. 31, no. 6, 2021. arXiv: 2106.00313.

[190] A. P. Verweij, "Electrodynamics of superconducting cables in accelerator magnets", Ph.D. dissertation, CM-P00081075, 1995.

[191] H. De Gersem and T. Weiland, "Finite-element models for superconductive cables with finite interwire resistance", *IEEE Trans. Magn.*, vol. 40, no. 2, pp. 667–670, 2004.

[192] M. Walker, W. Carr, and J. Murphy, "Loss behavior in twisted filamentary superconductors", *IEEE Transactions on Magnetics*, vol. 11, no. 5, pp. 1475–1477, 1975.

[193] C. Barbagallo, M. Mentink, L. Bortot, and A. Verweij, "Inter-filament coupling currents modelling in superconducting filamentary nb3sn strands and magnets", No. EDMS 2226896 (CERN, Geneva, 2019), Tech. Rep., 2019, https://edms.cern.ch/ui/#!master/navigator/document?D:100455350: 100455350:subDocs, accessed on 01 March 2022.

[194] M. Sorbi and V. Marinozzi, "Magnetization Heat in Superconductors and in Eddy Current Problems: A Classical Thermodynamic Approach", *IEEE Transactions on Applied Superconductivity*, vol. 26, no. 6, pp. 1–9, 2016.

[195]   Z. Stekly, J. Zar, *et al.*, "Stable superconducting coils", *IEEE Trans. Nucl. Sci.*, vol. 12, no. 3, pp. 367–372, 1965.

[196]   L. Bortot *et al.*, "A 2-d finite-element model for electrothermal transients in accelerator magnets", *IEEE Transactions on Magnetics*, vol. 54, no. 3, pp. 1–4, 2018. arXiv: 1710.01187.

[197]   A. Quarteroni and A. Valli, *Numerical Approximation of Partial Differential Equations* (Springer Series in Computational Mathematics). Berlin, Germany: Springer, 2008, vol. 23.

[198]   E. Hairer, S. P. Nørsett, and G. Wanner, *Solving Ordinary Differential Equations I: Nonstiff Problems* (Springer Series in Computational Mathematics), 2nd ed. Berlin, Germany: Springer, 2000.

[199]   P. Monk, *Finite Element Methods for Maxwell's Equations*. Oxford: Oxford University Press, 2003.

[200]   A. A. Rodríguez and A. Valli, *Eddy Current Approximation of Maxwell Equations: Theory, Algorithms and Applications*. Springer Science & Business Media, 2010, vol. 4.

[201]   I. Babuska and B. Szabo, "On the rates of convergence of the finite element method", *International Journal for Numerical Methods in Engineering*, vol. 18, no. 3, pp. 323–341, 1982.

[202]   L. Demkowicz, W. Rachowicz, and P. Devloo, "A fully automatic hp-adaptivity", *Journal of Scientific Computing*, vol. 17, no. 1, pp. 117–142, 2002.

[203]   B. Szabó and I. Babuška, *Finite element analysis*. John Wiley & Sons, 1991.

[204]   E. Hairer, S. P. Nørsett, and G. Wanner, *Solving Ordinary Differential Equations II: Stiff and Differential-Algebraic Problems* (Springer Series in Computational Mathematics), 2nd ed. Berlin, Germany: Springer, 2002.

[205]   D. Griffiths and D. J. Higham, *Numerical Methods for Ordinary Differential Equations: Initial Value Problems* (Springer Undergraduate Mathematics Series). London, UK: Springer, 2010.

[206]   J. C. Butcher, *Numerical Methods for Ordinary Differential Equations*. Wiley, 2016.

[207]   A. Nicolet and F. Delincé, "Implicit Runge-Kutta methods for transient magnetic field computation", *IEEE transactions on Magnetics*, vol. 32, no. 3, pp. 1405–1408, 1996.

[208]   R. Mattheij and J. Molenaar, *Ordinary Differential Equations in Theory and Practice*. Society for Industrial and Applied Mathematics, 2002.

[209]   K. E. Brenan, S. L. Campbell, and L. R. Petzold, *Numerical Solution of Initial-Value Problems in Differential-Algebraic Equations*. Philadelphia, PA, USA: Society for Industrial and Applied Mathematics, 1995.

[210]   E. Hairer, C. Lubich, and M. Roche, *The Numerical Solution of Differential-Algebraic Systems by Runge-Kutta Methods* (Lecture Notes in Mathematics). Berlin: Springer, 1989.

[211]   U. M. Ascher and L. R. Petzold, *Computer methods for ordinary differential equations and differential-algebraic equations*. Siam, 1998, vol. 61.

[212]   R. Lamour, R. März, and C. Tischendorf, *Differential-Algebraic Equations: A Projector Based Analysis* (Differential-Algebraic Equations Forum), A. Ilchmann and T. Reis, Eds. Heidelberg: Springer, 2013.

[213]   P. Deuflhard, *Newton methods for nonlinear problems: affine invariance and adaptive algorithms*. Springer Science & Business Media, 2011, vol. 35.

[214]   M. T. Heath, *Scientific Computing: An Introductory Survey*. McGraw-Hill, 2002.

[215]   L. N. Trefethen and D. Bau, *Numerical Linear Algebra*. Society for Industrial and Applied Mathematics, 1997.

[216] Y. Saad, *Iterative Methods for Sparse Linear Systems*, 2nd ed. Boston, MA, USA: Society for Industrial and Applied Mathematics, 2003. [Online]. Available: http://www-users.cs.umn.edu/~saad/books.html.

[217] G. H. Golub and C. F. van Loan, *Matrix Computations*, 3rd ed. Baltimore, MD, USA: The Johns Hopkins University Press, 1996.

[218] B. F. Smith, P. E. Bjørstad, and W. D. Gropp, *Domain Decomposition: Parallel Multilevel Methods for Elliptic Partial Differential Equations*. Cambridge University Press, 1996.

[219] A. Brandt, "Multi-Level Adaptive Solutions to Boundary-Value Problems", *Mathematics of Computation*, vol. 31, no. 138, pp. 333–390, 1977.

[220] P. Wesseling, *An Introduction to Multigrid Methods*. John Wiley & Sons Inc, 1992.

[221] C. C. Douglas, "Multigrid methods in science and engineering", *IEEE Computational Science and Engineering*, vol. 3, no. 4, pp. 55–68, 1996.

[222] L. Bortot *et al.*, "STEAM: A Hierarchical Co-Simulation Framework for Superconducting Accelerator Magnet Circuits", *IEEE Transactions on Applied Superconductivity*, vol. 28, no. 3, 2018.

[223] K. Park and C. A. Felippa, "Partitioned analysis of coupled systems", *Computational Methods for Transient Analysis*, vol. 1, pp. 157–219, 1983.

[224] COMSOL, *COMSOL Multiphysics, v. 5.6*, [CD-ROM]. Stockholm, Sweden: COMSOL AB, 2020.

[225] P. Dular and C. Geuzaine, *GetDP reference manual: the documentation for GetDP, a general environment for the treatment of discrete problems*, Available online: http://getdp.info, accessed on 01 March 2022.

[226] K. Burrage, *Parallel and sequential methods for ordinary differential equations*. Clarendon Press, Oxford, 1995.

[227] M. Maciejewski, "Co-Simulation of Transient Effects in Superconducting Accelerator Magnets", PhD Thesis, Lodz University of Technology, Lodz, Poland, 2018.

[228] E. Lelarasmee, "The Waveform Relaxation Method for Time Domain Analysis of Large Scale Integrated Circuits: Theory and Applications", PhD Thesis, EECS Department, University of California, Berkeley, 1982.

[229] E. Lelarasmee, A. E. Ruehli, and A. L. Sangiovanni-Vincentelli, "The Waveform Relaxation Method for Time-Domain Analysis of Large Scale Integrated Circuits", *IEEE Transactions on Computer-Aided Design of Integrated Circuits and Systems*, vol. 1, no. 3, pp. 131–145, 1982.

[230] L. Bortot *et al.*, "A Consistent Simulation of Electro-thermal Transients in Accelerator Circuits", *IEEE Transactions on Applied Superconductivity*, vol. 27, no. 4, 2016.

[231] A. M. Fernandez Navarro *et al.*, "Simulation of a Quench Event in the Upgraded High-Luminosity LHC Main Dipole Circuit Including the 11 T Nb_3Sn Dipole Magnets", *IEEE Transactions on Applied Superconductivity*, vol. 28, no. 4, 2018.

[232] B. Lindstrom *et al.*, "Fast failures in the LHC and the future high luminosity LHC", *Physical Review Accelerators and Beams*, vol. 23, no. 8, p. 081 001, 2020.

[233] M. Maciejewski *et al.*, "Application of the Waveform Relaxation Technique to the Co-Simulation of Power Converter Controller and Electrical Circuit Models", in *22nd International Conference on Methods and Models in Automation and Robotics (MMAR 2017)*, IEEE, 2017, pp. 837–842. arXiv: 1704.02839.

[234] Z. Jackiewicz and M. Kwapisz, "Convergence of Waveform Relaxation Methods for Differential-Algebraic Systems", *SIAM Journal on Numerical Analysis*, vol. 33, no. 6, pp. 2303–2317, 1996.

[235] A. Bartel, M. Brunk, and S. Schöps, "On the convergence rate of dynamic iteration for coupled problems with multiple subsystems", in *12th Seminar NUMDIFF on Numerical Solution of Differential and Differential-Algebraic Equations*, Halle, 2012.

[236] A. Bartel, M. Brunk, M. Günther, and S. Schöps, "Dynamic Iteration for Coupled Problems of Electric Circuits and Distributed Devices", *SIAM Journal on Scientific Computing*, vol. 35, no. 2, B315–B335, 2013.

[237] T. Schierz, M. Arnold, and C. Clauß, "Co-simulation with communication step size control in an FMI compatible master algorithm", in *Proceedings of the 9th International Modelica Conference*, München, 2012.

[238] S. Sadjina, L. T. Kyllingstad, S. Skjong, and E. Pedersen, "Energy conservation and power bonds in co-simulations: Non-iterative adaptive step size control and error estimation", *Engineering with Computers*, vol. 33, no. 3, pp. 607–620, 2017.

[239] M. J. Gander and T. Vanzan, "Heterogeneous optimized Schwarz methods for second order elliptic PDEs", *SIAM Journal on Scientific Computing*, vol. 41, no. 4, A2329–A2354, 2019.

[240] I. Cortes Garcia, "Mathematical Analysis and Simulation of Field Models in Accelerator Circuits", Springer Theses: Recognizing Outstanding Ph.D. Research, Dissertation, Technische Universität Darmstadt, Darmstadt, 2020.

[241] E. Lange, F. Henrotte, and K. Hameyer, "An Efficient Field-Circuit Coupling Based on a Temporary Linearization of FE Electrical Machine Models", *IEEE Transactions on Magnetics*, vol. 45, no. 3, pp. 1258–1261, 2009.

[242] S. Schöps, "Multiscale Modeling and Multirate Time-Integration of Field/Circuit Coupled Problems", VDI Verlag. Fortschritt-Berichte VDI, Reihe 21, Dissertation, Bergische Universität Wuppertal & Katholieke Universiteit Leuven, Düsseldorf, Germany, 2011.

[243] A. Bartel, M. Brunk, M. Günther, and S. Schöps, "Dynamic iteration for coupled problems of electric circuits and distributed devices", *SIAM Journal on Scientific Computing*, vol. 35, no. 2, B315–B335, 2013.

[244] R. Ahrem *et al.*, "MpCCI-Mesh Based Parallel Code Coupling Interface", *Institute for Algorithms and Scientific Computing (SCAI), GMD, http://www. mpcci. org*, 2000.

[245] M. Maciejewski *et al.*, "Coupling of Magnetothermal and Mechanical Superconducting Magnet Models by Means of Mesh-Based Interpolation", *IEEE Transactions on Applied Superconductivity*, vol. 28, no. 3, 2018.

[246] M. Barton and Z. Cendes, "New vector finite elements for three-dimensional magnetic field computation", *Journal of Applied Physics*, vol. 61, no. 8, pp. 3919–3921, 1987.

[247] M. Clemens, "Large systems of equations in a discrete electromagnetism: formulations and numerical algorithms", *IEE Proceedings - Science, Measurement and Technology*, vol. 152, no. 2, pp. 50–72, 2005.

[248] J. R. Shewchuk *et al.*, *An introduction to the conjugate gradient method without the agonizing pain*, 1994.

[249] M. Clemens and T. Weiland, "Transient eddy-current calculation with the FI-method", *IEEE Transactions on Magnetics*, vol. 35, no. 3, pp. 1163–1166, 1999.

[250] J. B. Manges and Z. J. Cendes, "A generalized tree-cotree gauge for magnetic field computation", *IEEE Transactions on Magnetics*, vol. 31, no. 3, pp. 1342–1347, 1995.

[251] M. D. Al-Khaleel, M. J. Gander, and A. E. Ruehli, "Optimization of transmission conditions in waveform relaxation techniques for RC circuits", *SIAM Journal on Numerical Analysis*, vol. 52, no. 2, pp. 1076–1101, 2014.

[252] W. Fu *et al.*, "Modeling of solid conductors in two-dimensional transient finite-element analysis and its application to electric machines", *IEEE Transactions on Magnetics*, vol. 40, no. 2, pp. 426–434, 2004.

[253] G. E. Collins and A. G. Akritas, "Polynomial Real Root Isolation using Descarte's Rule of Signs", in *Proceedings of the Third ACM Symposium on Symbolic and Algebraic Computation*, ACM, 1976, pp. 272–275.

[254] G. B. Arfken and H. J. Weber, *Mathematical methods for physicists*, 1999.

[255] H. E. Knoepfel, *Magnetic fields: a comprehensive theoretical treatise for practical use*. John Wiley & Sons, 2008.

[256] M. Kapolka *et al.*, "Three-dimensional modeling of the magnetization of superconducting rectangular-based bulks and tape stacks", *IEEE Transactions on Applied Superconductivity*, vol. 28, no. 4, pp. 1–6, 2018.

[257] E. H. Brandt and M. Indenbom, "Type-II-superconductor strip with current in a perpendicular magnetic field", *Physical review B*, vol. 48, no. 17, p. 12893, 1993.

[258] E. H. Brandt, "Superconductors of finite thickness in a perpendicular magnetic field: Strips and slabs", *Physical review B*, vol. 54, no. 6, p. 4246, 1996.

[259] J. J. Rabbers, "AC loss in superconducting tapes and coils.", Ph.D. dissertation, Twente U., Enschede, Enschede, 2003.

[260] A. Wuis, "AC magnetization loss: The role of dimensionality", M.S. thesis, Twente U., Enschede, Enschede, 2009.

[261] W. Norris, "Calculation of hysteresis losses in hard superconductors carrying ac: isolated conductors and edges of thin sheets", *Journal of Physics D: Applied Physics*, vol. 3, no. 4, p. 489, 1970.

[262] M. Sander and F. Grilli, "FEM-calculations on the frequency dependence of hysteretic losses in coated conductors", in *Journal of Physics: Conference Series*, IOP Publishing, vol. 234, 2010, p. 022030.

[263] E. Pardo *et al.*, "AC loss modeling in superconducting coils and motors with parallel tapes as conductor", *IEEE Transactions on Applied Superconductivity*, vol. 29, no. 5, pp. 1–5, 2019.

[264] E. Marquardt, J. Le, and R. Radebaugh, "Cryogenic material properties database", in *Cryocoolers 11*, Springer, 2002, pp. 681–687.

[265] J. Lu, E. Choi, and H. Zhou, "Physical properties of Hastelloy® C-276^{TM} at cryogenic temperatures", *Journal of applied physics*, vol. 103, no. 6, p. 064908, 2008.

[266] D. R. Smith and F. Fickett, "Low-temperature properties of silver", *Journal of research of the National Institute of Standards and Technology*, vol. 100, no. 2, p. 119, 1995.

[267] M. Pentella, "Magnetic characterization of pure iron for the HALO project", No. EDMS 2476554 (CERN, Geneva, 2021), Tech. Rep., 2021, Available online: https://edms.cern.ch/ui/#!master/navigator/document?D:100765686:100765686:approvalAndComments, accessed on 01 March 2022.

[268] P. Deuflhard, *Newton methods for nonlinear problems: affine invariance and adaptive algorithms*. Berlin: Springer, 2004.

[269] J. Roychowdhury and R. Melville, "Delivering global DC convergence for large mixed-signal circuits via homotopy/continuation methods", *IEEE Transactions on Computer-Aided Design of Integrated Circuits and Systems*, vol. 25, no. 1, pp. 66–78, 2005.

[270] S. Schöps, "Multiscale modeling and multirate time-integration of field/circuit coupled problems", Ph.D. dissertation, Katholieke Universiteit Leuven, 2011.

[271] P. Ferracin *et al.*, "Development of the EuCARD Nb_3Sn Dipole Magnet FRESCA2", *IEEE Transactions on Applied Superconductivity*, vol. 23, no. 3, pp. 4 002 005–4 002 005, 2013.

[272] E. Rochepault *et al.*, "Mechanical analysis of the FRESCA2 dipole during preload, cool-down, and powering", *IEEE Transactions on Applied Superconductivity*, vol. 28, no. 3, pp. 1–5, 2017.

[273] G. Willering *et al.*, "Cold powering tests and protection studies of the FRESCA2 100 mm bore Nb_3Sn block-coil magnet", *IEEE Transactions on Applied Superconductivity*, vol. 28, no. 3, pp. 1–5, 2018.

[274] D. M. Araujo *et al.*, "Preliminary Integration for Testing HTS Feather-M2 in the FRESCA2 Dipole Magnet", *IEEE Transactions on Applied Superconductivity*, vol. 30, no. 4, pp. 1–5, 2020.

[275] J. Van Nugteren *et al.*, "Powering of an HTS dipole insert-magnet operated standalone in helium gas between 5 and 85 K", *Superconductor science and technology*, vol. 31, no. 6, p. 065 002, 2018.

[276] C. Petrone *et al.*, "Measurement and analysis of the dynamic effects in an HTS dipole magnet", *IEEE Transactions on Applied Superconductivity*, vol. 28, no. 4, pp. 1–4, 2018.

[277] Sunam Co. Ltd., Available online: http://http://i-sunam.com, accessed on 01 August 2021.

[278] Y. Iijima, N. Tanabe, O. Kohno, and Y. Ikeno, "In-plane aligned YBa2Cu3O7- x thin films deposited on polycrystalline metallic substrates", *Applied Physics Letters*, vol. 60, no. 6, pp. 769–771, 1992.

[279] R. Reade, P. Berdahl, R. E. Russo, and S. Garrison, "Laser deposition of biaxially textured yttria-stabilized zirconia buffer layers on polycrystalline metallic alloys for high critical current Y-Ba-Cu-O thin films", *Applied Physics Letters*, vol. 61, no. 18, pp. 2231–2233, 1992.

[280] J. Fleiter *et al.*, "Characterization of Roebel cables for potential use in high-field magnets", *IEEE Transactions on Applied Superconductivity*, vol. 25, no. 3, pp. 1–4, 2014.

[281] W. Goldacker *et al.*, "ROEBEL assembled coated conductors (RACC): preparation, properties and progress", *IEEE Transactions on Applied Superconductivity*, vol. 17, no. 2, pp. 3398–3401, 2007.

[282] W. Goldacker *et al.*, "Roebel cables from ReBCO coated conductors: a one-century-old concept for the superconductivity of the future", *Superconductor Science and Technology*, vol. 27, no. 9, p. 093 001, 2014.

[283] L. Roebel, *Conductor for electrical machines, which consists two or more groups of partial conductors, DE Patent DE277012C*, 1914.

[284] Fujikura Ltd., Available online: https://www.fujikura.com/solutions/superconductingwire/, accessed on 01 March 2022.

[285] U. Römer, S. Schöps, and H. De Gersem, "A defect corrected finite element approach for the accurate evaluation of magnetic fields on unstructured grids", *Journal of Computational Physics*, vol. 335, pp. 688–699, 2017.

[286] S. Russenschuck, "Roxie: the routine for the optimization of magnet x-sections, inverse field computation and coil end design", CERN, Tech. Rep., 1993.

[287] D. C. Jiles and D. L. Atherton, "Theory of ferromagnetic hysteresis", *Journal of magnetism and magnetic materials*, vol. 61, no. 1-2, pp. 48–60, 1986.

[288]   R. Szewczyk and P. Cheng, "Open Source Implementation of Different Variants of Jiles-Atherton Model of Magnetic Hysteresis Loops", *Acta Physica Polonica. A,* vol. 133, no. 3, pp. 654–656, 2018.

[289]   M. Buzio, "Fabrication and calibration of search coils", *arXiv preprint arXiv:1104.0803*, 2011.

[290]   P. Arpaia, L. Bottura, L. Fiscarelli, and L. Walckiers, "Performance of a fast digital integrator in on-field magnetic measurements for particle accelerators", *Review of Scientific Instruments,* vol. 83, no. 2, p. 024 702, 2012.

[291]   L. Bortot *et al.*, "High-Temperature Superconducting Screens for Magnetic Field-Error Cancellation in Accelerator Magnets", *Superconductor Science and Technology*, no. 12, 2021. arXiv: 2103.14354.

[292]   L. Walckiers, "The harmonic-coil method, parts 1 and 2", in *CERN Accelerator School: Magnetic measurement and alignment*, CERN, 1992, pp. 138–165.

[293]   A. K. Jain, "Harmonic coils", in *CERN Accelerator School: Measurement and Alignment of Accelerator and Detector Magnets*, CERN, 1992, pp. 175–213.

[294]   Superpower Inc., Available online: https://www.superpower-inc.com/, accessed on 01 March 2022.

[295]   D. Hu *et al.*, "Modeling and comparison of in-field critical current density anisotropy in high-temperature superconducting (HTS) coated conductors", *IEEE Transactions on Applied Superconductivity*, vol. 26, no. 3, pp. 1–6, 2016.

[296]   *MATLAB version 9.5.0.944444 (R2018b)*, The Mathworks, Inc., Natick, Massachusetts, 2018.

[297]   J. Kennedy and R. Eberhart, "Particle swarm optimization", in *Proceedings of ICNN'95-International Conference on Neural Networks*, IEEE, vol. 4, 1995, pp. 1942–1948.

[298]   B. Bellesia, F. Bertinelli, C. Santoni, and E. Todesco, "Dependence of magnetic field quality on collar supplier and dimensions in the main LHC dipole", *IEEE transactions on applied superconductivity*, vol. 16, no. 2, pp. 196–199, 2006.

[299]   R. Gupta, "A common coil design for high field 2-in-1 accelerator magnets", in *Proceedings of the 1997 Particle Accelerator Conference (Cat. No. 97CH36167)*, IEEE, vol. 3, 1997, pp. 3344–3346.

[300]   F. Toral *et al.*, "EuroCirCol 16 T common-coil dipole option for the FCC", *IEEE Transactions on Applied Superconductivity*, vol. 27, no. 4, pp. 1–5, 2016.

[301]   F. Toral, J. Munilla, and T. Salmi, "Magnetic and mechanical design of a 16 T common coil dipole for an FCC", *IEEE Transactions on Applied Superconductivity*, vol. 28, no. 3, pp. 1–5, 2018.

[302]   G. Barnes, M. McCulloch, and D. Dew-Hughes, "Computer modelling of type II superconductors in applications", *Superconductor Science and Technology*, vol. 12, no. 8, p. 518, 1999.

[303]   T. Coombs, A. Campbell, A. Murphy, and M. Emmens, "A fast algorithm for calculating the critical state in superconductors", *COMPEL-The international journal for computation and mathematics in electrical and electronic engineering*, 2001.

Acknowledgments

First of all, I would like to express deep gratitude to my supervisor at TU Darmstadt Prof. Dr. rer. nat. Sebastian Schöps, for giving me the amazing opportunity of working on this thesis in these years. His guidance, expert advise, and wise suggestions were determinant in keeping me focused and motivated, especially during challenging times. The very same gratitude goes to Dr. ir. Matthias Mentink, for his brilliant day-to-day supervision at CERN, and for constantly supporting this thesis with great enthusiasm and optimism.

Secondly, I am also very grateful to Dr. Arjan Verweij for giving me the opportunity to work on this thesis in the TE-MPE-PE section at CERN. I would like to thank him for his continued support, valuable suggestions and feedback, and all the scientific discussions and informal chats we had in front of a good coffee.

I am grateful to Dr. Ing. Idoia Cortes Garcia and Prof. Herbert De Gersem at TU Darmstadt, and to Dr. Ing. Bernhard Auchmann at PSI. Thanks for having guided me through the intricacies of the mathematical analysis of electromagnetic fields. Your valuable support was determinant for the development of the theoretical part of this work.

One of the most exciting parts of this work was collaborating with Dr. Jeroen van Nugteren. I would like to thank him for having shared his knowledge, supported the development of the numerical models, and for that crucial coffee-break which led to the idea of HALO. A conceptual idea needs also experimental evidence. Luckily, I met valuable colleagues supporting the proof of concept. I would like to thank Glyn Kirby, Francois-Olivier Pincot, Juan Carlos Perez, and Torsten Koettig for the design and manufacturing of the prototype, and Carlo Petrone, Guy Deferne, and Mariano Pentella for the magnetic characterization. A special thanks to Erik Schnaubelt and Michał Maciejewski, who shared their enthusiasm about this thesis, and patiently proofread it. In addition, a special thanks to the administrative staff both CERN and TU Darmstadt.

I would also thank my CERN colleagues Dimitri, Mariusz, Emmanuele, Christoph, and Giovanni for all fruitful discussions and their company during the workdays. A heartfelt thanks also to my dear friends Marco and Giuliana, Elena, Mattia, Yuri and Francesca, Elia and Francesca, Federico and Alessia, Marcello, Paolo, and Giovanni; all the nice moments we shared will stay with me forever.

A special thanks goes to my parents, whose hard work and sacrifices allowed me to access higher education, changing my life. A big thanks to all my family, for all your love and support. Finally, my deepest gratitude goes to Jenny, who always believed in me, keeping me motivated during the research and especially the writing process. She never gave up in reminding me that there is always the sun behind the clouds.